NANOCOMPOSITES OF 2D NANOMATERIALS AND METAL OXIDES FOR MULTIFUNCTIONAL APPLICATIONS

THESIS

Submitted to
Delhi Technological University
in fulfilment of the requirements for the degree of

DOCTOR OF PHILOSOPHY

by

NIKITA JAIN
(2K18/PHDAP/509)

Under the supervision of

PROF. NITIN K. PURI

DEPARTMENT OF APPLIED PHYSICS
DELHI TECHNOLOGICAL UNIVERSITY
DELHI-110042, INDIA

OCTOBER 2024

DEDICATION

This dissertation is dedicated to my family and supervisor.

ACKNOWLEDGEMENT

Above all, I extend my heartfelt gratitude to the almighty for providing me with the strength and patience needed to persevere throughout these years of hard work.

I hope this acknowledgement serves as a little token of my sincere appreciation to everyone who helped me in this journey.

I wholeheartedly want to thank my supervisor, **Prof. Nitin K. Puri**, for his excellent mentorship, patience, motivation, enthusiasm, immense knowledge, and continuous support through all these years. His persistent commitment and rich reservoir of knowledge have not only made the journey easier but have also been instrumental in shaping the core of my thesis. His mentorship is a rare gem and I consider myself extraordinarily fortunate to have had the privilege of being nurtured under his unparalleled guidance. He is not just an advisor; he is a beacon of inspiration and mentorship that is truly one of a kind, a rare gem in the realm of academia.

My sincere thanks also go to **Prof. Prateek Sharma** Hon'ble Vice-Chancellor, DTU for providing marvellous research environment and ample research facilities to conduct this research. My heartfelt recognition to **Prof. Rinku Sharma**, Dean (Academic-PG), DTU, **Prof. S.C. Sharma**, DRC Chairperson, Department of Applied Physics, DTU, **Prof. Vinod Singh**, Head of the Department of Applied Physics, DTU and all other faculties and staff members for their help and cooperation throughout my research. Thanks to the **Department of Applied Physics, Delhi Technological University (DTU)**, for providing the required facilities so that I can work voraciously, barring the time limit.

A special thanks to my friend and senior **Dr. Ritika Khatri** whose unwavering support and assistance have been indispensable throughout these years. She has consistently stood by my side, offering guidance and aid at every turn. Her enduring warmth and comforting presence have been a source of great solace during challenging times. I am truly grateful for the countless moments we've shared together at DTU. Each interaction with her has been a treasure trove of wisdom and camaraderie, leaving an indelible mark on my journey. These memories, filled with laughter, shared insights, and mutual support, will forever hold a special place in my heart as cherished golden moments. Her friendship has been a beacon of light, illuminating my path and enriching my experiences. I am profoundly thankful for her unwavering kindness, support, and friendship.

I express my sincere thanks to **Dr. Pawan Kr. Tyagi,** Associate Professor at Delhi Technological University, **Dr. Senthil Kumar Kandasamy,** Associate Professor at Kongu Engineering College, and **Dr. Savita Sharma**, Assistant Professor at Kalinda College, Delhi University for their invaluable time and expertise in our scientific and technical discussions. Their insights have greatly enriched my understanding and approach to various challenges. I extend my gratitude to **Dr. Saurabh Srivastava**, Assistant Professor at Rajkiya Engineering College, Ambedkar Nagar, Uttar Pradesh, India, for providing me with invaluable guidance and direction in the field of gas-sensing.

I am immensely grateful to my labmates **Mr. Saroj Kumar Jha, Mr. Hemant Kumar Arora, and Mr. Sunil Kumar** who stood by me unwaveringly, serving as pillars of support through every high and low. The memories we shared will forever hold a special place in my heart, and bidding farewell to this chapter leaves me with a profound sense of nostalgia. I am truly grateful for the friendship and camaraderie we've cultivated. The laughter, the shared experiences, and the bonds forged during our time together will remain etched in my memory as cherished moments of joy and companionship. Their support and companionship have undoubtedly left a lasting impression on me, for which I am immensely thankful. I am grateful to my seniors, **Dr. Deepika Sandil, Dr. Kamal Arora, and Dr. Vikash Sharma**, for illuminating the path of research and for their accessibility during valuable discussions. Additionally, I extend my thanks to **Dr. Archit Dhingra** for generously dedicating his time and engaging in insightful discussions pertaining to our research topic.

I extend my gratitude to **Ms. Ashi Mittal and Mr. Anmol Aggarwal** for their unwavering support, invaluable assistance, and the precious time they've dedicated to me. Engaging in discussions with them has always been incredibly fruitful; their insights and perspectives have added immense value to my endeavors. The camaraderie shared with them has been a source of joy and inspiration. Whether it was brainstorming ideas, tackling challenges, or simply enjoying each other's company, every moment spent with them has been enriching and fulfilling. Their presence has infused a sense of positivity and enthusiasm into our interactions, making every discussion meaningful and every experience memorable.

Furthermore, I wish to express my gratitude to my friends at DTU, including **Dr. Manjot Kaur, Dr. Vishal Singh, Dr. Kailash Chandra, Mr. Anurag, Dr. Km. Komal, and Ms. Shilpa Rana** for their unwavering technical guidance, valuable suggestions, and support throughout this journey. I am deeply thankful for the enriching discussions and invaluable guidance they provided throughout our research endeavors. I extend my heartfelt appreciation to the other members of my lab and my esteemed colleagues **Mr. Sandeep Sarpal, Mr. Abhishek Kumar, and Mr. Vishwas Kumar** for their invaluable cooperation and camaraderie.

I want to pay high regard to my husband, **Mr. Deepak Jain**, my father, **Mr. Sushil Jain**, my father-in-law, **Mr. K.C. Jain**, my mother, **Mrs. Anita Jain** and my mother-in-law, **Mrs. Santosh Jain**, for their unwavering love, care, and emotional support. My father has been the most significant pillar of support during these years. He has invested all of his time in trying to make me a successful person. He always taught me to work beyond my limits. I would like to extend a special thank you to my beloved daughter **Gurvi Jain**. Her patience, understanding, and encouragement have been invaluable throughout this journey. I am grateful for your love and understanding, which have made this achievement possible. The encouragement and support from my younger brother and sister **Mr. Vaibhav Jain and Ms. Shruti Jain** always motivated me to accomplish this thesis work. Their faith, trust and confidence in me always pushed me towards my goal. Their contagious laughter and light hearted presence, which lightened my challenging Ph.D. journey and offered a welcome feeling of joy and innocence. The support, compassion, tolerance, and encouragement from my family got me through this challenging journey. I sincerely appreciate all that you have done for me over the years.

Nikita Jain

2K18/PHDAP/509

DELHI TECHNOLOGICAL UNIVERSITY
(Govt. of National Capital Territory of Delhi)
Shahbad Daulatpur, Bawana Road, Delhi-110042

CANDIDATE’S DECLARATION

I, **Ms. Nikita Jain**, hereby certify that the thesis titled **“*Nanocomposites of 2D Nanomaterials and Metal Oxides for Multifunctional Applications*”** submitted in the fulfilment of the requirements for the award of the degree of Doctor of Philosophy is an authentic record of my research work carried out under the supervision of **Prof. Nitin K. Puri**. This work in the same form or any other form has not been submitted by me or anyone else earlier for any purpose. Any material borrowed or referred to is duly acknowledged.

Nikita Jain
(2K18/PHDAP/509)
Department of Applied Physics
Delhi Technological University
Delhi – 110042, India

DELHI TECHNOLOGICAL UNIVERSITY
(Govt. of National Capital Territory of Delhi)
Shahbad Daulatpur, Bawana Road, Delhi-110042

CERTIFICATE

This is to certify that the thesis entitled **“*Nanocomposites of 2D Nanomaterials and Metal Oxides for Multifunctional Applications*”** submitted by **Ms. Nikita Jain (2K18/PHDAP/509)** to Delhi Technological University (DTU), Delhi, India for the degree of Doctor of Philosophy, is a bonafide record of the research work carried out by her under my supervision and guidance. The work embodied in this thesis has been carried out in the Nanomaterials Research Laboratory (NRL), Department of Applied Physics, Delhi Technological University (DTU), Delhi, India. The work of this thesis is original and has not been submitted in parts or fully to any other Institute or University for the award of any other degree or diploma.

Prof. Nitin K. Puri
Supervisor
Delhi Technological University
Delhi-110042, India

Prof. Vinod Singh
Head of the Department
Department of Applied Physics
Delhi Technological University

Prof. Binay Kumar

Examiner
Department of Physics & Astrophysics
University of Delhi, Delhi-110007

ABSTRACT

Nanocomposites of 2D Nanomaterials and Metal Oxides for Multifunctional Applications

With the progression of science and technology, air pollution has emerged as a significant concern for society. The emission of hazardous gases and volatile organic compounds (VOCs) into the environment not only poses a threat to atmospheric conditions but also poses risks to human health. VOCs are organic substances capable of vaporizing rapidly and dispersing into the air, even at room temperature, due to their low boiling points. According to the World Health Organization (WHO), air pollution stands as the primary cause of premature death and various illnesses. Consequently, it becomes imperative to detect and regulate the release of these pollutants to mitigate their adverse effects on both the environment and human health. Ethanol a common VOC, is deeply ingrained in our daily lives. However, it's important to acknowledge that prolonged exposure to ethanol can pose serious risks to human health, including irritation of the nose and throat, vomiting, kidney failure, nausea, headaches, and damage to the central nervous system. In extreme cases, it has even been linked to cancer. Additionally, as a flammable gas with an explosion range of 3.3 – 19%, ethanol contributes to numerous traffic accidents. Its vapor can form explosive mixtures when combined with other gases, further exacerbating safety concerns. Given these risks, addressing the immediate and potential dangers associated with ethanol exposure has become a paramount concern. Hence, it is crucial to implement timely monitoring and detection systems for ethanol gas, particularly at room temperature, as an integral component of safety measures.

With this aim, a room temperature chemiresistive ethanol gas sensor based on hydrothermally synthesized zinc oxide (ZnO) incorporated-molybdenum diselenide ($MoSe_2$) nanosheets has been investigated. The sensing properties of the $MoSe_2$/ZnO nanocomposite sensor have been investigated systematically by exposing the sensor to various ethanol gas concentrations (10- 500 ppm) in dry N_2 and dry air. The synergistic

effect due to the incorporation of ZnO nanorods in $MoSe_2$ nanosheets has been found to enhance the sensor response to ethanol gas (when operated in dry N_2) with improved response and recovery time of 8.4 and 14.7 seconds respectively, high selectivity, stability, and reproducibility. The nanocomposite-based sensor has shown a high gas sensing response (R_g/R_a) of 37.8 to 500 ppm of ethanol gas in dry N_2. While the response of the nanocomposite-based sensor has decreased to 15.3 to 500 ppm of ethanol gas in dry air which suggests that the sensor has performed better when operated in dry N_2 than in dry air. The sensor has demonstrated a p-type characteristic response. Importantly, the sensor has operated at RT and has been able to detect ethanol down to 10 ppm. Besides, the sensor has also established prolific long-term stability of 4 weeks. The sensor has exhibited improved response (8.4 s) and recovery (14.7 s) time to 500 ppm ethanol gas compared to previously reported values. The enhancement in performance of the sensor has been due to the formation of a p-n junction at the interface of the $MoSe_2$/ZnO nanocomposite sensor. Furthermore, potential barrier modulation at the interface has provided a positive effect on sensitivity performance.

After studying the enhanced performance of the $MoSe_2$/ZnO nanocomposite sensor due to the formation of p-n heterojunction at the interface of $MoSe_2$ nanosheets and ZnO nanorods, we have explored a ternary nanocomposite of $MoSe_2$-ZnO heterojunctions decorated rGO ($MoSe_2$/ZnO/rGO). In this work a highly stable, exceptionally selective, and reliably repeatable ethanol gas sensing device has been successfully developed using the ternary $MoSe_2$/ZnO/rGO nanocomposite, promising long-term stability. Importantly, the ternary nanocomposite sensing device has exhibited a fantabulous sensing response of 50.2 to 500 ppm ethanol gas. The ternary nanocomposite sensing device has been able to detect ethanol down to 1 ppm at room temperature. The developed ternary nanocomposite sensing device has shown a considerably fast response time (6.2 s) and recovery time (12.9 s) to 500 ppm ethanol gas. Besides, the sensing device also establishes prolific long-term stability of 6 weeks. The superior performance of the developed ternary nanocomposite sensing device has been owed to the formation of a p-n heterojunction between $MoSe_2$ nanosheets and ZnO nanorods with the aid of rGO nanosheets. The attachment of the

$MoSe_2$ nanosheets and ZnO nanorods onto rGO nanosheets has not only provided various p-n heterojunctions but has also offered more active sites for the adsorption and desorption of ethanol molecules. This has improved the gas-sensing response of the sensing device toward ethanol significantly. Additionally, the conductive network of rGO nanosheets has facilitated fast electron transfer between $MoSe_2$ nanosheets and ZnO nanorods, endowing the ternary nanocomposite sensing device with quick response and recovery time.

The widespread adoption of Internet of Things (IoT) technology has created an increasing demand for reliable gas sensor networks across a variety of applications, including air pollution monitoring, industrial safety, smart cities, and personal healthcare. In this context, we have investigated self-powered devices that seamlessly integrate gas sensing capabilities with energy generation. This exploration aims to enhance the efficiency and sustainability of sensor networks, ensuring they meet the growing demands of modern applications. In this study, a novel self-powered ethanol gas sensor, exhibiting excellent selectivity, sensitivity, and stability, has been developed based on n-type SnS nanoflakes at room temperature. The n-type SnS-based HEC serves as the power source for self-powered ethanol gas sensors, enabling the detection of various concentrations of ethanol gas at RT. Consequently, the power supply and gas sensor have been effectively combined into a single device, demonstrating a successful integration of both functionalities. X-ray diffraction (XRD), field emission scanning electron microscopy (FESEM), high-resolution transmission electron microscopy (HRTEM), Energy dispersive X-ray (EDX) and Brunauer-Emmett-Teller (BET) analysis have confirmed the formation of orthorhombic SnS nanoflakes with a high specific surface area (6.15 $m^2\ g^{-1}$). The observed voltage-current (V-I) characteristic curves of the HEC at RT have shown a maximum current (I_{max}) of 40 μA and voltage of 1.03 V. The sensing performance of the self-powered ethanol gas sensor has been analysed for various concentrations of ethanol gas (10 - 100 ppm). The sensor has exhibited a response value (R_a/R_g) of 41.3 to 100 ppm ethanol gas concentration, with quick response/recovery times of 27.3 s/31.4 s respectively at RT. The sensor has shown promising potential for prolonged ethanol gas detection (30 days). The experimental results have demonstrated that the n-type SnS-based self-powered ethanol gas sensor represents a promising platform for integration into future large-scale IoT systems. This breakthrough paves the way for more versatile and scalable IoT solutions, enabling continuous environmental monitoring and data collection across various settings.

LIST OF PUBLICATIONS

Publications in Peer Reviewed Journals:

1. **Nikita Jain**, and Nitin K. Puri. "*Zinc oxide incorporated molybdenum diselenide nanosheets for chemiresistive detection of ethanol gas.*" Journal of Alloys and Compounds 955 (2023): 170178. (**Impact Factor** – 6.3)

2. **Nikita Jain**, and Nitin K. Puri. "*A Proposed Device Based on $MoSe_2$-ZnO Heterojunctions on rGO for Enhanced Ethanol Gas Sensing Performances at Room Temperature.*" Nanotechnology, 35 (2024): 405502. (**Impact Factor** – 2.9)

Communicated:

3. **Nikita Jain,** Hemant K. Arora, Sunil Kumar, and Nitin K. Puri, *"First Report on Hydroelectric Cell-Driven Gas Sensor for the Detection of Ethanol at Room Temperature: A Novel Approach"*.

Publications not included in this thesis:

4. **Nikita Jain**, Savita Sharma, and Nitin K. Puri. "Investigation of charge transport mechanism in hydrothermally synthesized reduced graphene oxide (rGO) incorporated zinc oxide (ZnO) nanocomposite films." *Journal of Materials Science: Materials in Electronics* 33, no. 3 (2022): 1307-1323. (**Impact Factor** – 2.8)

5. Hemant K. Arora, **Nikita Jain**, Sunil Kumar, and Nitin K. Puri. *"Vertically aligned 2D tin sulfide (SnS) nanoplates for selective detection of ethanol gas at room temperature."* Semiconductor Science and Technology 39, no. 10 (2024): 105002. (**Impact Factor** – 2.1)

6. Shreya, Anukool Yadav, Ritika Khatri, **Nikita Jain**, Anurag Bhandari, and Nitin K. Puri. "*Double zone thermal CVD and plasma enhanced CVD systems for deposition of films/coatings with eminent conformal coverage.*" In Advances in Manufacturing Technology and Management: Proceedings of 6th International Conference on Advanced Production and Industrial Engineering (ICAPIE)—2021, pp. 273-283. Singapore: Springer Nature Singapore, 2022.

7. Sunil Kumar, **Nikita Jain**, Hemant K. Arora, and Nitin K. Puri, *“Highly Selective Chemiresistive Ethanol Sensing Based on Vanadium Disulfide (VS_2) Nanoflowers at Room Temperature.”,* Springer Proceedings in Physics (2nd International Conference on Atomic, Molecular, Material, Nano and Optical Physics with Applications) (ICAMNOP – 2023).

Conference Contributions-Poster:

1. **Nikita Jain** and Nitin K. Puri, *“Room Temperature Chemiresistive Detection of Ethanol Gas Based on Zinc Oxide Incorporated Molybednum Diselenide Nanosheet.s*”, ICAMNOP 2024, at Delhi Technological University, New Delhi, India, 20th – 22nd Dec 2023. **(POSTER)**

2. **Nikita Jain** and Nitin K. Puri, *“Investigation of Electrochemical Properties: Influence of Morphology of Hydrothermally Synthesized ZnO Nanostructures.”*, ICNOC 2022, at Jamia Millia Islamia, New Delhi, India, 28th – 30th Nov 2022. **(POSTER) (Received Best Poster Award)**

3. **Nikita Jain** and Nitin K. Puri, “*Fabrication and Characterization of WS2 thin films sensor for hydrogen gas sensing application*”, IEEE – ICEE 2020, at IIT Delhi, New Delhi, India, 26th - 28th Nov, 2020. **(POSTER)**

TABLE OF CONTENTS

Page No.

Chapter 4: A Proposed Device based on $MoSe_2$-ZnO Heterojunctions on rGO for Enhanced Ethanol Gas Sensing Performances at Room Temperature 81-105

Chapter 5: First Report on Hydroelectric Cell-Driven Gas Sensor for the Detection of Ethanol at Room Temperature: A Novel Approach 106-126

LIST OF TABLES

Table No. **Page No.**

Chapter 1

Chapter 3

Chapter 4

Chapter 5

LIST OF FIGURES

Figure No. **Page No.**

Chapter 1

Chapter 2

Chapter 3

Chapter 4

Chapter 5

LIST OF ABBREVIATIONS

Acronyms	**Meaning**
RT	Room temperature
VOCs	Volatile organic compounds
C_2H_5OH	Ethanol
ITO	Indium tin oxide
0D	Zero-dimensional
1D	One-dimensional
2D	Two-dimensional
3D	Three-dimensional
TMCs	Transition metal chalcogenides
TMDs	Transition metal dichalcogenides
MCs	Metal monochalcogenides
TMTs	Transition metal trichalcogenides
$MoSe_2$	Molybdenum diselenide
ZnO	Zinc oxide
SnS	Tin sulphide
GO	Graphene oxide
rGO	reduced Graphene oxide
XRD	X-ray diffraction
SEM	Scanning electron microscopy
FESEM	Field-emission scanning electron microscopy
TEM	Transmission electron microscopy
HRTEM	High-resolution transmission electron microscopy
FTIR	Fourier transform infrared spectroscopy
EPD	Electrophoretic deposition technique
SAED	Selected area electron diffraction
BET	Brunauer-Emmett-Teller
BJH	Barret-Joyner-Halenda
RE	Reference electrode
WE	Working electrode

MFC	Mass flow controller
SMU	Source measuring unit
R_a	Resistance in the presence of air
R_g	Resistance in the presence of target gas molecules
t_{resp}	Response time
t_{rec}	Recovery time
HEC	Hydroelectric cell
SPEG	Self-powered ethanol gas

CHAPTER 1

Introduction and Scientific Motivation

Chapter 1 gives a brief introduction to the growing interest in developing ethanol gas sensors that operate efficiently at room temperature while consuming minimal power. It starts with an in-depth exploration of the pressing need for ethanol sensors with sensitivity, stability, and selectivity, particularly capable of operating at room temperature and detecting a wide range of ethanol concentrations. It then discusses the various categories of existing ethanol sensing technologies with an emphasis on chemiresistive sensors. Further, the chapter focuses on the integration of nanotechnology and material science with sensing technologies for improving various sensing parameters across a wide range of applications. In this regard, special attention is given to nanocomposites of 2D nanomaterials and metal oxides-based ethanol gas sensors. Through this detailed discussion, the chapter identifies existing knowledge gaps and outlines the objectives of the thesis, thereby setting the stage for further exploration and research in this field.

1.1 Need for volatile organic compounds (VOCs) sensing

Environmental pollution has become a critical concern due to the rapid growth of industrialization and urbanization [1, 2]. As the economy and industry improve, the release of volatile organic compounds (VOCs) into the atmosphere also increases [3]. VOCs have low boiling points due to high vapor pressure because of which they can easily evaporate into the atmosphere even at room temperature (RT) [4]. VOCs are found in both outdoor and indoor environments [5]. Generally driving a car, house paint, making a fire, or simply breathing results in the release of organic compounds [6]. The use of personal care and consumable products also adds up to a significant amount of VOCs in the atmosphere [6]. Almost every daily life activity of humans leads to the release of organic compounds in the environment. The concentration of VOCs is almost ten times higher in indoor environments compared to outdoor [7]. Further, it has been estimated that approximately 50-300 VOCs are present in the indoor air at offices, homes, schools, shopping complexes, and various commercial buildings. The various sources of VOCs and their percentage contribution to the environment are shown in Fig. 1.1 [5].

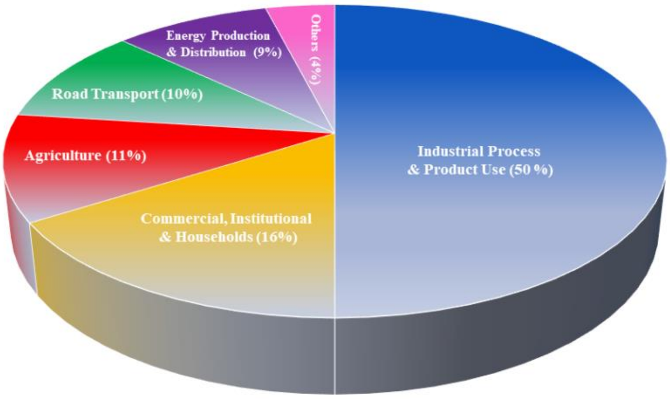

Fig. 1.1: Various sources of VOCs and their percentage contribution to the environment

The most common VOCs are ethanol (C_2H_5OH), methanol (CH_3OH), acetone (CH_3COCH_3), formaldehyde (HCHO), benzene (C_6H_6), toluene (C_7H_8), acetylene (C_2H_2), cyclohexane (C_6H_{10}), etc. Exposure to VOCs is considered to be hazardous not only to humans, and living bodies but also to the environment [8, 9]. The adverse effects and threshold values of some VOCs on human health are listed in Table 1.1 [10].

Table 1.1: The name of VOCs, their chemical formula, their effect on human health, and threshold values

VOC Name	Chemical Formula	Effect on Human Health	Threshold Value
Ethanol	C_2H_5OH	Nose and throat irritation, vomiting, kidney failure, nausea, headaches, central nervous system damage, and can even cause cancer	1000 ppm
Methanol	CH_3OH	Airway narrowing, vertigo, headache, bronchial constriction, nausea, headache, bronchial constriction, nausea	200 ppm
Acetone	CH_3COCH_3	Headache, fatigue, mouth dryness, nausea, and dizziness	750 ppm
Formaldehyde	HCHO	Eye irritation, shortness of breath, chest tightness or pain	0.75 ppm
Benzene	C_6H_6	Narcotic effects, convulsion, respiratory failure	1 ppm
Toluene	C_7H_8	Serious damage to the liver, skin, kidneys, and the central nervous system	100 ppm
Acetylene	C_2H_2	Dizziness, fatigue, headache, tachycardia, nausea, vomiting	N/A
Cyclohexane	C_6H_{10}	Irritation to the eyes, throat, respiratory tract	300 ppm

Ethanol is one of the most consumable VOCs used in paints industries, cosmetic industries, agricultural production, alcoholic beverages, food industries, chemical and pharmaceutical communities, etc. [11, 12]. Exposure to high concentrations of ethanol strongly affects human health by causing nose and throat irritation, vomiting, kidney failure, nausea, headaches, central nervous system damage, and can even cause cancer [13, 14]. According to the World Health Organisation (WHO), excessive consumption and various health issues caused by ethanol are the cause of deaths of over 3 million people [15]. It is a flammable gas with an explosion range of 3.3 – 19%, which can lead to many traffic accidents [16]. Importantly, ethanol in its vapor form combines with other gasses which creates an explosive mixture, making it the most dangerous and combustible among other VOC gases [12]. Thus, it is the topmost priority to resolve the potential risk associated with exposure to ethanol gas on human health as well as the environment. Moreover, human sensory organs cannot detect the leakage of ethanol gas timely and accurate [1]. Therefore, it is crucial to establish effective and timely monitoring and detection mechanisms for ethanol gas, particularly at RT. Gas sensors operating at RT with high sensing properties are particularly appealing due to their low power consumption, ease of miniaturization, simple fabrication, long-term stability, and consistent performance [17].

The widespread implementation of Internet of Things (IoT) technology has led to a growing need for reliable gas sensor networks across diverse applications such as air pollution monitoring, industrial safety, smart cities, and personal healthcare [18, 19]. However, the scale of these networks demands sensors with specific attributes: they must be micro- or nanosized, exhibit reliable selectivity, have shorter response times, and consume significantly less power than existing commercial devices [18]. Traditional battery-powered sensors rely on integrated batteries for power, which poses several limitations. Firstly, these batteries have finite energy storage capacities and require regular replacement, leading to maintenance challenges and high costs, especially in remote or inaccessible environments [17]. Moreover, battery dependence introduces performance degradation in harsh conditions due to safety and stability concerns [20]. This reliance on integrated batteries not only limits the sensor's performance but also escalates operational costs and maintenance efforts, particularly in remote or inaccessible areas [19]. Additionally, batteries pose safety and stability risks in harsh environments, further compromising the sensor’s performance. To overcome these challenges, scientists are trying to reduce the power consumption of sensors, meantime exploring self-powered devices integrated with sensing and power generation [21].

1.2 Classification of sensors

Interaction of ethanol with the sensing element of an ethanol sensor can change its resistance, capacitance, temperature, mass, pressure, or other properties. These changes are then transduced into recognizable electrical signals. Based on the method of transduction, sensor technologies can be classified as electrical, optical, gravimetric, or thermal [22-24]. Various types of sensors and the subcategories are shown in Fig. 1.2.

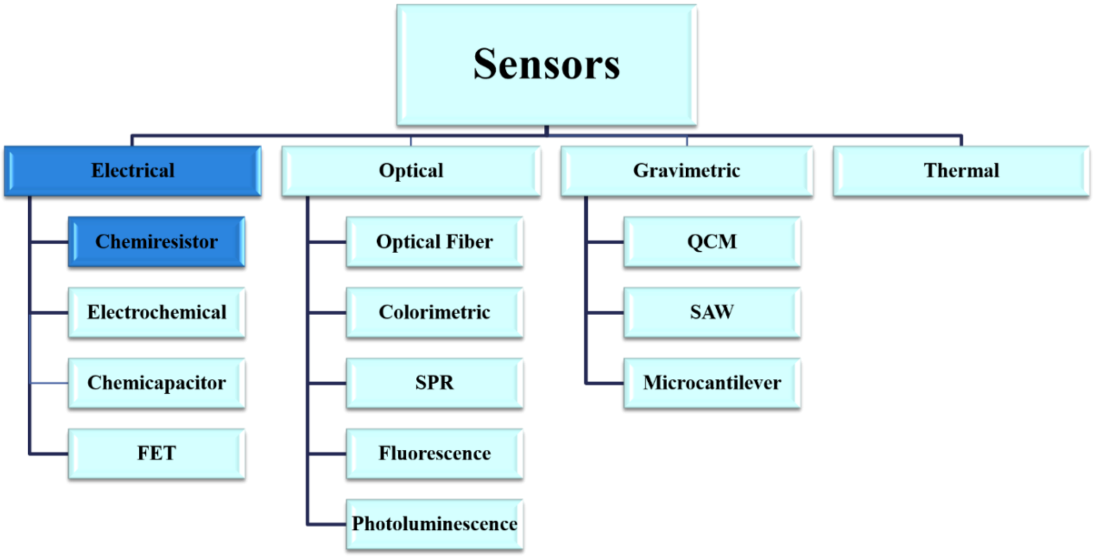

Fig. 1.2: Various types of sensors and sub-categories

Based on the type of device architecture, electrical sensors can be sub-categorized into chemiresistors, chemicapacitors, and field effect transistors (FETs) based sensors. Optical sensors can be sanctioned into the optical fiber, colorimetric, fluorescence, photoluminescence, and surface plasmon resonance (SPR) sensors. The gravimetric sensors can be divided into quartz crystal microbalance (QCM), surface acoustic wave (SAW), and microcantilever sensors. The present thesis emphasizes the development of chemiresistor sensors based on nanocomposites of 2D nanomaterials and metal oxides for gas sensing applications.

Chemiresistor sensors are chemical sensors whose resistance changes upon exposure to VOCs [25, 26]. The change in resistance of the sensor is in proportion to the amount of VOC exposed on the sensor, thus enabling the VOC to be detected. Since the 1960s, chemiresistor sensors have gained huge interest for VOC sensing due to ease of fabrication, simple monitoring technique, easy design, low cost, high chemical and thermal stability, easy integration in existing electronic circuits, high sensitivity, wide acceptance of sensing materials, etc. [16, 27]. Chemiresistor sensors have a variety of applications in environmental air quality monitoring, hazardous gas sensing, food quality control and processing, military applications, industrial production monitoring, the automobile industry, medical care, disease diagnosis, and many more [28-36].

A chemiresistor sensor contains active sensing materials coated on a solid substrate i.e., glass, indium tin oxide (ITO) coated corning glass substrate, fluorine tin oxide (FTO) coated corning glass substrate, etc. Upon the sensing material conducting electrodes (like aluminum (Al), silver (Ag), gold (Au), etc.) are deposited for attaining the electrical connections. A multimeter is connected to the sensing material through these electrodes to record its resistance change. The schematic diagram of the chemiresistor sensor is shown in Fig. 1.3.

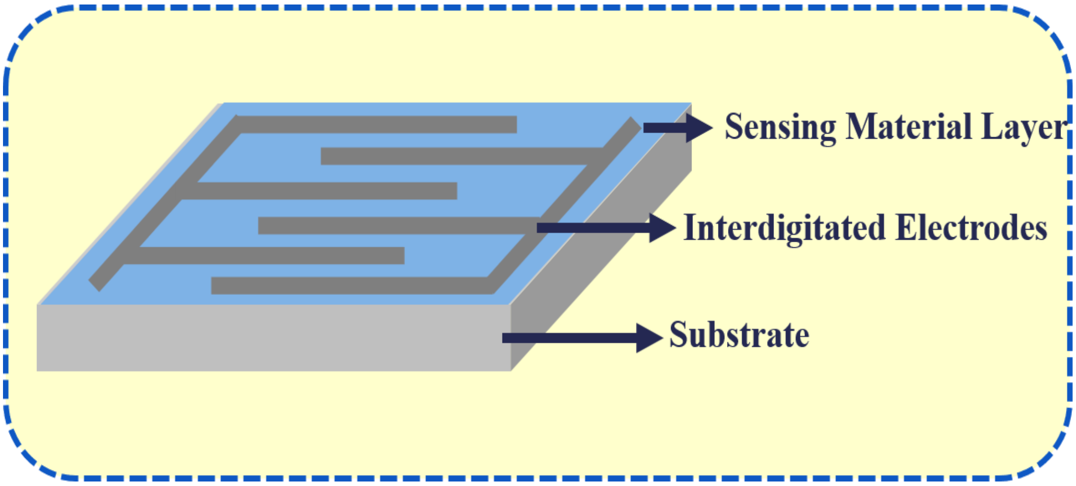

Fig. 1.3: Schematic diagram of a simple chemiresistor sensor

So far wide range of nanomaterials have been incorporated in chemiresistor sensors for the detection of VOCs which includes 2D nanomaterials, metal oxides, metal nanoparticles, conducting polymers, nanocomposites, etc. [8, 12, 37-39].

1.2.1 Important gas sensing performance parameters

To differentiate the gas sensors according to their performance, some of the key features are as follows:

1. **Response:** A sensor response depicts the alteration in the resistance or current under the exposure of target gas molecules. The change in the resistance of the sensor can be estimated using different methods.

(1) When the target gas is reducing and the material is p-type, the response is defined as the ratio between the sensor's resistance in the presence of target gas molecules (R_g) and its resistance in the presence of air (R_a). The response is defined as R_a/R_g when the target gas is oxidative.

Response= R_g/R_a (for reducing gas) (1.1)

Response= R_a/R_g (for oxidizing gas) (1.2)

(2) Relative response is defined by the following equations for the reducing and oxidizing gases, respectively.

Relative response (%) = $(R_g-R_a)/R_a \times 100$ (for reducing gas) (1.3)

Relative response (%) = $(R_a-R_g)/R_g \times 100$ (for oxidizing gas) (1.4)

(3) Sensitivity is the change in the response of a sensor per unit gas concentration. For a good sensor, its sensitivity should be high.

Sensitivity = Response/gas concentration (1.5)

2. **Response time:** The response time of a sensor is defined as the time required by the sensor to reach 90% of the full response from the baseline. Response time should be as short as possible for an ideal sensor at a particular gas concentration.

3. **Recovery time:** The recovery time of a sensor is defined as the time required to obtain 10% of the baseline (initial value of the sensor) from the maximum sensing response. Recovery time should also be minimal for an ideal gas sensor at a particular gas concentration.

4. **Selectivity:** Selectivity is the ability of the sensor to generate the maximum sensing response towards a particular gas, while other undesired gases should not be detected by the sensor simultaneously under similar conditions. Thus, a sensor should be highly selective.

5. **Reproducibility:** The sensor should give the same sensing response for the same sensor under similar operating conditions.

6. **Stability:** The sensor should produce the same sensing output when the experimental conditions remain the same for an extended time.

1.3 Choice of gas sensing materials

Over the past decade, researchers across the globe have extensively exploited the advantages of nanomaterials in the field of gas sensing. A variety of nanomaterials-based sensors have been developed for various sensing applications. This section presents a glimpse of various nanomaterials used for gas sensing.

Nanomaterials can be categorized as zero-dimensional (0D), one-dimensional (1D), two-dimensional (2D), and three-dimensional (3D) materials. 0D nanomaterials have all three dimensions in the nanoscale (< 100 nm). Examples of 0D nanomaterials include quantum dots or nanodots. 1D nanomaterials have any of the one dimension outside the nanoscale. Nanotubes, nanorods, nanowires, etc. are some of the structures of 1D nanomaterials. 2D nanomaterials have any two dimensions that cannot be measured on the nanoscale, which structurally exist as nanosheets, nanoflakes, nanoplates, nanomembranes, etc. 3D nanomaterials (polycrystals, foams, etc.) have all three dimensions outside the nanoscale. Fig. 1.4 shows the classification of sensing nanomaterials based on dimensionality.

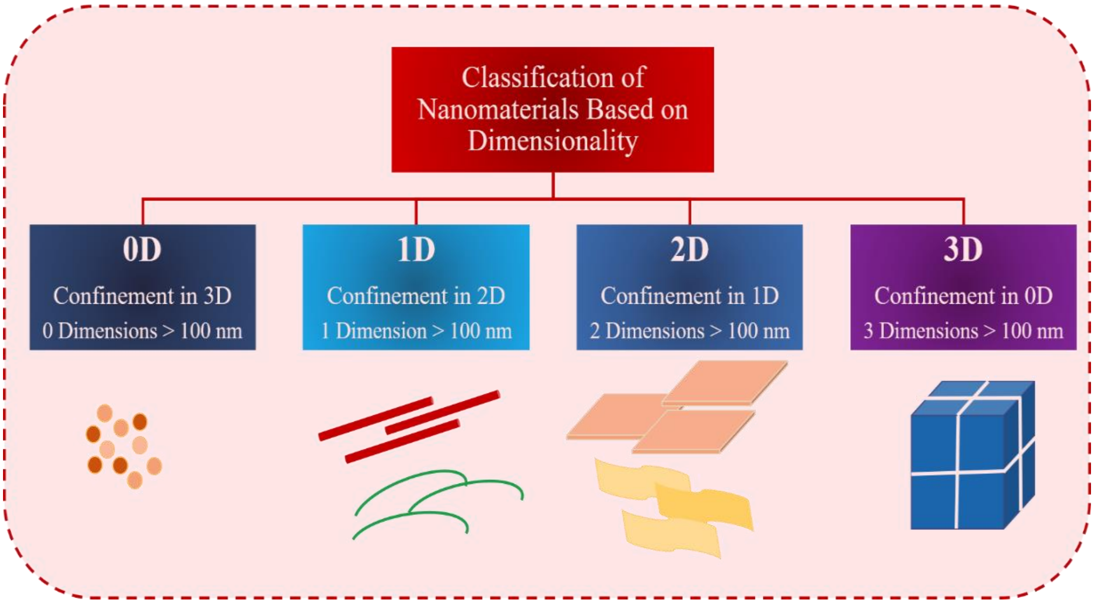

Fig. 1.4: Classification of sensing nanomaterials based on dimensionality

Since the groundbreaking discovery of graphene in 2004, the exploration of 2D nanomaterials has grown exponentially [40]. The unique electronic, physical, and chemical properties of 2D nanomaterials, resulting from electron confinement in two dimensions, make them highly attractive for gas sensors. Their high surface-to-volume ratios, coupled with van der Waals gaps between layers, contribute to their distinctive surface configurations. These characteristics, along with their two-dimensional nature, position 2D nanomaterials as exceptional candidates for gas sensing applications [41]. Apart from gas sensing, their appealing properties render them very promising for multiple fields, including energy storage and harvesting, electronics/optoelectronics, catalysis, biosensing, etc. [42-45]. They are generally classified as either 2D allotropic elements or covalently bonded compounds. Graphene, transition metal chalcogenides (TMCs), graphitic carbon-nitride (g-C_3N_4), and MXenes, are some of the examples of materials that belong to this class [46].

Transition metal chalcogenides (TMCs) are the materials with unique optical, electrical, and catalytic properties. They have a two-dimensional (2D) structure that includes three subsets [47]:

1. Transition metal dichalcogenides (TMDs) are the semiconductors with the form of MX_2 where M is the transition metal atom from the groups 4, 5, and 10 in the periodic table and X is the chalcogen atom such as sulfur (S), selenium (Se), and tellurium (Te),
2. Metal monochalcogenides (MCs), with the form of MX (where M typically refers to elements such as aluminum (Al), gallium (Ga), indium (In), thallium (Tl), germanium (Ge), tin (Sn), lead (Pb), antimony (Sb), etc. and X is the chalcogen atom such as sulfur (S), selenium (Se), and tellurium (Te))
3. The less explored transition metal trichalcogenides (TMTs), with the form of MX_3 (where M typically refers to elements such as titanium (Ti), zirconium (Zr), hafnium (Hf), rutherfordium (Rf), vanadium (V), niobium (Nb), chromium (Cr), etc.) and X is the chalcogen atom such as sulfur (S), selenium (Se), and tellurium (Te).

1.3.1 Transition metal dichalcogenides (TMDs)

Alongside graphene and its derivatives, TMDs are the most studied class of 2D nanomaterials [46]. They display versatile chemistry and remarkable semiconducting properties that are much more beneficial for fabricating practical gas sensors. The ability of TMDs to identify the target analyte at RT makes them appealing to be focussed in-depth for high-performance gas sensors [48]. However, there are a few challenges that need to be tackled to make TMDs to be used for the industrial sensing market. A few of their challenges include slow response and incomplete recovery, poor selectivity for a cross-response to different sensed gases, and unstable response signal [31]. Therefore, surface structure modifications such as sensitizing the surface with noble metals, surface functionalization, chemical doping or hybridizing with other materials, and fabricating heterostructures were investigated by many research groups to improve the sensing performance of TMDs [41-43]. Therefore, efforts to utilise TMDs for gas sensing have moved to the exploration of nanocompositing metal oxides into TMDs. Metal oxides especially, oxide nanostructures of zinc, copper, and titanium can be fabricated in various morphologies such as nanoparticles, nanocubes, nanocuboids, nanocircular and nanohexagonal discs, nanorods, nanowires, nanotapes, nanobelts, nanotetra nanopods, nanoflowers, etc. These morphologies can be synthesized using various cheap physical and chemical routes in the powder, colloid as well and nanostructures films phase. They can be deposited on any type of substrate such as metals, semiconductors, crystalline as well as amorphous, polymers, and flexible plastics.

Following are the collective benefits of nanocomposites of TMDs and metal oxides for gas sensing applications [41, 49]: (1) TMDs provide support for the uniform nucleation, growth, or assembling of metal-oxides with well-defined size, shape, and crystallinity. (2) Metal oxides act as a stabilizer against the aggregation and restacking of 2D nanomaterials. (3) The high surface area of TMDs provides easy incorporation of metal oxides on their surface. (4) The synergistic effect of the nanocomposites improves various properties such as electrical, optical, electrochemical, etc.

Among various TMDs, molybdenum diselenide ($MoSe_2$) has attracted considerable attention for gas sensing applications due to its significant physical and chemical properties like high carrier mobility, high adsorption energy with chemical molecules, easy functionalization, large surface areas, high yield synthesis process, variety of synthesis routes available, easy dispersion in various solvents, enhanced air stability, availability of surface defects, and facile hybridization with other materials [38, 50-52]. The reports on gas sensing utilizing intrinsic $MoSe_2$ as a sensing material, have proven that it can be a promising material targeting several analytes such as ethanol, H_2S, NH_3, NO_2, etc. [53-56]. But its response time is sluggish, and takes a long time to restore to its original state which challenges the use of intrinsic $MoSe_2$-based gas sensors. Recently, efforts to utilise $MoSe_2$ for gas sensing applications and its modification with metal oxides provide an alternate strategy for the development of practical sensors with enhanced sensing performance.

ZnO is an important II-VI semiconductor material with a direct bandgap of 3.37 eV and a high exciton binding energy of 60 meV [57]. Zinc oxide (ZnO) is an important n-type semiconductor material that has been widely studied for gas sensing applications. It is non-toxic and can be produced by simple and inexpensive synthesis techniques, easy engineering of morphology, good chemical stability, and low production cost [58]. Driven by the large number of properties possessed by ZnO, it finds application in gas sensing to a variety of reducing as well as oxidizing gasses [59]. Recent research has focused extensively on one-dimensional (1D) nanostructures of ZnO, such as nanotubes, nanorods, nanofibers, and nanowires, for potential applications in gas sensors [60]. Among these, ZnO nanorods stand out as the most suitable due to their high electron mobility along the growth direction, excellent crystallinity, and large surface-to-volume ratio. Additionally, their good thermal and chemical stability under various operating conditions enhances their potential for high-performance sensing [61, 62]. In ZnO nanocrystalline films, electron mobility is improved by a factor of 50 when using 1D rod-like ZnO crystals instead of spherical ones [63]. For these reasons, 1D ZnO has been chosen for synthesising nanocomposites with $MoSe_2$ for the development of ethanol gas sensors.

1.3.2 Metal monochalcogenides (MCs)

MCs are the materials that have surged as star 2D nanomaterials and have registered their presence in the field of gas sensing field because of their high surface-to-volume ratio, low-cost, earth-abundance, environment-friendly, and excellent physical or chemical adsorption capabilities toward gas molecules [41, 64-66]. These are layered materials and atoms are connected with strong covalent bonds within the layer and each layer is connected with other layers in a stack form through weak van der Waals force [67, 68]. A variety of physical and chemical routes are available to synthesize these materials with high quality and quantity. Moreover, the electrical, optical, and mechanical properties of MCs materials can be easily tuned and controlled by modulating the number of layers in a material [69-71]. In the context of gas detection, the MCs materials-based gas sensors show a direct charge-transfer gas sensing mechanism similar to TMDs allowing them to detect gases at RT without additional energy sources like heat or light. Direct charge transfer between gas molecules and sensing materials depends on the nature of both the gas and the material’s surface. Gas molecules interacting with the basal plane of MCs materials result in a small charge transfer due to weak electrostatic or van der Waals interactions. However, increasing structural defects or functionalizing the surface can enhance charge transfer and improve the gas-sensing characteristics of the sensor.

In recent years, tin sulfide (SnS) a 2D MC has attracted significant attention from researchers in fields such as sensor technology, photodetectors, solid-state batteries, photovoltaic cells, and holographic recording media [72]. It is non-toxic, cheap, highly stable, widely available, and has a distinctive layered structure [73, 74]. It has an indirect bandgap, a high concentration of majority charge carriers, and a high Hall mobility [75, 76]. SnS naturally exhibits p-type properties due to an excess of sulfur atoms [77]. However, studies have shown that sulfur vacancies can induce n-type properties in SnS. Experimental and theoretical studies have shown that the gas-sensing performance of 2D-based sensors is highly dependent on the presence of cation and anion vacancies [78]. Thus, controlling these vacancies is considered a crucial strategy for improving the low-temperature detection capabilities of 2D MC-based gas sensors.

1.4 Gas sensing mechanism

2D nanomaterials: The basic principle of gas sensing in 2D nanomaterials is based on the charge transfer process between the surface of the 2D nanomaterials and the gas molecules. When they are exposed to reactive gasses, the gas molecules are adsorbed on the surface of these materials. This adsorption is accompanied by the transfer of charges between the sensing material and the adsorbed gasses. Transfer of charges leads to a change in the resistance of the material. The direction of transfer of charges depends on the type of gas, i.e., either reducing or oxidizing. If the sensing material is re-exposed to air, desorption of gasses takes place thereby recovering to the initial value of resistance. Taking p-type TMD as a sensing material as an example, the resistance of the sensing material will increase from initial base resistance under the exposure of reducing gas and vice versa for oxidizing gas [41, 79].

Metal oxides: The gas sensing mechanism of metal oxides semiconductor-based sensors is based on the adsorption of oxygen molecules onto the surface of metal oxides from the atmosphere. Depending upon the different operating temperatures different forms of oxygen ions are possible as shown in equation 1.1 - 1.3.

$$O_2\,(\text{gas}) + e^- \leftrightarrow O_2^-\,(\text{adsorbed})\ [\text{below } 200\ °C] \tag{1.6}$$

$$\tfrac{1}{2}O_2 + e^- \leftrightarrow O^-\ (\text{adsorbed})\ [\text{above } 250\ °C] \tag{1.7}$$

$$\tfrac{1}{2}O_2 + 2e^- \leftrightarrow O^{2-}\ (\text{adsorbed})\ [\text{above } 250\ °C] \tag{1.8}$$

The interaction of reactive gasses with the oxygen ions adsorbed on the surface of metal oxides depends on the type of metal oxide i.e., p-type or n-type. Taking n-type metal oxide as a sensing material as an example, the electrons in the conduction band of the metal oxide decrease due to the reactions of equation 1.6 - 1.8, which increases the resistance of the metal oxide at the operating temperature. Under the exposure of reducing gas, electrons are transferred from the reducing gas to the conduction band of the metal oxide, thereby decreasing the resistance of the n-type metal oxide semiconducting materials. For oxidizing gases, the opposite change in resistance occurs. Oxygen ions play a dominant role in the gas-sensing mechanism of metal oxide semiconductors, hence sensors based on these materials are operated at elevated temperatures [41].

1.5 Primary challenges and strategies

Despite significant advancements in gas sensor design and fabrication, there remains a critical gap in our understanding of the material properties that influence their operational efficiency. To enhance their applicability in industrial contexts, scaling up the sensing capabilities of these devices is essential. Advances in nanotechnology present a promising path for improving material sensing qualities through precise manipulation of properties at the nanoscale. By focusing on the interactions between gas molecules and sensor materials, researchers can unlock new opportunities for optimizing sensitivity, selectivity, and response times, ultimately leading to more effective and versatile gas detection solutions. Given that the effectiveness of a gas sensor is closely related to the surface area of the sensing material, optimizing this material to enhance the gas sensing effect holds significant promise. By increasing the surface area, we can facilitate more interactions between the gas molecules and the sensor, which can lead to improved sensitivity and faster response times. This multifaceted approach not only enhances the sensor's performance but also allows for the development of sensors that can operate in diverse environments and detect a wider range of gases, ultimately broadening their industrial applications. The preference for 2D nanomaterials over other morphologies stems from their high surface-to-volume ratios and the unique Van der Waals gaps present between their layered structures. These characteristics make 2D nanomaterials exceptional candidates for gas sensors. Additionally, the synergistic effects observed in nanocomposites combining 2D materials with metal oxides hold great promise for enhancing sensing properties. This combination can potentially lead to improved sensitivity, selectivity, and response times, paving the way for more effective gas detection solutions.

1.6 Thesis problem

In the present thesis, we have focussed primarily on the following prospects for the development of ethanol gas sensors:

1. **RT operation:** We aim to develop ethanol gas sensors that operate effectively at RT, facilitating easier integration with electronic circuits while consuming less power.
2. **Enhanced performance:** We have explored ways to improve the stability, response time, and recovery time of existing 2D nanomaterial-based ethanol sensors at RT.

3. **Self-powered sensors:** We have also investigated the development of self-powered sensors to enhance operational efficiency and reduce reliance on external power sources.

Therefore, in the present thesis, ZnO-incorporated- $MoSe_2$ nanosheets were synthesized using a facile and low-cost hydrothermal method for the chemiresistive detection of ethanol gas at RT (discussed in **Chapter 3**). Then, in **Chapter 4** we explored a ternary nanocomposite of rGO decorated $MoSe_2$-ZnO ($MoSe_2$/ZnO/rGO) for ethanol gas sensing applications at RT. Finally, in **Chapter 5** we have developed a novel self-powered n-type SnS-based ethanol gas sensor driven by hydroelectric cell (HEC).

1.7 Objectives of the thesis

The main objective of the thesis is the development of a nanocomposite of 2D nanomaterials and metal oxides for multifunctional applications with a focus on gas sensing. For the development of the gas sensor, chemiresistive device architecture has been explored with nanocomposites of 2D nanomaterials and metal oxides as a sensing platform. The above section explains the thesis problem to pursue the research work, based on which the objectives of the thesis are designed which are as follows:

1. Extensive literature survey on metal oxides/2D nanomaterials/their nanocomposites for multifunctional applications.
2. Synthesis of metal oxides/2D nanomaterials/their nanocomposites using different synthesis routes.
3. Characterization of metal oxides/2D nanomaterials/their nanocomposite.
4. Fabrication of thin films of metal oxides/2D nanomaterial/their nanocomposite using spin coating/ electrophoretic deposition/ drop casting.
5. Study the properties of metal oxides/2D nanomaterials/their nanocomposites.
6. Multifunctional applications of metal oxides, 2D nanomaterials/their nanocomposites.

With extensive optimization of synthesis parameters based on results of characterization studies, and application in gas sensing, the output of the research work towards achieving the above-mentioned objectives has been organized into six chapters and the summary of each of the chapters is given below.

1.6 Organisation of the thesis

The complete thesis work is presented in six chapters.

Chapter 1: Introduction and Scientific Motivation

Chapter 1 gives a brief introduction to the growing demand for efficient and reliable gas sensing technologies has led to increased interest in the development of ethanol gas sensors, particularly those that operate effectively at RT while minimizing power consumption. This thesis addresses the pressing need for advanced ethanol sensors that exhibit high sensitivity, stability, and selectivity across a broad range of ethanol concentrations. The study begins with a comprehensive overview of existing ethanol sensing technologies, with a primary focus on chemiresistive sensors, which are renowned for their simplicity and cost-effectiveness. To enhance sensor performance, this research emphasizes the integration of nanotechnology and material science, particularly through the use of nanocomposites of 2D nanomaterials with metal oxides. These innovative materials have shown significant promise in improving key sensing parameters, including response time, selectivity, and overall stability. By leveraging these advancements, the thesis explores the potential for self-powered gas sensors that not only exhibit superior sensing capabilities but also cater to various applications in environmental monitoring, industrial safety, and healthcare. Through a detailed examination of current knowledge gaps in ethanol gas sensing technologies, this work outlines specific research objectives aimed at optimizing sensor design and functionality. Ultimately, this research seeks to contribute to the advancement of ethanol gas sensors, providing a foundation for future innovations in the field and addressing the critical challenges of detection efficiency and application versatility.

Chapter 2: Methodologies: Synthesis, Characterization Techniques, Sensor Fabrication, and Gas Sensing Measurements

Chapter 2 provides a comprehensive overview of the selected methodologies for synthesizing nanocomposites of 2D nanomaterials and metal oxides, the technique used for fabricating their film-based gas sensors, and the various characterization techniques utilised in this research endeavor. In the synthesis of nanocomposites of 2D nanomaterials and metal oxides, the hydrothermal approach has been predominantly utilised. Various characterization techniques have been employed to investigate the formation of nanocomposites of 2D nanomaterials and metal oxides such as X-ray diffraction (XRD) has been used for examining crystal structures, field-emission scanning electron microscopy (FESEM) and high-resolution transmission electron microscopy (HRTEM) for exploring surface morphology, Raman spectroscopy for the analysis of vibrational modes, Fourier transform infrared spectroscopy (FTIR) for examining the functional groups, and the specific surface area has been analysed using Brunauer-Emmett-Teller (BET). Further, for the gas-sensing studies, the fabrication of a gas sensor involves utilising thermal evaporation technique to deposit metal electrodes onto synthesized thin films. A customized chemiresistive gas sensing set-up is used to investigate the gas sensing behavior of the fabricated gas sensors. All these techniques are succinctly summarized within this chapter.

Subsequently, three technical chapters are presented.

Chapter 3: Zinc Oxide Incorporated Molybdenum Diselenide Nanosheets for Chemiresistive Detection of Ethanol Gas

This chapter demonstrates an RT chemiresistive ethanol gas sensor based on hydrothermally synthesized zinc oxide (ZnO) incorporated-molybdenum diselenide ($MoSe_2$) nanosheets. The sensing properties of the $MoSe_2$/ZnO nanocomposite sensor were investigated systematically by exposing the sensor to various ethanol gas concentrations (10 - 500 ppm) in dry N_2 and dry air. The synergistic effect due to the incorporation of ZnO nanorods in $MoSe_2$ nanosheets was found to enhance the sensor response to ethanol gas (when operated in dry N_2) with improved response and recovery time of 8.4 and 14.7 seconds respectively, high selectivity, stability, and reproducibility. The nanocomposite-based sensor showed a high gas sensing response

(R_g/R_a) of 37.8 to 500 ppm of ethanol gas. While the response of the nanocomposite-based sensor decreased to 15.3 to 500 ppm of ethanol gas in dry air which suggests that the sensor performs better when operated in dry N_2 than in dry air. Based on experimental results, a plausible mechanism has been proposed based on the formation of p-n heterojunction and potential barrier modulation at the interface of the $MoSe_2$/ZnO nanocomposite sensor. The results demonstrated that $MoSe_2$/ZnO-based nanocomposite may pave the way for the fabrication of ethanol gas sensors for real-time electronics applications.

Chapter 4: A Proposed Device Based on $MoSe_2$-ZnO Heterojunctions on rGO for Enhanced Ethanol Gas Sensing Performances at Room Temperature

In the previous chapter, we explored $MoSe_2$/ZnO nanocomposite-based sensor for ethanol gas sensing at RT. The ethanol gas sensing results of the nanocomposite sensor exhibited higher response value, improved response time, and recovery time than the pristine- $MoSe_2$ sensor to 500 ppm ethanol gas. To further enhance the ethanol gas sensing properties of the sensing device at RT, we have explored a ternary nanocomposite of $MoSe_2$-ZnO heterojunctions decorated rGO ($MoSe_2$/ZnO/rGO) for ethanol gas sensing at RT. The sensing performance of the ternary nanocomposite sensing device was analysed for various concentrations of ethanol gas (1 - 500 ppm). The gas-sensing results revealed that for 500 ppm ethanol gas concentration, the sensing device exhibited an enhanced response value (R_g/R_a) of 50.2. Significantly, the sensing device displayed a quick response and recovery time of 6.2 s and 12.9 s respectively. In addition to this, the sensing device detected ethanol at remarkably low concentrations of 1 ppm. The enhanced sensing performance of the ternary nanocomposite sensing device highlighted the effective synergistic effect between $MoSe_2$ nanosheets, ZnO nanorods, and rGO nanosheets. This has been attributed to a large number of p-n heterojunctions of $MoSe_2$ nanosheets and ZnO nanorods onto the rGO nanosheets matrix.

Chapter 5: First report on hydroelectric cell-driven gas sensor for the detection of ethanol at room temperature: A novel approach

This chapter proposes a novel self-powered ethanol gas sensor, exhibiting excellent selectivity, sensitivity, and stability, based on n-type SnS nanoflakes at RT. The n-type SnS-based HEC serves as the power source for self-powered ethanol gas sensors, enabling the detection of various concentrations of ethanol gas at RT. Consequently, the power supply and gas sensor have been effectively combined into a single device, demonstrating a successful integration of both functionalities. XRD, FESEM, HRTEM, Energy dispersive X-ray (EDX), and BET analysis confirmed the formation of orthorhombic SnS nanoflakes with a high specific surface area (6.15 m^2 g^{-1}). The observed voltage-current (V-I) characteristic curves of the HEC at RT showed a maximum current (I_{max}) of 40 µA and voltage of 1.03 V. The sensing performance of the self-powered ethanol gas sensor was analysed for various concentrations of ethanol gas (10 - 100 ppm). The sensor exhibited a response value (R_a/R_g) of 41.3 to 100 ppm ethanol gas concentration, with quick response/recovery times of 27.3 s/31.4 s respectively at RT. The sensor showed promising potential for prolonged ethanol gas detection, operating successfully for 30 days with measurements taken every 5 days. The experimental results demonstrate that the n-type SnS-based self-powered ethanol gas sensor is a promising platform for integration into future large-scale IoT systems. This breakthrough paves the way for more versatile and scalable IoT solutions, enabling continuous environmental monitoring and data collection across various settings.

Chapter 6: Summary, Conclusions, and Future Scope of Work

This chapter summarises the key findings and major conclusions of the thesis, while also highlighting potential areas for future research. The organizational flowchart of the thesis is illustrated in Figure 1.5.

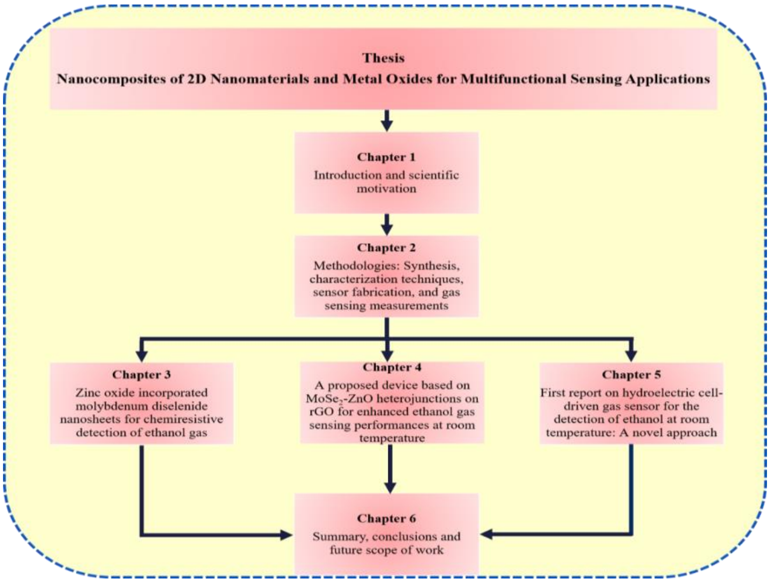

Fig. 1.5: Flowchart for the organisation of the thesis

References

[1] J. Hu, W. Guan, X. Xiong, Y. Chen, and H. Long, "Modulation of rGO-Co3O4 heterojunction with multi-walled carbon nanotubes for efficient ethanol detection," *Sensors and Actuators B: Chemical,* vol. 368, p. 132202, 2022.

[2] X. Wang, Y. Gao, Q. Zhang, X. He, and X. Wang, "Synthesis of MoO3 (1D)@ SnO2 (2D) core-shell heterostructures for enhanced ethanol gas sensing performance," *Sensors and Actuators B: Chemical,* vol. 382, p. 133484, 2023.

[3] L.-Y. Gai *et al.,* "Recent advances in ethanol gas sensors based on metal oxide semiconductor heterojunctions," *Rare Metals,* vol. 41, no. 6, pp. 1818-1842, 2022.

[4] P. Wolkoff, "Volatile organic compounds," *Indoor air,* vol. 3, pp. 1-73, 1995.

[5] A. Pathak and C. Viphavakit, "A review on all-optical fiber-based VOC sensors: Heading towards the development of promising technology," *Sensors and Actuators A: Physical,* vol. 338, p. 113455, 2022.

[6] J. Bartzis *et al.*, "On organic emissions testing from indoor consumer products' use," *Journal of hazardous materials,* vol. 285, pp. 37-45, 2015.

[7] A. Tiwary and I. Williams, *Air pollution: measurement, modelling and mitigation*. Crc Press, 2018.

[8] P. Tiwary, S. Chatterjee, S. Singha, R. Mahapatra, and A. K. Chakraborty, "Room temperature ethanol sensing by chemically reduced graphene oxide film," *FlatChem,* vol. 30, p. 100317, 2021.

[9] Y. R. Kumar, K. Deshmukh, T. Kovářík, and S. K. Pasha, "A systematic review on 2D materials for volatile organic compound sensing," *Coordination Chemistry Reviews,* vol. 461, p. 214502, 2022.

[10] A. Mirzaei, S. Leonardi, and G. Neri, "Detection of hazardous volatile organic compounds (VOCs) by metal oxide nanostructures-based gas sensors: A review," *Ceramics international,* vol. 42, no. 14, pp. 15119-15141, 2016.

[11] S. Singh and S. Sharma, "Temperature dependent selective detection of ethanol and methanol using MoS2/TiO2 composite," *Sensors and Actuators B: Chemical,* vol. 350, p. 130798, 2022.

[12] M. J. Ahemad, T. D. Le, D.-S. Kim, and Y.-T. Yu, "Bimetallic AgAualloy@ ZnO core-shell nanoparticles for ultra-high detection of ethanol: Potential impact of alloy

composition on sensing performance," *Sensors and Actuators B: Chemical,* vol. 359, p. 131595, 2022.

[13] S. S. Scindia, R. B. Kamble, and J. A. Kher, "Organic surfactant assisted polypyrrole materials as effective chemiresistive gas sensors for VOCs and toxic gas detection," *IEEE Sensors Journal,* vol. 20, no. 23, pp. 14072-14080, 2020.

[14] D. Zhang, Y. Cao, J. Wu, and X. Zhang, "Tungsten trioxide nanoparticles decorated tungsten disulfide nanoheterojunction for highly sensitive ethanol gas sensing application," *Applied Surface Science,* vol. 503, p. 144063, 2020.

[15] W. H. Organization, *Global status report on alcohol and health 2018*. World Health Organization, 2019.

[16] T. T. N. Phan *et al.*, "Hierarchically structured LaFeO3 with hollow core and porous shell as efficient sensing material for ethanol detection," *Sensors and Actuators B: Chemical,* vol. 354, p. 131195, 2022.

[17] Z. Wu, T. Cheng, and Z. L. Wang, "Self-powered sensors and systems based on nanogenerators," *Sensors,* vol. 20, no. 10, p. 2925, 2020.

[18] S. Wei *et al.*, "A Self-Powered Portable Nanowire Array Gas Sensor for Dynamic NO2 Monitoring at Room Temperature," *Advanced Materials,* vol. 35, no. 12, p. 2207199, 2023.

[19] M. Shirvanimoghaddam *et al.*, "Towards a green and self-powered Internet of Things using piezoelectric energy harvesting," *Ieee Access,* vol. 7, pp. 94533-94556, 2019.

[20] H.-X. Zou *et al.*, "A self-regulation strategy for triboelectric nanogenerator and self-powered wind-speed sensor," *Nano Energy,* vol. 95, p. 106990, 2022.

[21] M. Zhang *et al.*, "Electrochemical humidity sensor enabled self-powered wireless humidity detection system," *Nano Energy,* vol. 115, p. 108745, 2023.

[22] M. Khatib and H. Haick, "Sensors for volatile organic compounds," *ACS nano,* vol. 16, no. 5, pp. 7080-7115, 2022.

[23] Y. Y. Broza, R. Vishinkin, O. Barash, M. K. Nakhleh, and H. Haick, "Synergy between nanomaterials and volatile organic compounds for non-invasive medical evaluation," *Chemical Society Reviews,* vol. 47, no. 13, pp. 4781-4859, 2018.

[24] Y. Jian *et al.*, "Gas sensors based on chemi-resistive hybrid functional nanomaterials," *Nano-Micro Letters,* vol. 12, pp. 1-43, 2020.

[25] T. Seiyama, A. Kato, K. Fujiishi, and M. Nagatani, "A new detector for gaseous components using semiconductive thin films," *Analytical Chemistry,* vol. 34, no. 11, pp. 1502-1503, 1962.

[26] G. Neri, "First fifty years of chemoresistive gas sensors," *Chemosensors,* vol. 3, no. 1, pp. 1-20, 2015.

[27] N. Roy *et al.*, "Paper based enzymatic chemiresistor for POC detection of ethanol in human breath," *IEEE Sensors Journal,* vol. 20, no. 5, pp. 2278-2286, 2019.

[28] J. Saini, M. Dutta, and G. Marques, "A comprehensive review on indoor air quality monitoring systems for enhanced public health," *Sustainable environment research,* vol. 30, no. 1, pp. 1-12, 2020.

[29] V. Manikandan *et al.*, "A reliable chemiresistive sensor of nickel-doped tin oxide (Ni-SnO 2) for sensing carbon dioxide gas and humidity," *RSC advances,* vol. 10, no. 7, pp. 3796-3804, 2020.

[30] R. Kumar *et al.*, "Room temperature ammonia gas sensor using Meta Toluic acid functionalized graphene oxide," *Materials Chemistry and Physics,* vol. 240, p. 121922, 2020.

[31] Y. Jiang, N. Tang, C. Zhou, Z. Han, H. Qu, and X. Duan, "A chemiresistive sensor array from conductive polymer nanowires fabricated by nanoscale soft lithography," *Nanoscale,* vol. 10, no. 44, pp. 20578-20586, 2018.

[32] F. Mustafa and S. Andreescu, "Nanotechnology-based approaches for food sensing and packaging applications. RSC Adv 10: 19309–19336," ed, 2020.

[33] K. Dai, Q. Yu, Z. Zhang, Y. Wang, and X. Wang, "Aromatic hydrocarbons in a controlled ecological life support system during a 4-person-180-day integrated experiment," *Science of the Total Environment,* vol. 610, pp. 905-911, 2018.

[34] S. Kanaparthi and S. G. Singh, "Highly sensitive and ultra-fast responsive ammonia gas sensor based on 2D ZnO nanoflakes," *Materials Science for Energy Technologies,* vol. 3, pp. 91-96, 2020.

[35] Y. Seekaew, W. Pon-On, and C. Wongchoosuk, "Ultrahigh selective room-temperature ammonia gas sensor based on tin–titanium dioxide/reduced graphene/carbon nanotube nanocomposites by the solvothermal method," *ACS omega,* vol. 4, no. 16, pp. 16916-16924, 2019.

[36] A. Manzoli *et al.*, "Volatile compounds monitoring as indicative of female cattle fertile period using electronic nose," *Sensors and Actuators B: Chemical,* vol. 282, pp. 609-616, 2019.

[37] K. Arora and N. K. Puri, "Chemiresistive sensing platform based on PdO-PANI/ITO heterostructure for room temperature hydrogen detection," *Materials Chemistry and Physics*, vol. 247, p. 122850, 2020.

[38] N. Jain and N. K. Puri, "Zinc oxide incorporated molybdenum diselenide nanosheets for chemiresistive detection of ethanol gas," *Journal of Alloys and Compounds*, vol. 955, p. 170178, 2023.

[39] Y. Ding *et al.*, "Hollow Cu2O nanospheres loaded with MoS2/reduced graphene oxide nanosheets for ppb-level NO2 detection at room temperature," *Journal of Hazardous Materials*, vol. 416, p. 126218, 2021.

[40] C. Anichini, W. Czepa, D. Pakulski, A. Aliprandi, A. Ciesielski, and P. Samorì, "Chemical sensing with 2D materials," *Chemical Society Reviews*, vol. 47, no. 13, pp. 4860-4908, 2018.

[41] E. Lee, Y. S. Yoon, and D.-J. Kim, "Two-dimensional transition metal dichalcogenides and metal oxide hybrids for gas sensing," *ACS sensors*, vol. 3, no. 10, pp. 2045-2060, 2018.

[42] R. Khatri and N. K. Puri, "Electrochemical biosensor utilizing dual-mode output for detection of lung cancer biomarker based on reduced graphene oxide-modified reduced-molybdenum disulfide multi-layered nanosheets," *Journal of Materials Research*, vol. 37, no. 8, pp. 1451-1463, 2022.

[43] V. Singh, D. Meena, H. Sharma, A. Trivedi, and B. Singh, "Investigating the role of chalcogen atom in the piezoelectric performance of PVDF/TMDCs based flexible nanogenerator," *Energy*, vol. 239, p. 122125, 2022.

[44] S. Ruan *et al.*, "Synthesis and functionalization of 2D nanomaterials for application in lithium-based energy storage systems," *Energy Storage Materials*, vol. 38, pp. 200-230, 2021.

[45] X. Li, S. Han, Z. Qiao, X. Zeng, D. Cao, and J. Chen, "Ru monolayer island doped MoS2 catalysts for efficient hydrogen evolution reaction," *Chemical Engineering Journal*, vol. 453, p. 139803, 2023.

[46] C. Tan *et al.*, "Recent advances in ultrathin two-dimensional nanomaterials," *Chemical reviews*, vol. 117, no. 9, pp. 6225-6331, 2017.

[47] K. Dashtian *et al.*, "Metal chalcogenides for sensing applications," in *Fundamentals of Sensor Technology*: Elsevier, 2023, pp. 551-589.

[48] F. Mustafa and S. Andreescu, "Nanotechnology-based approaches for food sensing and packaging applications," *RSC advances,* vol. 10, no. 33, pp. 19309-19336, 2020.

[49] D. R. Miller, S. A. Akbar, and P. A. Morris, "Nanoscale metal oxide-based heterojunctions for gas sensing: A review," *Sensors and Actuators B: Chemical,* vol. 204, pp. 250-272, 2014.

[50] G. Jeevanandham, K. Vediappan, Z. A. ALOthman, T. Altalhi, and A. K. Sundramoorthy, "Fabrication of 2D-MoSe2 incorporated NiO Nanorods modified electrode for selective detection of glucose in serum samples," *Scientific reports,* vol. 11, no. 1, p. 13266, 2021.

[51] T. Li, S. Yu, Q. Li, M. Chi, and P. Li, "Room temperature ethanol gas-sensing properties based on Ag-doped MoSe 2 nanoflowers: experimental and DFT investigation," *New Journal of Chemistry,* vol. 45, no. 45, pp. 21423-21428, 2021.

[52] A. Abun, B.-R. Huang, A. Saravanan, D. Kathiravan, and P.-D. Hong, "Exfoliated MoSe2 nanosheets doped on the surface of ZnO nanorods for hydrogen sensing applications," *ACS Applied Nano Materials,* vol. 3, no. 12, pp. 12139-12147, 2020.

[53] R. K. Jha, J. V. D'Costa, N. Sakhuja, and N. Bhat, "MoSe2 nanoflakes based chemiresistive sensors for ppb-level hydrogen sulfide gas detection," *Sensors and Actuators B: Chemical,* vol. 297, p. 126687, 2019.

[54] D. J. Late, T. Doneux, and M. Bougouma, "Single-layer MoSe2 based NH3 gas sensor," *Applied physics letters,* vol. 105, no. 23, 2014.

[55] S. Singh, J. Deb, U. Sarkar, and S. Sharma, "MoSe2 crystalline nanosheets for room-temperature ammonia sensing," *ACS Applied Nano Materials,* vol. 3, no. 9, pp. 9375-9384, 2020.

[56] S. Zhang, W. Zhang, T. H. Nguyen, J. Jian, and W. Yang, "Synthesis of molybdenum diselenide nanosheets and its ethanol-sensing mechanism," *Materials Chemistry and Physics,* vol. 222, pp. 139-146, 2019.

[57] R. S. Ganesh *et al.*, "Surfactant free controllable synthesis of 2D–1D ZnO hierarchical nanostructure and its gas sensing properties," *Applied Surface Science,* vol. 449, pp. 838-845, 2018.

[58] A. Janotti and C. G. Van de Walle, "Fundamentals of zinc oxide as a semiconductor," *Reports on progress in physics,* vol. 72, no. 12, p. 126501, 2009.

[59] H. Yan, P. Song, S. Zhang, Z. Yang, and Q. Wang, "Facile synthesis, characterization and gas sensing performance of ZnO nanoparticles-coated MoS2 nanosheets," *Journal of Alloys and Compounds,* vol. 662, pp. 118-125, 2016.

[60] A. Kolmakov and M. Moskovits, "Chemical sensing and catalysis by one-dimensional metal-oxide nanostructures," *Annu. Rev. Mater. Res.,* vol. 34, no. 1, pp. 151-180, 2004.

[61] S. Öztürk, N. Kılınç, and Z. Z. Öztürk, "Fabrication of ZnO nanorods for NO2 sensor applications: effect of dimensions and electrode position," *Journal of Alloys and Compounds,* vol. 581, pp. 196-201, 2013.

[62] B. Sun and H. Sirringhaus, "Solution-processed zinc oxide field-effect transistors based on self-assembly of colloidal nanorods," *Nano letters,* vol. 5, no. 12, pp. 2408-2413, 2005.

[63] P. Rai, Y.-S. Kim, H.-M. Song, M.-K. Song, and Y.-T. Yu, "The role of gold catalyst on the sensing behavior of ZnO nanorods for CO and NO2 gases," *Sensors and Actuators B: Chemical,* vol. 165, no. 1, pp. 133-142, 2012.

[64] J. Ping, Z. Fan, M. Sindoro, Y. Ying, and H. Zhang, "Recent advances in sensing applications of two-dimensional transition metal dichalcogenide nanosheets and their composites," *Advanced Functional Materials,* vol. 27, no. 19, p. 1605817, 2017.

[65] R. Kumar, X. Liu, J. Zhang, and M. Kumar, "Room-temperature gas sensors under photoactivation: from metal oxides to 2D materials," *Nano-Micro Letters,* vol. 12, pp. 1-37, 2020.

[66] C. Mackin *et al.*, "Chemical sensor systems based on 2D and thin film materials," *2D Materials,* vol. 7, no. 2, p. 022002, 2020.

[67] S. Manzeli, D. Ovchinnikov, D. Pasquier, O. V. Yazyev, and A. Kis, "2D transition metal dichalcogenides," *Nature Reviews Materials,* vol. 2, no. 8, pp. 1-15, 2017.

[68] J. T. Gibbon and V. R. Dhanak, "Properties of Transition Metal Dichalcogenides," *Two Dimensional Transition Metal Dichalcogenides: Synthesis, Properties, and Applications,* pp. 69-106, 2019.

[69] Y. Li, S. Tongay, Q. Yue, J. Kang, J. Wu, and J. Li, "Metal to semiconductor transition in metallic transition metal dichalcogenides," *Journal of Applied Physics,* vol. 114, no. 17, 2013.

[70] G. H. Han, D. L. Duong, D. H. Keum, S. J. Yun, and Y. H. Lee, "van der Waals metallic transition metal dichalcogenides," *Chemical reviews,* vol. 118, no. 13, pp. 6297-6336, 2018.

[71] N. M. Ravindra, W. Tang, and S. Rassay, "Transition metal dichalcogenides properties and applications," *Semiconductors: Synthesis, Properties and Applications,* pp. 333-396, 2019.

[72] M. Afsar, M. Rafiq, and A. Tok, "Two-dimensional SnS nanoflakes: synthesis and application to acetone and alcohol sensors," *RSC advances,* vol. 7, no. 35, pp. 21556-21566, 2017.

[73] I. Kherchachi *et al.*, "Structural, optical and electrical properties of SnxSy thin films grown by spray ultrasonic," *Journal of Semiconductors,* vol. 37, no. 3, p. 032001, 2016.

[74] A. Degrauw, R. Armstrong, A. A. Rahman, J. Ogle, and L. Whittaker-Brooks, "Catalytic growth of vertically aligned SnS/SnS2 p–n heterojunctions," *Materials Research Express,* vol. 4, no. 9, p. 094002, 2017.

[75] Y. Zi, J. Zhu, L. Hu, M. Wang, and W. Huang, "Nanoengineering of tin monosulfide (SnS)-based structures for emerging applications," *Small Science,* vol. 2, no. 3, p. 2100098, 2022.

[76] J. H. Bang *et al.*, "SnS-functionalized SnO2 nanowires for low-temperature detection of NO2 gas," *Materials Characterization,* vol. 175, p. 110986, 2021.

[77] Q. Sun *et al.*, "SnS 2/SnS p–n heterojunctions with an accumulation layer for ultrasensitive room-temperature NO 2 detection," *Nanoscale,* vol. 11, no. 29, pp. 13741-13749, 2019.

[78] N. Manh Hung *et al.*, "Defect-induced gas-sensing properties of a flexible SnS sensor under UV illumination at room temperature," *Sensors,* vol. 20, no. 19, p. 5701, 2020.

[79] S. Yang, C. Jiang, and S.-h. Wei, "Gas sensing in 2D materials," *Applied Physics Reviews,* vol. 4, no. 2, 2017.

CHAPTER 2

Methodologies: Synthesis, Characterization Techniques, Sensor Fabrication, and Gas Sensing Measurements

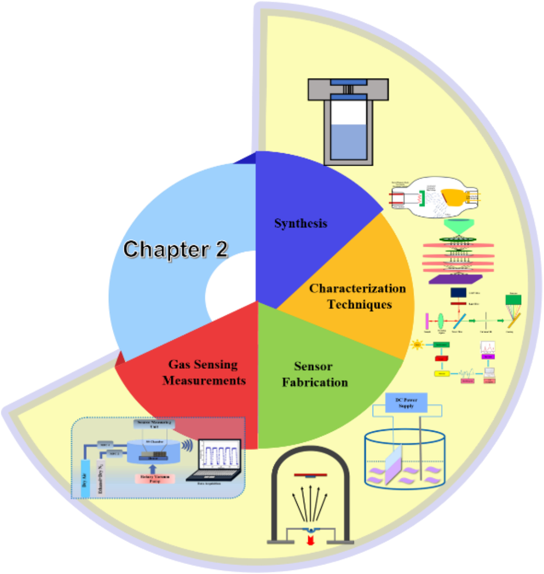

This chapter provides a comprehensive overview of the selected methodologies for synthesising nanocomposites of 2D nanomaterials and metal oxides, the technique used for fabricating their film-based gas sensors, and the various characterization techniques utilised in the research endeavor. The hydrothermal approach has been predominantly used for the synthesis. X-ray diffraction (XRD) has been used for examining crystal structures, field-emission scanning electron microscopy (FESEM) and high-resolution transmission electron microscopy (HRTEM) for exploring surface morphology, Raman spectroscopy has been used for the analysis of vibrational modes, and Fourier transform infrared spectroscopy (FTIR) for examining the functional groups. Further, the fabrication of a gas sensor involves fabricating the films using the electrophoretic deposition technique (EPD) followed by thermal evaporation to deposit metal electrodes onto synthesised films. A customized chemiresistive gas sensing set-up has been used to investigate the gas sensing behavior of the fabricated gas sensors. All these techniques are succinctly summarized within this chapter.

2.1 Synthesis of nanocomposites of 2D nanomaterials and metal oxides

Various techniques are available for the synthesis of nanocomposites of two-dimensional (2D) nanomaterials and metal oxides to obtain desirous structures and properties to suit diverse applications. These methods can be broadly categorized into two groups: 1) Top-down and 2) Bottom-up approaches. The Top-down process involves extracting nanostructures from their bulk forms. This method entails solid-solid and gas-solid transformations from bulk materials to nanomaterials. It is achieved through physical methods involving processes such as grinding, crushing, and decomposition. Conversely, the Bottom-up process involves the creation of desired nanostructures by facilitating interactions between atoms and molecules, leading to the accumulation and formation of material clusters. Choosing the appropriate synthesis route is essential before embarking on property investigation and targeted applications. Successful commercialization and industrialization require the synthesis of high yields of high-quality nanomaterials [1]. In our work, we employed a simple and environmentally friendly hydrothermal approach for synthesizing nanocomposites of 2D nanomaterials and metal oxides. Additionally, the modification of nanocomposites involves the use of reduced graphene oxide (rGO). Graphene oxide (GO), which is prepared using the improved Hummers' method, is incorporated into the synthesis of nanocomposites comprising 2D nanomaterials and metal oxides through a hydrothermal process. During this synthesis, GO is reduced to rGO in situ, ensuring that the reduction process occurs simultaneously with the formation of the nanocomposites. The various synthesis methods employed are briefly outlined in the following sections. Detailed descriptions of these synthesis procedures are provided in Chapters 3, 4, and 5.

2.1.1 Hydrothermal synthesis route

In 1845, Karl Emil von Schafhäutl, a German geologist, published the first report detailing crystal formation through hydrothermal method. Since then, collaborative efforts by researchers worldwide have propelled the advancement of this method. Hydrothermal synthesis involves creating nanomaterials through chemical reactions that take place within a sealed teflon-lined stainless-steel autoclave, containing reagents dissolved in water, all under specific temperature and pressure conditions. To facilitate the production of nanomaterials with desired properties and morphology, a precise volume of aqueous reagents is introduced into the teflon liner, ensuring the necessary pressure is maintained. Care must be taken to prevent teflon overflow during the reaction. By optimizing temperature, pressure, and reaction time in a high-temperature oven, a substantial yield of well-crystallized nanomaterials can be achieved [2]. Fig. 2.1 illustrates the setup of the hydrothermal autoclave used in the hydrothermal synthesis. The constituents involved in the hydrothermal reaction are outlined as follows:

1. **Reactant precursors:** These compounds serve as the initial reactants that undergo chemical reactions within suitable solvents, ultimately leading to the formation of the desired final product.
2. **Mineralizing agents and supplementary additives:** Various acids and bases are introduced throughout the reaction to attain specific pH levels. These compounds, known as mineralizers, play a pivotal role in the process. Additionally, supplementary additives such as reducing agents, chelating agents, capping agents, and stabilizers are used for controlling the morphology of the resulting nanomaterial.

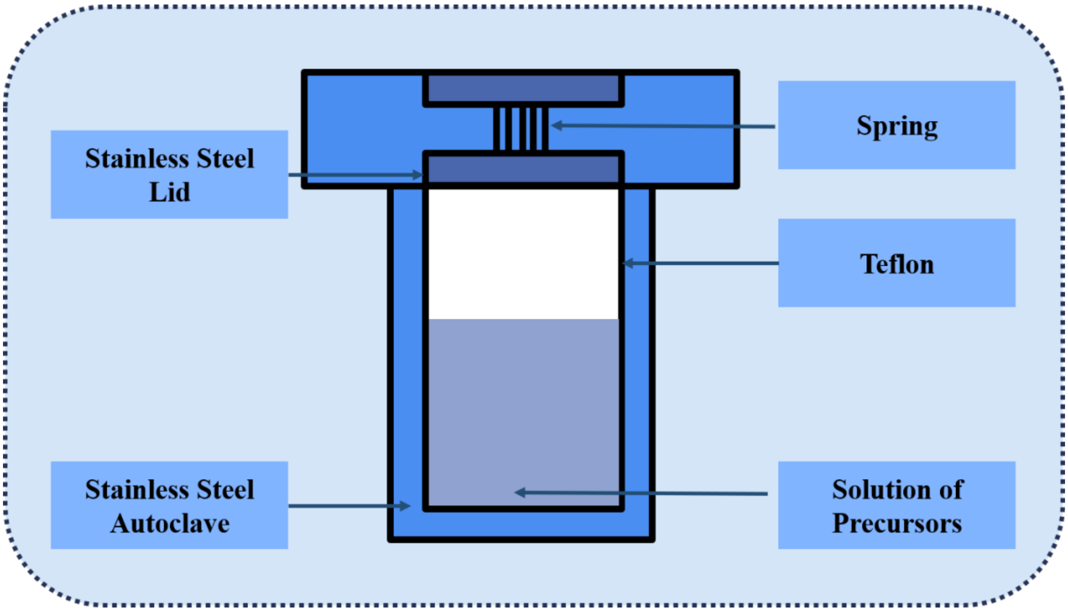

Fig. 2.1: Set-up of the hydrothermal autoclave used in the hydrothermal synthesis

The advantages of the hydrothermal method include:

1. **Cost-effectiveness and scalability:** This method is highly feasible for the inexpensive and large-scale production of nanomaterials.
2. **Morphology and size control:** It offers precise control over the morphology and size of nanomaterials, enhancing its versatility.
3. **Integration with other synthesis techniques:** The method can be seamlessly integrated with other techniques such as sonochemical and electrochemical microwave synthesis, expanding the possibilities for synthesizing new nanomaterials.
4. **Convenient experimental setup:** The experimental setup is straightforward and convenient. Once installed, it can be utilised multiple times for synthesizing nanomaterials, adding to its practical appeal.

2.1.2 Improved Hummer's method

The improved Hummer's method is an advanced procedure designed for the efficient synthesis of graphene oxide (GO) from graphite, utilizing powerful oxidizing agents like potassium permanganate ($KMnO_4$) and potassium chlorate ($KClO_3$). This enhanced method builds on the traditional Hummer's process, which was originally developed by William S. Hummers and Richard E. Offerman.

The key features of the improved Hummer's method are:

1. **Enhanced oxidation agents:** Potassium Permanganate ($KMnO_4$) and Potassium Chlorate ($KClO_3$) are used as strong oxidizers. Their high oxidation states contribute to more effective and controlled oxidation of graphite, leading to a higher degree of oxidation and better quality GO.
2. **Optimized reaction conditions:** The improved method operates under mild temperatures and often at low temperatures (e.g., 0-5 °C), which helps in controlling the reaction rate and minimizing side reactions. This control results in a more consistent product and a higher carbon-to-oxygen (C/O) ratio, enhancing the quality of the GO.

3. **Safety and efficiency:** Compared to the conventional methods, the improved procedure is designed to be less hazardous. By optimizing reaction conditions and using safer reagents or protocols, the process reduces the risks associated with the synthesis and handling of potentially dangerous chemicals.
4. **Faster processing:** Enhanced reaction kinetics and better control mechanisms contribute to a more efficient synthesis process, reducing the overall time required to produce GO.
5. **High carbon-to-oxygen ratio (C/O):** The process ensures a high C/O ratio in the resulting GO. This characteristic is important for maintaining the structural integrity and functionality of GO, making it suitable for various applications.

The improved Hummer’s method is widely adopted for its effectiveness and practicality in producing high-quality graphene oxide with desirable properties. The advancements in this method offer better control over the synthesis process, enhance safety, and provide a higher quality material suitable for diverse applications in research and industry [3].

2.2 Characterization techniques

Various characterization techniques have been employed to verify the successful formation of nanocomposites of 2D nanomaterials and metal oxides. The structural study begins with X-ray diffraction (XRD), followed by morphological analysis using field-emission scanning electron microscopy (FESEM) and high-resolution transmission electron microscopy (HRTEM). Raman spectroscopy has been utilised for the analysis of vibrational modes. Fourier transform infrared spectroscopy (FTIR) has been employed for examining the functional groups. This section provides a concise overview of the operating principles of each characterization approach used in our research.

2.2.1 X-ray diffraction (XRD)

XRD is a powerful analytical technique used across a variety of applications, including crystallography, compound identification, strain measurement, crystallite size determination, assessment of thermal expansion coefficients and densities, crystal texture investigation, sample crystallinity quantification, dislocation density evaluation, and other analytical processes [4]. The foundational work in powder X-ray diffraction began in the early 20th century with pioneering contributions from Debye, Scherrer, and Hull between 1916 and 1917, marking the inception of powder diffraction research [5, 6].

These early contributions established the fundamental principles of powder diffraction. However, the field has dramatically evolved over the decades, particularly with the advent of advanced computing technology in the 21st century. A pivotal moment occurred approximately fifty years after the initial powder diffraction studies when Hugo Rietveld introduced a groundbreaking approach to the field. His innovative use of computer-assisted fitting of entire powder diffraction patterns marked a significant advancement in the analysis of crystalline materials. This development was made possible by the burgeoning computational power of the time and represented a watershed moment in powder diffraction analysis.

In contemporary practice, sophisticated algorithms are employed to analyse and interpret crystal structures within powder samples. This evolution from early transmission experiments and the identification of basic cubic crystal structures to advanced methods that enable the precise refinement of complex structures with thousands of atoms per unit cell reflects the significant progress in the field over the past century.

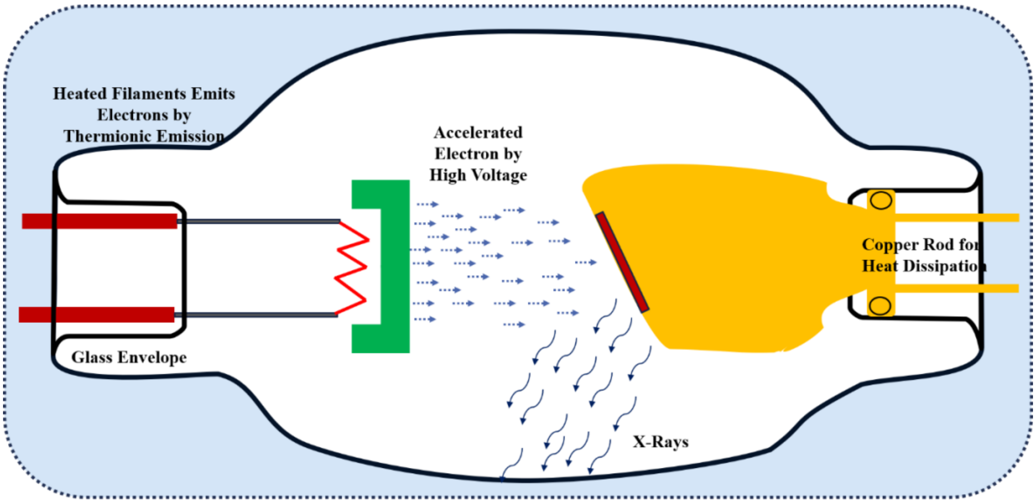

Fig. 2.2: Schematic showing the generation of X-rays in an X-ray tube

The X-ray generation process involves the use of a vacuum tube to produce X-rays, which are electromagnetic waves with wavelengths ranging from 0.1 Å to 100 Å. For effective diffraction analysis, X-rays with wavelengths between 0.5 Å and 2.5 Å are used, as these wavelengths are comparable to the sizes of the crystal lattices being studied. The X-ray generation setup, illustrated in Fig. 2.2, consists of an X-ray tube and a vacuum chamber containing a cathode and an anode.

In this setup, the cathode is typically a tungsten filament, and the anode is made of copper. High-energy electrons emitted from the tungsten filament are accelerated toward the copper anode with a voltage ranging from 30 to 60 kV. Upon collision, these high-energy electrons eject electrons from the innermost shell of the copper atoms. Electrons from the L and M shells then transition to the K shell to fill these vacancies, emitting X-rays known as CuK_α and CuK_β, with wavelengths of 1.54 Å and 1.39 Å, respectively. To obtain monochromatic radiation at 1.54 Å, a nickel filter is used to remove the CuK_β radiation, ensuring that the analysis relies on the desired CuKα line [7].

In 1913, W. H. Bragg and W. L. Bragg made a ground breaking discovery regarding crystalline materials: they observed that X-rays are reflected in a distinctive pattern when interacting with crystals. This phenomenon is characterized by prominent peaks in scattered radiation occurring at specific angles and wavelengths. W. L. Bragg proposed that a crystal can be conceptualized as a series of parallel planes with a defined spacing, denoted as ‘d’. When X-rays are reflected off the ions in these parallel planes, they produce sharp peaks in intensity. If these X-rays are reflected from successive parallel planes, they interfere constructively, resulting in enhanced peak formation, as illustrated in Fig. 2.3.

To achieve Bragg's condition for constructive interference, the path difference between the reflected X-rays must equal an even integer multiple of half the wavelength. This requirement is mathematically expressed by the equation:

$$2d\,sin\,\theta\; = n\,\lambda \qquad (2.1)$$

Here, the integer "n" denotes the order of diffraction.

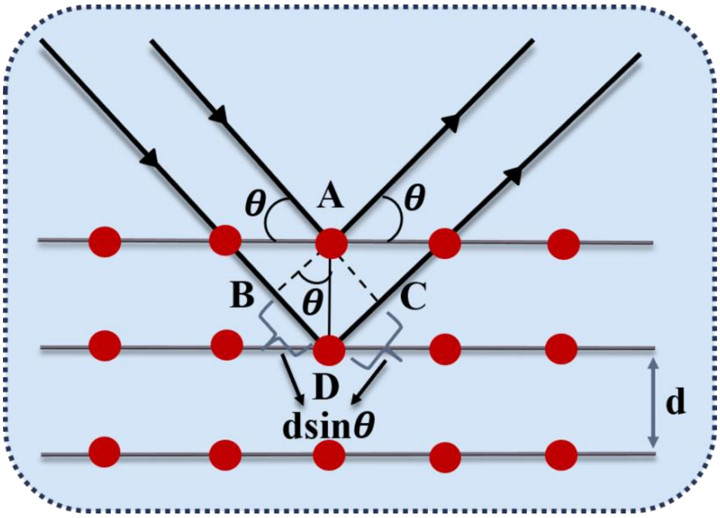

Fig. 2.3: Schematic showing the diffraction of X-rays obeying Brags law

Bragg's reflection is significant for X-rays with wavelengths $\lambda \leq 2d$, which is the range where diffraction from crystalline structures is observed. The positioning of diffraction peaks is influenced by several factors, including the size of the unit cell, the space group symmetry, and the overall crystal symmetry. These factors collectively determine the intensity of the diffraction peaks, as described by the equation:

$$F_{hkl} = \Sigma f_n e^{2\pi(hu_n+kv_n+lw_n)} \tag{2.2}$$

In this context, the coordinates of the elements within the crystal are denoted as (uvw), the Miller indices are represented by (hkl), and the electron scattering density is given by (f_n). This approach is typically employed for powdered samples, where the powder interacts with incident X-ray radiation across all accessible planes within the material, following Bragg's law. The resulting diffraction peaks correspond to parallel planes and vary with angle, reflecting constructive interference [8]. X-ray diffraction can also be utilised to determine the crystallite sizes by applying the correlation expressed in the following equation:

$$D=k\lambda\ \beta cos\theta \tag{2.3}$$

For this study, X-ray diffraction patterns were generated using a D8 Advance Bruker diffractometer (Germany) available in the Advanced Instrumentation Centre (AIC), Department of Applied Physics, Delhi Technological University, Delhi, India, employing CuK_α radiation with a wavelength of 1.5406 Å. The measurements were conducted at RT with a step size of 0.02º and a scan rate of 2º per minute. The resulting diffraction patterns were analysed by comparing them with data from the JCPDS database and with information from previously published literature.

2.2.2 Field-emission scanning electron microscopy (FESEM)

FESEM is an advanced microscopy technique that utilizes a field emission source to scan the specimen in a zigzag pattern. Compared to the tungsten filament used in conventional Scanning Electron Microscopy (SEM), the electron emitters in a field emission gun have an emission capacity up to 1000 times greater [9]. Similar to SEM, FESEM collects secondary electrons using a scintillator detector that converts these electrons into photons. However, FESEM operates under higher vacuum levels and requires the sample to be coated with a very thin layer of gold (Au) or palladium (Pd) to enhance conductivity and imaging quality. After the electrons leave the field emission gun, they are focused into a thin, monochromatic beam using metal apertures and magnetic lenses. A visual depiction of fundamental FESEM components is illustrated in Fig. 2.4.

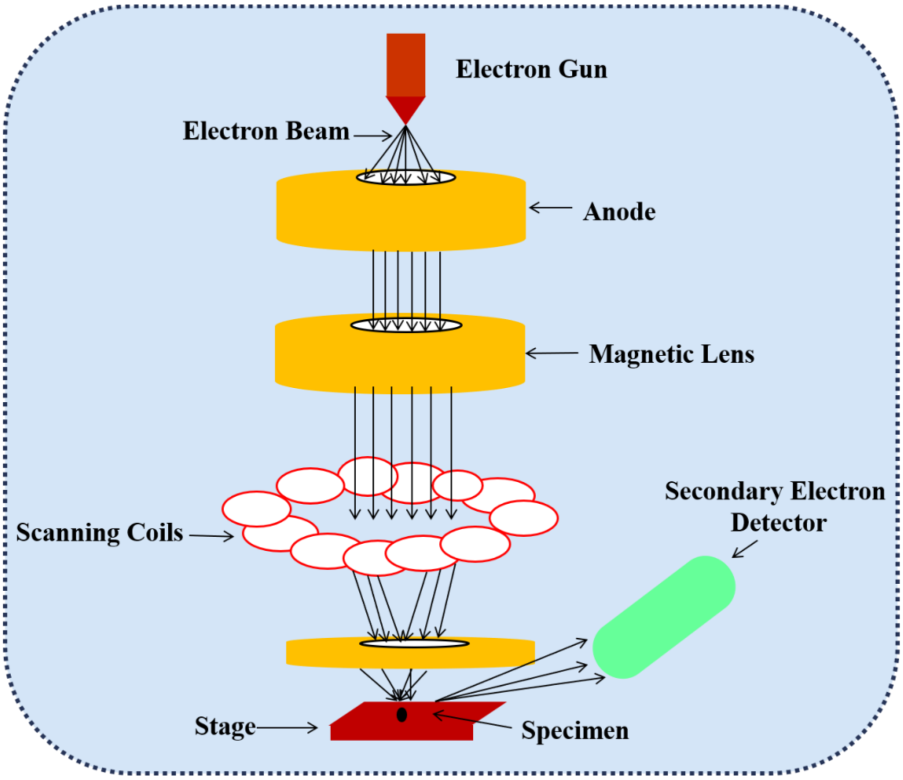

Fig. 2.4: Schematic showing the components of a FESEM

In FESEM, the interaction of the electron beam with the specimen is a complex process that produces various types of electrons, each with distinct characteristics and significance (Fig. 2.5).

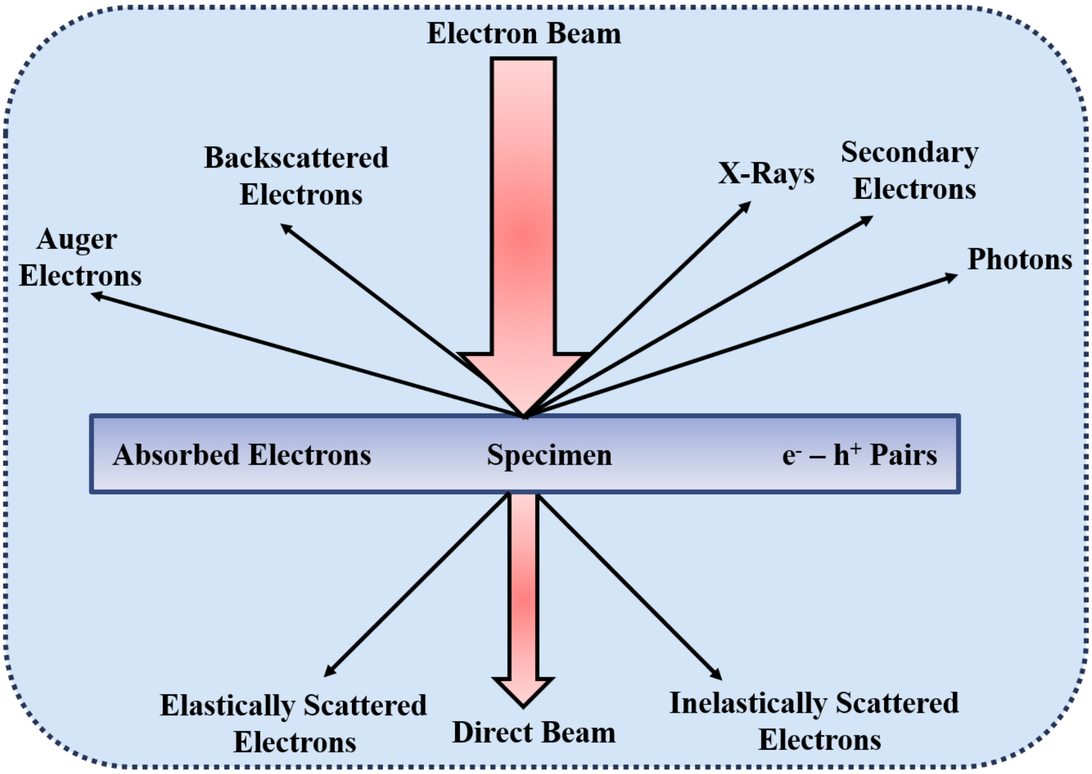

Fig. 2.5: Interaction of electrons with the specimen

Secondary electrons are emitted when primary electrons collide with the specimen, they can transfer enough energy to eject lower-energy electrons from the outer shells of the atoms. Secondary electrons are crucial for topographic imaging due to their low energy and high sensitivity to surface features. They provide high-resolution images with excellent surface detail. Backscattered electrons are primary electrons scattered elastically off the atomic nuclei of the specimen, bouncing back toward the detector. They carry information about the atomic number (Z) of the elements in the specimen. Higher Z materials will produce more backscattered electrons, allowing for enhanced contrast in images based on composition. This is useful for differentiating materials in multi-phase specimens. Characteristic X-rays are emitted when primary electrons displace inner-shell electrons in the specimen atoms, the resulting vacancies are filled by outer-shell electrons. This transition releases energy in the form of X-rays. The emitted X-rays are unique to each element, enabling qualitative and quantitative elemental analysis. These signals are very useful in the identification of elements present in the specimen. The unique atomic profile of each element gives X-rays to give qualitative information about elements using energy-dispersive X-ray analysis (EDX). Auger electrons are similar to X-ray generation, and are emitted when an electron from an outer shell fills a vacancy in an inner shell, resulting in the release of energy that can eject another electron. They can provide additional elemental information, especially in surface analysis, and can be used in conjunction with X-ray analysis for detailed compositional studies.

This technique offers exceptional information on both topography and elemental composition at extremely high magnifications, with a nearly unlimited depth of field. FESEM is notably more effective than conventional SEM, providing images with spatial resolutions as fine as 0.5 nanometers and significantly reduced electrostatic distortions [10]. FESEM is renowned for its ability to produce crisper, more accurate images with minimal electrostatic distortions. This capability makes it an invaluable tool for a broad range of scientific disciplines. Physicists use it for detailed structural analysis of materials, chemists for studying surface reactions, biologists for cellular imaging, material scientists for examining the properties of advanced materials, and electronic engineers for inspecting microchip structures. Its versatility and high-resolution imaging make FESEM indispensable in both research and industry, where observing fine details and understanding complex structures are crucial. The model of the instrument used to study surface morphology of nanocomposites of 2D nanomaterials and metal oxides described in the research work discussed in upcoming chapters is Zeiss Gemini SEM 500 (Germany), available in the University Science Instrumentation Centre (USIC), Delhi University, Delhi, India.

2.2.3 High-resolution transmission electron microscopy (HRTEM)

Transmission electron microscopy (TEM) is a sophisticated imaging technique that uses an electron beam to pass through an ultrathin specimen, revealing detailed insights into the sample's structure. As the electron beam traverses the specimen, it provides valuable information about the material's morphology and crystallography. TEM operates with electron beams at the nanometer scale, which, due to their shorter wavelength compared to visible light, achieve much higher resolution imaging [11]. The interactions between the electron beam and the specimen contribute to the formation of images. Various imaging technologies are employed to capture these interactions, including fluorescent screens, photographic film, and charge-coupled devices (CCDs). TEM can operate in two primary modes: diffraction mode and image mode.

The typical TEM setup includes an electron gun that generates a high-energy electron beam, which travels through a vacuum tube within the microscope. The beam is focused by condenser lenses and directed onto a specimen mounted on a motorized stage, typically a copper grid coated with the sample. The core components of the TEM apparatus include the objective lens and the specimen chamber, where the transmitted electron beam interacts with the thin specimen [12].

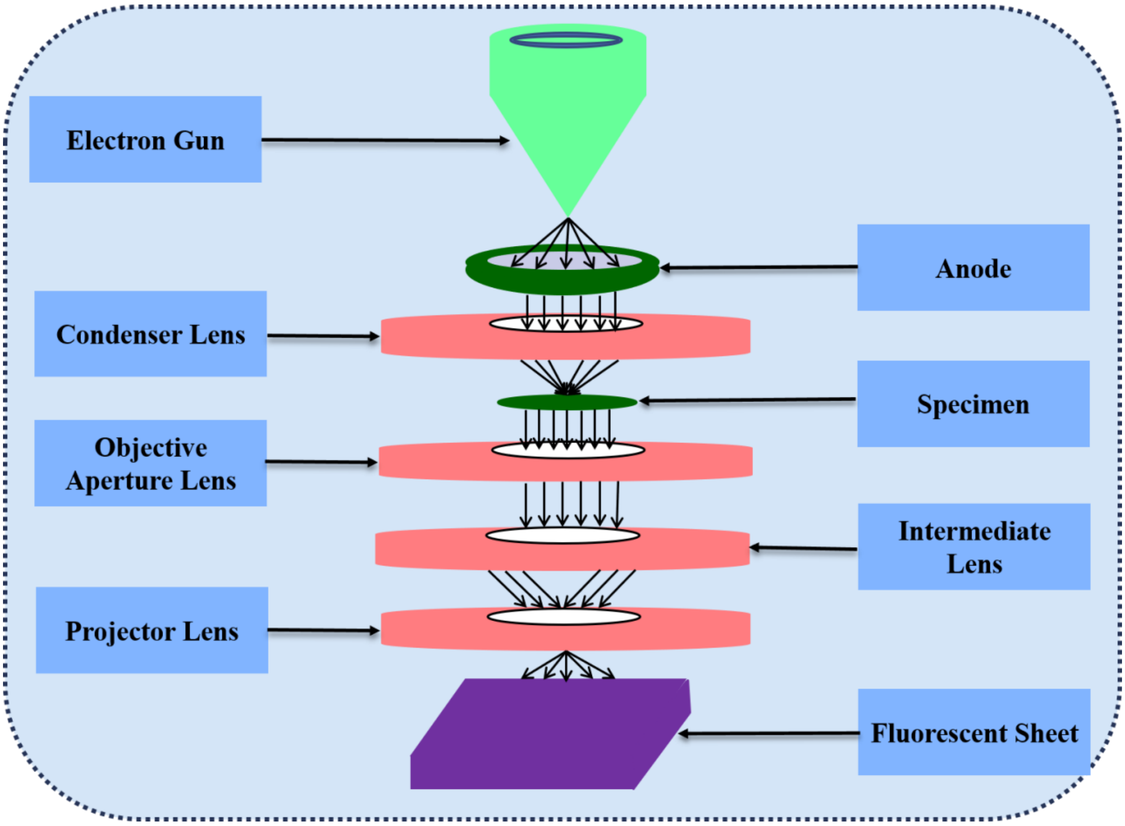

Fig. 2.6: Schematic showing the setup of HRTEM

For optimal imaging, the sample thickness should be between 100 and 200 nm, as electrons have difficulty penetrating samples thicker than 200 nm. High-resolution images and diffraction patterns are produced using an imaging system that consists of an objective lens and additional lenses. The electron beam, after passing through the sample, is projected onto a fluorescent screen via a three-stage lens system, and the resulting image is captured by a CCD camera, which converts the electron intensity into digital pixels [13].

TEM can operate in several modes, including HRTEM, Selected Area Electron Diffraction (SAED), and conventional TEM. These modes are used to analyse various sample characteristics such as particle size, morphology, lattice parameters, and material expansion direction. A schematic of the TEM setup is shown in Fig. 2.6.

The TEM system operates within a high vacuum chamber and is connected to a graphical user interface (GUI) for data acquisition. As electron beams interact with the sample, they undergo scattering, which can be categorized into elastic and inelastic scattering. Elastic scattering, influenced by the atomic arrangement in nanostructures, results in coherent beam scattering and produces spot patterns. Inelastic scattering, on the other hand, involves energy absorption or emission, which is specific to the chemical structure of the nanomaterials.

Imaging contrast in TEM is achieved through Bright-field and Dark-field imaging techniques. In bright-field imaging, the entire specimen is illuminated uniformly, producing a dark image against a bright background. In dark-field imaging, contrast is achieved by capturing diffracted waves on the back focal plane of the objective lens through an objective aperture [14].

To enhance image resolution, the electron wavelength can be reduced by increasing the accelerating voltage of the field emission gun up to a maximum of 300 kV. This high accelerating voltage improves the point resolution of the images, resulting in HRTEM images with exceptional clarity. The model of the HRTEM instrument used in the research work presented in chapters 3 to 6, is JEOL (Japan) JEM-2100F, available in the Advanced Instrumentation Research Facility (AIRF), Jawaharlal Nehru University (JNU) and FEI Tecnai 200 (United States) in the Sophisticated Analytical Instrument Facility, AIIMS, New Delhi, Delhi, India.

2.2.4 Raman spectroscopy

Raman spectroscopy is utilised to observe the rotational, vibrational, and other frequency modes of a system. This method reveals insights into the bonding and structure of molecules, thereby offering a unique fingerprint for their identification. Raman spectroscopy operates on the principle of inelastic light scattering, known as the Raman Effect [15]. When monochromatic radiation interacts with the sample, it behaves differently upon incidence. This interaction encompasses scattering, reflection, and absorbance, all occurring consistently. Molecular structural information is gleaned through the scattering of radiation. The coherent source typically employed for specimen analysis is a laser [16]. The bulk of incoming radiation disperses elastically, generating Rayleigh scattered light. Only a minute fraction, approximately 1 in 10^{-6}, undergoes inelastic scattering, predominantly manifesting as Stokes and anti-Stokes lines. This fraction is instrumental in gathering information about the specimen.

Firstly, in Rayleigh Raman scattering, the frequency of the incident and scattered light remains the same. Secondly, in anti-Stokes Raman scattering, the frequency of the scattered light is higher than that of the incident light. Thirdly, in Stokes Raman scattering, the frequency of the scattered beam light is lower than that of the incident beam light [17]. Fig. 2.7 depicts a block diagram of a Raman spectrometer.

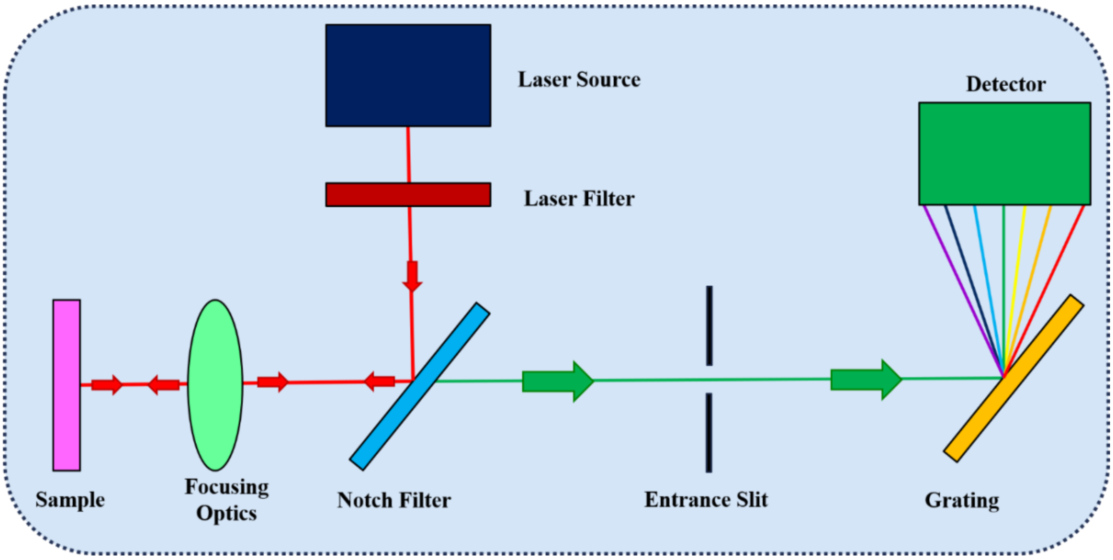

Fig. 2.7: Schematic representation of Raman spectrometer

The Raman spectrum is graphed to represent the relationship between the intensity of scattered light and the energy difference. When photons interact with a molecule, they induce a dipole moment in the molecule's electric field, expressed as

$$P = \alpha . E \tag{2.4}$$

where α is a proportionality constant. This phenomenon provides insights into the distortion of the electron cloud around the molecule [18]. The specific energy transitions associated with changes in polarizability within molecular bonds result in the emergence of Raman active modes. Modern Raman spectroscopy comprises three primary components: a laser source, a means of illuminating the sample, and a suitable spectrometer. Lasers, favored for their monochromaticity and high-intensity beams, stand as the most prevalent sources employed in studying Raman spectra, ensuring favorable signal-to-noise (S/N) ratios. Raman spectrometers commonly rely on either CCD or FTIR technology outfitted with cooled germanium detectors. Raman spectroscopy often surpasses IR spectroscopy due to its applicability in examining inorganic systems within aqueous solutions. This technique has found extensive application in the study of biological systems. Its benefits lie in its minimal susceptibility to water interference, requirement for small sample sizes, and ability to detect environmental and conformational changes with high sensitivity. Raman spectroscopy proves invaluable in identifying molecular impurities and additives, serving as a non-destructive method for both quantitative and qualitative analysis across various contexts. The model of the instrument used to study the rotational, vibrational, and other frequency modes of nanocomposites of 2D nanomaterials and metal oxides as described in the research work discussed in upcoming chapters is WITec alpha 300 RA (Germany), available in Advanced Instrumentation Research Facility (AIRF), Jawaharlal Nehru University (JNU), Delhi, India.

2.2.5 Fourier-transform infrared spectroscopy (FTIR)

Materials consist of various chemical elements bonded together by strong covalent bonds, forming molecules where the nature of bonds is dictated by the electronic configuration of the constituent atoms. These bonds undergo continuous dynamic movements such as vibration, stretching, and rotation within the material's structure, with their energy residing in the ground state. FTIR spectroscopy employs infrared radiation spanning a broad spectrum from 400 cm^{-1} to 4000 cm^{-1}. It is predominantly utilised in research laboratories to discern various compounds within a given sample. This technique, while straightforward, holds significant importance in characterization, boasting a multitude of applications. FTIR spectroscopy finds application in analysing thin films and coatings to identify their functional groups. Notably, this method offers several advantages, including rapid scanning speeds in comparison to other dispersive methods, and its versatility in analysing solids, liquids, and gases alike. The technique relies on the molecular bonds within the compounds present in the sample. The type of molecular bonds in different molecules depends on the constituent atoms.

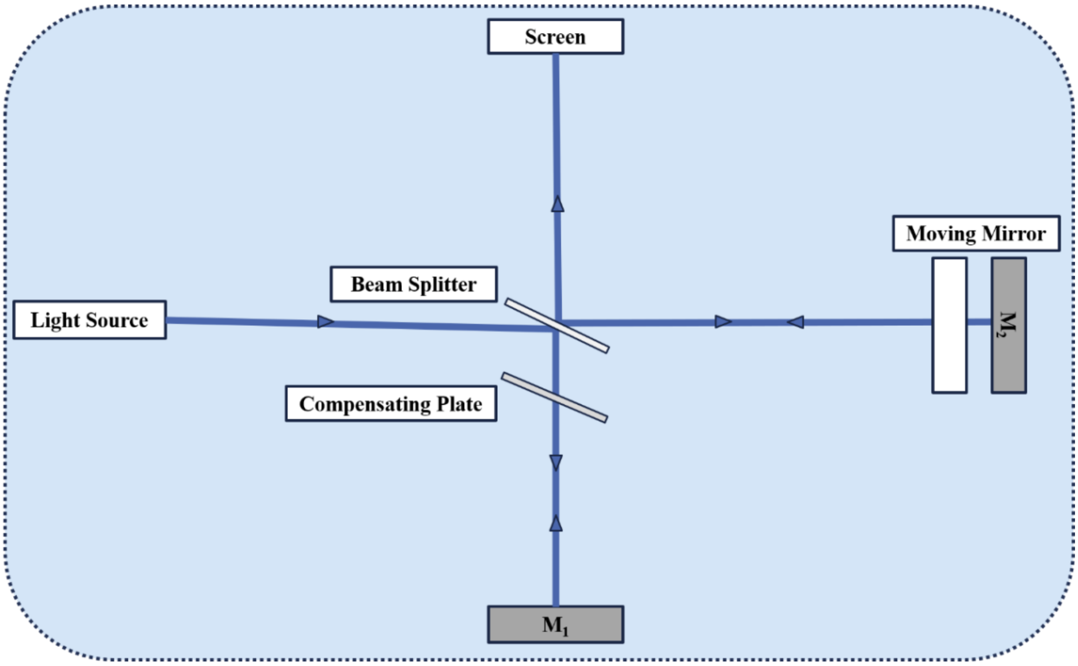

Fig. 2.8: Schematic of Michelson interferometer

When substances in a sample are exposed to IR radiation, their molecules absorb energy, transitioning to a higher energy state**.** As these molecules transition back to their original (de-excited) state, they release radiation with energy equivalent to the difference between the energies of the de-excited and excited states of the molecules. Every substance selectively absorbs a distinct wavelength of IR light from the magnitude of wavelengths found in the incident light [19]. The FTIR measures these absorbed wavelengths, allowing it to discern the nature of the substance and its bonds. The resulting graph can display either the "transmittance" or "absorption" of the IR radiation on the y-axis plotted against the wavenumber on the x-axis**.** The graph may exhibit multiple peaks depending on the molecule's characteristics. These peaks are subsequently scrutinized and compared to known standard IR peaks associated with various materials and bonds. This method holds utmost significance in identifying organic molecules containing robust dipoles and polar chemical bonds (such as NH, OH, CH, etc.) [20-22].

When mid-infrared (MIR) radiation emitted by the source lamp reaches the interferometer, it undergoes a process where it is divided into two beams. These beams then travel through an optical assembly before converging again at the beam splitter. This results in the formation of an optically interfered beam, which contains all MIR wavelengths combined into a single beam, known as an interferogram. The interferogram is directed through the sample, where it absorbs wavelengths of radiation corresponding to its properties. The Michelson interferometer which is depicted in Fig. 2.8 is a commonly used technique in FTIR spectroscopy. This absorption causes the molecules in the sample to transition to an excited state before returning to their ground state, emitting radiation characteristic of the energy gap in the process. The MIR detector captures the output interferogram and transforms the beam into an electrical signal. The signals are then decoded using the mathematical technique known as Fourier transform, facilitated by specialized computer software. The resulting spectrum is presented by plotting transmittance against wavenumber, as depicted in Fig. 2.9.

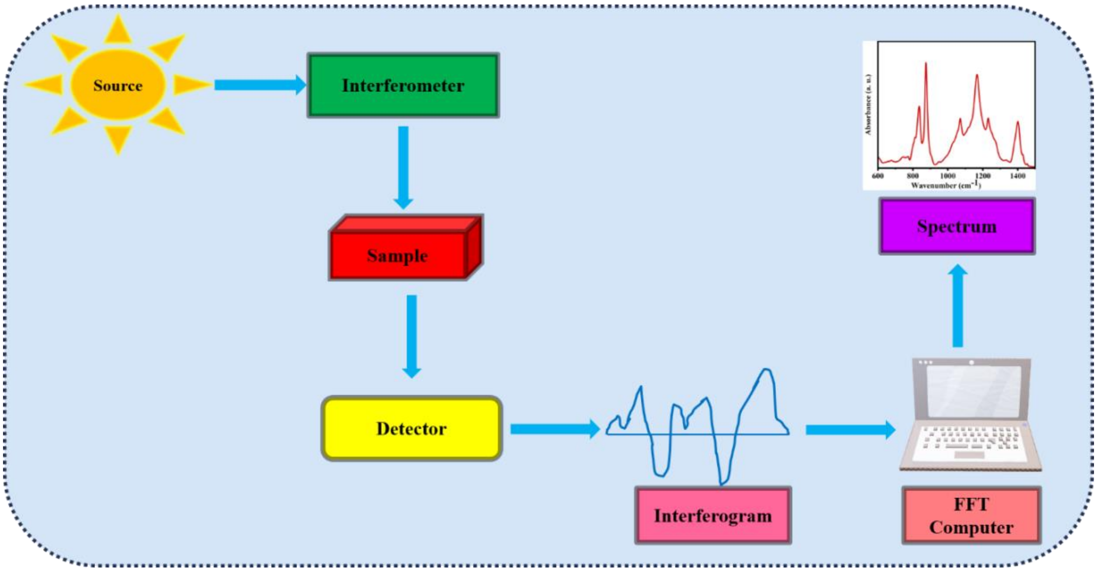

Fig. 2.9: Schematic showing FTIR spectroscopy

The model used for analysing the nature and type of bonds along with inter-bonds interaction between molecules of nanocomposites of 2D nanomaterials and metal oxides as described in the research work presented in chapters 3, 4, and 5 respectively is Perkin Elmer (U.S.) Spectrum two L160000A series, available in the Nanomaterials Research Laboratory (NRL), Department of Applied Physics, Delhi Technological University, Delhi, India.

2.2.6 Brunauer-Emmett-Teller (BET) Analysis

The most widely recognized technique for identifying the porous microstructure of a material is nitrogen adsorption-desorption isotherm analysis. This technique assesses two critical properties of porous materials: effective surface area and pore volume, which are essential for various functional applications. Nitrogen gas, acting as the adsorbate, is commonly used due to its inert behavior, availability in high purity, relatively high boiling point at 77 K, and cost-effectiveness compared to other inert gases such as Ar, Kr, and CO_2 [23]. The isotherm is typically measured using the BET (Brunauer, Emmett, and Teller) method, which is a model developed for multilayer molecular gas adsorption on porous surfaces [24]. Before the BET theory, the Langmuir model, which considered only monolayer adsorption, was dominant. The BET model, however, introduced the idea of multilayer adsorption, where gas molecules adsorb on specific sites to form a monolayer, and subsequent layers can form on top of the adsorbed molecules. This model assumes that the upper layers exhibit liquid-like behavior, in equilibrium with the vapor phase of the lower layers.

Capillary condensation becomes significant when gas pressure falls below its critical value, allowing for the determination of effective surface area and mesopore structure. Nitrogen adsorption is measured at different pressure levels, typically between 0.05 and 0.995 relative pressure, at a constant temperature of 77 K. The resulting isotherm shape and hysteresis patterns, when present, help to elucidate the physisorption mechanisms and the material's porous structure. According to IUPAC, there are six types of adsorption isotherms and four types of hysteresis behaviors that help classify mesopore morphology. At low relative pressures (0.05-0.3), a monolayer or multilayer adsorption occurs on the walls of micro- or mesopores. A distinct "knee" in the isotherm curve at low pressure indicates the complete coverage of the surface with a monolayer of nitrogen gas. The monolayer capacity is then used to calculate the specific surface area of the material. BET theory is most effective for non-porous, macroporous, and mesoporous materials but is not suitable for microporous materials.

At higher pressures, capillary condensation occurs in mesopores, resulting in a liquid-like phase. Pores of different sizes will condense vapor at different relative pressures, which provides insights into the pore volume and size distribution. The BJH (Barrett, Joyner, and Halenda) theory is used to estimate pore size distribution, assuming cylindrical, non-intersecting pores.

Porosity is defined as the ratio of the volume occupied by pores to the volume of the solid material, calculated using the formula:

$$\text{Porosity} = (1 - d_{bulk}/d_{exp}) \times 100 \qquad (2.5)$$

Where d_{bulk} is the X-ray density of the bulk crystallite, and d_{exp} is the experimental density measured using Archimedes water displacement principle. The model used for analysing the specific surface area as described in the research work presented in chapter 5 is Quantachrome NOVA 2200e (U.S.), available in the Department of Physics & Astrophysics, Delhi University, Delhi, India.

2.3 Gas sensor fabrication

For fabricating the sensor, films of nanocomposites of 2D nanomaterials and metal oxides are fabricated using the electrophoretic deposition technique. Following this, metal electrodes are deposited onto the synthesised films using the thermal evaporation technique.

2.3.1 Electrophoretic deposition (EPD) technique

Electrophoretic Deposition (EPD) is a technique used to produce homogeneous films by applying an electric field to charged particles suspended in liquids such as de-ionized water, ethanol, acetonitrile, or isopropanol. It is cost-efficient and versatile for film production. The EPD cell typically consists of a glass beaker containing two electrodes separated by a certain distance. One electrode serves as the reference electrode (RE), usually a thin platinum (Pt) rod, while the other electrode is a copper (Cu) rod onto which the working electrode (WE) is attached, forming the substrate for film deposition. To ensure uniform deposition onto the substrate, the particles must be evenly dispersed in the liquid. Common solvents used for dispersion include acetone, distilled water, ethanol, acetonitrile, isopropanol, and chloroform. Optimization of applied potential and deposition time is essential to achieve films of the desired thickness [25-28]. However, it is important to note that the technique requires conducting substrates and the addition of dispersant may result in impurities. In some cases, heat treatment may be applied to the films to enhance adhesion. Fig. 10 illustrates a typical EPD setup, where charged particles suspended in the liquid are deposited onto the substrate upon the application of a DC power supply for an optimized period.

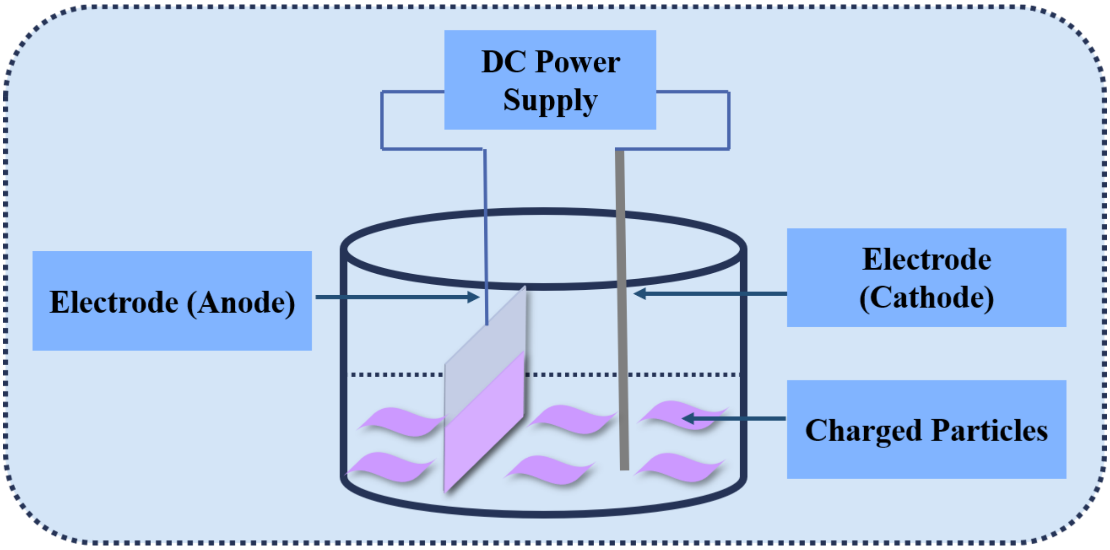

Fig. 2.10: Schematic showing the fabrication of film via EPD technique

2.3.2 Thermal evaporation technique for electrode deposition

The thermal evaporation technique is widely utilised for producing electrodes due to its versatility and effectiveness. This method relies on carefully controlling the sublimation and condensation of materials under vacuum conditions, resulting in the creation of uniform and precisely deposited electrodes.

Operating on the principle of vapor-phase deposition, this technique involves heating a solid substance within a vacuum chamber causing it to sublimate or evaporate. The vaporized material then condenses onto a substrate, forming a thin layer. Condensation occurs as vapor molecules interact with the substrate surface, leading to the development of a film that exhibits characteristics similar to those of the source material [29, 30]. Its applications span various fields such as electronics, optoelectronics, and energy conversion devices.

Thermal evaporation fabrication typically involves the following sequential steps [31]:

1. **Preparation of vacuum chamber:** A vacuum chamber is prepared to accommodate both the substrate and the evaporation source. Maintaining a low-pressure environment is crucial to prevent unwanted reactions and ensure controlled deposition.

2. **Heating the evaporation source:** The evaporation source, often in the form of pellets, wires, or rods, is heated using resistive or electron beam heating methods. As the source reaches its evaporation temperature, it undergoes sublimation, releasing vaporized atoms or molecules.

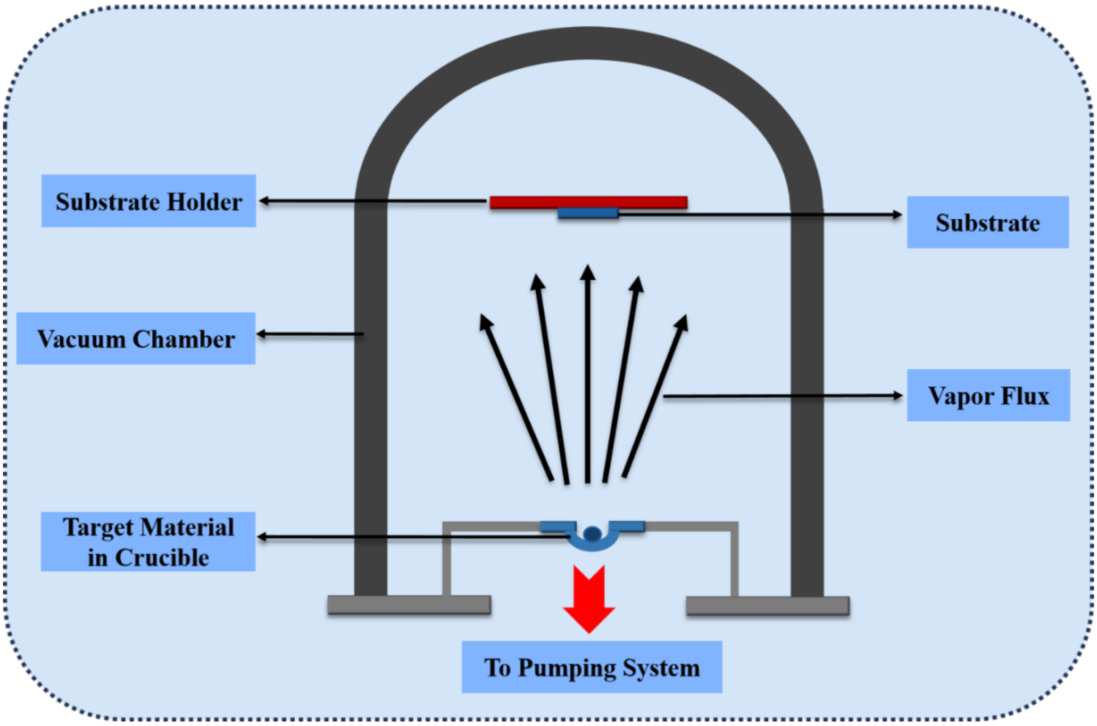

Fig. 2.11: Schematic representation of thermal evaporation system

3. **Deposition process:** Vaporised material travels within the vacuum chamber and reaches the surface of the substrate. Upon collision with the substrate, the vapor condenses and adheres to form a thin film. Factors such as the temperature of the evaporation source and the distance between the source and substrate regulate the deposition rate.
4. **Film growth:** The duration of deposition determines the thickness of the coating. Various parameters, including substrate temperature, pressure, and deposition rate, influence the characteristics of the resulting film, such as its shape, crystallinity, and thickness uniformity.

In our current study, we have utilised thermal evaporation to deposit metal electrodes onto films synthesised by the EPD technique, facilitating the fabrication of gas sensors (as illustrated in Fig. 2.11). The model used for the electrode deposition as described in the research work discussed in upcoming chapters is Smart Coat 3.0, Hind High Vacuum, available in Computational Functional Materials Research Laboratory (CFMRL), Department of Applied Physics, Delhi Technological University, Delhi, India. After depositing metal electrodes, the electrical analysis of the sensors has been conducted utilising the Keithley Sorce Measuring Unit (SMU) 2450 available in the Nanomaterials Research Laboratory (NRL), Department of Applied Physics, Delhi Technological University, Delhi, India.

2.4 Gas sensing measurements

The gas sensing behavior of the sensing device is investigated using an indigenously constructed chemiresistive gas sensing setup available in the Nanomaterials Research Laboratory (NRL), Department of Applied Physics, DTU (as shown in Fig. 2.12). The setup consists of a stainless steel (SS) chamber attached to two gas mass flow controllers (MFC). A constant current supply to the sensing device is provided by the source measuring unit (SMU). At the beginning of the gas detection process, rough vacuum pressure is created inside the SS chamber using a rotary pump. Then, dry air is introduced to obtain the baseline resistance. After that mixture of ethanol gas and dry nitrogen gas is introduced inside the SS chamber. Inside the SS chamber, the concentration of ethanol gas is calculated in parts per million (ppm) according to the following equation:

$$C = \frac{22.4 \times \Psi \times \rho \times V_1}{M \times V_2} \times 1000 \tag{2.6}$$

In the above formula (equation 2.6), the ethanol gas concentration is depicted by C (ppm), gas volume fraction is denoted as Ψ, density of ethanol is represented as ρ ($kg.m^{-3}$), volume of ethanol gas is indicated as V_1 (L), molecular weight of ethanol is expressed as M ($kg.mol^{-1}$), and volume of the SS chamber is denoted as V_2 (m^3) [32]. A digital hygrometer is employed to measure the relative humidity (RH) in the SS chamber. The change in resistance of sensing films is recorded using a Lab-View data acquisition software connected to the source measuring unit or a Keithley digital multimeter (DMM7510) is used. The gas sensing measurements of the sensing films are carried out at RT (27 °C).

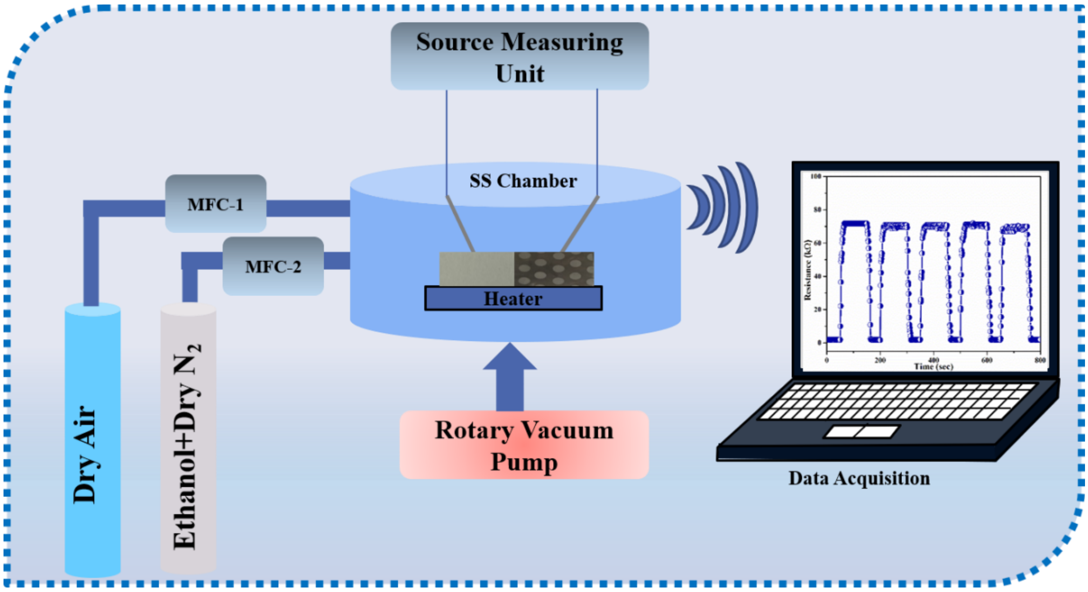

Fig. 2.12: Chemiresistive gas sensing setup

References

[1] H. Zhang, H.-M. Cheng, and P. Ye, "2D nanomaterials: beyond graphene and transition metal dichalcogenides," *Chemical Society Reviews,* vol. 47, no. 16, pp. 6009-6012, 2018.

[2] J. Li, Q. Wu, and J. Wu, "Synthesis of Nanoparticles via Solvothermal and Hydrothermal Methods 12," ed, 2016.

[3] W. S. Hummers Jr and R. E. Offeman, "Preparation of graphitic oxide," *Journal of the american chemical society,* vol. 80, no. 6, pp. 1339-1339, 1958.

[4] P. Debye and P. Scherrer, "Interferenzen an regellos orientierten Teilchen im Röntgenlicht. I," *Nachrichten von der Gesellschaft der Wissenschaften zu Göttingen, Mathematisch-Physikalische Klasse,* vol. 1916, pp. 1-15, 1916.

[5] A. W. Hull, "A new method of X-ray crystal analysis," *Physical Review,* vol. 10, no. 6, p. 661, 1917.

[6] M. Etter and R. E. Dinnebier, "A century of powder diffraction: a brief history," *Zeitschrift für anorganische und allgemeine Chemie,* vol. 640, no. 15, pp. 3015-3028, 2014.

[7] C. Kittel and P. McEuen, *Introduction to solid state physics*. John Wiley & Sons, 2018.

[8] B. B. He, *Two-dimensional X-ray Diffraction*. John Wiley & Sons, 2018.

[9] M. A. Sutton, N. Li, D. Joy, A. P. Reynolds, and X. Li, "Scanning electron microscopy for quantitative small and large deformation measurements part I: SEM imaging at magnifications from 200 to 10,000," *Experimental mechanics,* vol. 47, pp. 775-787, 2007.

[10] A. Ul-Hamid, *A beginners' guide to scanning electron microscopy*. Springer, 2018.

[11] L. H. Schwartz, J. B. Cohen, L. H. Schwartz, and J. B. Cohen, "The nature of diffraction," *Diffraction from Materials,* pp. 46-76, 1987.

[12] F. Lin, "Preparation and characterization of polymer TiO 2 nanocomposites via in-situ polymerization," University of Waterloo, 2006.

[13] L. A. Bendersky and F. W. Gayle, "Electron diffraction using transmission electron microscopy," *Journal of research of the National Institute of Standards and Technology,* vol. 106, no. 6, p. 997, 2001.

[14] H. H. Willard, L. L. Merritt Jr, J. A. Dean, and F. A. Settle Jr, "Instrumental methods of analysis," 1988.

[15] M. J. Pelletier, "Quantitative analysis using Raman spectrometry," *Applied spectroscopy,* vol. 57, no. 1, pp. 20A-42A, 2003.

[16] I. R. Lewis and H. Edwards, *Handbook of Raman spectroscopy: from the research laboratory to the process line*. CRC press, 2001.

[17] P. Graves and D. Gardiner, "Practical raman spectroscopy," *Springer,* vol. 10, pp. 978-3, 1989.

[18] J. R. Ferraro, *Introductory raman spectroscopy*. Elsevier, 2003.

[19] D. Titus, E. J. J. Samuel, and S. M. Roopan, "Nanoparticle characterization techniques," in *Green synthesis, characterization and applications of nanoparticles*: Elsevier, 2019, pp. 303-319.

[20] W. M. Doyle, "Principles and applications of Fourier transform infrared (FTIR) process analysis," *Process Control Qual,* vol. 2, no. 1, pp. 11-41, 1992.

[21] H. Knözinger, "Dehydration of alcohols on aluminum oxide," *Angewandte Chemie International Edition in English,* vol. 7, no. 10, pp. 791-805, 1968.

[22] G. C. Schatz, R. P. Van Duyne, J. Chalmers, and P. Griffiths, "Handbook of vibrational spectroscopy," *New York: Wiley,* vol. 1, p. 759, 2002.

[23] S. J. Gregg, K. S. W. Sing, and H. Salzberg, "Adsorption surface area and porosity," *Journal of The electrochemical society,* vol. 114, no. 11, p. 279Ca, 1967.

[24] P. I. Ravikovitch, A. Vishnyakov, R. Russo, and A. V. Neimark, "Unified approach to pore size characterization of microporous carbonaceous materials from N2, Ar, and CO2 adsorption isotherms," *Langmuir,* vol. 16, no. 5, pp. 2311-2320, 2000.

[25] K. Arora and N. K. Puri, "Electrophoretically deposited nanostructured PdO thin film for room temperature amperometric H2 sensing," *Vacuum,* vol. 154, pp. 302-308, 2018.

[26] R. Khatri and N. K. Puri, "Electrochemical biosensor utilizing dual-mode output for detection of lung cancer biomarker based on reduced graphene oxide-modified reduced-molybdenum disulfide multi-layered nanosheets," *Journal of Materials Research,* vol. 37, no. 8, pp. 1451-1463, 2022.

[27] N. Jain and N. K. Puri, "Zinc oxide incorporated molybdenum diselenide nanosheets for chemiresistive detection of ethanol gas," *Journal of Alloys and Compounds*, vol. 955, p. 170178, 2023.

[28] R. Khatri and N. K. Puri, "Electrochemical studies of biofunctionalized MoS 2 matrix for highly stable immobilization of antibodies and detection of lung cancer protein biomarker," *New Journal of Chemistry,* vol. 46, no. 16, pp. 7477-7489, 2022.

[29] N. Nedelcu, *Thin Films: Processes and Characterization Techniques*. Springer Nature, 2023.

[30] H. Frey and H. R. Khan, *Handbook of thin film technology*. Springer, 2015.

[31] D. A. Glocker, S. I. Shah, and C. A. Morgan, *Handbook of thin film process technology*. Institute of Physics Bristol, 1995.

[32] Q. Chen *et al.*, "Optimization ethanol detection performance manifested by gas sensor based on In2O3/ZnS rough microspheres," *Sensors and Actuators B: Chemical*, vol. 264, pp. 263-278, 2018.

CHAPTER 3

Zinc Oxide incorporated Molybdenum Diselenide Nanosheets for Chemiresistive Detection of Ethanol Gas

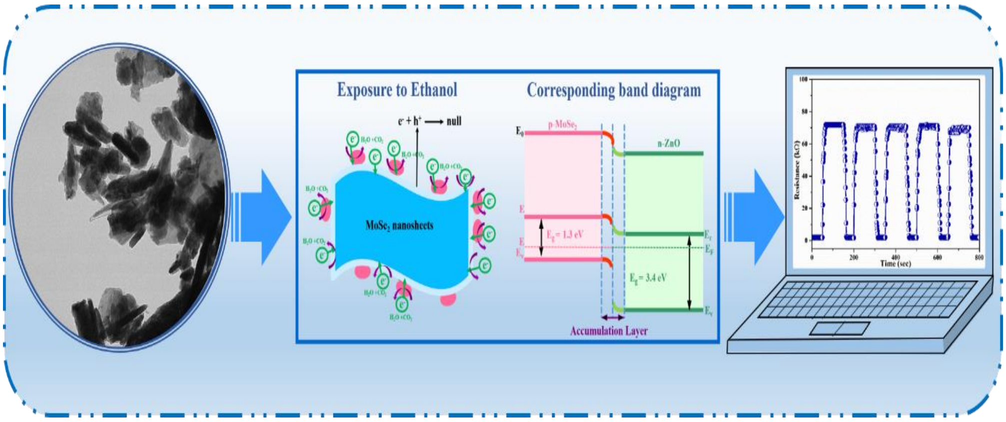

In this chapter, we have demonstrated a room temperature chemiresistive ethanol gas sensor based on hydrothermally synthesised zinc oxide (ZnO) incorporated-molybdenum diselenide ($MoSe_2$) nanosheets. The sensing properties of the $MoSe_2$/ZnO nanocomposite sensor were investigated systematically by exposing the sensor to various ethanol gas concentrations (10- 500 ppm) in dry N_2 and dry air. The synergistic effect due to the incorporation of ZnO nanorods in $MoSe_2$ nanosheets was found to enhance the sensor response to ethanol gas (when operated in dry N_2) with improved response and recovery time of 8.4 and 14.7 seconds respectively, high selectivity, stability, and reproducibility. The nanocomposite-based sensor showed a high gas sensing response (R_g/R_a) of 37.8 to 500 ppm of ethanol gas. While the response of the nanocomposite-based sensor decreased to 15.3 to 500 ppm of ethanol gas in dry air which suggests that the sensor performs better when operated in dry N_2 than in dry air. Based on experimental results, a plausible mechanism has been proposed based on the formation of p-n heterojunction and potential barrier modulation at the interface of the $MoSe_2$/ZnO nanocomposite sensor. The results demonstrated that $MoSe_2$/ZnO-based nanocomposite may pave the way for the fabrication of ethanol gas sensors for real-time electronics applications.

3.1 Introduction

Rapid industrialization and socio-economic development have resulted in the release of volatile organic compounds (VOCs) in the environment [1, 2]. Exposure to most VOCs, not only causes environmental pollution but is also detrimental to human health. One of the typical VOCs "ethanol gas", is extensively used as a valuable ingredient in alcoholic beverages, paints, medicines, cosmetics, etc [3, 4]. Despite its numerous applications in a variety of fields, its long-term exposure causes various ailments such as eye and skin irritation, headaches, nausea, vomiting, kidney failure, and even damage to the central nervous system [5, 6]. Therefore, it is the need of the hour to timely monitor and detect ethanol gas, especially at room temperature (RT) as a part of the safety system. Among various types of sensors developed by scientists for the effective detection of VOCs, chemiresistive sensors have generated huge interest due to their low-cost, simple monitoring techniques, easy design, and high chemical and thermal stability [7, 8].

Recently molybdenum diselenide ($MoSe_2$), a two-dimensional (2D) transition metal dichalcogenides (TMDs) has attracted considerable attention for multifunctional applications due to its significant physical and chemical properties [9, 10]. Its outstanding gas sensing properties have been explored owing to the large surface-to-volume ratio which provides elevated sites for the adsorption and desorption of target gasses [11]. In addition to this, it also exhibits higher adsorption energy with chemical molecules [12]. Some pioneering studies based on the gas sensing properties of $MoSe_2$ have been investigated (targeting several analytes like H_2S, NH_3, NO_2 C_2H_5OH, etc.) which led a path to explore this material in-depth [13-16]. Jha et al. studied the gas sensing properties of $MoSe_2$ for the detection of H_2S gas down to the ppb level. But pristine $MoSe_2$ showed a recovery time of 5 min at 90 ºC [13]. Late et al. used a single-layer $MoSe_2$-based NH_3 gas sensor at RT. The sensor displayed a bit large response (2.5 min) and recovery (9 min) time [14]. In another report, Singh et al. made use of liquid-exfoliated $MoSe_2$ nanosheets for RT ammonia sensing. The corresponding response and recovery times were 15 s and 135 s respectively [15]. In another study, Zhang et al. reported the sensing potential of $MoSe_2$ toward ethanol gas at 90 ºC. It was observed that the nanosheets took a long time to restore their original state at RT. Although the temperature was raised higher, still the recovery time was 5 min [16]. Therefore, these studies demonstrate that pristine $MoSe_2$-based gas sensors exhibit sluggish response and recovery time which challenges the use of intrinsic $MoSe_2$-based gas sensors. In this regard, various strategies have been employed to improve the sensor performance of $MoSe_2$ gas sensors such as synthesising composites, combining with noble metals (gold (Au), silver (Ag), platinum (Pt), etc.), surface functionalization, and many more. For instance, Jha et al. demonstrated the use of reduced graphene oxide/molybdenum diselenide nanocomposite for the detection of ammonia at RT. The sensor showed the limit of detection down to 300 ppb, with an operating voltage of 2 mV [17]. Li et al. prepared pristine $MoSe_2$ and Ag-modified $MoSe_2$-based ethanol gas sensors at RT. The sensor exhibited a low detection limit, good response properties, and excellent repeatability [10]. Abun et al. fabricated a hydrogen gas sensor based on p-n heterostructures comprising exfoliated $MoSe_2$ nanosheets doped on the surface of n-type ZnO nanorods. The hybrid p-n heterostructure showed better sensor response in comparison to pristine ZnO and $MoSe_2$ [18]. Hence it is clear from the above studies that modification of $MoSe_2$ with other elements provides alternate strategies for the development of practical gas sensors. This encourages us to explore $MoSe_2$/ZnO nanocomposite for ethanol sensing application which can effectively improve the response/recovery time of the existing 2D nanomaterials-based ethanol sensors.

To the best of our knowledge, there are no reports available focussing on hydrothermal synthesis of ZnO incorporated- $MoSe_2$ nanosheets-based nanocomposite towards their utilization for the chemiresistive detection of ethanol gas at RT. The sensor was recovered in two different environments i.e., in dry N_2 and dry air. Various characterization techniques are employed to confirm the successful synthesis of the as-synthesised nanocomposite. For fabricating the ethanol sensor, $MoSe_2$/ZnO nanocomposite powder so-obtained is deposited on indium tin oxide (ITO) coated corning glass substrate using a facile electrophoretic deposition (EPD) technique. The as-fabricated sensor is exposed to various ethanol gas concentrations (10-500 ppm) and its response is systematically investigated at RT. The synergistic effect due to the incorporation of ZnO in $MoSe_2$ is explained in detail and a sensing mechanism is proposed based on this.

3.2. Experimental

3.2.1 Chemical profile

The chemicals used in the synthesis were Sodium Molybdate Dihydrate ($Na_2MoO_4.2H_2O$), Selenium (Se) powder, Hydrazine Hydrate-86% ($N_2H_4.H_2O$), Zinc Acetate ($Zn(CH_3COO)_2 \cdot 2H_2O$), Sodium Hydroxide (NaOH) pellets, and Ethanol (C_2H_5OH). All the chemicals were purchased from Sigma Aldrich and were employed without further purification.

3.2.2 Synthesis procedure

A facile hydrothermal method was used to synthesise ZnO incorporated- $MoSe_2$ nanosheet-based nanocomposite. Fig. 3.1 displays the schematic of the fabrication process. Firstly, $MoSe_2$ nanosheets were synthesised. Typically, 2 mmol of sodium molybdate dihydrate was dissolved in deionized (DI) water and ethanol (volume 1:1) with stirring for 45 min to obtain a clear solution. Meanwhile, a solution containing selenium powder (4 mmol) was prepared separately in 10 mL hydrazine hydrate-86% with stirring. It was followed by the addition of selenium solution in sodium molybdate dehydrate solution dropwise under continuous stirring for 45 min. Then, the above mixture was transferred into a 50 mL hydrothermal autoclave and was kept at 220 °C for 24 h. After several washings with DI and ethanol, the black color powder was obtained which was then dried overnight at 100 °C.

Then, ZnO nanorods were prepared by dropping 5 mol of sodium hydroxide solution in 0.5 mol of zinc acetate dihydrate solution under continuous stirring for 45 min. Then, the above solution was kept in an oven at 120 °C in a 100 mL hydrothermal autoclave for 24 h. After washing it with DI water and ethanol, the white color powder so obtained was left for drying at 80 °C.

For preparing $MoSe_2$/ZnO nanocomposite, a quantitative amount of $MoSe_2$ and ZnO synthesised by the above procedure were dispersed in ethanol and sonicated for 2 h. The dispersed solution was transferred to a 100 mL hydrothermal autoclave and heated at 120 °C for 24 h. The final product was washed with DI and ethanol to yield grey color powder which was then dried overnight in a vacuum.

3.2.3 Sensor fabrication for ethanol gas sensing

For fabricating the ethanol sensor, the $MoSe_2$/ZnO nanocomposite powder so-obtained was deposited on a pre-hydrolysed indium tin oxide (ITO) coated corning glass substrate using electrophoretic deposition (EPD) technique. $MoSe_2$/ZnO nanocomposite powder was dispersed in a suitable solvent with a concentration of 1 mg/mL. This dispersion was ultrasonicated for 2 h. The dispersed solution was then poured into a 2-electrode glass cell comprising copper as a connector to attach the working electrode (WE) and platinum as the counter electrode (CE). The ITO was attached to WE and an optimized constant potential was applied for 60 s. The film so formed of $MoSe_2$/ZnO nanocomposite was left for drying. Finally, silver (Ag) contacts were made on the prepared films with the help of the thermal evaporation technique. A similar process was devised to obtain pristine-$MoSe_2$ and pristine-ZnO films. These films were used for performing sensing measurements.

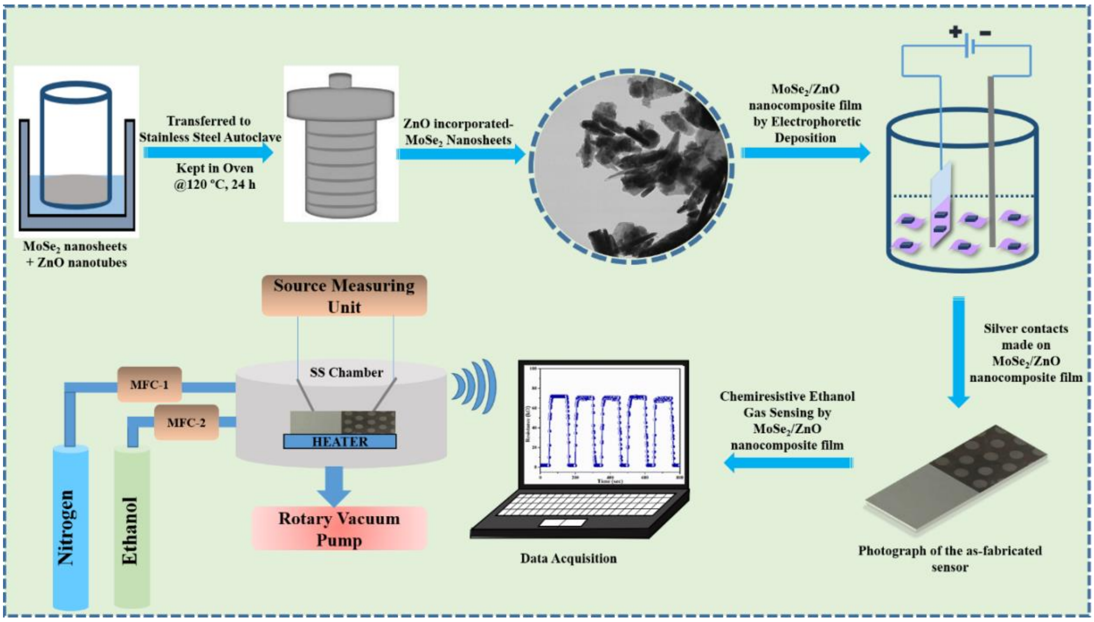

Fig. 3.1: Step-by-step preparation of $MoSe_2$/ZnO nanocomposite sensor for the detection of ethanol gas

3.2.4 Gas sensing experimental set-up

The gas sensing behavior of the $MoSe_2$/ZnO nanocomposite-based chemiresistive gas sensor was investigated in a customized stainless steel (SS) chamber by the use of 1% ethanol balanced with nitrogen (N_2) gas. The chamber was attached to two gas mass flow controllers (MFC). The MFC was used to maintain the flow of the target gas analyte and dry N_2/ dry air (standard composition: N_2 = 79% and O_2 = 21% by volume) inside the chamber. A source measuring unit was employed to provide a constant current supply to the as-fabricated ethanol gas sensor. A rotary pump was connected to the SS chamber to create rough vacuum pressure. A digital hygrometer was employed to measure the relative humidity (RH) in the SS chamber. Ethanol gas sensing was performed by introducing the dry N_2/ dry air first to sustain standard ambient conditions for 50 s. Thereafter, ethanol (1 %) / nitrogen (99 %) mixture was introduced inside the SS chamber for 100 s at different concentrations like 10, 100, 200, 300, 400, and 500 ppm at RT. The formula given below (eqn. 1) was used to calculate the concentration of ethanol gas in the SS chamber:

$$C = \frac{22.4 \times \Psi \times \rho \times V_1}{M \times V_2} \times 1000 \tag{3.1}$$

In the above formula (equation 3.1), C is the concentration of ethanol gas (ppm), Ψ is the required gas volume fraction, ρ is the density of ethanol ($kg.m^{-3}$), V_1 is the volume of ethanol gas, M is the molecular weight of ethanol ($kg.mol^{-1}$), and V_2 is the volume of the SS chamber (m^3) [19, 20]. The change in resistance of sensing films was recorded using a Lab-View data acquisition software connected to the source measuring unit. The gas sensing measurements of the sensing films were carried out at RT (27 °C) and relative humidity (29 %). The selectivity performance of as-fabricated ethanol gas sensors was investigated with other VOC gases like acetone, benzene, and formaldehyde.

3.3 Results and discussions

3.3.1 Structural analysis using XRD

The crystallographic structure of the as-synthesised pristine-$MoSe_2$, pristine-ZnO, and $MoSe_2$/ZnO nanocomposite was investigated using XRD (Fig. 3.2). The diffraction peaks of as-synthesised pristine-$MoSe_2$ (Fig. 3.2(a)) are attributed to the (002), (100), (103) and (110) planes of the hexagonal phase of $MoSe_2$ (JCPDS 029-0914) [21]. XRD pattern of ZnO (Fig. 3.2(b)) shows all the diffraction peaks which are congruous with the standard data available for the wurtzite structure of ZnO (JCPDS 36-1451)

[22]. The diffractogram of the $MoSe_2$/ZnO nanocomposite (Fig. 3.2(c)) consists of all the peaks corresponding to ZnO nanorods and some major planes of (002), (100), and (110) corresponding to $MoSe_2$ which indicates the successful interaction between $MoSe_2$ nanosheets and ZnO nanorods. The reason for the invisibility of two other planes of $MoSe_2$ i.e. (004) and (103) can be ascribed to the much higher intensity of ZnO diffraction peaks [23]. In addition to this, there is a decrease in the intensity of diffraction peaks of $MoSe_2$ and ZnO in $MoSe_2$/ZnO nanocomposite which further confirms the formation of nanocomposite [24].

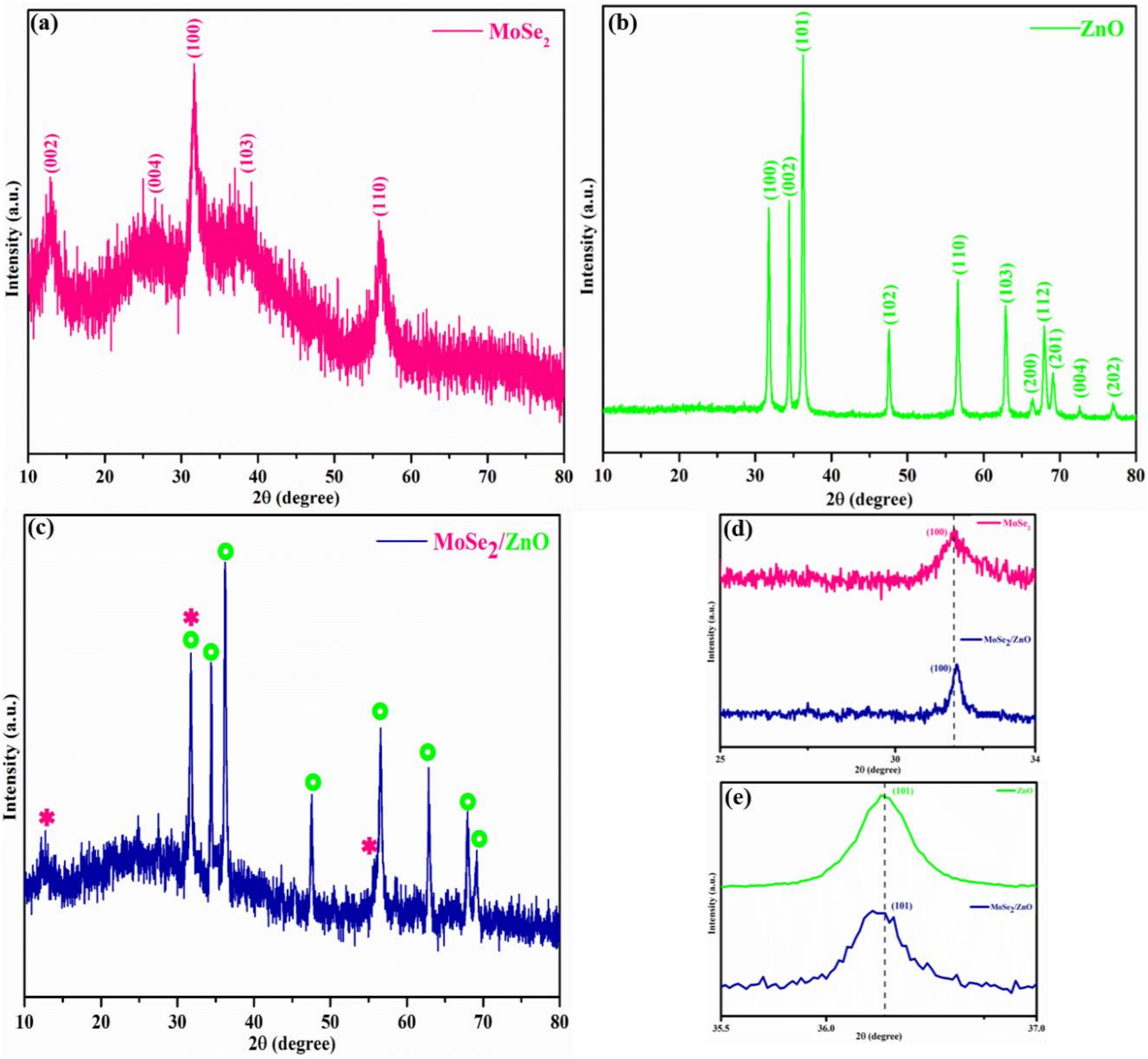

Fig. 3.2: XRD pattern of the as-synthesised (a) pristine-$MoSe_2$, (b) pristine-ZnO, (c) $MoSe_2$/ZnO nanocomposite, (d) zoomed (100) diffraction peak of pristine-$MoSe_2$ and $MoSe_2$/ZnO nanocomposite, and (e) zoomed (101) diffraction peak of pristine-ZnO and $MoSe_2$/ZnO nanocomposite

It is also observed that there is a shift in the diffraction peaks of the nanocomposite with respect to the pristine materials in Fig. 3.2(a) and 3.2(b). To confirm the shifting of diffraction peaks in the nanocomposite, zoomed highest intensity diffraction peaks of pristine-$MoSe_2$ (100) and ZnO (101) were considered (Fig. 3.2(d) and Fig. 3.2(e)) for comparison. As can be seen in Fig. 3.2(d), the (100) diffraction peak of $MoSe_2$/ZnO nanocomposite is slightly shifted to a higher diffraction angle (31.76°) compared to the (100) diffraction peak of pristine-$MoSe_2$ (31.67°). Similarly, in Fig. 3.2(e), the (101) diffraction peak of the nanocomposite is slightly shifted to a lower diffraction angle (36.24°) compared to the (101) diffraction peak of pristine-ZnO (36.27°). This shift can correspond to the lattice mismatch between the pristine materials or strain generated in the nanocomposite after interaction during the synthesis [25].

3.3.2 Microstructure analysis using HRTEM

The HRTEM images of pristine-$MoSe_2$, pristine-ZnO, and $MoSe_2$/ZnO nanocomposite are shown in Fig. 3.3. Fig. 3.3(a) and 3.3(b) display a large area of $MoSe_2$ nanosheets stacked over one another, which are wrinkled and curled at the edges. The fine lattice fringes of $MoSe_2$ nanosheets can be seen in Fig. 3.3(c) with the interplanar spacing of 0.28 nm which is related to the (100) lattice plane of $MoSe_2$. Fig. 3.3(d) shows an HRTEM image of ZnO nanorods and Fig. 3.3(e) shows the measured interplanar spacing of 0.24 nm which corresponds to the (101) lattice plane of ZnO nanorods. Evidence for modification of the $MoSe_2$ nanosheets by ZnO nanorods is given in Fig. 3.3(f) and 3.3(g), which shows the successful incorporation of ZnO nanorods in $MoSe_2$ nanosheets. A clear heterogeneous interface between $MoSe_2$ nanosheets and ZnO nanorods can be seen in $MoSe_2$/ZnO nanocomposite at a 200 nm and 100 nm scale bar. The corresponding selected area electron diffraction (SAED) pattern of the $MoSe_2$/ZnO nanocomposite is shown in Fig. 3.3(h). Hence from the HRTEM analysis, the successful incorporation of ZnO nanorods in $MoSe_2$ nanosheets is evident, which is consistent with the XRD analysis as well.

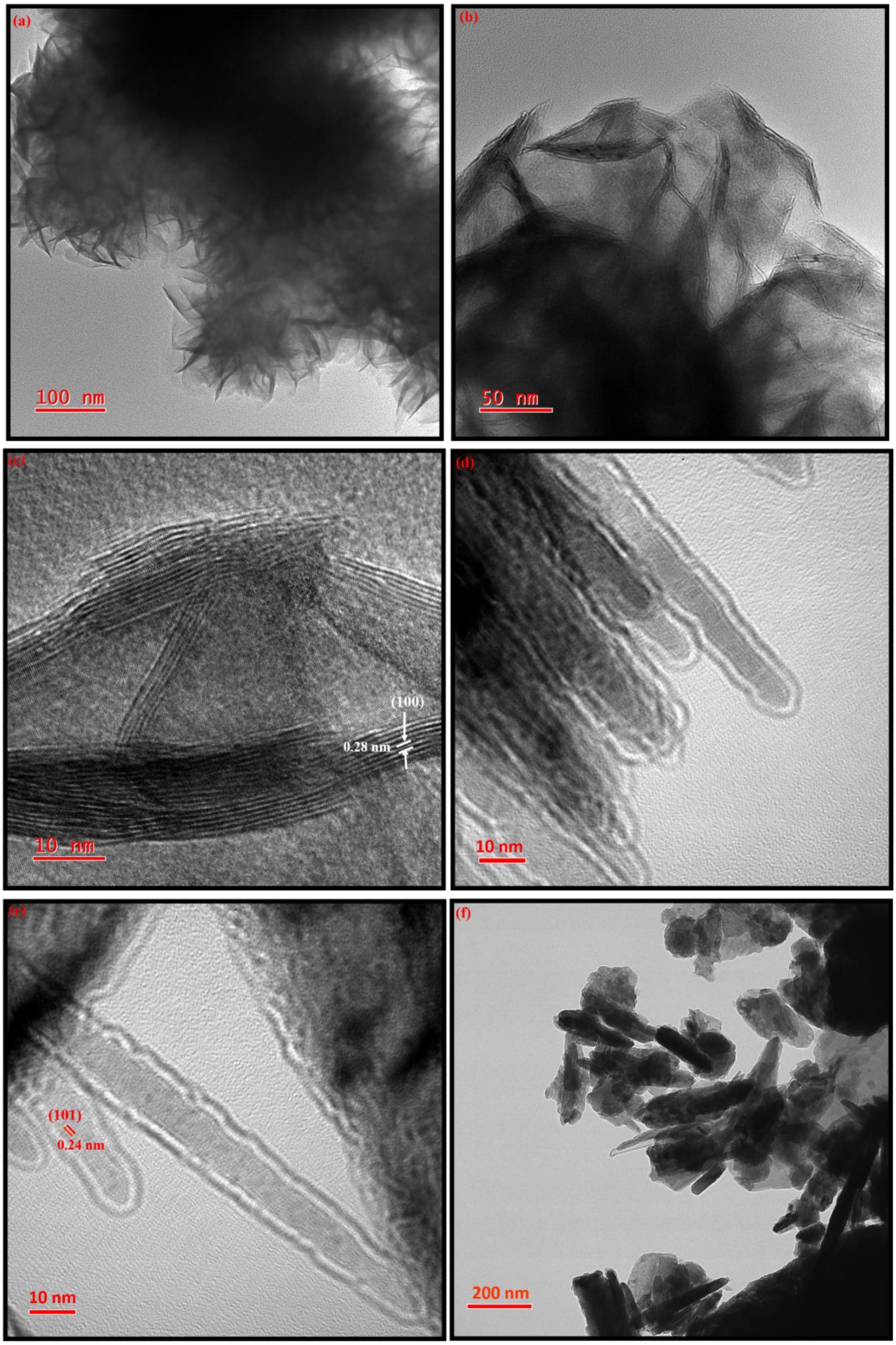
(a)
100 nm
(b)
50 nm
(c)
(100)
0.28 nm
10 nm
(d)
10 nm
(e)
(101)
0.24 nm
10 nm
(f)
200 nm

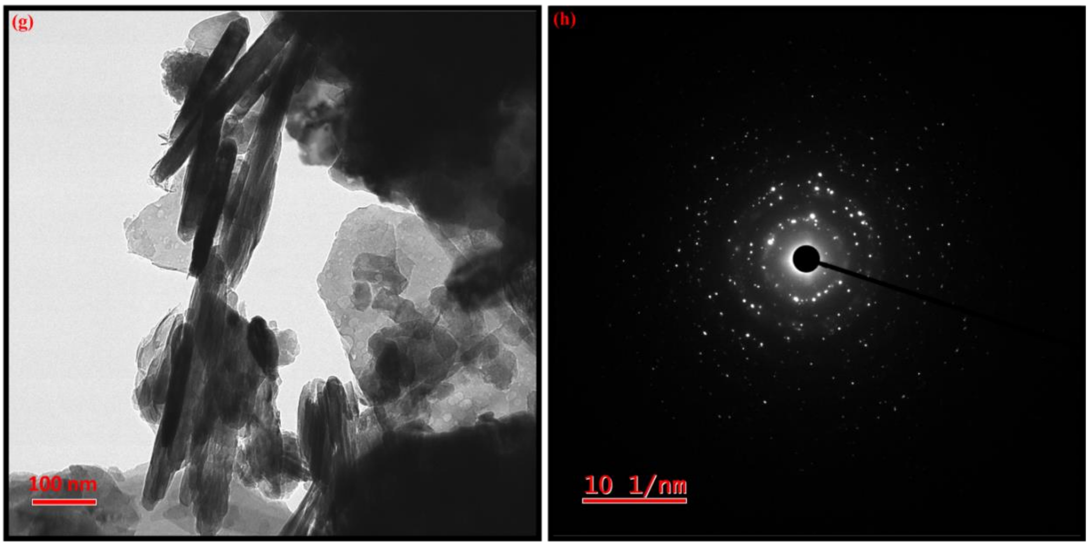

Fig. 3.3: HRTEM images of as-synthesised (a) and (b) pristine-$MoSe_2$ nanosheets (c) Lattice fringes of $MoSe_2$ nanosheets with measured interplanar spacing, (d) pristine-ZnO nanorods, (e) Measured Interplanar spacing of pristine-ZnO nanorods (f, g) $MoSe_2$/ZnO nanocomposite, and (h) corresponding SAED pattern of $MoSe_2$/ZnO nanocomposite

3.3.3 Study of vibrational modes using Raman spectroscopy

The Raman spectrum of pristine-$MoSe_{2,}$ pristine-ZnO, and $MoSe_2$/ZnO nanocomposite acquired using an excitation wavelength of 532 nm was shown in Fig. 3.4. Raman spectroscopy measurements of $MoSe_2$ shows a strong out-of-plane mode A_{1g} mode at 238 cm^{-1} which is the characteristic peak of $MoSe_2$ [26]. The other two in-plane modes E_{1g} and E^1_{2g} of $MoSe_2$ are observed at 167 cm^{-1} and 283 cm^{-1} which are in good agreement with the earlier reports [15]. Fig. 3.4 shows an intense Raman peak of ZnO at 437 cm^{-1} (E_2^{high}) which is the characteristic peak of the hexagonal wurtzite phase of ZnO [27].

The corresponding spectrum of $MoSe_2$/ZnO nanocomposite in Fig. 3.4 displays the presence of modes belonging to both $MoSe_2$ and ZnO. In addition to this, it is noted that the modes in $MoSe_2$/ZnO nanocomposite are shifted from their respective position in their individual spectrum. In the $MoSe_2$/ZnO nanocomposite, there is a red shift in the A_{1g} mode (233.7 cm^{-1}) corresponding to $MoSe_2$ as well as in the E_2^{high} (431.3 cm^{-1}) mode corresponding to ZnO. This is attributed to the defects produced due to electronic interactions between $MoSe_2$ and ZnO during the hydrothermal synthesis process [28]. Hence, the Raman spectrum of $MoSe_2$/ZnO nanocomposites confirms that the nanocomposite is successfully synthesised, as confirmed by XRD and HRTEM analysis.

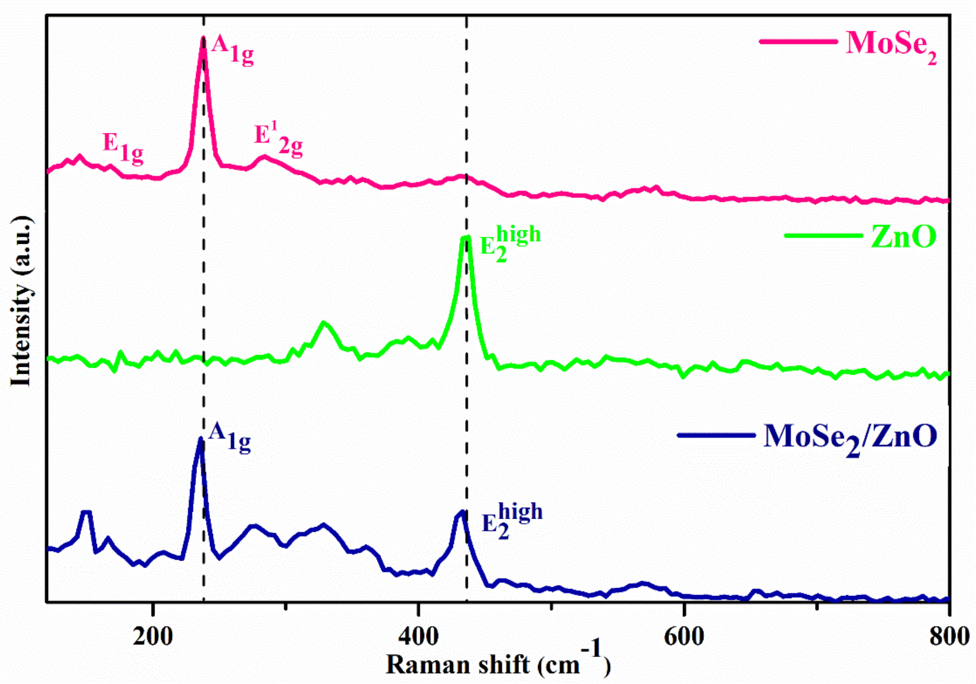

Fig. 3.4: Raman spectrum of the as-synthesised pristine-MoSe$_2$, pristine-ZnO, and MoSe$_2$/ZnO nanocomposite

3.3.4 Identification of functional groups using FTIR spectroscopy

FTIR spectroscopy was performed to investigate and elucidate the presence of functional groups in the prepared samples of pristine-MoSe$_2$, pristine-ZnO, and MoSe$_2$/ZnO nanocomposite in the range of 400 – 4000 cm^{-1}. Peaks in the FTIR spectrum of MoSe$_2$ nanosheets are observed corresponding to O-H (3420 cm^{-1}), C-H (2910 cm^{-1}), COO^{-1} (1620 cm^{-1}), Mo-O (1000-750 cm^{-1}), and Se-O-Se (420 cm^{-1}) as shown in Fig. 3.5 [29, 30]. The FTIR spectrum of ZnO nanorods (Fig. 3.5) consists of peaks corresponding to O-H (3438 cm^{-1}), COOH (1620 and 1480 cm^{-1}), Zn-OH (920 cm^{-1}), and Zn-O (577 and 427 cm^{-1}) [27]. The corresponding spectrum of MoSe$_2$/ZnO nanocomposite in Fig. 3.5 displays the peaks corresponding to both MoSe$_2$ and ZnO. Furthermore, the peaks in the as-synthesised nanocomposite are shifted as compared to pristine-MoSe$_2$ and ZnO indicating the electronic interaction between the pristine materials. Hence, from the FTIR spectrum of MoSe$_2$/ZnO nanocomposite, the coexistence of both $MoSe_2$ and ZnO is confirmed which is in good accordance with the XRD analysis, Raman spectroscopy, and HRTEM observations.

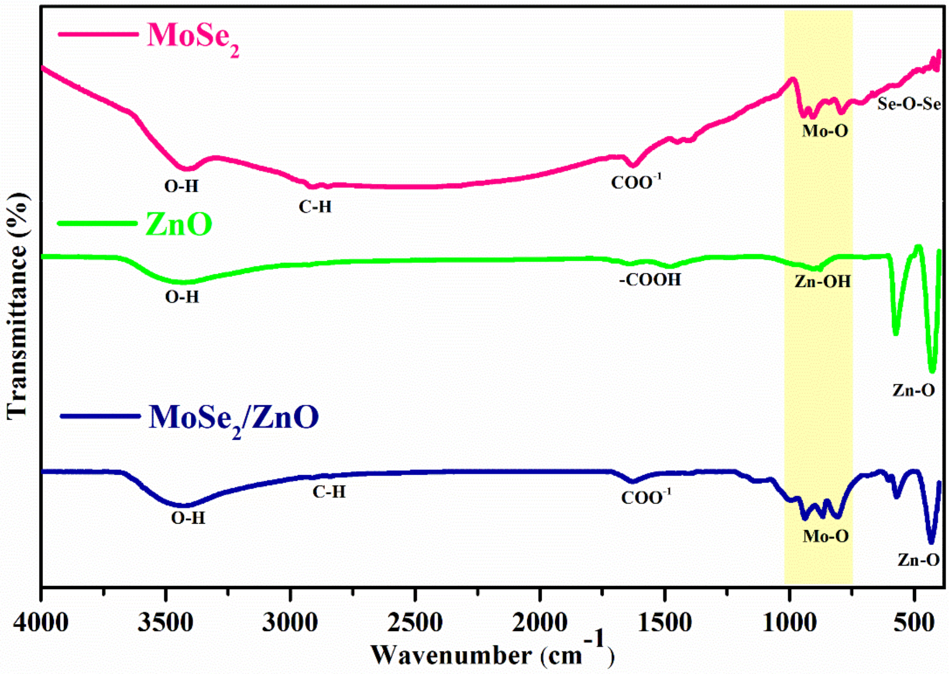

Fig. 3.5: FTIR spectrum of the as-synthesised pristine-$MoSe_2$, pristine-ZnO, and $MoSe_2$/ZnO nanocomposite

3.3.5 Gas sensing performance

The gas sensor response characteristics of pristine-$MoSe_2$ and $MoSe_2$/ZnO nanocomposite were investigated towards different ethanol concentrations ranging from 10-500 ppm at RT in dry N_2 as illustrated in Fig. 3.6(a). Fig. 3.6(b) shows the response characteristics of pristine-ZnO towards different ethanol concentrations at RT in dry N_2. It can be observed in Fig. 3.6(a) that the sensing response (resistance versus time graph) of pristine-$MoSe_2$ is low and the resistance changes slightly under exposure to different concentrations of ethanol gas. It can be seen in Fig. 3.6(b) that the sensing behavior of the pristine-ZnO sensor shows an n-type characteristic response during ethanol gas exposure. However, the $MoSe_2$/ZnO nanocomposite sensor (Fig 3.6(a)) exhibited a much higher response towards the same concentration of ethanol gas. The response value (R_g/R_a or R_a/R_g) of the pristine-$MoSe_2$, pristine-ZnO, and $MoSe_2$/ZnO nanocomposite sensor is 14.8, 1.6, and 37.8 to 500 ppm ethanol gas where R_g and R_a represent the value of the sensor's resistance in presence of ethanol gas mixture and dry N_2 respectively.

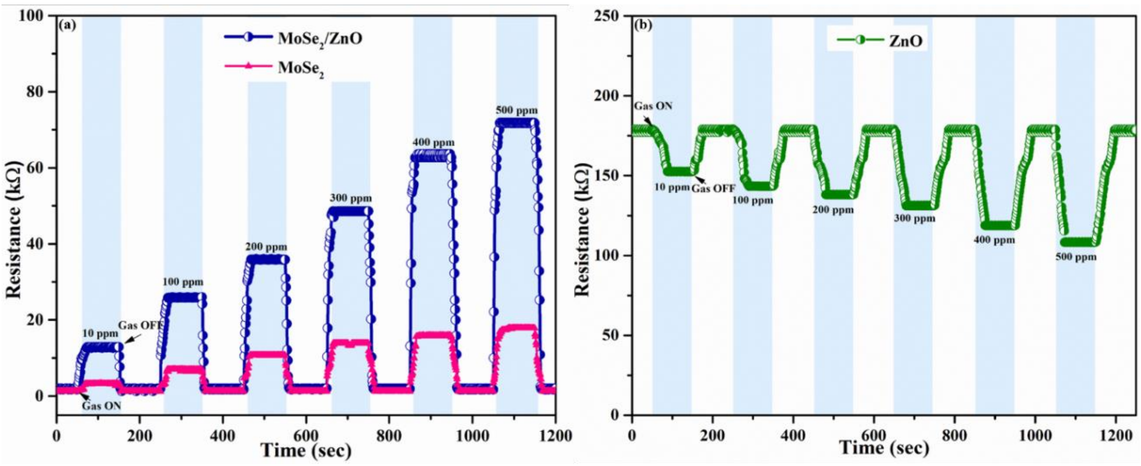

Fig. 3.6: (a) Resistance variation of pristine-$MoSe_2$ and $MoSe_2$/ZnO nanocomposite sensor and (b) Resistance variation of pristine-ZnO sensor wrt. to various ethanol concentrations at RT in dry N_2

However, the response from the same pristine-$MoSe_2$ and $MoSe_2$/ZnO nanocomposite sensor decreased significantly when recovered in dry air as depicted in Fig. 3.7. Specifically, the response of 4.5 and 15.3 was obtained to 500 ppm ethanol gas for pristine-$MoSe_2$ and $MoSe_2$/ZnO nanocomposite sensor at RT. Therefore, the improved response of the nanocomposite sensor when operated in dry N_2 than dry air encouraged us to measure sensor performance in this environment.

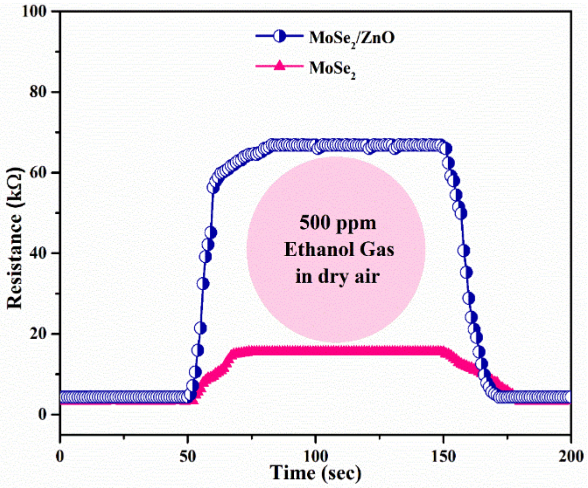

Fig. 3.7: Resistance variation of pristine-$MoSe_2$ and $MoSe_2$/ZnO nanocomposite sensor wrt. to 500 ppm ethanol at RT in dry air

Fig. 3.8(a) defines three parameters that describe the properties of the sensor which are: the sensing response (R_g/R_a), the response time (t_{resp}), and the recovery time (t_{rec}). Firstly, we note that the resistance of the $MoSe_2/ZnO$ nanocomposite sensor increased from base resistance R_a = 1.9 kΩ in dry N_2 to R_g = 71.9 kΩ when the sensor was exposed to 500 ppm of ethanol. The sensing response of the nanocomposite sensor was calculated using R_g and R_a values obtained and was found to be 37.8 at 500 ppm ethanol. This also suggests that the response of the nanocomposite sensor is p-type towards ethanol gas [10, 16]. Furthermore, full recovery to the same base resistance is observed for both pristine and nanocomposite sensors. This reveals the reversible interaction between the as-fabricated nanocomposite sensor and ethanol gas due to the physisorption process. It is also evident from Fig. 3.6(a) that the base resistance of the $MoSe_2/ZnO$ nanocomposite sensor is higher as compared to the pristine-$MoSe_2$ sensor. The other two parameters are t_{resp} and t_{rec} which were calculated to be 11 s and 18 s for the pristine-$MoSe_2$ sensor respectively. An improvement in t_{resp} and t_{rec} was observed for the $MoSe_2/ZnO$ nanocomposite sensor and are found to be 8.4 s and 14.7 s respectively. Fig. 3.8(b) shows that the resistance of the pristine-ZnO sensor decreased from base resistance R_a = 179 kΩ in dry N_2 to R_g = 108.4 kΩ when the sensor was exposed to 500 ppm of ethanol. The t_{resp} and t_{rec} were calculated for the pristine-ZnO sensor and found to be 22 s and 38 s respectively.

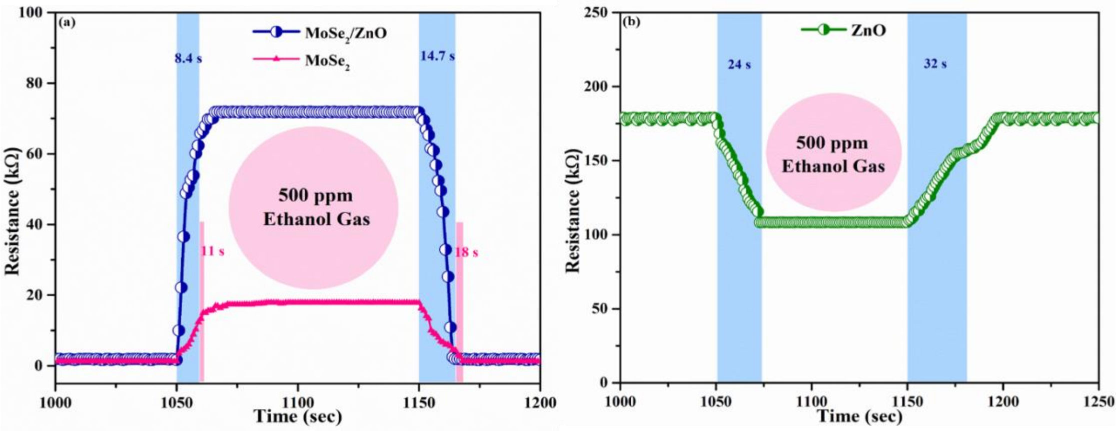

Fig. 3.8: The t_{resp} and t_{rec} characteristics of (a) $MoSe_2$ and $MoSe_2/ZnO$ nanocomposite sensor and (b) pristine-ZnO sensor exposed to 500 ppm ethanol at RT in dry N_2

A comparison of performance parameters such as sensing response, response, and recovery time of pristine- $MoSe_2$, pristine-ZnO, and $ZnO/MoSe_2$ nanocomposite sensor in dry N_2 is shown in Table 3.1. Therefore, from the table, it is concluded that the ZnO/$MoSe_2$ nanocomposite sensor exhibits a faster response than the individual pristine sensors.

Table 3.1: Performance comparisons of as-fabricated sensors in dry N_2

Materials	**Sensor Response**	**Response Time (t_{res} in sec)**	**Recovery Time (t_{rec} in sec)**
Pristine-$MoSe_2$	14.8	11	18
Pristine-ZnO	1.6	22	38
$MoSe_2$/ZnO	37.8	8.4	14.7

Similarly, t_{resp} and t_{rec} of the $MoSe_2$/ZnO nanocomposite sensor were calculated for different ethanol gas concentrations and shown in Fig. 3.9(a). It was observed that the t_{resp} decreases and the t_{rec} increases as the ethanol gas concentration increases from 10 to 500 ppm. The reason for a decrease in t_{resp} may be attributed to the availability of large sites on the sensor's surface for gas adsorption. On the other hand, the increase in t_{rec} may be due to the chemisorption of ethanol molecules and their reaction products which took time to desorb from the surface of the sensor [26].

Fig. 3.9(b) and 3.9(c) demonstrate the repeatability of the $MoSe_2$/ZnO nanocomposite sensor exposed to 10 ppm and 500 ppm ethanol gas at RT for five consecutive cycles respectively. The results suggest that the sensor exhibited almost the same response during each cycle.

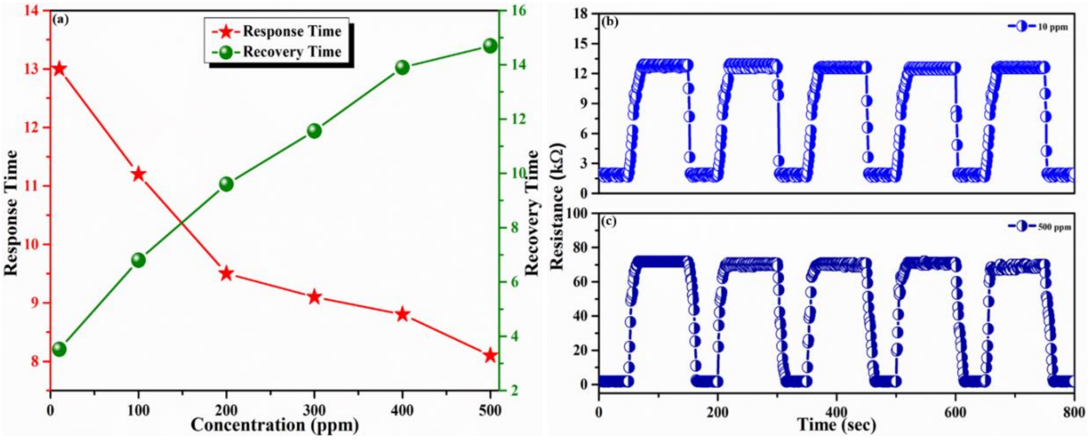

Fig. 3.9: (a) Response and recovery time versus concentration curves of ethanol for the $MoSe_2$/ZnO nanocomposite sensor at RT in dry N_2, (b) and (c) Five consecutive sensing cycles of the $MoSe_2$/ZnO nanocomposite sensor exposed to 10 and 500 ppm ethanol at RT in dry N_2

For real-life applications, the gas sensor should have good stability. As shown in Fig. 3.10(a) the long-term stability of the $MoSe_2$/ZnO nanocomposite sensor was also conducted to evaluate its stability. The sensor was tested under 10 and 500 ppm of ethanol gas at RT at an interval of 7 days. The response values of the sensor showed no distinct changes in 4 weeks which confirmed the excellent stability of the $MoSe_2$/ZnO nanocomposite sensor.

Selectivity is also a very important parameter for evaluating the sensor's performance. Fig. 3.10(b) shows the response of pristine-$MoSe_2$ and $MoSe_2$/ZnO nanocomposite sensors toward a few VOCs with a concentration of 500 ppm at RT, which involved ethanol, acetone, benzene, and formaldehyde. The corresponding bar chart depicts that the $MoSe_2$/ZnO nanocomposite sensor was highly selective towards ethanol.

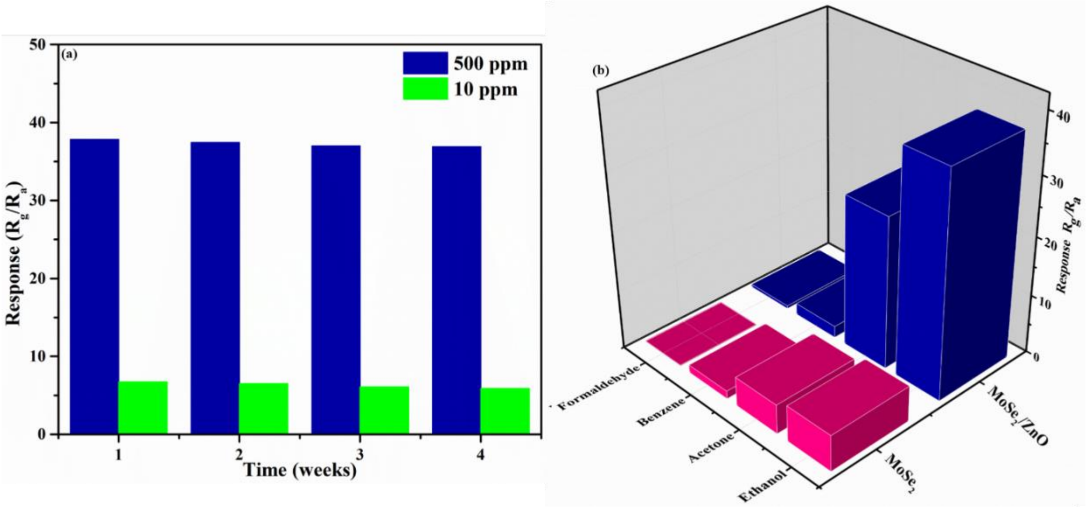

Fig. 3.10: (a) Long-term stability (4 weeks) under 500 ppm and 10 ppm ethanol at RT for the $MoSe_2$/ZnO nanocomposite sensor in dry N_2, and (b) Corresponding response bar chart showing the selectivity of the $MoSe_2$/ZnO nanocomposite sensor towards a few VOCs with a concentration of 500 ppm at RT in dry N_2.

Table 3.2 compares the ethanol sensing properties of previous research work in terms of working temperature, response, and recovery time with our work. The comparative results demonstrate that $MoSe_2$/ZnO nanocomposite sensor have better response and recovery time, and operate at RT. Therefore, the MoSe2/ZnO nanocomposite sensor exhibited better sensing characteristics than others, indicating that it had great potential as a candidate for ethanol gas sensing.

Table 3.2: A comparison of performance parameters of this work with previous work for ethanol gas sensing.

Sensor Materials	Concentration (ppm)	Sensor Response	Operating Temperature (°C)	Response/Recovery Time (sec)	Refs.
MoS_2/TiO_2	500	100 %	300	70 ± 10 s / 90 ± 20 s	[3]
ZnO	500	32	160	14 / 13	[31]
Pd decorated ZnO	500	81%	260	6 / 95	[32]
WO_3/g-C_3N_4	500	62.5%	RT	30 / 25	[33]
$MoSe_2$/ZnO	500	37.8	RT	8.4 / 14.7	This work

3.4 Ethanol sensing mechanism

The gas sensing mechanism is attributed to the change in resistance with respect to baseline due to the interaction of ethanol molecules with the surface of the sensing material. From the response curves (Fig. 3.6(a) and 3.6(b)), the pristine-$MoSe_2$ nanosheets exhibit a p-type character, pristine-ZnO exhibits an n-type character and $MoSe_2$/ZnO nanocomposite sensor exhibits a p-type character. Based on these data, the sensing mechanism of pristine sensors as well as nanocomposite sensor is explained as follows:

The sensing behavior of $MoSe_2$ nanosheets showed a p-type characteristic response during ethanol gas exposure (Fig. 3.6(a)). It has been proved in the literature that, although semiconducting TMD nanosheets are intrinsically n-type, adsorption of oxygen molecules from the air atmosphere can introduce p-type doping [17, 34]. During the synthesis, a number of defects are created in the $MoSe_2$ nanosheets. These defects act as an active point for the adsorption of oxygen molecules from the air atmosphere during the fabrication process of the sensor [35]. The adsorbed oxygen molecules tend to trap electrons from the $MoSe_2$ nanosheets which creates a large number of oxygen ion species. These oxygen ion species induce the formation of a thick accumulation layer near the surface of $MoSe_2$ nanosheets. When the $MoSe_2$ nanosheets are exposed to ethanol gas, the electrons are donated by the ethanol to the $MoSe_2$ nanosheets as ethanol is a reducing agent. This results in decreasing the majority charge carrier concentration in $MoSe_2$ nanosheets and hence an increase in sensor resistance [13, 36].

The sensing behavior of ZnO nanorods showed an n-type characteristic response during ethanol gas exposure (Fig. 3.6(a)). The generally accepted mechanism for n-type metal-oxide semiconductors (MOS) involves interaction between adsorbed oxygen molecules on the surface of the sensor material and the target gas [37, 38]. The adsorbed oxygen molecules tend to trap electrons from the conduction band of ZnO nanorods which creates a large number of oxygen ion species. Upon ethanol exposure, the gas molecules react with the oxygen ion species adsorbed on the surface thereby releasing trapped electrons back to the conduction band of ZnO nanorods. This leads to the oxidation of ethanol into the water and carbon dioxide (eqn. 2 and 3). Hence, there is a decrease in the resistance of the sensor. The reaction between ethanol and oxygen ion species can be represented in equations 3.2 and 3.3:

$$O_{2gas} + ZnO_{adsorption} \leftrightarrow O_{2adsorption} + 2e^- \leftrightarrow 2O^-_{2adsorption} \tag{3.2}$$

$$2C_2H_5OH + 6O^-_{2adsorption} \rightarrow 4CO_2 + 6H_2O + 6e^- \tag{3.3}$$

A plausible mechanism for enhanced ethanol gas sensing of the $MoSe_2$/ZnO nanocomposite sensor compared to the pristine-$MoSe_2$ and pristine-ZnO sensor can be explained by considering the p-n heterojunction generated at the interface of p-$MoSe_2$ and n-type ZnO [39]. Fig. 3.12 shows the schematic representation and energy band diagram of p-$MoSe_2$ nanosheets and n-type ZnO nanorods in air. The band gap of $MoSe_2$ and ZnO is 1.3 eV and 3.4 eV respectively [12, 40, 41]. The discrepancy of the bandgap in the nanocomposite is attributed to the formation of heterojunction between $MoSe_2$ and ZnO. The current-voltage characteristic curve of the $MoSe_2$/ZnO nanocomposite sensor was also obtained at RT using Keithley 2450 SMU to confirm the existence of p-n heterojunction in the nanocomposite sensor (Fig. 3.11). Under the scanning voltage of -2 V to 2 V, it can be seen that the reverse current of the nanocomposite sensor is smaller than the forward current which indicates the existence of p-n heterojunction at the interface of $MoSe_2$ nanosheets and ZnO nanorods [20, 42].

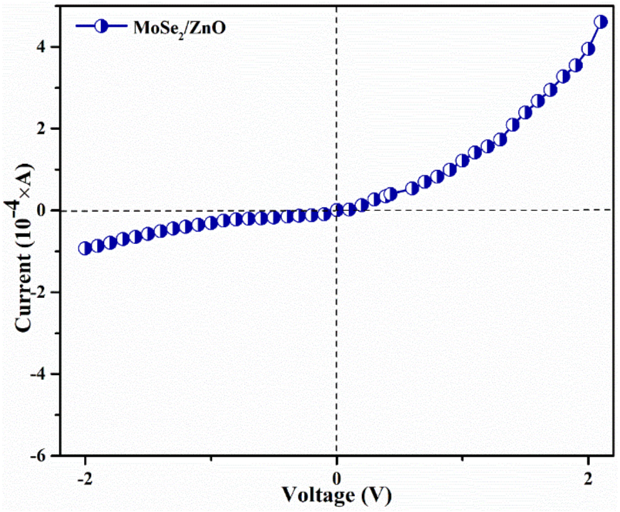

Fig. 3.11: Current-voltage curve of $MoSe_2$/ZnO nanocomposite sensor at RT

According to the literature, the work function of pure $MoSe_2$ is 4.65 eV, and the withdrawal of electrons from the nanosheets would increase the work function of $MoSe_2$ [43]. The work function of n-type ZnO is 4.5 eV [44]. Therefore, the work function of ZnO is lower than that of $MoSe_2$. The distinction in the work function of $MoSe_2$ and n-type ZnO results in the diffusion of electrons from ZnO to $MoSe_2$ and the holes will diffuse from $MoSe_2$ to ZnO until an equilibrium of Fermi level is achieved. The energy band bends at the interface of $MoSe_2$ and ZnO as shown in Fig. 3.12(b). An accumulation layer is formed at the interface of $MoSe_2$ to ZnO, where the electrons accumulate at the side of $MoSe_2$ and the holes accumulate at the side of ZnO. A potential barrier is formed due to carrier trapping at the interface of the $MoSe_2$/ZnO nanocomposite which increases the resistance of the nanocomposite films in the air. As mentioned above, the R_a value of the $MoSe_2$/ZnO nanocomposite sensor is higher as compared to the pristine-$MoSe_2$ sensor owing to the presence of an enhanced potential barrier (Fig. 3.6(a)). When the nanocomposite sensor is exposed to ethanol molecules (Fig. 3.12(c)), this results in the broadening of the charge carrier accumulation layer near the surface of $MoSe_2$ nanosheets.

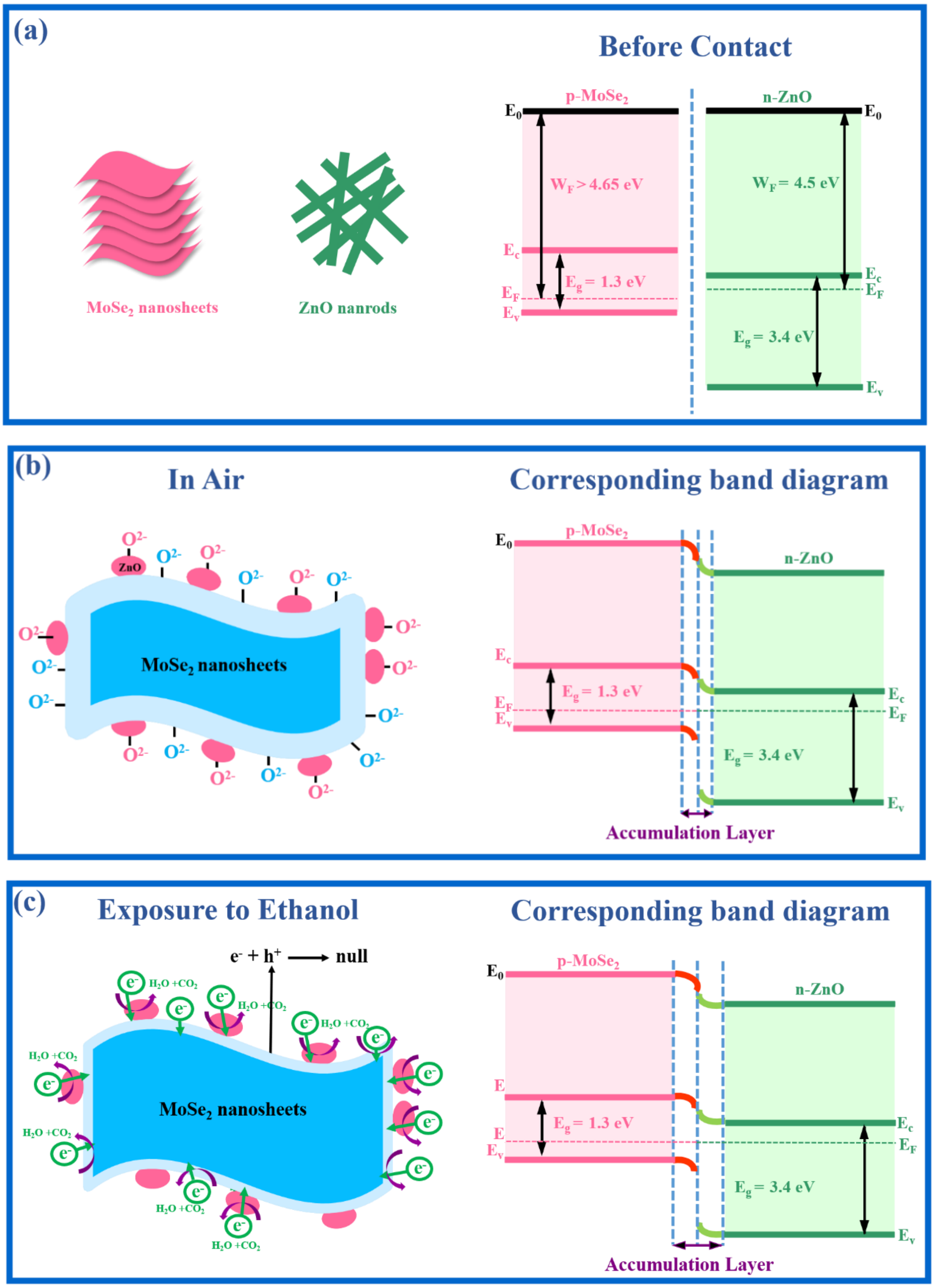

Fig. 3.12: Schematic representation and energy band diagram of ethanol gas sensing mechanism of MoSe$_2$/ZnO nanocomposite sensor in (a) before contact, (b) air condition, and (c) ethanol atmosphere.

The free electrons so released during this process neutralize the majority of charge carriers in the $MoSe_2$ nanosheets. Similarly, the released electrons on the surface of ZnO lead to more electron-hole recombination on the interface of $MoSe_2$ nanosheets and ZnO. Finally, the electron transfer from the ZnO to the $MoSe_2$ is impeded which overall results in an increased change in resistance and enhanced sensitivity [45]. The p-type behavior of the $MoSe_2$/ZnO nanocomposite sensor is similar to the pristine-$MoSe_2$ sensor, which suggests a synergistic effect between $MoSe_2$ nanosheets and ZnO nanorods in which p-type $MoSe_2$ nanosheets act as majority charge carriers [41, 46].

The reason for a better response of pristine-$MoSe_2$ and $MoSe_2$/ZnO nanocomposite sensor to ethanol gas in dry N_2 than dry air can be explained as: It is evident from the literature that adsorption of oxygen on the surface of the $MoSe_2$ trap electrons from the $MoSe_2$ nanosheets by occupying the reactive sites on the surface of the sensing layer [35, 47, 48]. An increase in the baseline resistance of the sensor in the presence of dry air compared to dry N_2 (Fig. 3.6(a) indicates that more reactive sites are occupied by oxygen thereby reducing the sensing response of the pristine-$MoSe_2$ sensor. As mentioned above, the p-type response of the nanocomposite sensor indicates that $MoSe_2$ nanosheets act as majority charge carriers. Hence, the response from the $MoSe_2$/ZnO nanocomposite sensor also decreased significantly when recovered in dry air.

From the above ethanol gas sensing results, we surmise that the superior gas sensing properties of $MoSe_2$/ZnO nanocomposite sensor in the presence of dry N_2 can contribute to the development of ethanol gas sensors with high sensitivity, good selectivity, stable repeatability, and fast adsorption/desorption at RT, which are suitable for practical applications.

3.5 Conclusions

A highly selective, stable, and reproducible chemiresistive ethanol gas sensor based on $MoSe_2$/ZnO nanocomposite was developed. Specifically, the response value of the as-fabricated nanocomposite sensor was 37.8 to 500 ppm ethanol gas when operated in dry N_2 and 15.3 to 500 ppm ethanol gas when operated in dry air. This suggests that the sensor performs better when operated in dry N_2 than in dry air. The sensor demonstrated a p-type characteristic response. Importantly, the sensor operates at RT and can detect ethanol down to 10 ppm. The sensor also exhibited improved response (8.4 s) and recovery (14.7 s) time to 500 ppm ethanol gas compared to previously reported values. The enhancement in performance of the sensor was due to the formation of a p-n heterojunction at the interface of the $MoSe_2$ nanosheets and ZnO nanorods in the $MoSe_2$/ZnO nanocomposite sensor. Furthermore, potential barrier modulation at the interface provided a positive effect on sensitivity performance. The results demonstrated that this work may open new avenues to engineer 2D nanomaterials/metal-oxide-based nanocomposites for the fabrication of ethanol gas sensors for real-time electronics applications.

References

[1] V. Shah, J. Bhaliya, G. M. Patel, and P. J. T. i. C. Joshi, "Recent Advancement in Pd-Decorated Nanostructures for Its Catalytic and Chemiresistive Gas Sensing Applications: A Review," *Topics in Catalysis*, pp. 1-41, 2022.

[2] A. Mirzaei, S. Leonardi, and G. J. C. i. Neri, "Detection of hazardous volatile organic compounds (VOCs) by metal oxide nanostructures-based gas sensors: A review," *Ceramics International,* vol. 42, no. 14, pp. 15119-15141, 2016.

[3] S. Singh, S. J. S. Sharma, and A. B. Chemical, "Temperature dependent selective detection of ethanol and methanol using MoS2/TiO2 composite," *Sensors and Actuators B: Chemical,* vol. 350, p. 130798, 2022.

[4] M. J. Ahemad, T. D. Le, D.-S. Kim, Y.-T. J. S. Yu, and A. B. Chemical, "Bimetallic AgAualloy@ ZnO core-shell nanoparticles for ultra-high detection of ethanol: Potential impact of alloy composition on sensing performance," *Sensors and Actuators, B: Chemical* vol. 359, p. 131595, 2022.

[5] S. S. Scindia, R. B. Kamble, and J. A. J. I. S. J. Kher, "Organic surfactant assisted polypyrrole materials as effective chemiresistive gas sensors for VOCs and toxic gas detection," *IEEE Sensors Journal,* vol. 20, no. 23, pp. 14072-14080, 2020.

[6] D. Zhang, Y. Cao, J. Wu, and X. J. A. S. S. Zhang, "Tungsten trioxide nanoparticles decorated tungsten disulfide nanoheterojunction for highly sensitive ethanol gas sensing application," *Applied Surface Science,* vol. 503, p. 144063, 2020.

[7] T. T. N. Phan *et al.*, "Hierarchically structured LaFeO3 with hollow core and porous shell as efficient sensing material for ethanol detection," *Sensors and Actuators B: Chemical,* vol. 354, p. 131195, 2022.

[8] N. Roy *et al.*, "Paper based enzymatic chemiresistor for POC detection of ethanol in human breath," *IEEE Sensors Journal* vol. 20, no. 5, pp. 2278-2286, 2019.

[9] G. Jeevanandham, K. Vediappan, Z. A. ALOthman, T. Altalhi, and A. K. J. S. r. Sundramoorthy, "Fabrication of 2D-MoSe2 incorporated NiO Nanorods modified electrode for selective detection of glucose in serum samples," *Scientific Reports,* vol. 11, no. 1, pp. 1-13, 2021.

[10] T. Li, S. Yu, Q. Li, M. Chi, and P. J. N. J. o. C. Li, "Room temperature ethanol gas-sensing properties based on Ag-doped MoSe 2 nanoflowers: experimental and DFT investigation," *New Journal of Chemistry,* vol. 45, no. 45, pp. 21423-21428, 2021.

[11] S. Zhang, T. H. Nguyen, W. Zhang, Y. Park, and W. J. A. P. L. Yang, "Correlation between lateral size and gas sensing performance of MoSe2 nanosheets," *Applied Physics Letters,* vol. 111, no. 16, p. 161603, 2017.

[12] Z. Yang, D. Zhang, D. J. S. Wang, and A. B. Chemical, "Carbon monoxide gas sensing properties of metal-organic frameworks-derived tin dioxide nanoparticles/molybdenum diselenide nanoflowers," *Sensors and Actuators B: Chemical,* vol. 304, p. 127369, 2020.

[13] R. K. Jha, J. V. D'Costa, N. Sakhuja, N. J. S. Bhat, and A. B. Chemical, "MoSe2 nanoflakes based chemiresistive sensors for ppb-level hydrogen sulfide gas detection," *Sensors and Actuators B: Chemical,* vol. 297, p. 126687, 2019.

[14] D. J. Late, T. Doneux, and M. J. A. p. l. Bougouma, "Single-layer MoSe2 based NH3 gas sensor," *Applied Physics Letters,* vol. 105, no. 23, p. 233103, 2014.

[15] S. Singh, J. Deb, U. Sarkar, and S. J. A. A. N. M. Sharma, "MoSe2 crystalline nanosheets for room-temperature ammonia sensing," *ACS Applied Nano Materials,* vol. 3, no. 9, pp. 9375-9384, 2020.

[16] S. Zhang, W. Zhang, T. H. Nguyen, J. Jian, W. J. M. C. Yang, and Physics, "Synthesis of molybdenum diselenide nanosheets and its ethanol-sensing mechanism," *Materials Chemistry and Physics,* vol. 222, pp. 139-146, 2019.

[17] R. Jha, A. Nanda, and N. J. I. S. J. Bhat, "Ammonia Sensing Performance of rGO-Based Chemiresistive Gas Sensor Decorated With Exfoliated MoSe 2 Nanosheets," *IEEE Sensors Journal,* vol. 21, no. 9, pp. 10211-10218, 2021.

[18] A. Abun, B.-R. Huang, A. Saravanan, D. Kathiravan, and P.-D. J. A. A. N. M. Hong, "Exfoliated MoSe2 Nanosheets Doped on the Surface of ZnO Nanorods for Hydrogen Sensing Applications," *ACS Applied Nano Materials,* vol. 3, no. 12, pp. 12139-12147, 2020.

[19] Q. Chen *et al.*, "Optimization ethanol detection performance manifested by gas sensor based on In2O3/ZnS rough microspheres," *Sensors and Actuators B: Chemical*, vol. 264, pp. 263-278, 2018.

[20] J. Zhang, T. Li, J. Guo, Y. Hu, and D. J. A. S. S. Zhang, "Two-step hydrothermal fabrication of CeO2-loaded MoS2 nanoflowers for ethanol gas sensing application," *Applied Surface Science*, vol. 568, p. 150942, 2021.

[21] H. R. Inta, S. Ghosh, A. Mondal, G. Tudu, H. V. Koppisetti, and V. J. A. A. E. M. Mahalingam, "Ni0. 85Se/MoSe2 interfacial structure: an efficient electrocatalyst for alkaline hydrogen evolution reaction," *ACS Applied Energy Materials*, vol. 4, no. 3, pp. 2828-2837, 2021.

[22] Y. Navale, S. Navale, M. Chougule, N. Ramgir, and V. J. J. o. M. S. M. i. E. Patil, "NO2 gas sensing properties of heterostructural CuO nanoparticles/ZnO nanorods," *Journal of Materials Science: Materials in Electronics*, vol. 32, no. 13, pp. 18178-18191, 2021.

[23] Y. Huang, Y.-E. Miao, J. Fu, S. Mo, C. Wei, and T. J. J. o. M. C. A. Liu, "Perpendicularly oriented few-layer MoSe 2 on SnO 2 nanotubes for efficient hydrogen evolution reaction," *Journal of Materials Chemistry A*, vol. 3, no. 31, pp. 16263-16271, 2015.

[24] N. Elavarasan *et al.*, "Integrating gC3N4 nanosheet with MoS2 and ZnO-Ag: Remarkably enhanced photocatalytic performance under visible-light irradiation," *Colloid and Interface Science Communications*, vol. 44, p. 100474, 2021.

[25] N. Roy, R. Sinha, H. B. Nemade, T. K. J. J. o. A. Mandal, and Compounds, "Synthesis of MoS2-CuO nanocomposite for room temperature acetone sensing application," *Journal of Alloys and Compounds*, vol. 910, p. 164891, 2022.

[26] X. T. Tran, S. Poorahong, and M. J. R. a. Siaj, "One-pot hydrothermal synthesis and selective etching method of a porous MoSe 2 sand rose-like structure for electrocatalytic hydrogen evolution reaction," *RSC advances*, vol. 7, no. 82, pp. 52345-52351, 2017.

[27] N. Jain, S. Sharma, and N. K. J. J. o. M. S. M. i. E. Puri, "Investigation of charge transport mechanism in hydrothermally synthesized reduced graphene oxide (rGO) incorporated zinc oxide (ZnO) nanocomposite films," *Journal of Materials Science: Materials in Electronics*, vol. 33, no. 3, pp. 1307-1323, 2022.

[28] U. Krishnan *et al.*, "MoS2/ZnO nanocomposites for efficient photocatalytic degradation of industrial pollutants," *Materials Research Bulletin,* vol. 111, pp. 212-221, 2019.

[29] M. S. Vidhya, R. Yuvakkumar, P. S. Kumar, G. Ravi, and D. J. T. i. C. Velauthapillai, "Hydrothermal Synthesis of Flower Like MnSe2@ MoSe2 Electrode for Supercapacitor Applications," *topics in Catalysis,* vol. 65, no. 5, pp. 615-622, 2022.

[30] A. Mishra, J. Narang, C. S. Pundir, R. Pilloton, and M. J. A. o. Khanuja, "Morphology-preferable MoSe2 nanobrooms as a sensing platform for highly selective apta-capturing of salmonella bacteria," *ACS Omega,* vol. 3, no. 10, pp. 13020-13027, 2018.

[31] G. Ren *et al.*, "ZnO@ ZIF-8 core-shell microspheres for improved ethanol gas sensing," *Sensors and Actuators B: Chemical,* vol. 284, pp. 421-427, 2019.

[32] P. Cao *et al.*, "Ethanol sensing behavior of Pd-nanoparticles decorated ZnO-nanorod based chemiresistive gas sensors," *Sensors and Actuators B: Chemical,* vol. 298, p. 126850, 2019.

[33] S. Vijayakumar, S. J. O. Vadivel, and L. Technology, "Fiber optic ethanol gas sensor based WO3 and WO3/gC3N4 nanocomposites by a novel microwave technique," *Optics & Laser Technology,* vol. 118, pp. 44-51, 2019.

[34] H. Nan *et al.*, "Strong photoluminescence enhancement of MoS2 through defect engineering and oxygen bonding," *ACS Nano,* vol. 8, no. 6, pp. 5738-5745, 2014.

[35] H. Qiu, L. Pan, Z. Yao, J. Li, Y. Shi, and X. J. A. P. L. Wang, "Electrical characterization of back-gated bi-layer MoS2 field-effect transistors and the effect of ambient on their performances," vol. 100, no. 12, p. 123104, 2012.

[36] J. Jaiswal, A. Das, V. Chetry, S. Kumar, R. J. S. Chandra, and A. B. Chemical, "NO2 sensors based on crystalline MoSe2 porous nanowall thin films with vertically aligned molecular layers prepared by sputtering," *Sensors and Actuators B: Chemical,* vol. 359, p. 131552, 2022.

[37] P. Shankar and J. B. B. Rayappan, "Room temperature ethanol sensing properties of ZnO nanorods prepared using an electrospinning technique," *Journal of Materials Chemistry C,* vol. 5, no. 41, pp. 10869-10880, 2017.

[38] A. V. Raghu, K. K. Karuppanan, J. Nampoothiri, and B. Pullithadathil, "Wearable, flexible ethanol gas sensor based on TiO2 nanoparticles-grafted 2D-titanium carbide nanosheets," *ACS Applied Nano Materials,* vol. 2, no. 3, pp. 1152-1163, 2019.

[39] P. Zhao *et al.*, "One-dimensional MoS2-decorated TiO2 nanotube gas sensors for efficient alcohol sensing," vol. 674, pp. 252-258, 2016.

[40] S. Li *et al.*, "Heterojunction engineering of MoSe2/MoS2 with electronic modulation towards synergetic hydrogen evolution reaction and supercapacitance performance," *Chemical Engineering Journal,* vol. 359, pp. 1419-1426, 2019.

[41] Y. Han *et al.*, "Design of hetero-nanostructures on MoS2 nanosheets to boost NO2 room-temperature sensing," *ACS Applied Materials & Interfaces,* vol. 10, no. 26, pp. 22640-22649, 2018.

[42] Y. Zhou, G. Liu, X. Zhu, Y. J. S. Guo, and A. B. Chemical, "Ultrasensitive NO2 gas sensing based on rGO/MoS2 nanocomposite film at low temperature," *Sensors and Actuators B: Chemical,* vol. 251, pp. 280-290, 2017.

[43] P. Panigrahi, T. Hussain, A. Karton, and R. J. A. s. Ahuja, "Elemental substitution of two-dimensional transition metal dichalcogenides (MoSe2 and MoTe2): implications for enhanced gas sensing," *ACS Sensors,* vol. 4, no. 10, pp. 2646-2653, 2019.

[44] Y. Han *et al.*, "Design of hetero-nanostructures on MoS2 nanosheets to boost NO2 room-temperature sensing," *ACS applied materials & interfaces,* vol. 10, no. 26, pp. 22640-22649, 2018.

[45] A. V. Raghu, K. K. Karuppanan, J. Nampoothiri, and B. J. A. A. N. M. Pullithadathil, "Wearable, flexible ethanol gas sensor based on TiO2 nanoparticles-grafted 2D-titanium carbide nanosheets," *ACS Applied Nano Materials,* vol. 2, no. 3, pp. 1152-1163, 2019.

[46] M. Ikram, H. Lv, Z. Liu, K. Shi, and Y. J. J. o. M. C. A. Gao, "Hydrothermally derived p–n MoS 2–ZnO from p–p MoS 2-ZIF-8 for an efficient detection of NO 2 at room temperature," *Journal of Materials Chemistry A,* vol. 9, no. 26, pp. 14722-14730, 2021.

[47] R. Kumar *et al.*, "Growth of MoS2–MoO3 hybrid microflowers via controlled vapor transport process for efficient gas sensing at room temperature," vol. 5, no. 10, p. 1800071, 2018.

[48] W. Park *et al.*, "Oxygen environmental and passivation effects on molybdenum disulfide field effect transistors," vol. 24, no. 9, p. 095202, 2013.

CHAPTER 4

A Proposed Device based on $MoSe_2$-ZnO Heterojunctions on rGO for Enhanced Ethanol Gas Sensing Performances at Room Temperature

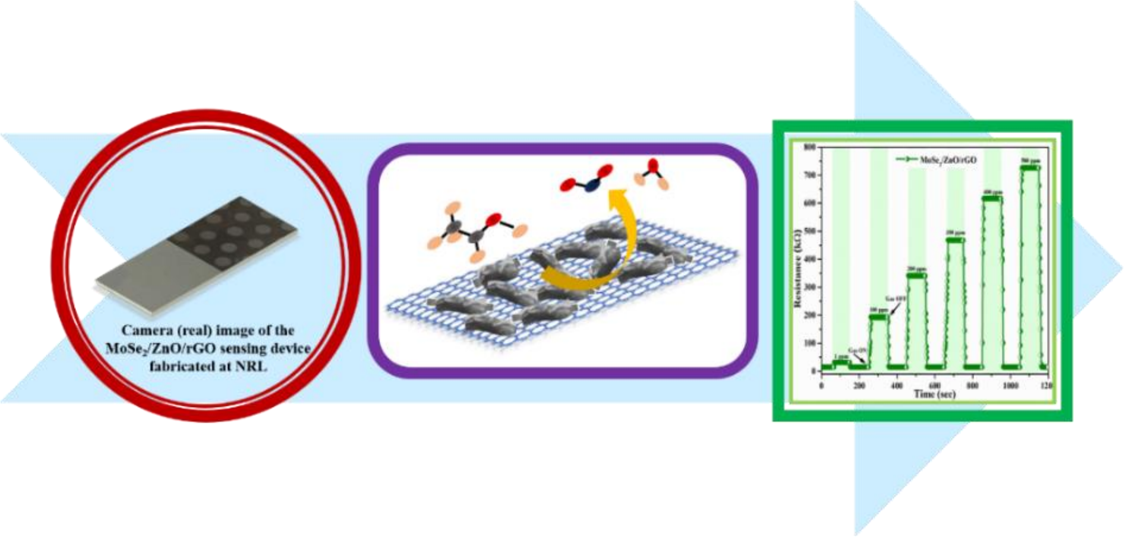

In the previous chapter, we explored $MoSe_2$/ZnO nanocomposite-based sensor for ethanol gas sensing at RT. The ethanol gas sensing results of the nanocomposite sensor exhibited higher response value, improved response time, and recovery time than the pristine- $MoSe_2$ sensor to 500 ppm ethanol gas. To further enhance the ethanol gas sensing properties of the sensing device at RT, we have explored a ternary nanocomposite of $MoSe_2$-ZnO heterojunctions decorated rGO ($MoSe_2$/ZnO/rGO) for ethanol gas sensing at room temperature. The sensing performance of the ternary nanocomposite sensing device was analysed for various concentrations of ethanol gas (1-500 ppm). The gas-sensing results have revealed that for 500 ppm ethanol gas concentration, the sensing device exhibited an enhanced response value (R_g/R_a) of 50.2. Significantly, the sensing device displayed a quick response and recovery time of 6.2 s and 12.9 s respectively. In addition to this, the sensing device can detect ethanol at remarkably low concentrations of 1 ppm. The enhanced sensing performance of the ternary nanocomposite sensing device has highlighted the effective synergistic effect between $MoSe_2$ nanosheets, ZnO nanorods, and rGO nanosheets. This was attributed to a large number of p-n heterojunctions of $MoSe_2$ nanosheets and ZnO nanorods onto the rGO nanosheets matrix.

4.1 Introduction

Air pollution has become a major concern for society with the advancement in science and technology [1, 2]. The release of hazardous gases as well as volatile organic compounds (VOCs) in the environment is not only detrimental to the atmospheric environment but also deleterious to human health [3]. VOCs are organic substances that can quickly turn into vapor and float into the air, even at RT because they have a low boiling point [4]. As per the World Health Organisation (WHO), air pollution is the leading cause of early death and various diseases [4, 5]. As a result, it is critical to detect and control the release of these pollution-causing gases. As a typical representative of VOCs, ethanol is extensively used in various food industries, agricultural production, chemical and pharmaceutical communities, etc. [6, 7]. But its long-term exposure causes health problems, such as difficulty in breathing, kidney failure, headaches, drowsiness, eye and skin irritation, and even coma [1, 8, 9]. Thus, it becomes critically important to monitor and detect ethanol gas at the right time at RT [10-12].

Molybdenum diselenide ($MoSe_2$), a two-dimensional (2D) transition metal dichalcogenides (TMDs) has gained focus in the fields of gas sensing, energy storage, solar cells, etc. owing to its intriguing physical and chemical properties [13-17]. It possesses high adsorption energy with chemical molecules, exceptional adsorption-desorption properties, and a large surface-to-volume ratio which makes it a suitable candidate to be explored in-depth for gas sensing applications [18, 19]. Over the past few years, significant efforts have been devoted to developing gas sensors based on $MoSe_2$ [3, 20, 21]. However, gas sensors relying on pristine $MoSe_2$ exhibit drawbacks such as poor response, slow response, and recovery time. This limits the utilization of pristine $MoSe_2$ for gas sensors [20-22]. To meet the requirements of practical gas sensors, recently $MoSe_2$-metal-oxide semiconductor (MOS) hybrids have aroused worldwide attention. For instance, Pan et al. report an RT H_2S sensor based on metal-organic framework (MOF)- derived α-Fe_2O_3/$MoSe_2$ composite exhibiting prominent sensing performances compared to pristine- α-Fe_2O_3 and pristine- $MoSe_2$ sensors [23]. Yang et al. designed a novel MOF-derived SnO_2/$MoSe_2$ nanocomposite sensor with improved CO sensing properties at RT compared to pristine $MoSe_2$ and SnO_2 sensors [19].

In order to further strengthen the sensing performance of 2D TMDs – MOS hybrids, researchers are focussing on compositing them with carbon materials forming a ternary nanocomposite [24, 25]. In comparison to the binary hybrids, ternary nanocomposites develop multiple heterojunctions which modulate the charge transfer behavior in the gas sensing process thereby enhancing the sensing performance of the ternary nanocomposite sensors [26, 27]. Carbon materials such as reduced-graphene oxide (rGO) have been employed in the field of gas sensing owing to the presence of abundant residual oxygen functional groups, superior specific surface area, high carrier mobility, and chemically active defect sites for the adsorption of gases [4, 24, 28-30]. Ding et al. constructed an RT ppb-level CO gas sensor based on MoS_2/rGO/Cu_2O composite by hydrothermal and soft-template methods. The ternary composite sensor exhibits excellent sensing response, good selectivity, and long-term stability [24]. Yuan et. al. reports an NH_3 gas sensor based on MoO_3/MoS_2/rGO composite. The composite sensor operates at low temperatures with enhanced gas sensitivity compared to the pristine-MoO_3, pristine-MoS_2, and MoS_2/MoO_3 sensors [25]. Therefore, incorporating rGO in the binary hybrids serves to improve the uniform distribution of heterojunctions, thereby increasing the contact area between the sensing material and the gas. This improves the rate of gas adsorption [31, 32]. Furthermore, it creates a conductive network to transport carriers and improves the sensing material's ability to detect carriers generated in trace gas reactions [33, 34]. Thus, utilizing ternary nanocomposite promises enhanced sensing parameters for practical applications.

In our previous work [3], we explored $MoSe_2$/ZnO nanocomposite-based sensor for ethanol gas sensing at RT. The ethanol gas sensing results of the nanocomposite sensor exhibited higher response value, improved response time, and recovery time than the pristine- $MoSe_2$ sensor to 500 ppm ethanol gas. To further enhance the ethanol gas sensing properties of the sensing device at RT, we have explored a ternary nanocomposite of $MoSe_2$-ZnO heterojunctions decorated rGO ($MoSe_2$/ZnO/rGO) for the first time to the best of our knowledge. In the gas sensing performance, the as-fabricated sensing device has been exposed to various concentrations of ethanol gas ranging from 1 ppm to 500 ppm at RT. A sensing mechanism has been proposed to explain the enhanced sensing parameters of the as-fabricated sensing device. This work may uncover insights into the potential of ternary nanocomposites for ethanol gas sensing, presenting new avenues for progress and applications in the field.

4.2 Experimental section

4.2.1 Chemicals used for the synthesis of the ternary $MoSe_2$/ZnO/rGO nanocomposite

The chemicals essential for the synthesis included sodium molybdate dihydrate ($Na_2MoO_4.2H_2O$), selenium (Se) powder, hydrazine hydrate-86% ($N_2H_4.H_2O$), zinc acetate ($Zn(CH_3COO)_2{\cdot}2H_2O$), sodium hydroxide pellets (NaOH), graphite powder, concentrated sulphuric acid (H_2SO_4), orthophosphoric acid (H_3PO_4), hydrogen peroxide (H_2O_2), potassium permanganate ($KMnO_4$), ethanol (C_2H_5OH), and isopropyl alcohol (IPA). These chemicals were purchased from Sigma Aldrich.

4.2.2 Synthesis of the ternary $MoSe_2$/ZnO/rGO nanocomposite

A hydrothermal approach was utilised to synthesise $MoSe_2$/ZnO/rGO nanocomposite. $MoSe_2$ nanosheets and ZnO nanorods were synthesised using a hydrothermal method while GO nanosheets were synthesised via a modified Hummer's method as reported earlier in our previous work [3, 28, 35, 36].

Briefly, for the synthesis of $MoSe_2$ nanosheets, 2 mmol of $Na_2MoO_4.2H_2O$ was dissolved in deionized (DI) water and ethanol (1:1 volume ratio) with stirring for 45 min to obtain a clear solution. Separately, Se powder solution (4 mmol) was prepared in $N_2H_4.H_2O$-86% with continuous stirring. This solution was then added to $Na_2MoO_4.2H_2O$ solution dropwise. Finally, this reaction mixture was shifted into a 100 mL Teflon beaker. The Teflon beaker containing the reaction mixture was placed in an autoclave which was kept inside the vacuum oven at 220 °C for 24 h. Subsequently, the obtained solution was thoroughly washed multiple times with ethanol and dried overnight at 100 °C.

For the synthesis of ZnO nanorods, a solution of $Zn(CH_3COO)_2{\cdot}2H_2O$ (0.5 M) and NaOH (5 M) was prepared separately under continuous stirring. After half an hour, the solution of NaOH was added to the solution of $Zn(CH_3COO)_2{\cdot}2H_2O$ dropwise. This reaction mixture was shifted into a 100 mL Teflon beaker. The Teflon beaker was placed in an autoclave which was kept inside the oven at 180 °C. The resultant solution was centrifuged and dried to obtain a white-colored powder.

For the synthesis of GO nanosheets, H_2SO_4 and H_3PO_4 were added to 2 g of graphite powder in a ratio of 9:1. After some time, $KMnO_4$ was added to the above reaction mixture slowly which was followed by magnetic stirring at 50 °C overnight. Subsequent to this procedure, ice (300 ml) was introduced into the reaction mixture, followed by the addition of 2 mL of H_2O_2 to effectively quench the reaction. The resultant yellowish slurry was centrifuged until the pH reached 7 which was then dried to obtain GO.

Finally, $MoSe_2$, ZnO, and GO synthesised by the above procedure were taken in a quantitative amount and dispersed in a mixture of ethanol and DI water. This dispersion was subjected to ultrasonication for 4 h. This solution was put in a hydrothermal autoclave which was kept in a vacuum oven at 180 °C for 24 h. After cooling to RT, the black-color precipitate of the ternary $MoSe_2$/ZnO/rGO nanocomposite was centrifuged and dried subsequently in a vacuum oven.

4.2.3 Gas sensing device fabrication

A series of steps were followed to fabricate an ethanol sensing device using the ternary $MoSe_2$/ZnO/rGO nanocomposite. First, the glass slides coated with indium tin oxide (ITO) were hydrolyzed [37]. The hydrolysed ITO slides were cleaned using IPA and DI water several times. After cleaning, the slides were dried at 60 ˚C in the oven for 30 min. Next, a film of $MoSe_2$/ZnO/rGO nanocomposite was prepared using the electrophoretic deposition (EPD) technique. The as-obtained powder was dispersed in acetonitrile (0.75 mg/mL). Afterwards, it was transferred into a 2-electrode EPD cell, consisting of the working electrode (WE) and the counter electrode (CE) as illustrated in Fig. 4.1. An optimized potential was applied to the ITO clipped to the WE for 120 s. The prepared film was left to dry overnight. Finally, the thermal evaporation technique was utilised to deposit silver (Ag) electrodes onto the prepared film. The as-fabricated sensing device was used for performing ethanol sensing measurements.

4.2.4 Gas sensing measurements

The gas sensing was carried out in a customized stainless steel (SS) chamber. A constant current supply to the ternary $MoSe_2$/ZnO/rGO nanocomposite ethanol sensing device was provided by the source measuring unit (SMU). At the beginning of the ethanol detection process, rough vacuum pressure was created inside the SS chamber using a rotary pump. Then, dry air was introduced for 50 s to obtain the baseline resistance. After that 1% ethanol gas/ 99% dry nitrogen gas mixture was introduced inside the SS chamber. Inside the SS chamber, the concentration of ethanol gas was calculated in parts per million (ppm) according to the following equation:

$$C = \frac{22.4 \times \Psi \times \rho \times V_1}{M \times V_2} \times 1000 \tag{4.1}$$

In the above formula (equation 4.1), the ethanol gas concentration is depicted by C (ppm), gas volume fraction is denoted as Ψ, density of ethanol is represented as ρ ($kg.m^{-3}$), volume of ethanol gas is indicated as V_1 (L), molecular weight of ethanol is expressed as M ($kg.mol^{-1}$), and volume of the SS chamber is denoted as V_2 (m^3) [38, 39]. A data acquisition software (Lab-View) attached to the SMU was used to record the change in resistance of the sensing film.

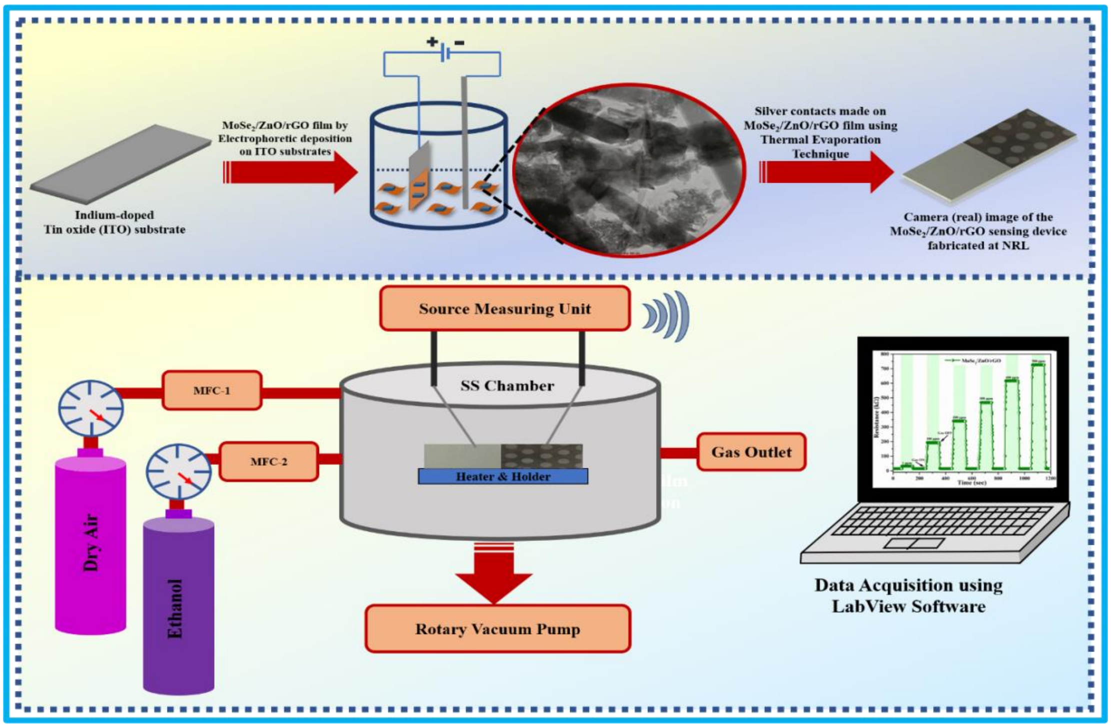

Fig. 4.1: Diagrammatic representation of fabrication of the ternary $MoSe_2$/ZnO/rGO nanocomposite ethanol sensing device and gas sensing setup

4.3 Results and discussions

4.3.1 Structural analysis of the ternary $MoSe_2$/ZnO/rGO nanocomposite using XRD

XRD was used to investigate the crystal structure of $MoSe_2$, ZnO, GO, and $MoSe_2$/ZnO/rGO nanocomposite as depicted in Fig. 4.2. All the diffraction peaks of as-synthesised $MoSe_2$ are attributed to the (002), (100), (103) and (110) planes of the hexagonal phase of $MoSe_2$ (JCPDS 029-0914) [40]. The XRD pattern of ZnO shows all the diffraction peaks which are congruous with the standard data available for the wurtzite structure of ZnO (JCPDS 36-1451) [41]. The XRD pattern of GO exhibits prominent and weak diffraction peaks at 11.7° and 42.6° which corresponds to the (002) and (100) planes of GO respectively [42]. The XRD pattern of the ternary $MoSe_2$/ZnO/rGO nanocomposite consists of diffraction peaks of (002), (004), (100), and (110) planes belonging to $MoSe_2$ along with all the diffraction peaks of ZnO. The reason for the invisibility of the (103) plane of $MoSe_2$ can be attributed to the strong characteristic peak intensities of $MoSe_2$ and ZnO [3, 43].

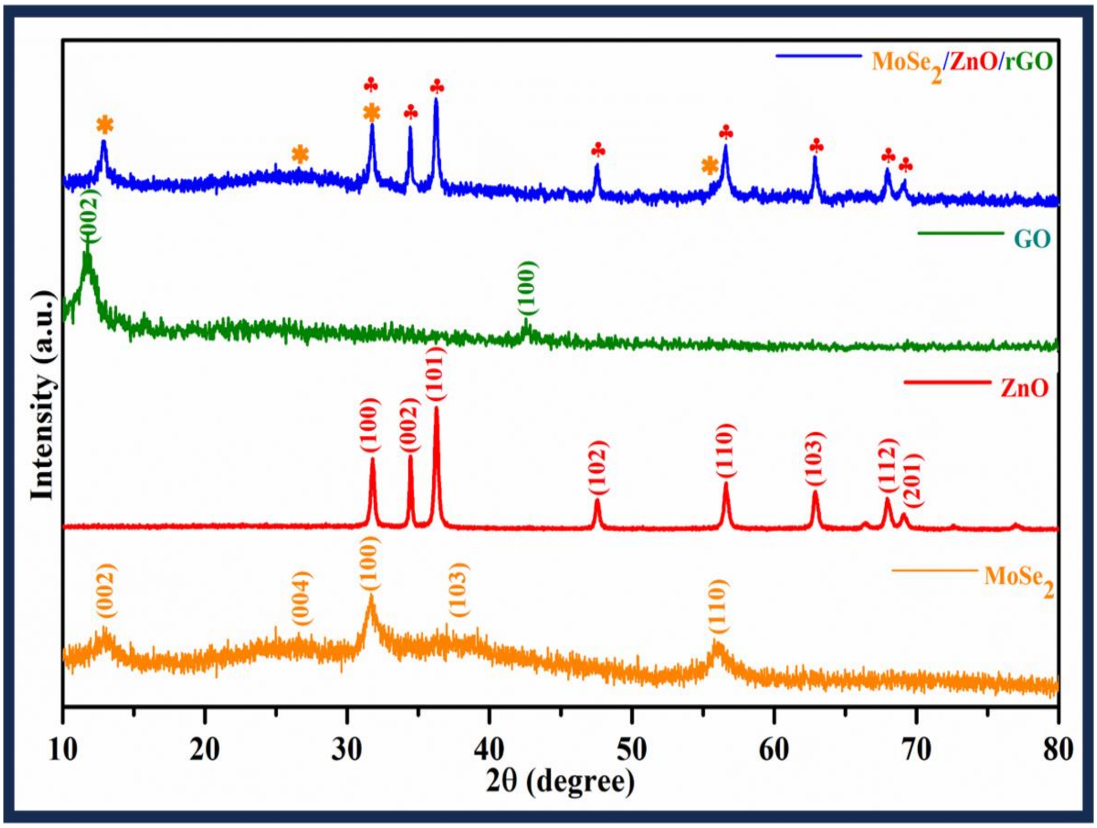

Fig. 4.2: XRD spectra of $MoSe_2$, ZnO, GO, and $MoSe_2$/ZnO/rGO nanocomposite

Noticeably, it is also difficult to find the reflection peaks of rGO in the $MoSe_2$/ZnO/rGO nanocomposite. The much higher intensity of the characteristic peak of $MoSe_2$, as well as ZnO in the ternary $MoSe_2$/ZnO/rGO nanocomposite, can be the reason for the suppression of the rGO peak in the nanocomposite [36]. Also, we believe that the $MoSe_2$-ZnO might attach to the surfaces of rGO which prevents their restacking and aggregation, which might have weakened the diffraction peak of rGO [44-46]. Therefore, further characterizations have been done to provide evidence for the coexistence of rGO in the ternary $MoSe_2$/ZnO/rGO nanocomposite.

4.3.2 Study of vibrational modes of the ternary $MoSe_2$/ZnO/rGO nanocomposite using Raman spectroscopy

To confirm the presence of rGO in the as-synthesised ternary $MoSe_2$/ZnO/rGO nanocomposite, Raman spectroscopy was utilised. Fig. 4.3 shows the Raman spectra of $MoSe_2$, ZnO, GO, and $MoSe_2$/ZnO/rGO nanocomposite. Fig. 4.3(a) shows the Raman peaks at 238 cm^{-1}, 167 cm^{-1} and 283 cm^{-1} which are ascribed to the A_{1g}, E_{1g}, and E^1_{2g} modes of $MoSe_2$ respectively [20, 47]. Fig. 4.3(b) shows a characteristic Raman peak of ZnO at 437 cm^{-1} (E_2^{high}) [35]. Fig. 4.3(c) displays the two distinct peaks of GO at 1353 cm^{-1} and 1590 cm^{-1} representing the D and G bands, respectively. The intensity ratio (I_D/I_G) corresponds to the ratio of the intensity of the D and G peaks respectively is determined to be 0.99.

The Raman spectrum of the ternary $MoSe_2$/ZnO/rGO nanocomposite is illustrated in Fig. 4.3(d). The peak at 233.7 cm^{-1} in $MoSe_2$/ZnO/rGO nanocomposite corresponds to the A_{1g} vibration mode of $MoSe_2$ and the characteristic peak identified at 431.3 cm^{-1} is specifically attributed to ZnO. Additionally, two prominant bands at 1345 cm^{-1} and 1585 cm^{-1} in the Raman spectrum of $MoSe_2$/ZnO/rGO nanocomposite are attributed to the D and G bands of rGO respectively.

The I_D/I_G ratio of rGO in $MoSe_2$/ZnO/rGO nanocomposite is calculated to be 1.02 which is higher than that of GO. The increase in intensity ratio from 0.99 to 1.02 indicates that GO was successfully reduced to rGO during the hydrothermal synthesis of $MoSe_2$/ZnO/rGO nanocomposite [36, 48, 49]. Therefore, the concurrent presence of Raman peaks attributed to $MoSe_2$, ZnO, and rGO validates the successful synthesis of the ternary $MoSe_2$/ZnO/rGO nanocomposite.

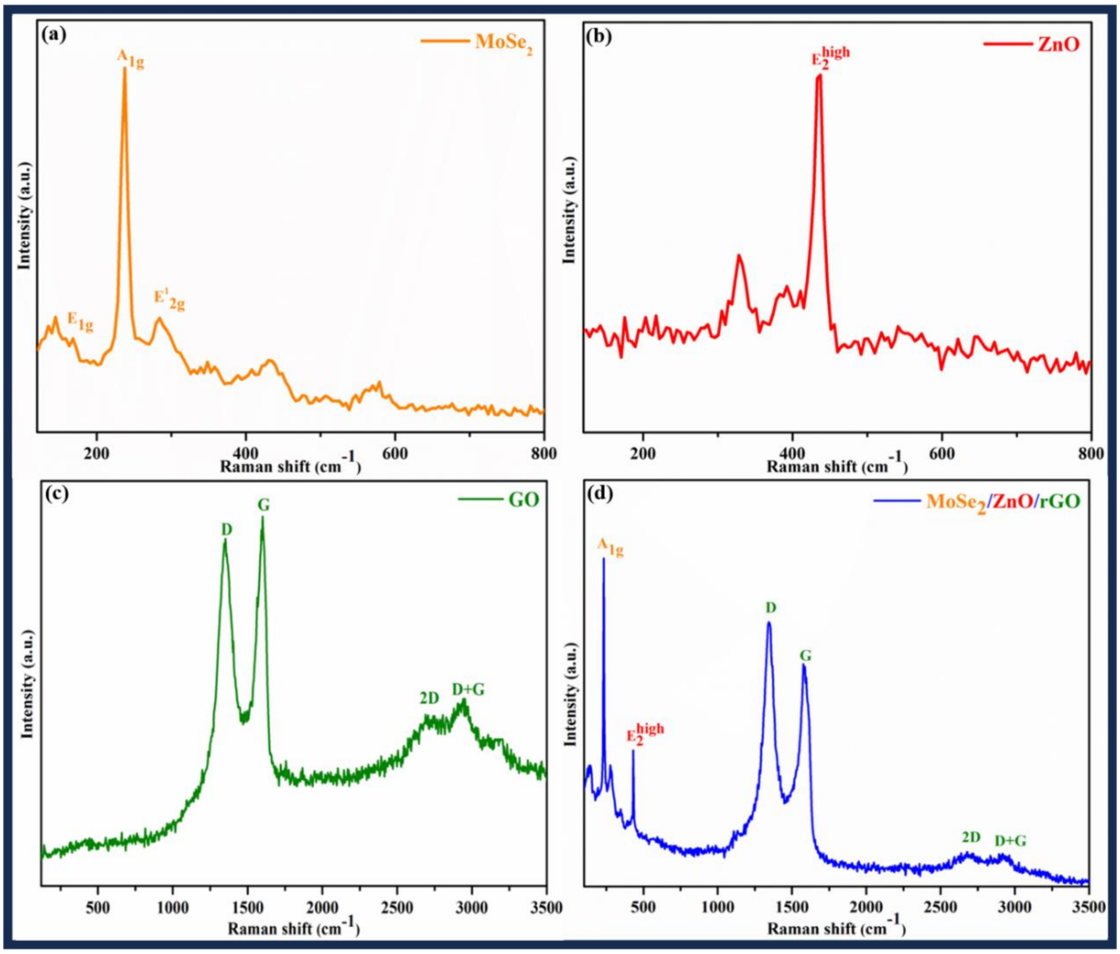

Fig. 4.3: Raman spectra of (a) $MoSe_2$, (b) ZnO, (c) GO, and (d) $MoSe_2$/ZnO/rGO nanocomposite

4.3.3 Microstructure analysis of the ternary $MoSe_2$/ZnO/rGO nanocomposite using HRTEM

The microstructure of $MoSe_2$, ZnO, GO, and $MoSe_2$/ZnO/rGO nanocomposite was analysed by HRTEM as displayed in Fig. 4.4. The wrinkled nanosheets of $MoSe_2$ stacked over one another are shown in Fig. 4.4(a). In addition to the wrinkles, the nanosheets are curled at the edges. Fig. 4.4(b) and 4.4(c) display the nanorods of ZnO and creased nanosheets of GO.

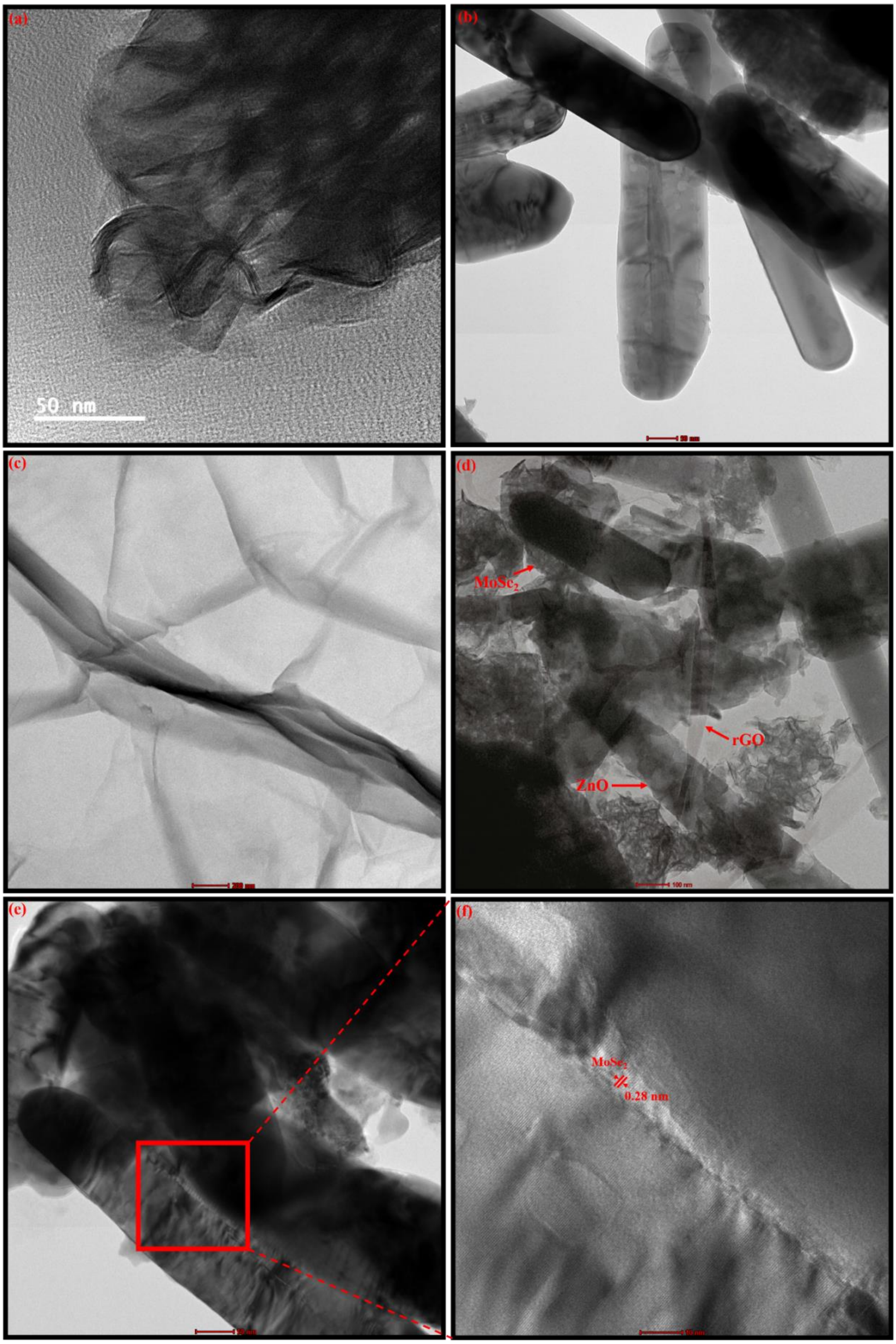

Fig. 4.4: HRTEM images of (a) $MoSe_2$ nanosheets (b) ZnO nanorods, (c) GO nanosheets, (d and e) $MoSe_2$/ZnO/rGO nanocomposite, and (f) Heterogeneous interface between $MoSe_2$ nanosheets and ZnO nanorods

The HRTEM image of the ternary $MoSe_2$/ZnO/rGO nanocomposite (Fig. 4.4(d) and 4.4(e) suggests that rGO nanosheets have been successfully decorated with $MoSe_2$ nanosheets wrapping the ZnO nanorods. These rGO nanosheets provide a large specific surface area and active sites for the deposition of $MoSe_2$ nanosheets and ZnO nanorods. Also, Fig. 4.4(f) shows the fine lattice fringes of $MoSe_2$ nanosheets wrapping the ZnO nanorods. This indicates the formation of a heterogeneous interface between $MoSe_2$ nanosheets and ZnO nanorods. The interplanar spacing of $MoSe_2$ nanosheets is calculated to be 0.28 nm corresponding to the (100) lattice plane of $MoSe_2$ as labeled in Fig. 4.4(f). Hence HRTEM results confirm the successful decoration of ZnO nanorods wrapped by $MoSe_2$ nanosheets onto rGO nanosheets in the ternary $MoSe_2$/ZnO/rGO nanocomposite.

4.3.4 Functional groups identification of the ternary $MoSe_2$/ZnO/rGO nanocomposite using FTIR

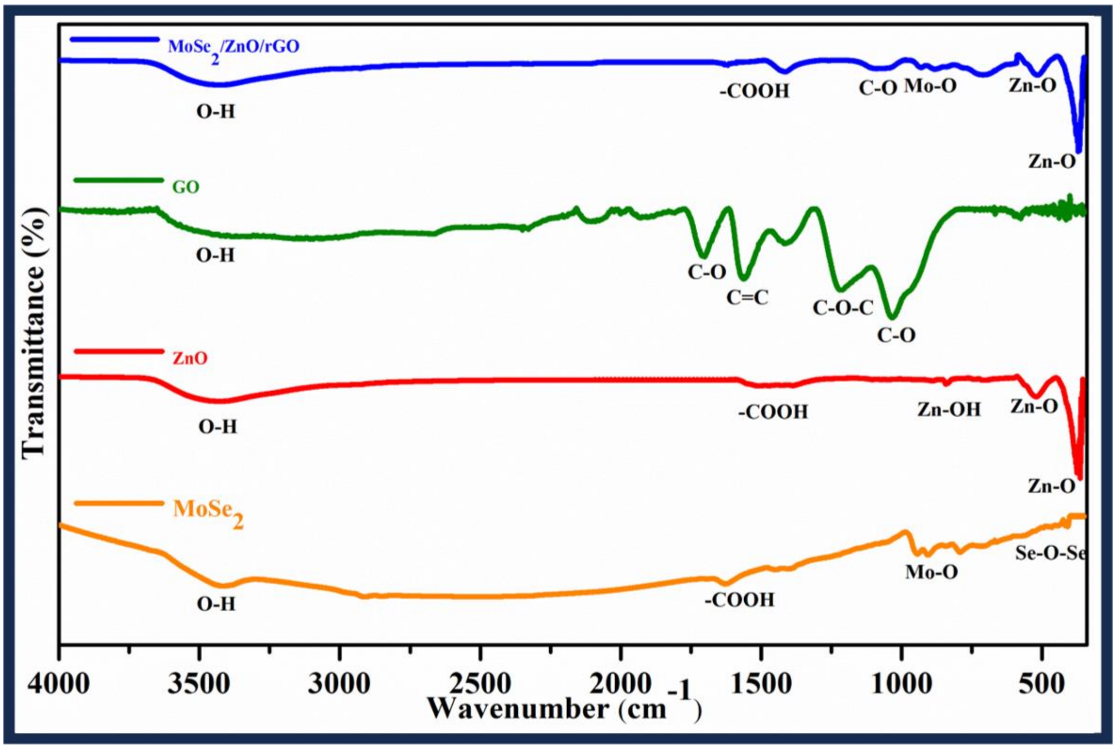

Fig. 4.5: FTIR spectra of $MoSe_2$, ZnO, GO, and $MoSe_2$/ZnO/rGO nanocomposite.

The FTIR spectra of $MoSe_2$, ZnO, GO, and $MoSe_2$/ZnO/rGO nanocomposite are depicted in Fig. 4.5. The spectrum of $MoSe_2$ spectrum exhibits a peak at 3424 cm^{-1} indicative of O-H stretching vibrations. Additionally, within the range of 1000-750

cm^{-1} peaks are observed corresponding to Mo-O bonds, while the peak at 464 cm^{-1} corresponds to Se-O-Se bonds [50, 51]. Peaks in the FTIR spectrum of ZnO are observed corresponding to O-H (3427 cm^{-1}), COOH (1510-1380 cm^{-1}), Zn-OH (836 cm^{-1}), and Zn-O (510 and 370 cm^{-1}) [35]. The FTIR spectrum of GO reveals several distinctive peaks: a broad peak at 3280 cm^{-1} is attributed to O-H groups, and peaks at 1700 cm^{-1} and 1562 cm^{-1} indicate C=O and C=C stretching, respectively. Additionally, a minor peak at 1400 cm^{-1} corresponds to O-H deformation, while two peaks at 1215 cm^{-1} and 1030 cm^{-1} correspond to epoxy C-O-C and alkoxy C-O stretching vibrations, respectively [35, 52]. The spectrum of ternary $MoSe_2$/ZnO/rGO nanocomposite displays the peak corresponding to Mo-O bonds, and Zn-O bonds. In addition to these peaks, some peaks corresponding to oxygen-containing functional groups with decreased intensity compared to GO are also seen. This implies a successful thermal reduction of GO into rGO during the hydrothermal synthesis of the ternary $MoSe_2$/ZnO/rGO nanocomposite [36, 53]. Hence, the presence of functional groups associated with $MoSe_2$, ZnO, and rGO in the $MoSe_2$/ZnO/rGO nanocomposite confirms its successful formation.

4.3.5 Ethanol Gas sensing performance of the ternary $MoSe_2$/ZnO/rGO nanocomposite sensing device at RT

4.3.5.1 Response of the sensing device toward various concentrations of ethanol gas

The gas sensing performance characteristics of the ternary $MoSe_2$/ZnO/rGO nanocomposite sensing device were analysed towards various ethanol gas concentrations ranging from 1 ppm to 500 ppm at RT as illustrated in Fig. 4.6(a). It is observed in Fig. 4.6(a) that as the ethanol concentration increases, there is an increase in resistance change of the device. As a result, the response value (R_g/R_a) of the ternary nanocomposite sensing device to ethanol gas concentrations of 1 ppm, 100 ppm, 200 ppm, 300 ppm, 400 ppm, and 500 ppm at RT was calculated as 2.2, 14.0, 23.5, 32.4, 42.6, and 50.2 respectively. R_a and R_g are the resistance of the device in the air and ethanol gas respectively.

4.3.5.2 Response and recovery time of the sensing device

Fig. 4.6(b) describes the response time (t_{resp}), and the recovery time (t_{rec}) of the ternary $MoSe_2$/ZnO/rGO nanocomposite sensing device. The device exhibited a t_{resp} of 6.2 s and t_{rec} of 12.9 s to 500 ppm ethanol gas. Moreover, the ternary nanocomposite sensing device exhibits a typical p-type gas sensing behavior, that is, an increased resistance induced by reducing gas. In addition to this, full recovery to the initial state is observed for the ternary $MoSe_2$/ZnO/rGO nanocomposite sensing device which reveals that the interaction was due to the physisorption process.

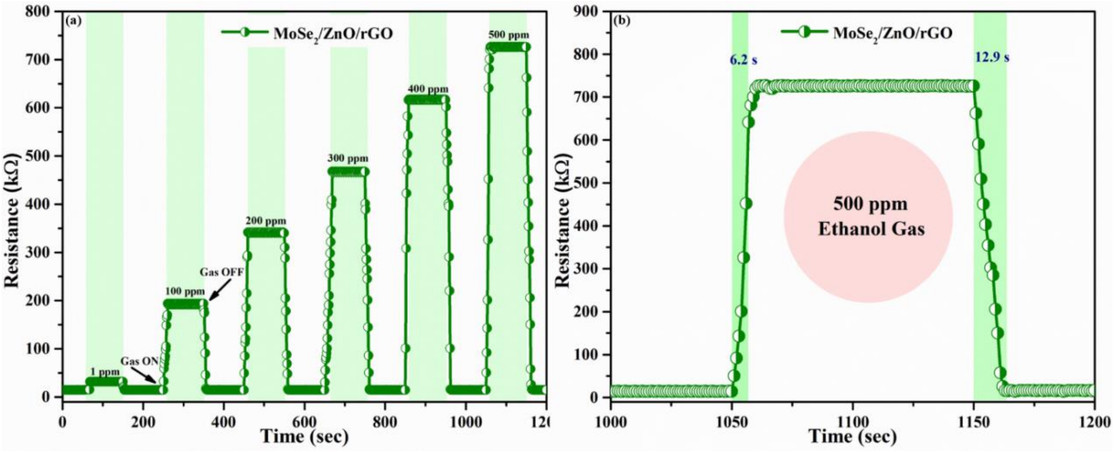

Fig. 4.6: (a) Ethanol concentration-dependent resistance change curves and (b) Response time and recovery time of the ternary $MoSe_2$/ZnO/rGO nanocomposite sensing device at RT

The response time and recovery time of the ternary $MoSe_2$/ZnO/rGO nanocomposite sensing device were systematically evaluated for various concentrations of ethanol gas ranging from 1 ppm to 500 ppm as depicted in Fig. 4.7(a). It is noticed that the as-fabricated ternary nanocomposite sensing device shows low t_{resp} and large t_{rec} when the device is exposed to a higher concentration of ethanol gas (500 ppm). The fall in t_{resp} could be explained by the abundant sites on the sensor's surface for gas adsorption. Conversely, the rise in t_{rec} may be attributed to a large number of ethanol gas molecules involved in the interaction with the sensor which required time to desorb from the sensor's surface [27].

4.3.5.3 Repeatability of the sensing device

A practical gas sensor should possess good repeatability under exposure to the same concentration of target gas. The repeatability of the ternary nanocomposite sensing device was tested for five successive cycles to 1 ppm and 500 ppm ethanol gas in the order of dry air-ethanol-dry air as shown in Fig. 4.7(b) and Fig. 4.7(c). It was observed that the resistance change of the as-fabricated ternary nanocomposite sensing device was approximately the same, exhibiting good repeatability to ethanol gas over cyclic measurements.

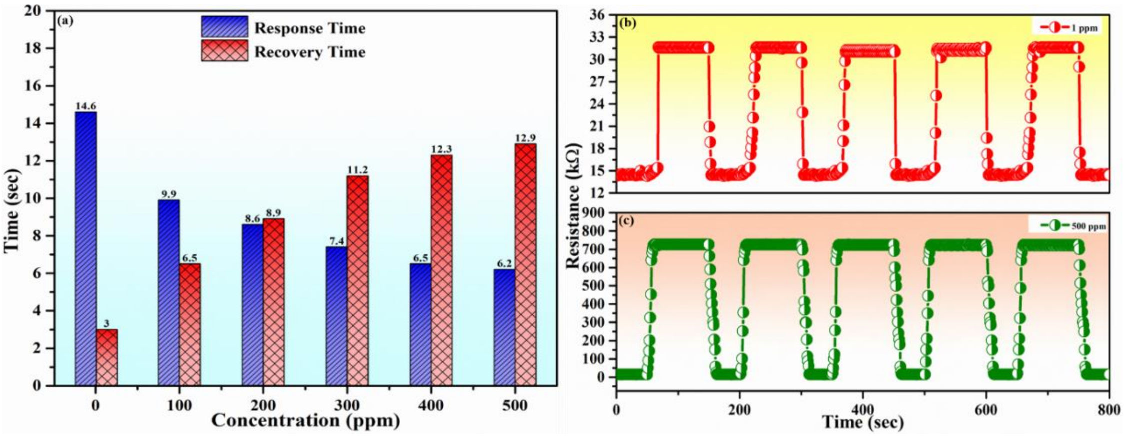

Fig. 4.7: (a) t_{resp} and t_{rec} versus concentration curves, (b) and (c) Repeatability toward 1 ppm and 500 ppm ethanol gas of the ternary $MoSe_2$/ZnO/rGO nanocomposite sensing device

4.3.5.4 Selectivity of the sensing device

Another vital aspect of a practical gas sensor is selectivity. The selectivity study of the ternary $MoSe_2$/ZnO/rGO nanocomposite sensing device for various VOCs (including ethanol, acetone, benzene, and formaldehyde) with a concentration of 500 ppm at RT is shown as radar plots in Fig. 4.8(a). It can be seen that the ternary $MoSe_2$/ZnO/rGO nanocomposite sensing device displays a response of 50.2 to ethanol gas. This suggests that the ternary nanocomposite sensing device displays a higher response to ethanol gas compared to other gases, which is ~ 1.8 times of acetone gas, ~ 16.2 times of benzene gas, and ~ 26.4 times of formaldehyde gas.

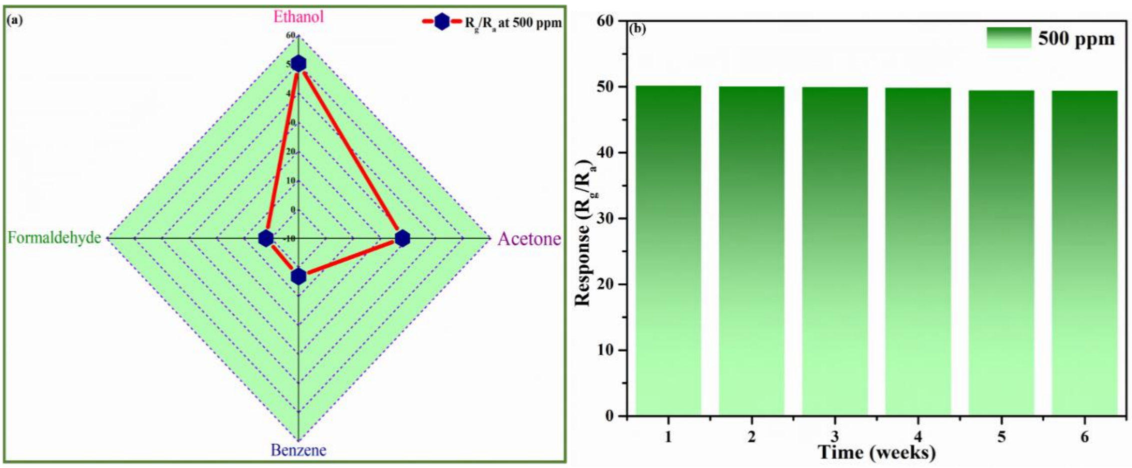

Fig. 4.8: (a) Selectivity test to 500 ppm of different VOCs, and (b) Long-term stability of response (6 weeks) towards 500 ppm of ethanol for the ternary $MoSe_2$/ZnO/rGO nanocomposite sensing device at RT

4.3.5.5 Stability of the sensing device

To evaluate the extended stability of the ternary $MoSe_2$/ZnO/rGO nanocomposite sensing device, its response to 500 ppm ethanol gas at RT is observed over a period of 6 weeks, with measurements taken at regular intervals of 7 days. As represented in Fig. 4.8(b), no obvious variation in the responses of the as-fabricated sensing device was observed within 42 days, inferring that the sensor has a great prospect for long-term detection of ethanol gas at RT.

The detailed comparison of ethanol gas sensing performances of the ternary nanocomposites and other reported literature with the present work is shown in Table 4.1. Compared to previously reported ethanol gas sensors, the ethanol sensor based on the ternary $MoSe_2$/ZnO/rGO nanocomposite exhibits higher response value (R_g/R_a), fast response and recovery time, outstanding long-term stability, and importantly operates at RT.

Table 4.1: A comparison of ethanol gas sensing performances of the ternary $MoSe_2$/ZnO/rGO nanocomposite sensor with other reported literature$^!$

Sensor Materials	Operating Temperature (°C)	Concentration (ppm)	Sensor Response (S)	Response Time (s)	Recovery Time (s)	Stability (days)
CuO-ZnO/g-C_3N_4 [54]	260	500	$16^{\$}$	87	169	30
Pd decorated ZnO [55]	260	500	$81^{\#}$	6	95	22
MoS_2/TiO_2 [56]	300	500	$100^{\wedge}$	70 ± 10 s	90 ± 20 s	56
ZnO [57]	275	500	$33^{\$}$	25	12	60
$MoSe_2$/ZnO [Previous work] [3]	27 (RT)	500	37.8^{*}	8.4	14.7	30
$MoSe_2$/ZnO/rGO [This Work]	**27 (RT)**	**500**	**50.2^{*}**	**6.2**	**12.9**	**42**

* indicates that $S = R_g/R_a$; ^ indicates that $S = (R_g\text{-}R_a/R_a) \times 100$; \$ indicates that $S = R_a/R_g$; # indicates that $S = (R_a\text{-}R_g/R_a) \times 100$

! indicates that the literature provided has been structured to follow the chronological order of their publishing.

4.3.5.6 Ethanol gas sensing mechanism

The gas-sensing mechanism of the sensor is based on the change in resistance due to the adsorption and desorption of ethanol molecules on the surface of the sensing material [58]. In general, $MoSe_2$ and rGO nanosheets show a p-type behavior, and ZnO nanorods show an n-type behavior towards ethanol gas [3, 59]. From the response curves (Fig. 4.5(a) and 4.5(b)), the $MoSe_2$/ZnO/rGO nanocomposite sensing device shows a p-type behavior which suggests that $MoSe_2$ and rGO nanosheets act as majority charge carriers during the ethanol sensing mechanism. The adsorption of oxygen and ethanol molecules on the surface of the ternary $MoSe_2$/ZnO/rGO nanocomposite sensor plays a crucial role as depicted in Fig. 4.9. When the sensing device is exposed to air, the oxygen molecules adsorbed on the surface of the sensor are transformed into oxygen species (O_2^-) by trapping free electrons from the conduction band of $MoSe_2$/ZnO/rGO nanocomposite sensor [24]. Generally, at RT the oxygen molecules can react as follows to produce O_2^- [12, 60]:

$$O_2\,(gas) \rightarrow O_2\,(ads) \qquad (4.2)$$

$$2O_2\,(ads) + 2e^- \leftrightarrow 2O_2^-\,(ads) \qquad (4.3)$$

Upon exposure of the sensing device to ethanol gas, the ethanol gas molecules react with the oxygen species adsorbed on the surface of the ternary $MoSe_2$/ZnO/rGO nanocomposite sensor. This causes the ternary nanocomposite to recapture the electrons carried away by the adsorbed oxygen in the air. Consequently, this process leads to an overall increase in the resistance of the ternary nanocomposite sensor. The reaction is shown in eqn. 4.

$$2C_2H_5OH + 6O_2^-\,(ads) \rightarrow 4CO_2 + 6H_2O + 6e^- \qquad (4.4)$$

The following aspects can be attributed to the high ethanol gas sensing performance of the ternary $MoSe_2$/ZnO/rGO nanocomposite sensing device: (I) A large number of active sites are provided by rGO for the deposition of $MoSe_2$ nanosheets and ZnO nanorods [46, 61]. Thus, various p-n heterojunctions are introduced onto the rGO nanosheets matrix due to p-type $MoSe_2$ and n-type ZnO as shown in Fig. 4.8. This is also evident in HRTEM images (Fig. 4.4(d), 4.4(e), and 4.4(f)) that $MoSe_2$/ZnO is deposited onto the rGO matrix. The sensing mechanism based on $MoSe_2$/ZnO p-n heterojunction has been elaborated in our previous work which clearly explains that the response of the sensor is enhanced due to the formation of p-n heterojunction [3].

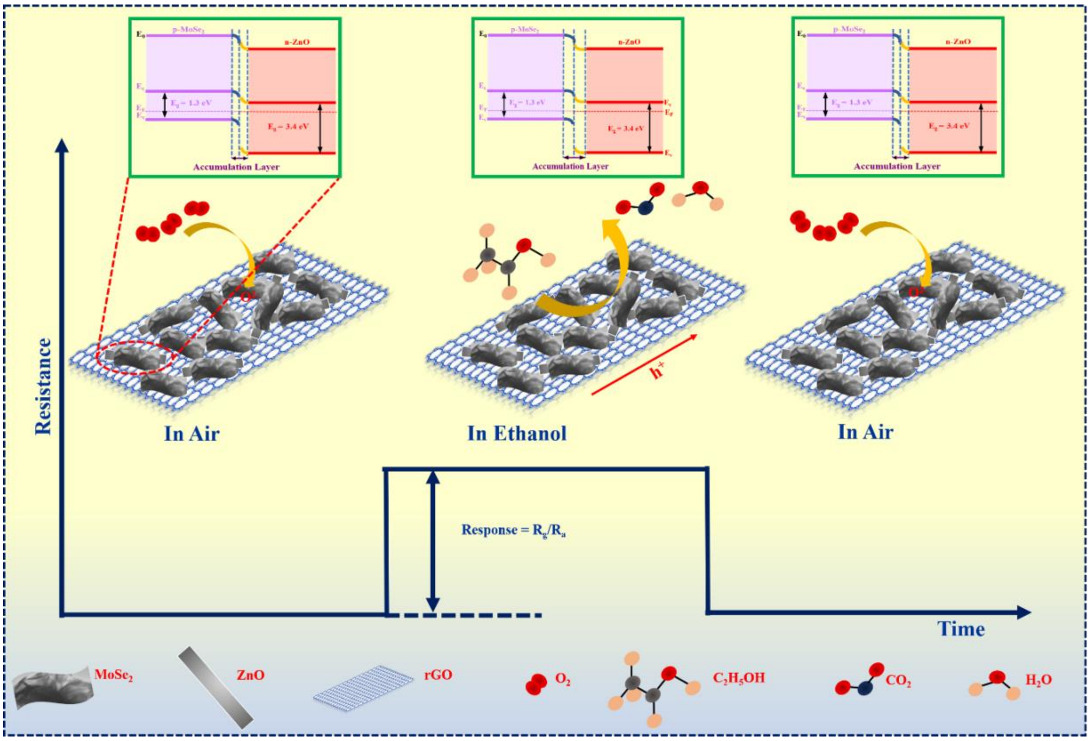

Fig. 4.9: Schematic representation of ethanol gas sensing mechanism of the ternary $MoSe_2$/ZnO/rGO nanocomposite sensing device

But, when the ternary nanocomposite sensor is exposed to ethanol molecules, we presume that the $MoSe_2$ nanosheets and ZnO nanorods are responsible for the receptor function while rGO serves to establish the electronic conduction pathway. The specific ternary structure provides increased active sites, enhancing the adsorption and desorption of ethanol molecules thereby improving the sensing response appreciably. (II) In addition to this, rGO also acts as a conductive network facilitating rapid electron transfer between $MoSe_2$ nanosheets and ZnO nanorods [42]. This leads to quick response and recovery time as shown in Fig. 4.5(b). (III) Furthermore, the bandgap of rGO is small, and slight changes in the carrier concentration on the surface of rGO have an obvious influence on the electrical conductivity of the $MoSe_2$/ZnO/rGO nanocomposite sensor [46]. Therefore, there is a great contribution of rGO in enhancing the ethanol gas sensing performance of the ternary $MoSe_2$/ZnO/rGO nanocomposite sensor.

Thus, we conclude that the as-fabricated ternary nanocomposite sensing device is capable of detecting ethanol gas at low concentration (1 ppm) with high sensitivity, good selectivity, long-term stability, fast adsorption and desorption, and stable repeatability.

4.4 Conclusions

In conclusion, a highly stable, exceptionally selective, and reliably repeatable ethanol gas sensing device was successfully developed using the ternary $MoSe_2$/ZnO/rGO nanocomposite, promising long-term stability. Importantly, the ternary nanocomposite sensing device exhibited a fantabulous sensing response of 50.2 to 500 ppm ethanol gas. The ternary nanocomposite sensing device can detect ethanol down to 1 ppm at RT. The developed ternary nanocomposite sensing device exhibited a considerably fast response time (6.2 s) and recovery time (12.9 s) to 500 ppm ethanol gas. Besides, the sensing device also established prolific long-term stability of 42 days. The superior performance of the developed ternary nanocomposite sensing device is owed to the formation of a p-n heterojunction between $MoSe_2$ nanosheets and ZnO nanorods with the aid of rGO nanosheets. The attachment of the $MoSe_2$ nanosheets and ZnO nanorods onto rGO nanosheets not only provides various p-n heterojunctions but also offers more active sites for the adsorption and desorption of ethanol molecules. This improved the gas-sensing response of the sensing device toward ethanol significantly. In addition to this, the conductive network of rGO nanosheets facilitates fast electron transfer between $MoSe_2$ nanosheets and ZnO nanorods, endowing the ternary nanocomposite sensing device with quick response and recovery time. The result provides a facile and effective approach for developing a ternary nanocomposite for the fabrication of ethanol gas sensing devices with enhanced properties.

References

[1] J. Hu, W. Guan, X. Xiong, Y. Chen, and H. Long, "Modulation of rGO-Co3O4 heterojunction with multi-walled carbon nanotubes for efficient ethanol detection," *Sensors and Actuators B: Chemical,* vol. 368, p. 132202, 2022.

[2] X. Wang, Y. Gao, Q. Zhang, X. He, and X. Wang, "Synthesis of MoO3 (1D)@ SnO2 (2D) core-shell heterostructures for enhanced ethanol gas sensing performance," *Sensors and Actuators B: Chemical,* vol. 382, p. 133484, 2023.

[3] N. Jain and N. K. Puri, "Zinc oxide incorporated molybdenum diselenide nanosheets for chemiresistive detection of ethanol gas," *Journal of Alloys and Compounds,* vol. 955, p. 170178, 2023.

[4] P. Tiwary, S. Chatterjee, S. Singha, R. Mahapatra, and A. K. Chakraborty, "Room temperature ethanol sensing by chemically reduced graphene oxide film," *FlatChem,* vol. 30, p. 100317, 2021.

[5] W. Yan *et al.*, "Chemical surface adsorption and trace detection of alcohol gas in graphene oxide-based acid-etched SnO2 aerogels," *ACS Applied Materials & Interfaces,* vol. 13, no. 17, pp. 20467-20478, 2021.

[6] M. J. Ahemad, T. D. Le, D.-S. Kim, and Y.-T. Yu, "Bimetallic AgAualloy@ ZnO core-shell nanoparticles for ultra-high detection of ethanol: Potential impact of alloy composition on sensing performance," *Sensors and Actuators B: Chemical,* vol. 359, p. 131595, 2022.

[7] H. Fan, X. Zheng, Q. Shen, W. Wang, and W. Dong, "Hydrothermal synthesis and their ethanol gas sensing performance of 3-dimensional hierarchical nano Pt/SnO2," *Journal of Alloys and Compounds,* vol. 909, p. 164693, 2022.

[8] S. K. Rao, S. M. Kamath, E. M. Abhinav, B. Renganathan, K. Jeyadheepan, and C. Gopalakrishnan, "Unraveling the potential of Gd doping on mullite Bi2Fe4O9 for fiber optic ethanol gas detection at room temperature," *Materials Chemistry and Physics,* vol. 278, p. 125646, 2022.

[9] N. Roy *et al.*, "Paper based enzymatic chemiresistor for POC detection of ethanol in human breath," *IEEE Sensors Journal,* vol. 20, no. 5, pp. 2278-2286, 2019.

[10] X. Wang, S. Wang, J. Tian, H. Cui, and X. Wang, "Synthesis of 1D SnO2 nanorods/2D NiO porous nanosheets pn heterostructures for enhanced ethanol gas sensing performance," *Vacuum,* vol. 205, p. 111399, 2022.

[11] P. Cao *et al.*, "Preparation and characterization of a novel ethanol gas sensor based on FeYO3 microspheres by using orange peels as bio-templates," *Vacuum,* vol. 177, p. 109359, 2020.

[12] S. Zhang, P. Song, Y. Zheng, Y. Ding, and Q. Wang, "MoO2/MoO3/MXene ternary nanocomposites for high-performance ethanol detection at room temperature," *Journal of Alloys and Compounds,* vol. 925, p. 166663, 2022.

[13] G. Jeevanandham, K. Vediappan, Z. A. ALOthman, T. Altalhi, and A. K. Sundramoorthy, "Fabrication of 2D-MoSe2 incorporated NiO Nanorods modified electrode for selective detection of glucose in serum samples," *Scientific reports,* vol. 11, no. 1, p. 13266, 2021.

[14] T. Li, S. Yu, Q. Li, M. Chi, and P. Li, "Room temperature ethanol gas-sensing properties based on Ag-doped MoSe 2 nanoflowers: experimental and DFT investigation," *New Journal of Chemistry,* vol. 45, no. 45, pp. 21423-21428, 2021.

[15] C. Anichini, W. Czepa, D. Pakulski, A. Aliprandi, A. Ciesielski, and P. Samorì, "Chemical sensing with 2D materials," *Chemical Society Reviews,* vol. 47, no. 13, pp. 4860-4908, 2018.

[16] M. A. Al-Tahan *et al.*, "Modulating of MoSe2 functional plane via doping-defect engineering strategy for the development of conductive and electrocatalytic mediators in Li-S batteries," *Journal of Energy Chemistry,* vol. 75, pp. 512-523, 2022.

[17] Z. Yao, C. Yu, H. Dai, J. Zhou, X. Liu, and G. Sun, "Hybrid fibers assembled from MoSe2/graphene heterostructures endow improved supercapacitive performance," *Carbon,* vol. 187, pp. 165-172, 2022.

[18] S. Zhang, T. H. Nguyen, W. Zhang, Y. Park, and W. Yang, "Correlation between lateral size and gas sensing performance of MoSe2 nanosheets," *Applied Physics Letters,* vol. 111, no. 16, 2017.

[19] Z. Yang, D. Zhang, and D. Wang, "Carbon monoxide gas sensing properties of metal-organic frameworks-derived tin dioxide nanoparticles/molybdenum

diselenide nanoflowers," *Sensors and Actuators B: Chemical,* vol. 304, p. 127369, 2020.

[20] S. Singh, J. Deb, U. Sarkar, and S. Sharma, "MoSe2 crystalline nanosheets for room-temperature ammonia sensing," *ACS Applied Nano Materials,* vol. 3, no. 9, pp. 9375-9384, 2020.

[21] S. Zhang, W. Zhang, T. H. Nguyen, J. Jian, and W. Yang, "Synthesis of molybdenum diselenide nanosheets and its ethanol-sensing mechanism," *Materials Chemistry and Physics,* vol. 222, pp. 139-146, 2019.

[22] R. K. Jha, J. V. D'Costa, N. Sakhuja, and N. Bhat, "MoSe2 nanoflakes based chemiresistive sensors for ppb-level hydrogen sulfide gas detection," *Sensors and Actuators B: Chemical,* vol. 297, p. 126687, 2019.

[23] W. Pan, Y. Zhang, S. Yu, X. Liu, and D. Zhang, "Hydrogen sulfide gas sensing properties of metal organic framework-derived α-Fe2O3 hollow nanospheres decorated with MoSe2 nanoflowers," *Sensors and Actuators B: Chemical,* vol. 344, p. 130221, 2021.

[24] Y. Ding *et al.*, "Hollow Cu2O nanospheres loaded with MoS2/reduced graphene oxide nanosheets for ppb-level NO2 detection at room temperature," *Journal of Hazardous Materials,* vol. 416, p. 126218, 2021.

[25] Z. Yuan, Y. Liu, J. Zhang, F. Meng, and H. Zhang, "Rose-like MoO_3/MoS_2/rGO low-temperature ammonia sensors based on multigas detection methods," *IEEE Transactions on Instrumentation and Measurement,* vol. 70, pp. 1-9, 2021.

[26] J. Liu *et al.*, "Mo2C/MoO3@ rGO Ternary Nanocomposites as High-Performance Gas Sensor for Trace NH3 Detection at Room Temperature," *ACS Applied Electronic Materials,* vol. 5, no. 9, pp. 5061-5073, 2023.

[27] G. Li *et al.*, "Detection of ppm-level H2 via rGO-SnO2-ZnO nanocomposites: Considering compositional matching in designing heterostructured gas-sensing materials," *Sensors and Actuators B: Chemical,* vol. 396, p. 134560, 2023.

[28] K. Arora, S. Srivastava, P. R. Solanki, and N. K. Puri, "Electrochemical hydrogen gas sensing employing palladium oxide/reduced graphene oxide (PdO-rGO) nanocomposites," *IEEE Sensors Journal,* vol. 19, no. 18, pp. 8262-8271, 2019.

[29] A. Choudhari, B. A. Bhanvase, V. K. Saharan, P. H. Salame, and Y. Hunge, "Sonochemical preparation and characterization of rGO/SnO2 nanocomposite: Electrochemical and gas sensing performance," *Ceramics International,* vol. 46, no. 8, pp. 11290-11296, 2020.

[30] F. Meng, Z. Yang, Z. Yuan, H. Zhang, and H. Zhu, "Hydrothermal synthesis of CuO/rGO nanosheets for enhanced gas sensing properties of ethanol," *Ceramics International,* vol. 49, no. 4, pp. 5595-5603, 2023.

[31] L. T. Duy *et al.*, "High performance three-dimensional chemical sensor platform using reduced graphene oxide formed on high aspect-ratio micro-pillars," *Advanced Functional Materials,* vol. 25, no. 6, pp. 883-890, 2015.

[32] R. Gao *et al.,* "The controllable assembly of the heterojunction interface of the ZnO@ rGO for enhancing the sensing performance of NO2 at room temperature and sensing mechanism," *Sensors and Actuators B: Chemical,* vol. 342, p. 130073, 2021.

[33] Y. Yang, S. Li, W. Yang, W. Yuan, J. Xu, and Y. Jiang, "In situ polymerization deposition of porous conducting polymer on reduced graphene oxide for gas sensor," *ACS applied materials & interfaces,* vol. 6, no. 16, pp. 13807-13814, 2014.

[34] W. S. Hummers Jr and R. E. Offeman, "Preparation of graphitic oxide," *Journal of the american chemical society,* vol. 80, no. 6, pp. 1339-1339, 1958.

[35] N. Jain, S. Sharma, and N. K. Puri, "Investigation of charge transport mechanism in hydrothermally synthesized reduced graphene oxide (rGO) incorporated zinc oxide (ZnO) nanocomposite films," *Journal of Materials Science: Materials in Electronics,* vol. 33, pp. 1307-1323, 2022.

[36] R. Khatri and N. K. Puri, "Electrochemical biosensor utilizing dual-mode output for detection of lung cancer biomarker based on reduced graphene oxide-modified reduced-molybdenum disulfide multi-layered nanosheets," *Journal of Materials Research,* vol. 37, no. 8, pp. 1451-1463, 2022.

[37] R. Khatri and N. K. Puri, "Electrochemical studies of biofunctionalized MoS 2 matrix for highly stable immobilization of antibodies and detection of lung cancer protein biomarker," *New Journal of Chemistry,* vol. 46, no. 16, pp. 7477-7489, 2022.

[38] Q. Chen *et al.*, "Optimization ethanol detection performance manifested by gas sensor based on In2O3/ZnS rough microspheres," *Sensors and Actuators B: Chemical,* vol. 264, pp. 263-278, 2018.

[39] J. Zhang, T. Li, J. Guo, Y. Hu, and D. Zhang, "Two-step hydrothermal fabrication of CeO2-loaded MoS2 nanoflowers for ethanol gas sensing application," *Applied Surface Science,* vol. 568, p. 150942, 2021.

[40] H. R. Inta, S. Ghosh, A. Mondal, G. Tudu, H. V. Koppisetti, and V. Mahalingam, "Ni0. 85Se/MoSe2 interfacial structure: an efficient electrocatalyst for alkaline hydrogen evolution reaction," *ACS Applied Energy Materials,* vol. 4, no. 3, pp. 2828-2837, 2021.

[41] Y. Navale, S. Navale, M. Chougule, N. Ramgir, and V. Patil, "NO 2 gas sensing properties of heterostructural CuO nanoparticles/ZnO nanorods," *Journal of Materials Science: Materials in Electronics,* vol. 32, pp. 18178-18191, 2021.

[42] J. Zhang, J. Wu, X. Wang, D. Zeng, and C. Xie, "Enhancing room-temperature NO2 sensing properties via forming heterojunction for NiO-rGO composited with SnO2 nanoplates," *Sensors and Actuators B: Chemical,* vol. 243, pp. 1010-1019, 2017.

[43] Y. Huang, Y.-E. Miao, J. Fu, S. Mo, C. Wei, and T. Liu, "Perpendicularly oriented few-layer MoSe 2 on SnO 2 nanotubes for efficient hydrogen evolution reaction," *Journal of Materials Chemistry A,* vol. 3, no. 31, pp. 16263-16271, 2015.

[44] C. Xu, X. Wang, J. Zhu, X. Yang, and L. Lu, "Deposition of Co 3 O 4 nanoparticles onto exfoliated graphite oxide sheets," *Journal of Materials Chemistry,* vol. 18, no. 46, pp. 5625-5629, 2008.

[45] S. Chen, J. Zhu, X. Wu, Q. Han, and X. Wang, "Graphene oxide− MnO2 nanocomposites for supercapacitors," *ACS nano,* vol. 4, no. 5, pp. 2822-2830, 2010.

[46] C. Wang *et al.*, "Reduced graphene oxide decorated with CuO–ZnO hetero-junctions: towards high selective gas-sensing property to acetone," *Journal of Materials Chemistry A,* vol. 2, no. 43, pp. 18635-18643, 2014.

[47] X. T. Tran, S. Poorahong, and M. Siaj, "One-pot hydrothermal synthesis and selective etching method of a porous MoSe 2 sand rose-like structure for electrocatalytic hydrogen evolution reaction," *RSC advances,* vol. 7, no. 82, pp. 52345-52351, 2017.

[48] S. Rana, V. Singh, and B. Singh, "Tailoring the Output Performance of PVDF-Based Piezo–Tribo Hybridized Nanogenerators via B, N-Codoped Reduced Graphene Oxide," *ACS Applied Electronic Materials,* vol. 4, no. 12, pp. 5893-5904, 2022.

[49] K. Komal, G. Gupta, M. Singh, and B. Singh, "Improved resistive switching of RGO and SnO2 based resistive memory device for non-volatile memory application," *Journal of Alloys and Compounds,* vol. 923, p. 166196, 2022.

[50] M. S. Vidhya, R. Yuvakkumar, P. S. Kumar, G. Ravi, and D. Velauthapillai, "Hydrothermal Synthesis of Flower Like MnSe 2@ MoSe 2 Electrode for Supercapacitor Applications," *Topics in Catalysis,* pp. 1-8, 2021.

[51] A. Mishra, J. Narang, C. S. Pundir, R. Pilloton, and M. Khanuja, "Morphology-preferable MoSe2 nanobrooms as a sensing platform for highly selective apta-capturing of salmonella bacteria," *ACS omega,* vol. 3, no. 10, pp. 13020-13027, 2018.

[52] M. E. Uddin, R. K. Layek, N. H. Kim, D. Hui, and J. H. Lee, "Preparation and properties of reduced graphene oxide/polyacrylonitrile nanocomposites using polyvinyl phenol," *Composites Part B: Engineering,* vol. 80, pp. 238-245, 2015.

[53] S. Kumar, V. Sharma, K. Bhattacharyya, and V. Krishnan, "Synergetic effect of MoS 2–RGO doping to enhance the photocatalytic performance of ZnO nanoparticles," *New Journal of Chemistry,* vol. 40, no. 6, pp. 5185-5197, 2016.

[54] C. Qin, Y. Wang, Y. Gong, Z. Zhang, and J. Cao, "CuO-ZnO hetero-junctions decorated graphitic carbon nitride hybrid nanocomposite: hydrothermal synthesis and ethanol gas sensing application," *Journal of Alloys and Compounds,* vol. 770, pp. 972-980, 2019.

[55] P. Cao *et al.*, "Ethanol sensing behavior of Pd-nanoparticles decorated ZnO-nanorod based chemiresistive gas sensors," *Sensors and Actuators B: Chemical,* vol. 298, p. 126850, 2019.

[56] S. Singh and S. Sharma, "Temperature dependent selective detection of ethanol and methanol using MoS2/TiO2 composite," *Sensors and Actuators B: Chemical,* vol. 350, p. 130798, 2022.

[57] Y. Zhang, Z. Dong, and H. Jia, "Preparation of ZnO nanorod-based gas sensor and its ethanol gas sensing performance," *Bulletin of Materials Science,* vol. 46, no. 3, p. 180, 2023.

[58] R. Kalidoss, S. Umapathy, and Y. Sivalingam, "An investigation of GO-SnO2-TiO2 ternary nanocomposite for the detection of acetone in diabetes mellitus patient’s breath," *Applied Surface Science,* vol. 449, pp. 677-684, 2018.

[59] R. Kumar and R. Ghosh, "Selective determination of ammonia, ethanol and acetone by reduced graphene oxide based gas sensors at room temperature," *Sensing and Bio-Sensing Research,* vol. 28, p. 100336, 2020.

[60] Y. Luo, D. Zhang, and X. Fan, "Hydrothermal Fabrication of Ag-Decorated $MoSe_2$/Reduced Graphene Oxide Ternary Hybrid for H_2S Gas Sensing," *IEEE Sensors Journal,* vol. 20, no. 22, pp. 13262-13268, 2020.

[61] S. Sen and S. Kundu, "Reduced graphene oxide (rGO) decorated ZnO-SnO2: A ternary nanocomposite towards improved low concentration VOC sensing performance," *Journal of Alloys and Compounds,* vol. 881, p. 160406, 2021.

CHAPTER 5

First Report on Hydroelectric Cell-Driven Gas Sensor for the Detection of Ethanol at Room Temperature: A Novel Approach

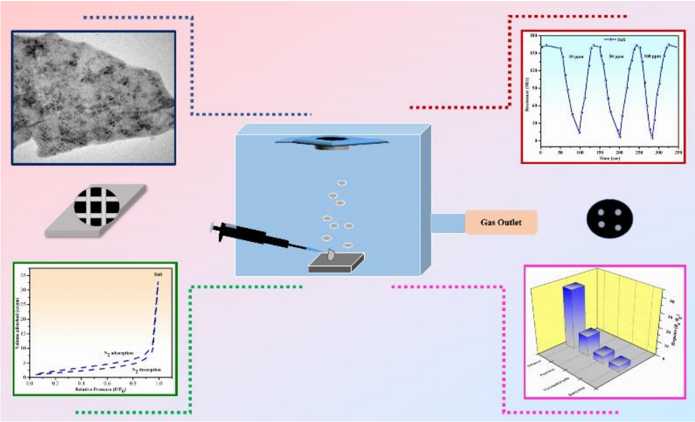

A novel self-powered ethanol gas sensor, exhibiting excellent selectivity, sensitivity, and stability, has been developed based on n-type SnS nanoflakes at room temperature. The n-type SnS-based HEC serves as the power source for self-powered ethanol gas sensors, enabling the detection of various concentrations of ethanol gas at RT. Consequently, the power supply and gas sensor have been effectively combined into a single device, demonstrating a successful integration of both functionalities. X-ray diffraction (XRD), field emission scanning electron microscopy (FESEM), high-resolution transmission electron microscopy (HRTEM), Energy dispersive X-ray (EDX) and Brunauer-Emmett-Teller (BET) analysis have confirmed the formation of orthorhombic SnS nanoflakes with a high specific surface area (6.15 m^2 g^{-1}). The observed voltage-current (V-I) characteristic curves of the HEC at RT have shown a maximum current (I_{max}) of 40 μA and voltage of 1.03 V. The sensing performance of the self-powered ethanol gas sensor has been analysed for various concentrations of ethanol gas (10 - 100 ppm). The sensor has exhibited a response value (R_a/R_g) of 41.3 to 100 ppm ethanol gas concentration, with quick response/recovery times of 27.3 s/31.4 s respectively at RT. The sensor has shown promising potential for prolonged ethanol gas detection. The experimental results demonstrate that the n-type SnS-based self-powered ethanol gas sensor is a promising platform for integration into future large-scale IoT systems. This breakthrough paves the way for more versatile and scalable IoT solutions, enabling continuous environmental monitoring and data collection across various settings.

5.1 Introduction

The widespread implementation of Internet of Things (IoT) technology has led to a growing need for reliable gas sensor networks across diverse applications such as air pollution monitoring, industrial safety, smart cities, and personal healthcare [1, 2]. However, the scale of these networks demands sensors with specific attributes: they must be micro- or nanosized, exhibit reliable selectivity, have shorter response times, and consume significantly less power than existing commercial devices [3]. Traditional battery-powered sensors rely on integrated batteries for power, which poses several limitations. Firstly, these batteries have finite energy storage capacities and require regular replacement, leading to maintenance challenges and high costs, especially in remote or inaccessible environments [4]. Moreover, battery dependence introduces performance degradation in harsh conditions due to safety and stability concerns [5]. This reliance on integrated batteries not only limits the sensor's performance but also escalates operational costs and maintenance efforts, particularly in remote or inaccessible areas [6, 7]. Additionally, batteries pose safety and stability risks in harsh environments, further compromising sensor performance. To overcome these challenges, the development of self-powered gas sensing systems has emerged as a promising solution [8, 9].

Notable technologies like thermoelectric generators, solar generators, triboelectric nanogenerators, and piezoelectric generators have been explored for developing integrated, miniaturized, and self-powered gas sensors [10-13]. In recent times, considerable attention has been directed towards a promising eco-friendly energy solution known as the hydroelectric cell (HEC) [14-16]. This innovative device has sparked widespread research interest due to its ability to generate green electricity through water splitting [17]. Extensive research has firmly established the hydroelectric cell (HEC) as a clean, portable, and highly efficient technology, offering cost-effective and eco-friendly benefits [18, 19]. Notably, it achieves water molecule splitting without relying on electrolytes, sunlight, or temperature adjustments, representing a significant advancement in sustainable energy solutions [20, 21]. Harnessing its numerous advantages, HECs present a novel opportunity to serve as a power source for gas sensors, paving the way for a groundbreaking self-powered sensing technology.

Ethanol, a common volatile organic compound (VOC), is extensively used in various food industries, agricultural production, chemical and pharmaceutical communities [22-24]. However, its prolonged exposure poses severe risks to human health, including nose and throat irritation, vomiting, kidney failure, nausea, headaches, and even potential carcinogenic effects [25, 26]. Moreover, as a flammable gas with an explosion range of 3.3 – 19%, ethanol contributes to numerous traffic accidents, while its vapor forms explosive mixtures when combined with other gases [27, 28]. Therefore, it is crucial to establish effective and timely monitoring and detection mechanisms for ethanol gas, particularly at RT.

In the field of gas sensing materials, researchers encounter significant challenges regarding sensitivity, selectivity, stability, and various other factors essential for creating highly efficient sensing devices [29]. As a result, there is a growing emphasis on developing innovative sensing materials capable of detecting volatile, toxic, and flammable gases. This development is critical to addressing major environmental challenges such as pollution, health risks, climate instability, and more [30, 31]. In recent years, tin sulfide (SnS) a two-dimensional (2D) metal chalcogenide (MCs) has attracted significant attention from researchers in fields such as sensor technology, photodetectors, solid-state batteries, photovoltaic cells, and holographic recording media [32]. It is a metal monochalcogenide semiconductor that is non-toxic, cheap, highly stable, widely available, and has a distinctive layered structure [33, 34]. It has an indirect bandgap, a high concentration of majority charge carriers, and a high Hall mobility [35, 36].

Experimental and theoretical studies have shown that the gas-sensing performance of 2D-based sensors is highly dependent on the presence of cation and anion vacancies [37]. Thus, controlling these vacancies is considered a crucial strategy for improving the low-temperature detection capabilities of 2D sensors. SnS naturally exhibits p-type properties due to an excess of sulfur atoms [38]. However, studies have shown that sulfur vacancies can induce n-type properties in SnS. Non-stoichiometry has been identified as an effective method for shifting the majority of carriers from holes to electrons in chalcogenides, accomplished by creating anion vacancies. Indeed, deficiency of sulfur has previously resulted in n-type behavior in SnS nanostructures [39].

In this study, an n-type SnS-based self-powered gas sensor has been designed for the detection of ethanol gas at RT. According to the available research, there has been no work conducted on self-powered ethanol gas sensors utilizing n-type SnS nanoflakes. XRD, FESEM, HRTEM, EDX, and BET analysis have confirmed the successful formation of SnS nanoflakes. The occurrence of redox reactions responsible for the generation of current and voltage in the HEC is verified by voltage-current (V-I) characteristics curves. The designed self-powered gas sensor has been tested for various ethanol gas concentrations ranging from 10 to 100 ppm. Comprehensive sensing assessments, including response evaluation, response time, recovery time, and selectivity indicate that the sensor exhibits high response at RT. In the concluding section of the paper, a thorough explanation of the working principle and sensing mechanism of the self-powered ethanol gas sensor based on n-type SnS nanoflakes has been provided.

5.2 Experimental section

5.2.1 Chemicals used in the synthesis

The chemicals essential for the synthesis included stannous chloride dihydrate ($SnCl_2.2H_2O$, 99%), citric acid ($C_6H_8O_7$, 99%), ethylene glycol ($C_6H_6O_2$, 99%), and thiourea (CH_4N_2S, 99%). All the chemicals belong to AR grade with the highest purity of 99%.

5.2.2 Synthesis of SnS nanoflakes

SnS nanoflakes were synthesised via a one-step hydrothermal process. Initially, 1.2 M citric acid solution was prepared in de-ionized water, 0.5 M stannous chloride dihydrate solution, and 1.5 M thiourea solution was prepared in ethylene glycol under continuous stirring for 30 min. Subsequently, the solution containing citric acid and thiourea was mixed with the stannous chloride dihydrate solution and stirred for an additional hour. The resulting solution was then transferred to a 100 ml stainless steel autoclave and placed in a hot air oven at 180 °C for 24 h. Following this, the precipitate was washed with DI water and ethanol, then dried overnight at 80 °C to obtain black-colored SnS powder.

5.2.3 Fabrication of self-powered ethanol gas sensor

The SnS powder so obtained was used to fabricate the self-powered gas sensor for the detection of ethanol gas. Firstly, a SnS-based hydroelectric cell (HEC) was fabricated which was utilised to power the SnS-based ethanol gas sensor. Then SnS gas sensor was fabricated for the detection of ethanol gas. For fabricating the HEC, the powder so obtained was processed in the form of a circular pellet of diameter 13 mm using a hydraulic press by applying pressure of 6 tons. The pellet was sintered in a muffle furnace at 320 °C for 2.5 h to induce sulphur defects, thereby shifting the behavior SnS from p-type to n-type. One face of the pellet was affixed with a zinc sheet serving as the anode, while the other face was coated with silver paste arranged in a comb pattern, acting as the inert cathode. Low-resistance wires were soldered to both electrodes to fabricate a SnS-based HEC. A similar process was used to fabricate the ethanol gas sensor as was used for fabricating the HEC, as mentioned above. In the final step, the thermal evaporation technique was employed to intricately generate silver (Ag) contacts on the as-prepared SnS-based ethanol gas sensor. This pellet was employed to conduct sensing measurements.

5.2.4 Gas sensing measurements

The gas-sensing performance of the self-powered ethanol gas sensor was evaluated in a custom-built glass chamber. The n-type SnS-based HEC was wire-bonded to the n-type SnS-based ethanol gas sensor to form a self-powered ethanol gas (SPEG) sensor. A voltage of 1.03 V produced from n-type SnS-based HEC was applied to the SPEG sensor during resistance measurements. The schematic illustration of the SPEG sensor driven by HEC is shown in Fig. 5.1. A known volume of each VOC was injected into the test chamber using a micropipette. Various VOC gases with different concentrations ranging from 10 – 100 ppm were generated by evaporating pure ethanol, acetone, isopropanol, and benzene on a small microheater located inside the glass chamber as shown in Fig. 5.1. The concentration in ppm was calculated using the following equation [24, 40]:

$$C = \frac{22.4 \times \rho \times T \times V_1}{273 \times M \times V_2} \times 1000 \tag{5.1}$$

where C is the concentration of different gases in ppm, ρ is the density of the liquid (g/ml), T is the temperature (K), V_1 is the volume of the evaporated liquid (μL), M is the molecular weight of the liquid (g/mol), and V_2 is the volume of the test chamber (L). The real-time output (resistance Vs time) signals of the SPEG sensor were measured using a digital multimeter connected to the SPEG sensor.

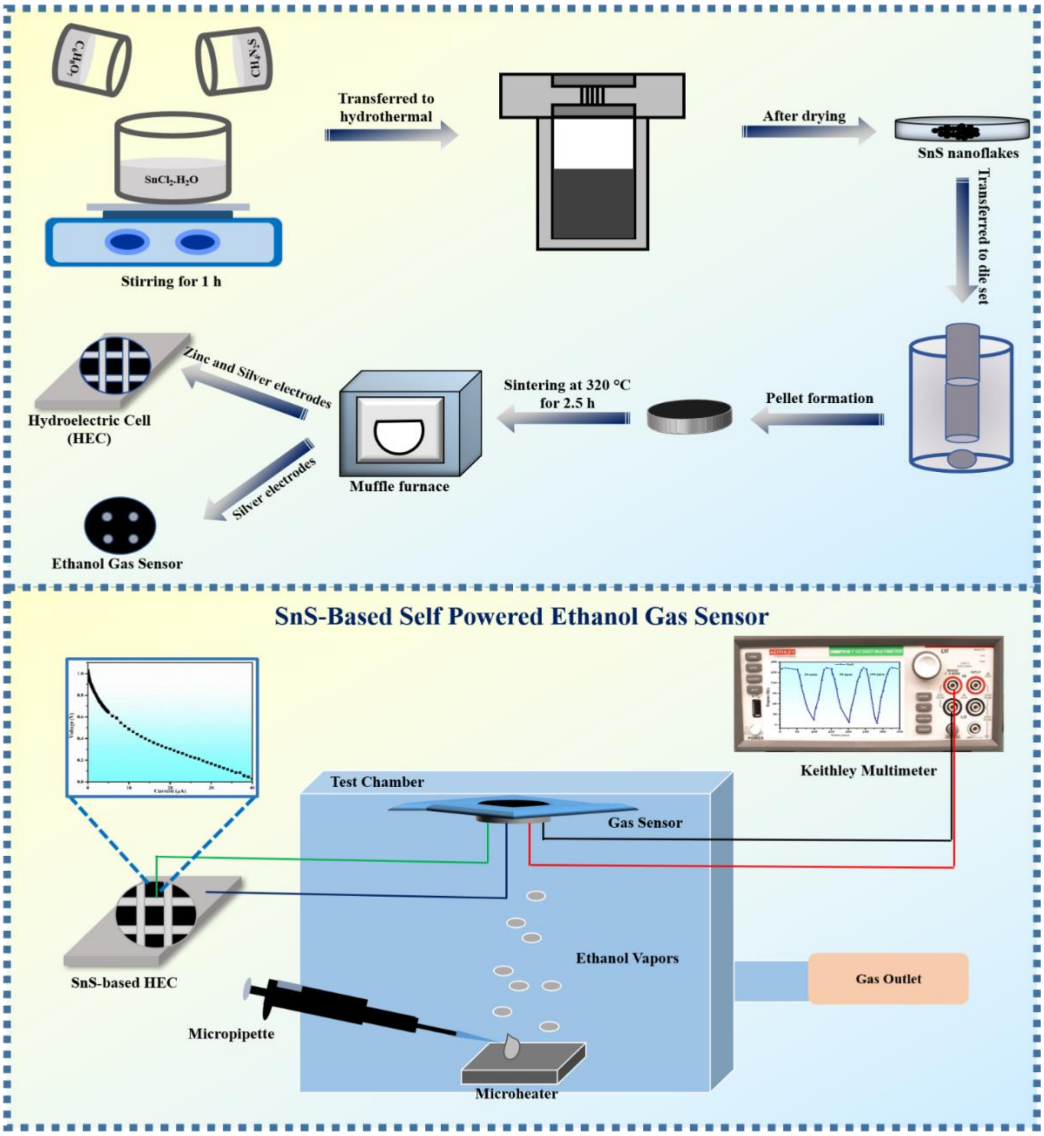

Fig. 5.1: Step-by-step preparation of n-type SnS-based self-powered ethanol gas sensor

5.3 Characterizations

The structural analysis of the SnS sample at RT was performed by X-ray diffractometer (XRD; Bruker D8 Advanced) using Cu (K_α) radiation ($\lambda = 0.154$ nm). The surface morphology and microstructure analysis was done using a field emission scanning electron microscope (FESEM; ZEISS) and high-resolution transmission electron microscopy (HRTEM; FEI Technai 200). The specific surface area was analysed using Brunauer-Emmett-Teller (BET; NOVA 2200e). The voltage-current (V-I) characteristics of the fabricated HEC were measured using a Keithley 2400 source meter. A Keithley digital multimeter (DMM7510) was used to measure the change in resistance of the sensor.

5.4 Results and discussions

5.4.1 Structural elucidation using XRD

Fig. 5.2 displays the XRD pattern of as-synthesised SnS within the 20° – 80° range. From the XRD pattern crystallinity studies (which include interplanar spacing and phase formation) of the as-synthesised sample is analysed.

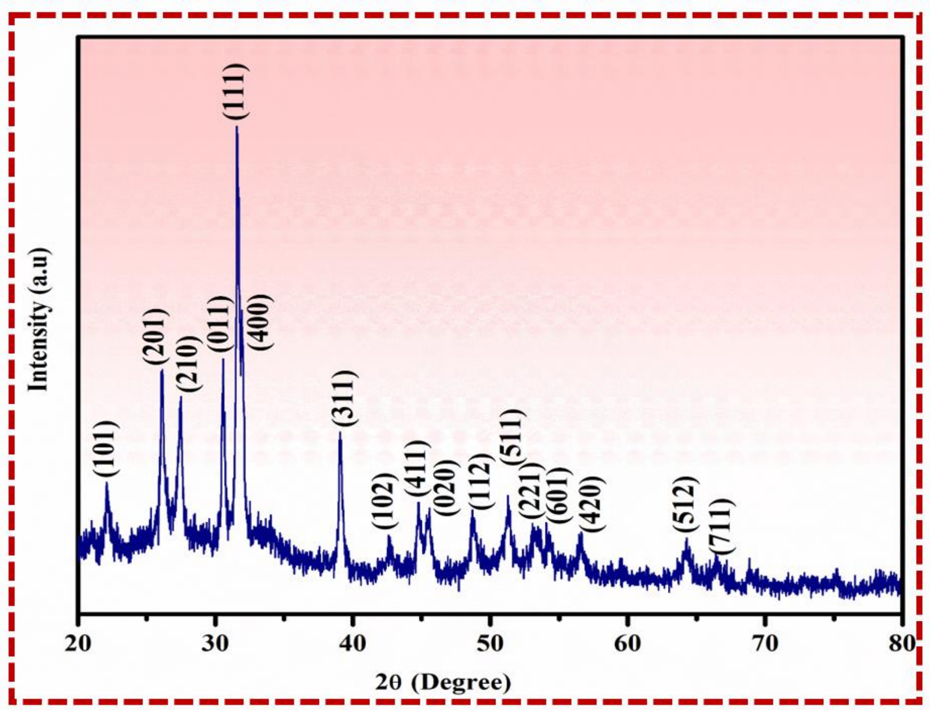

Fig. 5.2: XRD spectrum of as-synthesised SnS

The diffraction peaks observed in the XRD pattern of the as-synthesised SnS corresponds to the (101), (201), (210), (011), (111), (311), (102), (020), (112), (511), (221), (601), (420), (512), and (711) planes of the pure orthorhombic phase of SnS with the space group Pbnm (62) (JCPDS card no. 390-354) [41]. The interplanar spacing of the six highest intensity peaks was calculated using Bragg's relation: $n\lambda = 2d \sin\theta$, where 'n' represents an integer, and 'd' represents the spacing between crystal lattice planes [42]. Table 1. presents the calculated d-spacing values for various high-intensity planes of SnS.

Table 5.1: d-spacing values for various planes of as-synthesised SnS

Sample	**2θ (degree)**	**hkl planes**	**d spacing (nm)**
SnS	26.02	(201)	0.342
	27.40	(210)	0.325
	30.6	(011)	0.291
	31.5	(111)	0.283
	31.9	(400)	0.280
	39.08	(311)	0.230

5.4.2 Surface morphology and microstructure analysis using FESEM and HRTEM

Microstructure and surface morphology play very significant roles in gas-sensing applications [43]. The size and morphology of the as-prepared SnS were analysed by FESEM and HRTEM (Fig. 5.3 (a-c)). The as-prepared SnS exhibits a nanoflakes-like structure as shown in Fig. 5.3(a). The widths of the SnS nanoflakes vary from 100 nm to several micrometers, and their thickness ranges from 70 to 80 nm. Upon annealing at 320 °C, some of these sheet-like structures agglomerate, resulting in the formation of nanoparticles [44], as revealed by the HR-TEM images in Fig (5.3(b-c)). Several factors lead to the formation of SnS nanostructures in diverse forms such as circular structures, nanorods, and nanoflakes. These structural variations are influenced by temperature, the sintered process, alterations in the Sn/S ratio, and the introduction of dopants as evidenced by various studies [45, 46]. The stoichiometric composition of SnS nanoflakes (Sn: S = 76.14:23.86) is obtained by EDX as displayed in Fig. 5.3(d).

Stoichiometric ratios indicate that there are slight sulphur deficiencies in SnS nanoflakes.

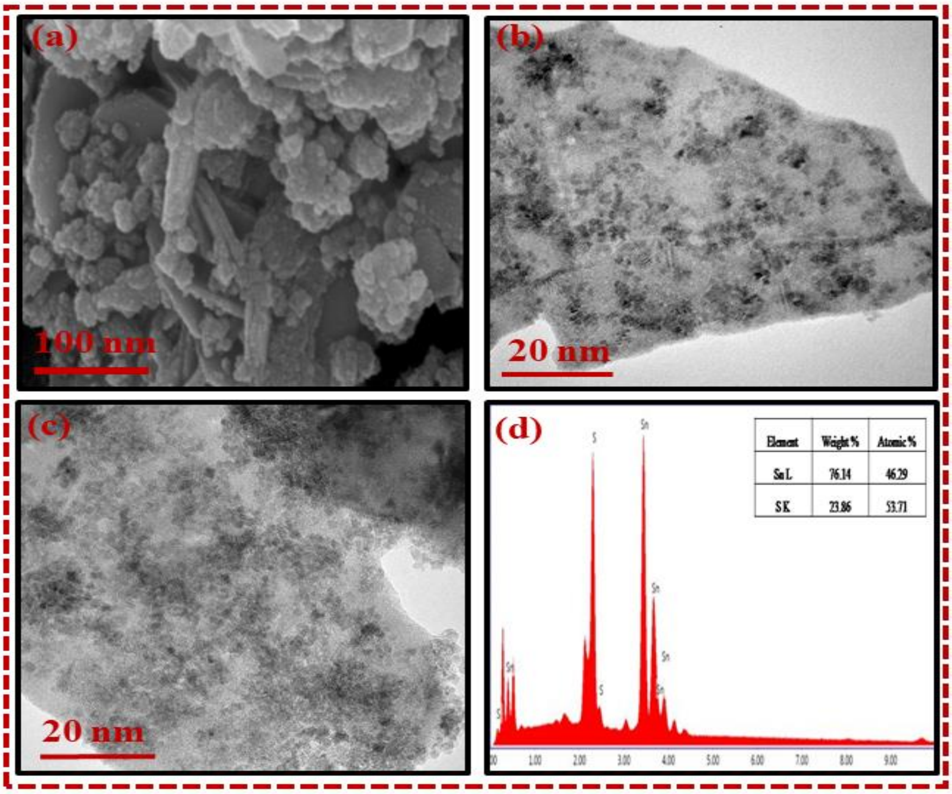

Element	Weight %	Atomic %
Sn L	76.14	46.29
S K	23.86	53.71

Fig. 5.3: (a) FESEM image, (b and c) HRTEM image, and (d) Corresponding EDX spectra of SnS nanoflakes

5.4.3 Surface area analysis using BET isotherm

In the context of gas sensor applications surface area and pore size are crucial parameters for enhancing sensor performance. To assess the specific surface area distribution in the as-prepared SnS, a Bruanauer-Emmett-Teller (BET) analysis was performed. Fig. 5.4(a) presents the nitrogen (N_2) adsorption-desorption isotherm and Barret-Joyner-Halenda (BJH) derived pore size distribution of SnS nanoflakes. The as-synthesised SnS exhibited type-IV isotherms with distinct hysteresis at P/P_o values ranging from 0.1 to 0.9, indicative of mesoporous structures [47]. As depicted in Fig. 5(b), the SnS displayed a wide range of pore sizes from 50-1050 Å. The analysis revealed that the SnS possesses a mesoporous structure with an average pore diameter of 16.8 nm, a pore volume of 4.5×10^{-2} cm^3g^{-1}, and a BET surface area of 6.15 m^2 g^{-1}.

This high porosity in the SnS is attributed to the removal of sulphur from specific sites, which created additional active sites for enhanced ethanol gas sensing.

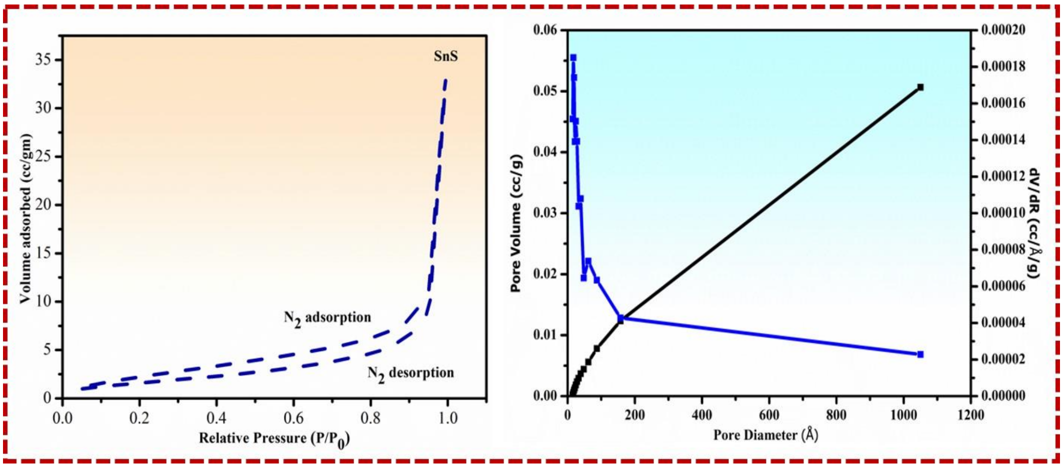

Fig. 5.4: (a) BET analysis: N_2 adsorption-desorption isotherm and (b) BJH pore size distribution of SnS

5.5 Ethanol gas sensing performance of the n-type SnS-based SPEG sensor

To investigate the gas sensing properties of the n-type SnS-based SPEG sensor, we tested ethanol response at different concentrations: 10 ppm, 50 ppm, and 100 ppm (Fig. 5.5). The response curve illustrates a clearly defined trend of increasing response with an increase in ethanol concentration. The following expression was utilised to calculate the sensing response of the device:

$$R = R_a/R_g \tag{5.2}$$

where R_a and R_g are the resistance of the n-type SnS-based SPEG sensor in air and ethanol environments respectively. Using equation 5.2, the sensor's response was calculated to be 14.9, 23.8, and 41.3 at ethanol gas concentrations of 10 ppm, 50 ppm, and 100 ppm, respectively. The resistance of the sensor swiftly returns to its initial value once the ethanol gas was completely removed from the chamber. Previous research has indicated that ethanol sensors utilizing 2D SnS nanostructures are effective primarily at high temperatures [32, 48, 49]. However, the current findings demonstrate that the n-type SnS-based SPEG sensor shows a significant response to ethanol gas even at RT.

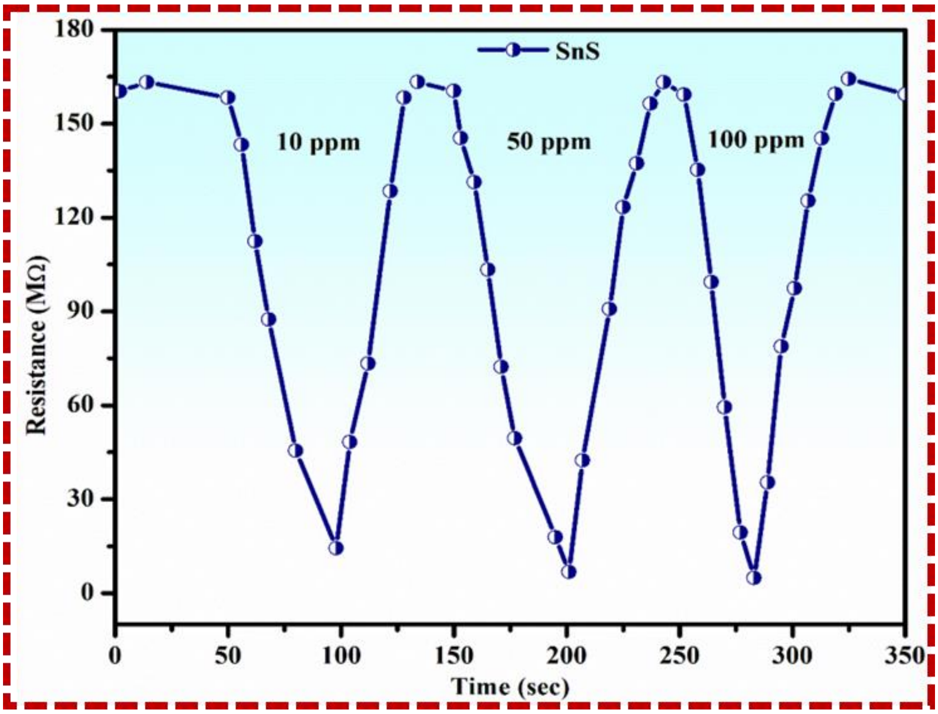

Fig. 5.5: Change in resistance of the n-type SnS-based SPEG sensor with various concentrations of ethanol gas

Fig. 5.6 elucidates three parameters that describe the sensor's properties: sensing response (R_a/R_g), response time (t_{resp}), and recovery time (t_{rec}). At first, it is evident that the resistance of the n-type SnS-based SPEG sensor decreases from a base resistance of R_a = 160.2 MΩ in air to R_g = 3.8 MΩ when the sensor is exposed to 100 ppm of ethanol gas. The resulting R_a and R_g values were used to calculate the sensing response of the sensor, yielding a value of 41.3 at 100 ppm ethanol gas. Moreover, the sensor exhibits a typical n-type gas sensing behavior, that is, a decreased resistance upon exposure to ethanol gas. The other two parameters of the sensor, t_{resp} and t_{rec}. The sensor’s response time (t_{resp}) was determined to be 38.7 s, 31.6 s, and 27.3 s for ethanol gas concentrations of 10 ppm, 50 ppm, and 100 ppm respectively as displayed in Fig. 5.6. The recovery time (t_{rec}) was calculated to be 21.1 s, 23.6 s, and 31.4 s for corresponding gas concentrations as displayed in Fig. 5.6. The shorter response time could be ascribed to the abundance of sites on the sensor’s surface, which facilitates efficient gas adsorption. Conversely, the extended recovery time may stem from the chemisorption of ethanol molecules and the subsequent desorption of their reaction products from the sensor’s surface, necessitating additional time.

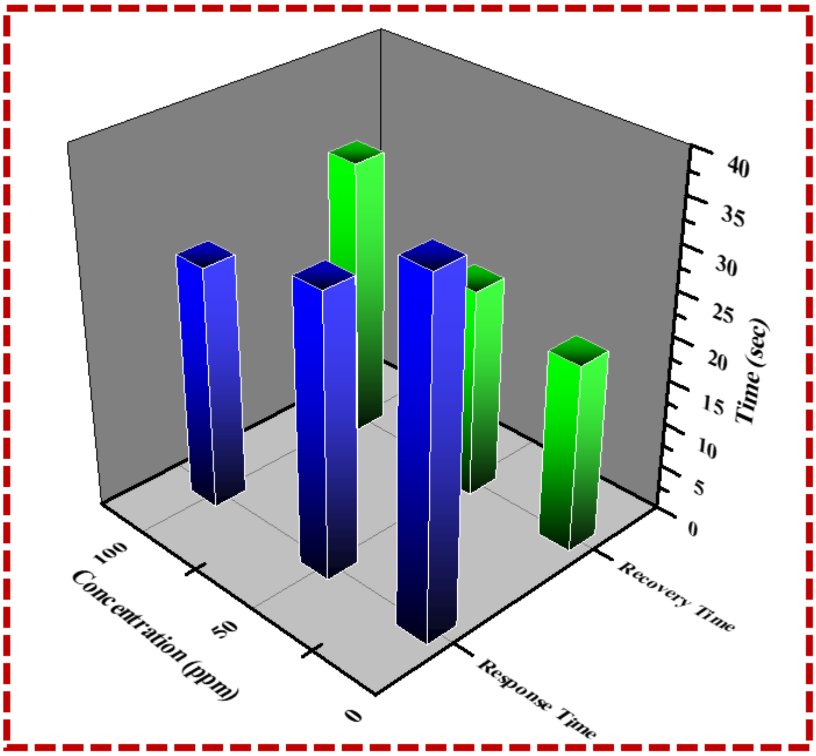

Fig. 5.6: The t_{resp} and t_{rec} characteristics of the n-type SnS-based SPEG sensor exposed to 100 ppm ethanol

For a gas sensor to be practical, it must exhibit reliable repeatability when subjected to the same concentration of the target gas. The repeatability of the SPEG sensor was assessed through three consecutive cycles with ethanol gas concentration of 10 ppm, 50 ppm, and 100 ppm RT, as depicted in Fig. 5.7(a), 5.7(b), and 5.7(c) respectively. It is observed that the resistance change of the SPEG sensor is consistently similar. This indicates the sensor's excellent repeatability, which is essential for practical applications.

A reliable sensor should have high selectivity to effectively identify its target gas while minimizing the impact of other VOCs. Analysing the sensor's cross-response entails comprehensive testing with various volatile organic compounds (VOCs), including benzene, isopropyl alcohol, and acetone, to evaluate its ability to selectively detect specific gases across diverse environments. The data presented in Fig. 5.8(a) vividly demonstrated the sensor's exceptional selectivity. Notably, the n-type SnS-based SPEG sensor demonstrates a substantial response of approximately 41.3 at a concentration of 100 ppm ethanol gas. The response of the sensor towards other

VOCs like benzene, formaldehyde, and acetone was notably low and is measured to be 3.8, 5.2, and 13.7, respectively. Hence, it is concluded that the as-fabricated sensor shows high selectivity towards ethanol gas.

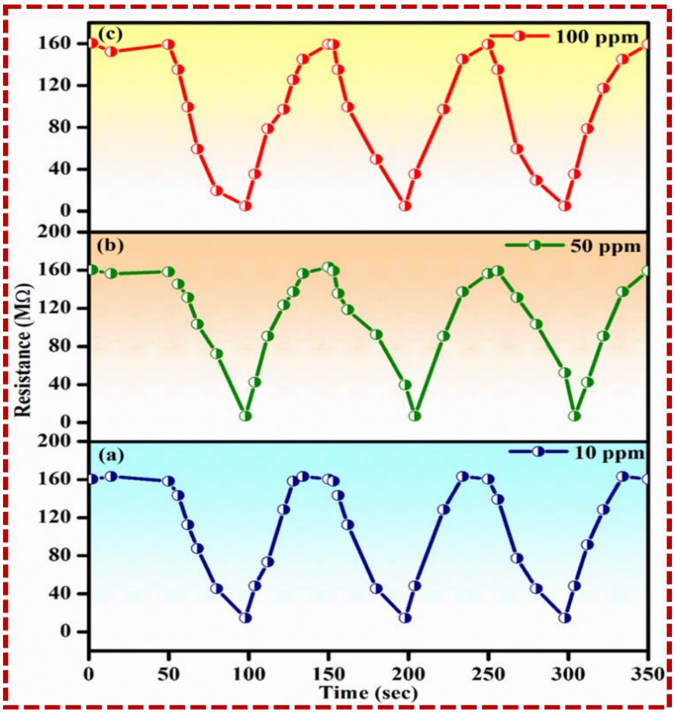

Fig. 5.7: (a), (b), and (c) Repeatability of the n-type SnS-based SPEG sensor toward 10 ppm, 50 ppm, and 100 ppm ethanol gas

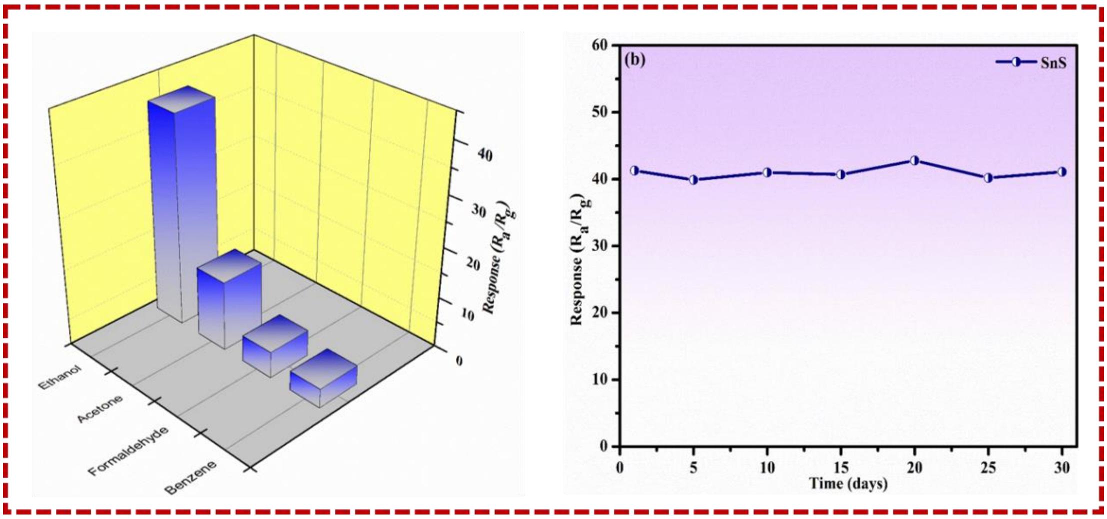

Fig. 5.8: (a) The cross-responses of the n-type SnS-based SPEG sensor towards 100 ppm ethanol gas and other VOCs, and (b) Long-term stability of response (30 days) towards 100 ppm of ethanol gas

To assess the prolonged stability of the n-type SnS-based SPEG sensor, its response to 100 ppm ethanol gas is observed over 30 days. The measurements were taken at regular 5-day intervals. As depicted in Fig. 5.8(b), the response of the sensor shows consistent behavior over 30 days, indicating its high stability. This implies that the sensor holds substantial promise for effectively detecting ethanol gas over a long period at RT.

5.6 Self-powered ethanol gas sensing mechanism

Understanding the gas sensing mechanism of the HEC-driven self-powered ethanol gas sensor based on n-type SnS nanoflakes requires a comprehension of the water dissociation process using HEC.

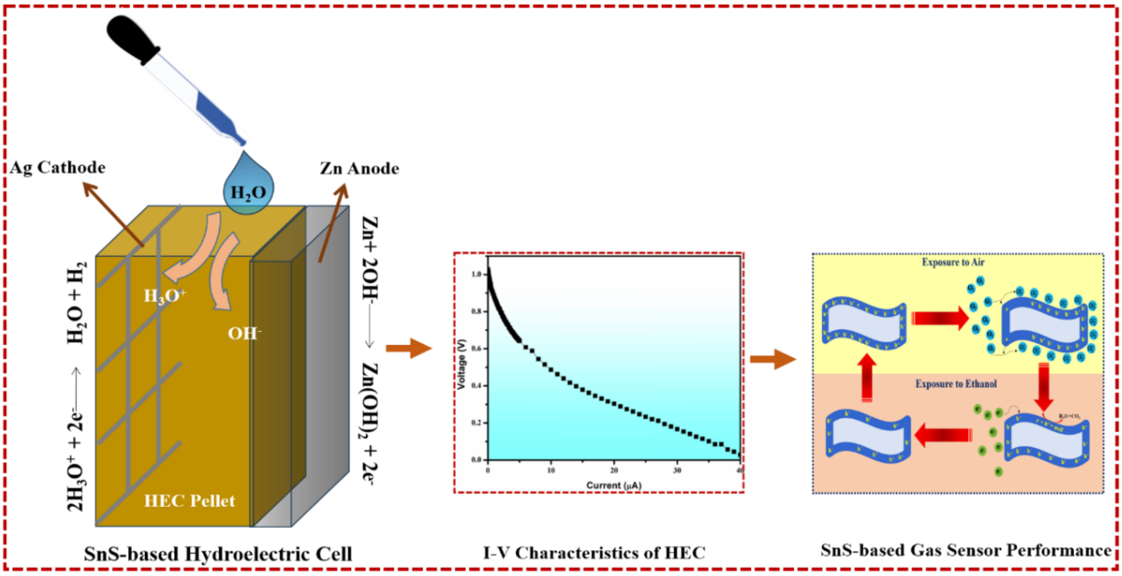

Fig. 5.9: Ethanol sensing mechanism for n-type SnS-based SPEG sensor

When water is dropped on the n-type SnS-based HEC, the water molecules dissociate into OH^- and H_3O^+ ions. The dissociated hydroxide and hydronium ions diffuse through the cell and migrate toward their respective electrodes. At the zinc electrode (anode), hydroxide ions react to form zinc hydroxide and release electrons. These electrons migrate through an external circuit to the silver electrode (cathode) [14]. Simultaneously, hydronium ions diffuse toward the silver electrode and produce hydrogen gas. This facilitates electricity generation through redox reactions at a zinc anode and a silver-inert cathode. The n-type SnS-based HEC delivers an offload current of 40 μA and a potential produced of 1.03 V (as shown in Fig. 5.9) which drives the n-type SnS-based SPEG sensor.

The following electrochemical half-reactions (equation 5.3 – 5.5) take place on the n-type SnS-based HEC surface and its electrodes.

At the surface of n-type SnS-based HEC

$$4H_2O \longrightarrow 2H_3O^+ + OH^- \qquad (5.3)$$

At the anode (At the zinc electrode)

$$Zn + 2OH^- \longrightarrow Zn(OH)_2 + 2e^- \; E_{oxd} = -0.76V \qquad (5.4)$$

At the cathode (At the silver electrode)

$$2H_3O^+ + 2e^- \longrightarrow H_2(g) + 2H_2O \;\; E_{red} = +0.22V \qquad (5.5)$$

The gas-sensing mechanism of the sensor is based on the change in resistance due to the adsorption and desorption of ethanol molecules on the surface of the sensing material [50]. From the response curves (Fig. 5.5), the n-type SnS-based SPEG sensor exhibits a typical n-type characteristic response when exposed to ethanol gas. In the presence of air, the sensor adsorbs oxygen molecules, which undergo partial ionization at RT, transforming into O_2^- ions by acquiring electrons from the valence band of the n-type SnS nanoflakes as described in equation 5.6 and 5.7:

$$O_2\,(gas) \rightarrow O_2\,(ads) \qquad (5.6)$$

$$2O_2\,(ads) + 2e^- \leftrightarrow 2O_2^-\,(ads)$$

(5.7)

The removal of these electrons from the valence band alters the surface charge of the n-type SnS nanoflakes, creating an electron depletion layer. Additionally, a negative charge layer of O_2^- ions form across the n-type SnS-based SPEG sensor surface. As a result, the overall resistance of the sensor increases until it stabilizes. Upon exposure to ethanol gas, the ethanol molecules react with the surface oxygen ions, releasing electrons and causing electron-hole annihilation, as shown in equation 5.8. This reaction increases the electron concentration, thereby decreasing the resistance of the n-type SnS-based SPEG sensor.

$$2C_2H_5OH + 6O_2^- \text{ (ads)} \rightarrow 4CO_2 + 6H_2O + 6e^- \qquad (5.8)$$

The results confirm the superior performance of the n-type SnS-based SPEG sensor for ethanol gas detection. The sensor exhibits a high response of 41.3 to 100 ppm ethanol gas and achieves complete recovery at RT. This enhancement is attributed to the unique surface morphology and sulphur defects present on the surface of the as-fabricated sensor which offers numerous adsorption sites for ethanol molecules. This morphology significantly reduces response/recovery times to 27.3 s/31.4 s to 100 ppm ethanol gas in addition to enhancing the overall ethanol gas sensing response.

5.7 Conclusions

In summary, a novel self-powered ethanol gas (SPEG) sensor was successfully developed using the SnS nanoflakes with high sensitivity, selectivity, and stability. The hydroelectric cell (HEC) was fabricated to power the gas sensor and make it capable of actively detecting ethanol gas at RT. Redox reactions in the HEC were verified through voltage-current (V-I) characteristic curves, which indicate a maximum current (Imax) of 40 μA and a voltage of 1.03 V. The SPEG sensor displayed a notable response of 41.3 and a swift response/recovery time of 27.3/31.4 sec when exposed to 100 ppm ethanol gas at RT. The sensor demonstrated an n-type characteristic response and can detect ethanol gas down to 10 ppm at RT. Besides, the sensor showed excellent repeatability for three consecutive cycles. The developed sensor demonstrates exceptional long-term stability of 30 days. The enhancement was attributed to the unique surface morphology and sulfur defects on the as-fabricated sensor, which provided numerous adsorption sites for ethanol molecules. These findings represented a promising step forward in the development of a next-generation self-powered sensing network for the Internet of Things (IoTs).

References

[1] S. Wei *et al.*, "A Self-Powered Portable Nanowire Array Gas Sensor for Dynamic NO_2 Monitoring at Room Temperature," *Advanced Materials,* vol. 35, no. 12, p. 2207199, 2023.

[2] M. Shirvanimoghaddam *et al.*, "Towards a green and self-powered Internet of Things using piezoelectric energy harvesting," *Ieee Access,* vol. 7, pp. 94533-94556, 2019.

[3] A. Ahmed *et al.*, "Integrated triboelectric nanogenerators in the era of the internet of things," *Advanced Science,* vol. 6, no. 24, p. 1802230, 2019.

[4] H.-X. Zou *et al.*, "A self-regulation strategy for triboelectric nanogenerator and self-powered wind-speed sensor," *Nano Energy,* vol. 95, p. 106990, 2022.

[5] A. Babu, I. Aazem, R. Walden, S. Bairagi, D. M. Mulvihill, and S. C. Pillai, "Electrospun nanofiber based TENGs for wearable electronics and self-powered sensing," *Chemical Engineering Journal,* vol. 452, p. 139060, 2023.

[6] V. A. Aksyuk, "Sensing without power," *Nature nanotechnology,* vol. 12, no. 10, pp. 940-941, 2017.

[7] H. Askari, E. Hashemi, A. Khajepour, M. B. Khamesee, and Z. L. Wang, "Towards self-powered sensing using nanogenerators for automotive systems," *Nano energy,* vol. 53, pp. 1003-1019, 2018.

[8] Z. Wu, T. Cheng, and Z. L. Wang, "Self-powered sensors and systems based on nanogenerators," *Sensors,* vol. 20, no. 10, p. 2925, 2020.

[9] M. H. Chung, S. Yoo, W.-N. Jung, H. Jeong, and K.-H. Yoo, "Self-Powered Airflow Sensor Based on Energy Harvesting of Ventilation Air in Buildings," *Advanced Fiber Materials,* vol. 5, no. 5, pp. 1788-1798, 2023.

[10] P. Naphon and S. Wiriyasart, "Investigation on performance analysis of a small solar electric generator," *Case Studies in Thermal Engineering,* vol. 27, p. 101224, 2021.

[11] S. Ezzitouni, P. Fernández-Yáñez, L. Sánchez, and O. Armas, "Global energy balance in a diesel engine with a thermoelectric generator," *Applied energy,* vol. 269, p. 115139, 2020.

[12] V. Singh and B. Singh, "MoS_2-PVDF/PDMS based flexible hybrid piezo-triboelectric nanogenerator for harvesting mechanical energy," *Journal of Alloys and Compounds,* vol. 941, p. 168850, 2023.

[13] J. Chen, N. Nabulsi, W. Wang, J. Y. Kim, M.-K. Kwon, and J.-H. Ryou, "Output characteristics of thin-film flexible piezoelectric generators: A numerical and experimental investigation," *Applied energy,* vol. 255, p. 113856, 2019.

[14] R. K. Kotnala and J. Shah, "Green hydroelectrical energy source based on water dissociation by nanoporous ferrite," *International Journal of Energy Research,* vol. 40, no. 12, pp. 1652-1661, 2016.

[15] S. Saini, J. Shah, R. Kotnala, and K. Yadav, "Nickel substituted oxygen deficient nanoporous lithium ferrite based green energy device hydroelectric cell," *Journal of alloys and compounds,* vol. 827, p. 154334, 2020.

[16] R. Kotnala, R. Gupta, A. Shukla, S. Jain, A. Gaur, and J. Shah, "Metal oxide based hydroelectric cell for electricity generation by water molecule dissociation without electrolyte/acid," *The Journal of Physical Chemistry C,* vol. 122, no. 33, pp. 18841-18849, 2018.

[17] S. Jain, J. Shah, S. Dhakate, G. Gupta, C. Sharma, and R. Kotnala, "Environment-friendly mesoporous magnetite nanoparticles-based hydroelectric cell," *The Journal of Physical Chemistry C,* vol. 122, no. 11, pp. 5908-5916, 2018.

[18] A. Manash *et al.*, "Studies on structural and magnetic properties of nanoporous Li+ substituted $MgFe_2O_4$ nanomaterials for its application in hydroelectric cell with other areas of science & technology," *Materials Today: Proceedings,* vol. 80, pp. 1002-1013, 2023.

[19] A. Gaur, P. Kumar, A. Kumar, J. Shah, and R. Kotnala, "An efficient green energy production by Li-doped Fe_3O_4 hydroelectric cell," *Renewable Energy,* vol. 162, pp. 1952-1957, 2020.

[20] R. Gupta, J. Shah, R. Das, S. Saini, and R. Kotnala, "Defect-mediated ionic hopping and green electricity generation in $Al_{2-x}Mg_xO_3$-based hydroelectric cell," *Journal of Materials Science,* vol. 56, pp. 1600-1611, 2021.

[21] J. Shah, A. Shukla, and R. Kotnala, "Highly accelerated, sustainable, abundant water splitting at room temperature generating green electricity by Sb-doped SnO_2 hydroelectric cell," *ACS Sustainable Chemistry & Engineering,* vol. 9, no. 45, pp. 15229-15238, 2021.

[22] W. Yan *et al.*, "Chemical surface adsorption and trace detection of alcohol gas in graphene oxide-based acid-etched SnO_2 aerogels," *ACS Applied Materials & Interfaces,* vol. 13, no. 17, pp. 20467-20478, 2021.

[23] M. J. Ahemad, T. D. Le, D.-S. Kim, and Y.-T. Yu, "Bimetallic AgAualloy@ ZnO core-shell nanoparticles for ultra-high detection of ethanol: Potential impact of alloy composition on sensing performance," *Sensors and Actuators B: Chemical,* vol. 359, p. 131595, 2022.

[24] N. Jain and N. Puri, "A proposed device based on $MoSe_2$-ZnO heterojunctions on rGO for enhanced ethanol gas sensing performances at room temperature," *Nanotechnology,* 2024.

[25] J. Hu, W. Guan, X. Xiong, Y. Chen, and H. Long, "Modulation of rGO-Co_3O_4 heterojunction with multi-walled carbon nanotubes for efficient ethanol detection," *Sensors and Actuators B: Chemical,* vol. 368, p. 132202, 2022.

[26] S. K. Rao, S. M. Kamath, E. M. Abhinav, B. Renganathan, K. Jeyadheepan, and C. Gopalakrishnan, "Unraveling the potential of Gd doping on mullite $Bi_2Fe_4O_9$ for fiber optic ethanol gas detection at room temperature," *Materials Chemistry and Physics,* vol. 278, p. 125646, 2022.

[27] N. Jain and N. K. Puri, "Zinc oxide incorporated molybdenum diselenide nanosheets for chemiresistive detection of ethanol gas," *Journal of Alloys and Compounds,* vol. 955, p. 170178, 2023.

[28] T. T. N. Phan *et al.*, "Hierarchically structured $LaFeO_3$ with hollow core and porous shell as efficient sensing material for ethanol detection," *Sensors and Actuators B: Chemical,* vol. 354, p. 131195, 2022.

[29] G. Thangamani *et al.*, "Graphene oxide nanocomposites based room temperature gas sensors: A review," *Chemosphere,* vol. 280, p. 130641, 2021.

[30] Y. Qin, Z. Wei, and Y. Bai, "Effect of vacancy defects of SnS on gas adsorption and its potential for selective gas detection," *Vacuum,* vol. 183, p. 109792, 2021.

[31] X. Wang, Y. Gao, Q. Zhang, X. He, and X. Wang, "Synthesis of MoO_3 (1D)@ SnO_2 (2D) core-shell heterostructures for enhanced ethanol gas sensing performance," *Sensors and Actuators B: Chemical,* vol. 382, p. 133484, 2023.

[32] M. Afsar, M. Rafiq, and A. Tok, "Two-dimensional SnS nanoflakes: synthesis and application to acetone and alcohol sensors," *RSC advances,* vol. 7, no. 35, pp. 21556-21566, 2017.

[33] I. Kherchachi *et al.*, "Structural, optical and electrical properties of Sn_xS_y thin films grown by spray ultrasonic," *Journal of Semiconductors,* vol. 37, no. 3, p. 032001, 2016.

[34] A. Degrauw, R. Armstrong, A. A. Rahman, J. Ogle, and L. Whittaker-Brooks, "Catalytic growth of vertically aligned SnS/SnS_2 p–n heterojunctions," *Materials Research Express,* vol. 4, no. 9, p. 094002, 2017.

[35] Y. Zi, J. Zhu, L. Hu, M. Wang, and W. Huang, "Nanoengineering of tin monosulfide (SnS)-based structures for emerging applications," *Small Science,* vol. 2, no. 3, p. 2100098, 2022.

[36] J. H. Bang *et al.*, "SnS-functionalized SnO_2 nanowires for low-temperature detection of NO_2 gas," *Materials Characterization,* vol. 175, p. 110986, 2021.

[37] N. Manh Hung *et al.*, "Defect-induced gas-sensing properties of a flexible SnS sensor under UV illumination at room temperature," *Sensors,* vol. 20, no. 19, p. 5701, 2020.

[38] Q. Sun *et al.*, "SnS_2/SnS p–n heterojunctions with an accumulation layer for ultrasensitive room-temperature NO_2 detection," *Nanoscale,* vol. 11, no. 29, pp. 13741-13749, 2019.

[39] T. Sajeesh, A. R. Warrier, C. S. Kartha, and K. Vijayakumar, "Optimization of parameters of chemical spray pyrolysis technique to get n and p-type layers of SnS," *Thin Solid Films,* vol. 518, no. 15, pp. 4370-4374, 2010.

[40] S. Singh and S. Sharma, "Temperature dependent selective detection of ethanol and methanol using MoS_2/TiO_2 composite," *Sensors and Actuators B: Chemical,* vol. 350, p. 130798, 2022.

[41] M. Choi, W. William, J. Hwang, D. Yoon, and J. Kim, "A supercritical ethanol route for one-pot synthesis of tin sulfide–reduced graphene oxides and their anode performance for lithium ion batteries," *Journal of industrial and engineering chemistry,* vol. 59, pp. 160-168, 2018.

[42] D. S. Rana *et al.*, "Molybdenum disulfide (MoS_2) and reduced graphene oxide (rGO) nanocomposite based electrochemical sensor for detecting mercury (II) ions," *Nano-Structures & Nano-Objects,* vol. 36, p. 101041, 2023.

[43] P. Kumar, S. Vashishth, I. Sharma, and V. Verma, "Porous SnO_2 ceramic-based hydroelectric cells for green power generation," *Journal of Materials Science: Materials in Electronics,* vol. 32, no. 1, pp. 1052-1060, 2021.

[44] H. K. Park, J. Jo, H. K. Hong, G. Y. Song, and J. Heo, "Structural, optical, and electrical properties of tin sulfide thin films grown with electron-beam evaporation," *Current Applied Physics,* vol. 15, no. 9, pp. 964-969, 2015.

[45] Y. Jayasree, U. Chalapathi, and P. U. Bhaskar, "Effect of precursor concentration and bath temperature on the growth of chemical bath deposited tin sulphide thin films," *Applied surface science,* vol. 258, no. 7, pp. 2732-2740, 2012.

[46] K. Takeuchi, M. Ichimura, E. Arai, and Y. Yamazaki, "SnS thin films fabricated by pulsed and normal electrochemical deposition," *Solar energy materials and solar cells,* vol. 75, no. 3-4, pp. 427-432, 2003.

[47] S. Nawaz *et al.*, "Polyaniline inside the pores of high surface area mesoporous silicon as composite electrode material for supercapacitors," *RSC advances,* vol. 12, no. 27, pp. 17228-17236, 2022.

[48] Y. Ma *et al.*, "Hydrothermal-synthesis flower-like SnS microspheres gas sensors bonded physically by PVDF for detecting ethanol," *Vacuum,* vol. 181, p. 109657, 2020.

[49] C. Rana, S. R. Bera, and S. Saha, "Growth of SnS nanoparticles and its ability as ethanol gas sensor," *Journal of Materials Science: Materials in Electronics,* vol. 30, pp. 2016-2029, 2019.

[50] S. Sen and S. Kundu, "Reduced graphene oxide (rGO) decorated ZnO-SnO_2: A ternary nanocomposite towards improved low concentration VOC sensing performance," *Journal of Alloys and Compounds,* vol. 881, p. 160406, 2021.

CHAPTER 6

Summary, Conclusions, and Future Scope of Work

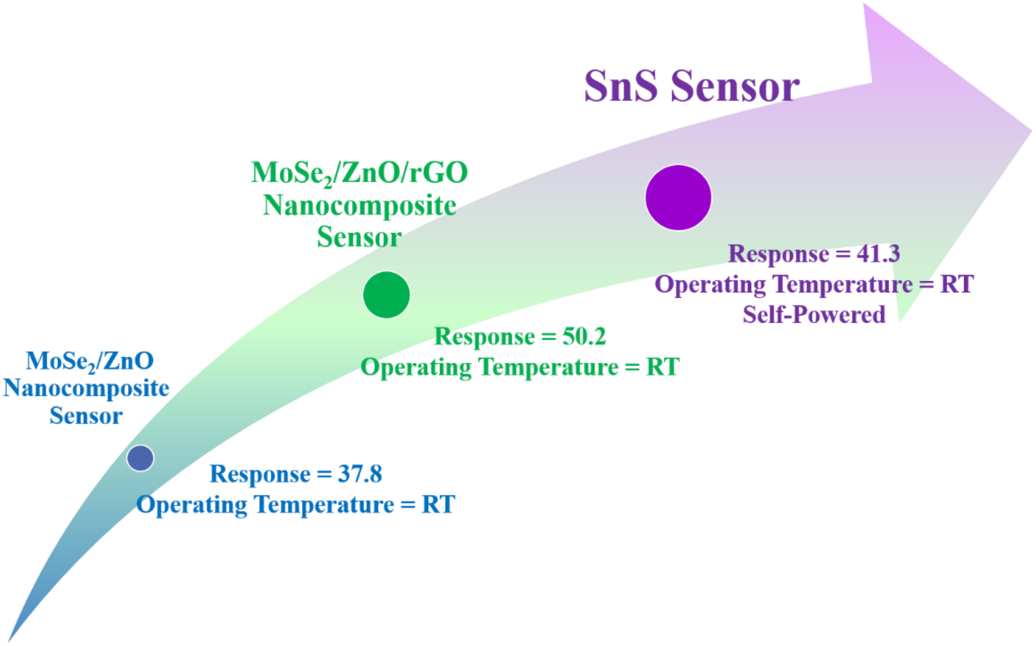

The primary objective of this chapter is to synthesise the key observations, findings, and conclusions derived from the research. It provides a detailed summary of each chapter, offering a comprehensive overview of the study's progression. Additionally, this chapter delves into the future prospects and potential research directions unveiled through our investigation, serving as a crucial platform for shaping ongoing and future scholarly endeavors.

6.1 Summary of research work

In summary, the present thesis takes advantage of the salient features of nanocomposites of 2D nanomaterials and metal oxides by employing them for multifunctional applications with a focus on gas sensing. The aim of the thesis was to develop gas sensors that operate at RT while consuming minimal power and explore self-powered gas sensors with high sensing properties. The scientific motivation, methodologies employed, and research activities undertaken to achieve the thesis objectives are comprehensively covered in Chapters 1 to 5. This chapter provides a concise summary of these key elements, encapsulating the rationale for the research, the methodological approach adopted, and the main research efforts undertaken, which are as follows:

Chapter 1 gives a brief introduction to the growing interest in developing ethanol gas sensors that operate efficiently at RT while consuming minimal power. It starts with an in-depth exploration of the pressing need for ethanol sensors with sensitivity, stability, and selectivity, particularly capable of operating at RT and detecting a wide range of ethanol concentrations. It then discusses the various categories of existing ethanol sensing technologies with an emphasis on chemiresistive sensors. Further, the chapter focuses on the integration of nanotechnology and material science with sensing technologies for improving various sensing parameters across a wide range of applications. In this regard, special attention is given to nanocomposites of 2D nanomaterials and metal oxides-based ethanol gas sensors. Through this detailed discussion, the chapter identifies existing knowledge gaps and outlines the objectives of the thesis, thereby setting the stage for further exploration and research in this field.

Chapter 2 provides a detailed exploration of the methods employed for synthesizing nanocomposites of 2D nanomaterials and metal oxides, along with the EPD technique used for film fabrication. It also covers a range of characterization techniques: XRD for structural analysis, FESEM, and HRTEM for morphological characterization, as well as FTIR for assessing functional groups, and Raman spectroscopy for analysing vibrational modes. Finally, for the gas-sensing studies, the fabrication of a gas sensor involves thermal evaporation to deposit metal electrodes onto synthesised sensing films. A customized chemiresistive gas sensing set-up is used to investigate the gas sensing behavior of the fabricated gas sensors.

Chapter 3 demonstrates an RT chemiresistive ethanol gas sensor based on hydrothermally synthesised ZnO incorporated with $MoSe_2$ nanosheets. The sensing properties of the $MoSe_2$/ZnO nanocomposite sensor were systematically investigated by exposing the sensor to various ethanol gas concentrations (10-500 ppm) in dry N_2 and dry air. The synergistic effect of incorporating ZnO nanorods into $MoSe_2$ nanosheets enhanced the sensor's response to ethanol gas (when operated in dry N_2), resulting in improved response and recovery times of 8.4 and 14.7 seconds, respectively, along with high selectivity, stability, and reproducibility. Additionally, the sensor detected ethanol at remarkably low concentrations of 10 ppm and showed excellent stability. The nanocomposite-based sensor exhibited a high gas sensing response (R_g/R_a) of 37.8 to 500 ppm of ethanol gas. In contrast, the sensor's response decreased to 15.3 to 500 ppm of ethanol gas in dry air, indicating that it performed better in dry N_2 than in dry air. The $MoSe_2$/ZnO nanocomposite sensor demonstrated better sensing characteristics compared to other similar reported sensors, suggesting that it had the potential to be an excellent candidate for ethanol gas sensing.

To further enhance the ethanol gas sensing properties of the sensing device at RT, **Chapter 4** explored a ternary nanocomposite of $MoSe_2$-ZnO heterojunctions decorated with rGO ($MoSe_2$/ZnO/rGO) for ethanol gas sensing. The sensing performance of this ternary nanocomposite sensing device was analysed for various concentrations of ethanol gas (1 - 500 ppm). The gas-sensing results revealed that, for 500 ppm ethanol gas concentration, the sensing device exhibited an enhanced response value (R_g/R_a) of 50.2. Significantly, the sensing device displayed a quick response time of 6.2 seconds and a recovery time of 12.9 seconds. Additionally, the sensing device could detect ethanol at remarkably low concentrations of 1 ppm and demonstrates excellent long-term stability of 6 weeks. The analysis of these results suggested that the $MoSe_2$/ZnO/rGO nanocomposite sensing device was a promising candidate for real-time ethanol gas detection.

In **Chapter 5**, a novel SPEG sensor was successfully developed using SnS nanoflakes, which offer high sensitivity, selectivity, and stability. The HEC was fabricated to power the gas sensor, enabling it to actively detect ethanol gas at RT. Redox reactions in the HEC were verified through V-I characteristic curves, showing a I_{max} of 40 µA and a voltage of 1.03 V. The SPEG sensor displayed a notable response of 41.3 and a swift response/recovery time of 27.3/31.4 seconds when exposed to 100 ppm ethanol gas at RT. The sensor exhibited an n-type characteristic response and can detect ethanol gas down to 10 ppm at RT. Additionally, the sensor showed excellent repeatability over three consecutive cycles and demonstrated exceptional long-term stability of 30 days. The experimental results indicated that the n-type SnS-based self-powered ethanol gas sensor can be a promising platform for integration into future large-scale IoT systems. This breakthrough may pave the way for more versatile and scalable IoT solutions, enabling continuous environmental monitoring and data collection across various settings.

6.2 Salient outcomes of the thesis

The salient outcomes of the thesis can be highlighted in the following ways,

- RT chemiresistive ethanol gas sensor based on ZnO incorporated with $MoSe_2$ nanosheets.
- The ternary nanocomposite of $MoSe_2$-ZnO heterojunctions decorated with rGO ($MoSe_2$/ZnO/rGO) for chemiresistive ethanol gas sensing at RT.
- A novel hydroelectric cell-driven gas sensor using SnS nanoflakes for the detection of ethanol at RT.

6.3 Future prospective

The thesis investigates the distinctive properties of nanocomposites formed from 2D nanomaterials and metal oxides for multifunctional applications with a focus on gas sensing. By delving into these advanced materials, the research paves the way for numerous future possibilities, such as:

1. **Scaling up monolayer synthesis:** Monolayers of 2D nanomaterials exhibit distinct properties compared to their bulk counterparts. Achieving true

miniaturization and practical applications of monolayer-based devices depends on synthesizing these monolayers on a large scale. Developing methods that ensure high yield and uniformity of monolayer production is crucial for realizing the full potential of 2D nanomaterials in commercial and industrial applications. Advances in scalable synthesis techniques are key to unlocking these potentials.

2. **Enhancing metal chalcogenides:** Exploring various modification strategies for metal chalcogenides such as incorporating metal oxides, polymers, and other materials can significantly enhance the efficiency of self-powered sensors. Integrating these different components allows for tailoring the properties of metal chalcogenides to improve their performance, stability, and sensitivity in sensor applications.
3. **Investigating other 2D nanomaterials:** Investigating other 2D nanomaterials, such as MXenes (e.g., Ti_2C_3) and borophene, offers exciting opportunities for advancing self-powered gas sensors. These materials could provide unique properties and performance enhancements, potentially leading to more efficient, sensitive, and versatile gas detection capabilities. Exploring their integration into sensor technologies opens new avenues for improving the functionality and applications of self-powered sensors. Efforts to improve the stability and sensitivity of these sensors are ongoing.
4. **Developing flexible sensors**: Investigating flexible sensors holds significant potential for advancing real-time wearable electronics applications. These sensors can be seamlessly integrated into clothing or accessories, offering continuous and reliable monitoring of various physiological parameters. By enhancing the adaptability, comfort, and responsiveness of wearable devices, flexible sensors have the potential to revolutionize health tracking, fitness monitoring, and personal safety, providing real-time data and insights directly from the wearer.
5. **Advancing lab-on-chip devices:** Advancing the fabrication of Lab-on-Chip devices and their subsequent commercialization holds substantial promise for transforming diagnostic and analytical processes. By developing more efficient,

cost-effective manufacturing techniques and scaling up production, these compact, multifunctional devices become more accessible for a broader range of applications. This advancement could lead to significant improvements in point-of-care diagnostics, environmental monitoring, and personalized medicine, driving innovation and expanding market opportunities in the field.

This proposed research aims to develop a highly sensitive, selective, and stable nanostructured sensing element capable of detecting ethanol gas at RT. By focusing on advanced nanomaterials and innovative fabrication techniques, the research seeks to enhance the performance of gas sensors, making them more efficient and reliable for real-world applications. The proposed work has the potential to contribute significantly to areas such as environmental monitoring, safety systems, and industrial processes by providing precise and responsive ethanol detection in diverse settings.

J Mater Sci: Mater Electron (2022) 33:1307–1323

Investigation of charge transport mechanism in hydrothermally synthesized reduced graphene oxide (rGO) incorporated zinc oxide (ZnO) nanocomposite films

Nikita Jain[1], Savita Sharma[2], and Nitin K. Puri[1,*]

[1] *Nanomaterials Research Laboratory (NRL), Department of Applied Physics, Delhi Technological University, Delhi 110042, India*
[2] *Physics Department, Kalindi College, University of Delhi, Delhi 110008, India*

Received: 26 July 2021
Accepted: 19 November 2021
Published online:
2 December 2021

ABSTRACT

The present study aims to investigate the impact of reduced graphene oxide (rGO) incorporation on the charge transport properties of zinc oxide (ZnO) nanocomposite films. ZnO and varied weight percentage of rGO (1.25% to 10%) in ZnO-rGO nanocomposites are synthesized via cost-effective and facile hydrothermal method. The effect of varying weight percentage of rGO in ZnO nanocomposite is analysed by techniques such as X-ray diffraction (XRD), Scanning electron microscopy (SEM), Energy dispersive X-ray (EDX), Fourier transform infra-red spectroscopy (FTIR), and Raman spectroscopy. The observed current–voltage (I–V) characteristics at room temperature show the enhancement in forward current with an increasing weight percentage of rGO (1.25% to 10%) in ZnO nanocomposite films. To study the charge transport mechanism in nanocomposite films, dual-logarithmic I–V characteristics are plotted. From the characteristic curves, we find that three different laws of space charge limited conduction (SCLC) model namely Ohm's law, Child's law, and trap-limited SCLC mechanism describe charge transport properties in the ZnO-rGO nanocomposite films. At a low weight percentage of rGO (1.25%) in ZnO-rGO nanocomposite films, a transition from Child's law to trap-limited SCLC mechanism (0.9 V being the cross-over voltage) is obtained. As the weight percentage of rGO in ZnO-rGO nanocomposite films is increased from 2.5 to 10%, the conduction is favored by Ohm's law at low applied voltages to Child's law at higher applied voltages. Best experimental results are shown with 5% of rGO in ZnO-rGO nanocomposite. The prepared nanocomposite films have potential applications in UV-photodetector devices.

Address correspondence to E-mail: nitinkumarpuri@dtu.ac.in

https://doi.org/10.1007/s10854-021-07445-6

1 Introduction

Nanocomposites are a blend of dissimilar materials with one or more of their constituents being at the nanoscale range. They offer an opportunity to tailor the properties of material towards a specific application. There has been an enormous interest in nanocomposite materials in recent times, owing to their cost-effectiveness and enhanced properties leading to improved device performance. Hybrid nanocomposites have been developed and explored for profound applications such as photodetectors, supercapacitors, gas sensors, solar cells. [1, 2]. Among the various metal-oxides, zinc oxide (ZnO) is a prominent semi-conductor with a wide range of applications due to its wide-bandgap, large exciton binding energy, abundant availability, non-toxicity, and high photon-absorption [3, 4]. A variety of morphologies can be synthesized by numerous chemical and physical methods widening up the research opportunities towards new technology [4]. Simultaneously, easy tuning of shape, size, and compositions of ZnO play an important role in altering its magnetic, optical, electrical, and other properties for numerous applications [5, 6].

Reduced graphene oxide (rGO), a two-dimensional (2D) material is an expeditious rising star on the horizon of material science and nanotechnology. Its exceptional mobility and conductivity, mechanical flexibility, optical transparency, chemical stability, and high specific surface area is attracting considerable research interest [7]. The sheets of rGO possess a large surface area which may provide support to load other functional nanomaterials. Furthermore, the oxygenated functional groups can act as nucleation centers to support nanomaterials onto graphene sheets which makes it viable to synthesize nanocomposites based on graphene [8].

Various hybrid nanocomposites based on ZnO and rGO have been explored in the field of photodetectors, gas sensors, batteries, supercapacitors, and many more due to their enhanced properties [9–14]. Previously, it has been widely reported about the charge transport properties of ZnO and rGO materials individually and their nanocomposites with other different materials (eg. n-type ZnO grown on plain and focussed ion beam GaN substrates, n-Gallium doped-ZnO on p-Silicon substrate, GaN/rGO nanocomposite with a different weight percentage of GaN, etc. [15–17]). Soylu et al. studied the effect of the molar concentration of precursors of ZnO on I–V characteristics [18]. Therefore, it is evident that ZnO, rGO, and their nanocomposites with other materials have been explored extensively. However, to the best of our knowledge, no reports are available focussing on a detailed study of the charge transport mechanism in ZnO-rGO nanocomposite films.

A plethora of experimental methods have been rigorously explored for binding of ZnO with rGO such as hydrothermal, aerosol spraying, microwave synthesis, chemical deposition, solvothermal, precipitation methods, and solution combustion synthesis [19–23]. Among these methods, hydrothermal synthesis is considered advantageous as it is cost-effective, uses mild synthesis conditions, and requires low energy with simple equipments resulting in uniform ZnO nanoparticles over rGO nanosheets [24].

In the present work, ZnO and ZnO-rGO nanocomposites with different weight percentage of rGO (from 1.25 to 10%) have been synthesized using hydrothermal method. The charge transport mechanism in the prepared Al/ZnO/ITO and Al/ZnO-rGO/ITO nanocomposite films (rGO varied from 1.25 to 10%) have been studied in detail towards their utilization for UV-photodetector devices.

2 Experimental

2.1 Chemical reagents

The chemicals used in the synthesis are Zinc acetate ($Zn(CH_3COO)_2{\cdot}2H_2O$), sodium hydroxide pellets (NaOH), graphite powder, concentrated sulphuric acid (H_2SO_4), orthophosphoric acid (H_3PO_4), hydrogen peroxide (H_2O_2), potassium permanganate ($KMnO_4$), hydrazine hydrate ($N_2H_4{\cdot}H_2O$), and ethanol (C_2H_5OH). All the chemicals are purchased from Fisher Scientific and Sigma Aldrich. All belong to AR grade purity and are employed without further purification.

2.2 Synthesis of ZnO twin-hexapods

Firstly, ZnO twin-hexapods are synthesized using the facile hydrothermal method. In the synthesis, a solution of Zinc acetate (0.2 M) and sodium hydroxide (1.25 M) is prepared separately, with continuous magnetic stirring for 30 min. Then, the solution of sodium hydroxide is added into zinc acetate solution drop-wise. The pH of the solution is observed to be 6.6. The final solution is kept for stirring for an hour which is then transferred to a 100 ml Teflon-lined steel autoclave, which is heated at 130 °C for 24 h. After several washings with DI and ethanol, the final product is dried overnight.

2.3 Synthesis of rGO

Firstly, GO is synthesized from graphite using improved modified Hummer's method as reported elsewhere [25, 26]. In detail, 2 g of graphite powder is added to a mixture of concentrated sulphuric acid and phosphoric acid in the ratio of 9:1 with continuous stirring. Thereafter, some amount of potassium permanganate is added at a very slow pace to the resulting solution followed by the magnetic stirring of 12 h at 50 °C. After this, the reaction is quenched by adding ice (300 ml) with 2.5 ml of hydrogen peroxide solution. Finally, the yellowish slurry mixture is washed (until the pH reached to 7), filtered, and dried to obtain the final product. For the synthesis of rGO, 200 mg of GO powder so obtained is dispersed in 200 ml of DI water and ultrasonicated for an hour. Then it is transferred onto the stirrer and 100 µL of hydrazine hydrate is added drop-wise into it which acts as a reducing agent and the solution is left for 12 h stirring at a particular temperature. The final solution turns black which then is washed, filtered, and dried to obtain rGO.

2.4 Synthesis of ZnO-rGO nanocomposites

Various nanocomposites of ZnO-rGO are synthesized via hydrothermal route by varying weight percentage of rGO (from 1.25 to 10%) in ZnO. Typically, a suitable amount of rGO (1 mg/ml) is dispersed in ethanol with ultrasonic treatment for an hour. Meanwhile, a solution of Zinc acetate (0.2 M) and sodium hydroxide (1.25 M) is prepared separately with stirring. It is followed by mixing of all three resulting solutions under continuous stirring for an hour. The observed pH of the solution (ZnO-rGO nanocomposite) is 6.6. At last, the solution is transferred to a Teflon-lined stainless-steel autoclave which is heated at 130 °C for 24 h. After several washings with DI water and ethanol, the grey color powder is obtained which is then dried overnight. Weight percent variation by volume (w/v) of 1.25%, 2.5%, 5%, and 10% of rGO to ZnO are prepared and named as ZG-1.25, ZG-2.5, ZG-5, and ZG-10, respectively. All these ZnO-rGO nanocomposites with various rGO content are prepared by above said process.

2.5 Film fabrication

ZnO-rGO nanocomposite films are fabricated on rectangular indium tin-oxide (ITO) coated corning-glass substrates. The standard wet cleaning method is employed to clean the ITO substrates. Briefly, soap solution, deionized ionized (DI) water, acetone, and finally with isopropyl alcohol. After cleaning, the substrates are dried at 100 °C on a hot plate for 30 min. In the first step, ZnO powder is dispersed in ethanol by ultrasonicating it for 30 min. In the second step, ZnO films are prepared via spin-coating technique, by dispensing the above solution on ITO substrates at 3000 rpm for 60 s. It is followed by drying the films in the open air at 70 °C for 10 min. A similar process is devised to obtain all the desired ZG-1.25, ZG-2.5, ZG-5, and ZG-10 nanocomposites films. Finally, 100 nm thick top Al metal electrodes are deposited on the prepared films using the thermal evaporation technique. Figure 1 shows the schematic description of the process of fabrication of Al/ZnO-rGO/ITO nanocomposites films.

3 Results and discussions

All the prepared samples are thoroughly characterized using various techniques such as X-ray diffraction (XRD), Scanning electron microscopy (SEM), Energy dispersive x-ray (EDX), Fourier transform infra-red spectroscopy (FTIR), and Raman spectroscopy. Charge transport properties of all the prepared films (Al/ZnO/ITO, Al/ZnO-rGO/ITO) have been studied via current–voltage (I–V) characteristics over the voltage range of − 2.5 to 2.5 V using Keithley 2450 SMU.

3.1 Structural analysis (X-ray diffraction)

The XRD pattern of ZnO, ZG-1.25, ZG-2.5, ZG-5, and ZG-10 nanocomposite is shown in Fig. 2. XRD pattern of ZnO shows all the diffraction peaks which are congruous with the standard data available for the

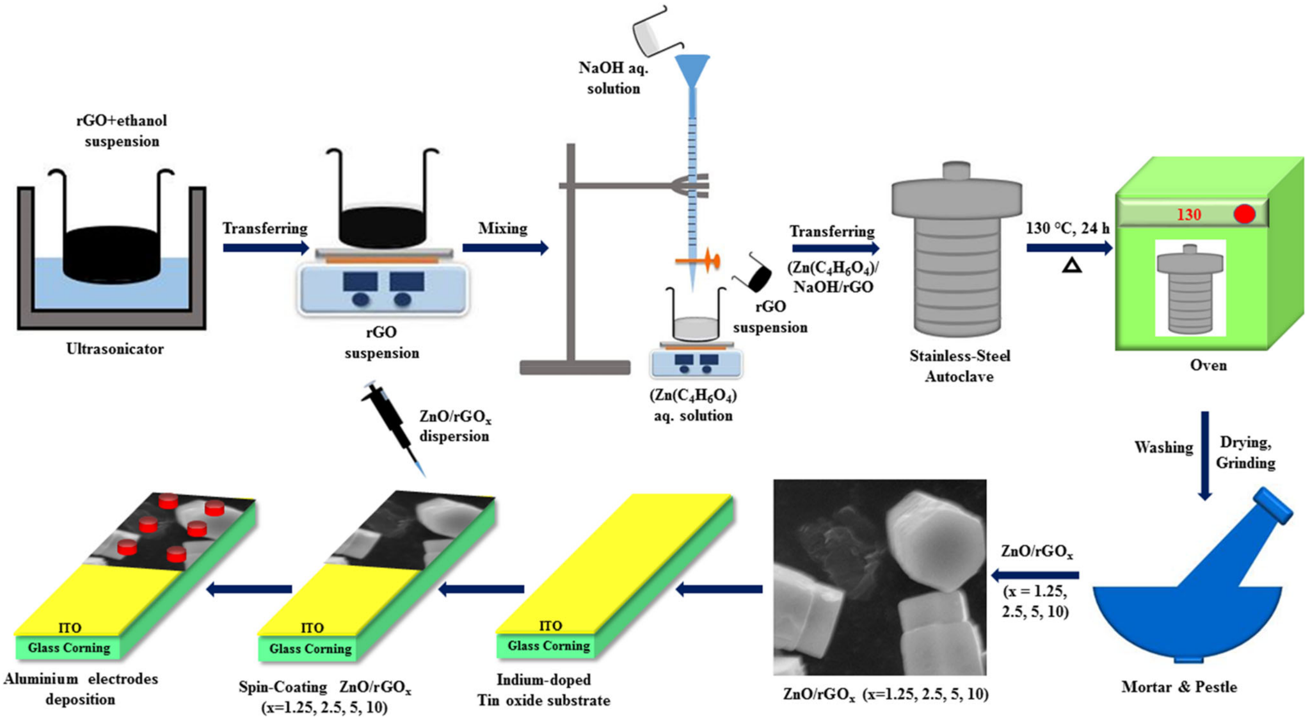

Fig. 1 Schematic description of fabrication of Al/ZnO-rGO/ITO nanocomposites films

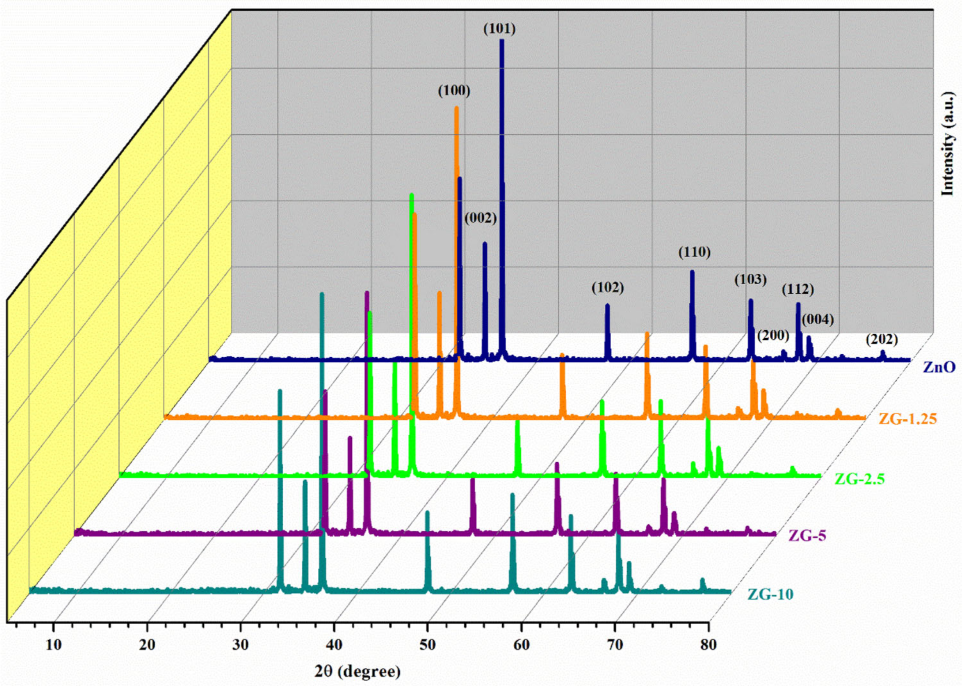

Fig. 2 XRD pattern of ZnO, ZG-1.25, ZG-2.5, ZG-5, and ZG-10 nanocomposites

wurtzite structure of ZnO (JCPDS 36-1451) [27]. A prominent diffraction peak of GO (Fig. S1a in the Supplementary Information) is found to be at 11.7° and a weak peak located at 42.6° corresponding to (002) and (100) reflection, respectively. The inset of Fig. S1a in the Supplementary Information shows the diffraction pattern of raw graphite which shows a highly crystalline and strong diffraction peak at 26.6° towards the (002) plane. The shift in GO peak at a lower diffraction angle confirms the successful oxidation of graphite [28]. The broadening and shifting of the distinct peak of GO from 11.7° to 23.1° can be attributed to the breakdown of the long-range order of GO [29]. Two broad diffraction peaks located at 23.1° and 43.6° correspond to rGO (Fig. S1b in the Supplementary Information). These two peaks confirm the formation of (002) and (100) planes of rGO [29]. The peak positions of ZnO remain the same in all ZnO-rGO nanocomposites (Fig. 2) while the two reflection peaks of rGO are absent in nanocomposites. The reason can be attributed to the low diffraction intensity of rGO in the dispersed state [30, 31].

The d-spacing of graphite, GO and rGO is calculated using Bragg's relation [32] and is found to be 0.33 nm, 0.75 nm, and 0.38 nm, respectively for the (002) plane. The increase of d-spacing of GO compared to graphite can be due to the intercalation of oxygenated functional groups (such as epoxide and hydroxyl groups) and intercalation of molecules of water in the interlayer spacing of carbon layers [28].

The average crystallite size of ZnO and ZnO-rGO nanocomposites is calculated using Scherrer's relation [33, 34]. The crystallite size calculated for ZnO, ZG-1.25, ZG-2.5, ZG-5, and ZG-10 samples is 81, 77, 76, 70, and 74 nm, respectively. It is observed that the crystallite size of ZnO decreases progressively as the weight percentage of rGO in the nanocomposites is increased to 5%. This suggests that the growth and nucleation stage of ZnO crystals in the nanocomposites is hindered by rGO [4]. Furthermore, the dislocation density (δ) of ZnO and ZnO-rGO nanocomposite is calculated using the following relation: $\delta = 1/D^2$ where D is the crystallite size of ZnO and ZnO-rGO nanocomposite. The highest and lowest dislocation density is found to be approximately 2.05×10^{-4} nm^{-2} and 1.49×10^{-4} nm^{-2} for ZG-5 nanocomposite and ZnO, respectively. When the dislocation density decreases, the crystallinity increases [35]. The intensity of the diffraction peak along the (101) diffraction plane is supporting this phenomenon. The diffraction peaks of the composite ZG-1.25 are stronger than those of other nanocomposites but weaker than the diffraction peak of pure ZnO which indicates that the crystallinity of the composite is affected by the addition of rGO [20].

The lattice parameters (lattice constants and volume of unit cell) are calculated by means of Rietveld refinement using FullProf Software. Best matching of the peaks for all the samples is observed for hexagonal structure with P6$_3$mc space group. Table 1 shows the calculated values of FWHM, lattice parameters, crystallite size, and dislocation density for all the prepared samples. It is clear from the table that the structural lattice parameters increases and the crystallite size decreases with the increasing weight percentage of rGO in the ZnO-rGO nanocomposites upto 5%. The obtained results are consistent with the literature [36–38].

On the other hand, the variation in the trend of certain crystal parameters of ZG-10 nanocomposite can be understood as: at this concentration, the ratio of zinc ions to rGO is not critical. Since the critical ratio is not maintained, the sorption of zinc ions is less on rGO nanosheets, due to which the synergetic effect could not follow the trend as followed by the other nanocomposites.

3.2 SEM and EDX observations

SEM analysis is done to investigate the surface morphology as well as to examine the average length of the prepared twin-hexapods of ZnO, ZG-1.25, ZG-2.5, ZG-5, and ZG-10 nanocomposites. Figure 3 shows the SEM images of the prepared ZnO and ZnO-rGO nanocomposite with variation in weight percentage of rGO from 1.25 to 10%. It is observed that the average length of the hexapods is closely related to the weight percentage of rGO in the ZnO-rGO nanocomposite. Figure 3a depicts the SEM image of ZnO. The observed average length of the top-hexapod is 2.7 μm and the average length of the bottom-hexapod is 5 μm. Compared to the crystallite size of the samples calculated by the XRD analysis, a bigger particle size of ZnO and ZnO-rGO nanocomposites (rGO varied from 1.25 to 10%) is obtained from SEM observations. This can be due to the fact that particles contain many smaller crystallites [39, 40]. When rGO is introduced in the ZnO framework, the morphology is maintained as can be seen (Fig. 3b–e). The top-hexapod of the ZG-1.25 nanocomposite (Fig. 3b) has an average length of 1.7 μm and the average length of the bottom-hexapod is 3.1 μm. Thus, we can clearly see that the size of ZnO hexapods decreases with the increase in the concentration of rGO in nanocomposites. Top-hexapods of average length 1.6 μm and bottom-hexapod of the average length of 2.9 μm is obtained when the rGO concentration is increased to 2.5% in ZnO (Fig. 3c). But, further increase in rGO concentration to 5% in ZnO-rGO nanocomposite the ZnO twin-hexapods are found to be comparatively

Table 1 Variation in FWHM, lattice parameters (lattice constants and volume of unit cell), crystallite size and dislocation density of (a) ZnO, (b) ZG-1.25, (c) ZG-2.5, (d) ZG-5, and (e) ZG-10 nanocomposites with variation in weight percentage of rGO

Sample	Plane	2θ (degree)	FWHM (degree)	Lattice parameters		Volume of unit cell (Å^3)	Crystallite size (nm)	Dislocation density (nm^{-2}) × 10^{-4}
				a (Å)	c (Å)			
ZnO	(101)	36.3	0.10	3.2465	5.2021	47.48	81	1.49
ZG-1.25	(101)	36.3	0.10	3.2477	5.2034	47.53	77	1.67
ZG-2.5	(101)	36.3	0.11	3.2481	5.2040	47.54	76	1.74
ZG-5	(101)	36.3	0.11	3.2485	5.2041	47.55	70	2.05
ZG-10	(101)	36.3	0.11	3.2480	5.2039	47.54	74	1.82

small with an average length of 1.2 µm and 2.4 µm (Fig. 3d) of top and bottom-hexapod, respectively. The reason is the formation of rGO sheets which creates a hindrance for further growth of ZnO hexapods which is consistent with the XRD analysis as well.

On the other hand, when the rGO concentration is increased to 10% in ZnO-rGO nanocomposite, most of the rGO sheets in the nanocomposite are agglomerated and some of the ZnO grow on graphene sheets. To understand and deduce the ongoing observation in surface morphology, the formation process of ZnO-rGO nanocomposite is surmised. There should be a critical ratio of zinc ions of ZnO and rGO to form well-dispersed nanocomposites. When the concentration of rGO is low, the ratio of zinc ions is relatively high in rGO. This leads to excess sorption of zinc ions on rGO sheets which results in well-dispersed ZnO-rGO nanocomposite. On increasing the concentration of rGO in ZnO, the sorption of zinc ions is less on rGO sheets. The negative charges on reduced graphene oxide are partially neutralized by the zinc ions. This lead to the coagulation of rGO sheets during the reaction process [41]. It is observed that the top-hexapod of ZnO in this nanocomposite has an average length of 1.5 µm and the bottom-hexapod has an average length of 2.7 µm (Fig. 3e). But, an increase in rGO concentration in the nanocomposites does not result in the agglomeration of ZnO hexapods. From the above observation, we can deduce that rGO nanosheets co-exist with the ZnO twin-hexapods in the fabricated ZnO-rGO nanocomposites.

The elemental composition of ZnO and ZnO-rGO nanocomposites are analysed by the EDX spectrum. It is inapt to determine the exact content of the elements present in the ZnO and ZnO-rGO nanocomposites using EDX because of the presence of light elements (O and C) [42]. EDX spectra and the weight percent composition of ZnO and ZnO-rGO nanocomposites are shown in Fig. S2 in Supplementary Information. As can be seen from the EDX spectra of ZnO (S2a in Supplementary Information), no peak corresponding to carbon is found. With the addition of rGO in the ZnO framework, increasing weight percent of carbon peak is observed in all the ZnO-rGO nanocomposites (Fig. S2b–e in Supplementary Information). However, an impurity peak of sodium is also found in all the samples. This impurity peak could be due to the precursor (NaOH) used in the synthesis of ZnO and ZnO-rGO nanocomposites. Although its weight percent composition is negligibly small, yet it may be one of the reasons for the creation of traps inside ZnO and ZnO-rGO nanocomposite [43].

3.3 FTIR Spectroscopy analysis

FTIR Spectroscopy is performed to investigate and elucidate the presence of functional groups related to ZnO, GO, rGO along with the other functional groups which may arise after hybridization in prepared samples. Figure 4 shows the FTIR spectra of ZnO, ZG-1.25, ZG-2.5, ZG-5, and ZG-10 nanocomposites. The spectrum of ZnO (Fig. 4a) exhibits a broad peak at 3278 cm^{-1} which corresponds to O–H stretching vibrations [44]. Few narrow peaks 2830 to 2955 cm^{-1} correspond to C–H bonds [45]. Several peaks appearing between 1360 and 1710 cm^{-1} can be attributed to the stretching modes of COOH group, which are believed to be adsorbed on the surface of

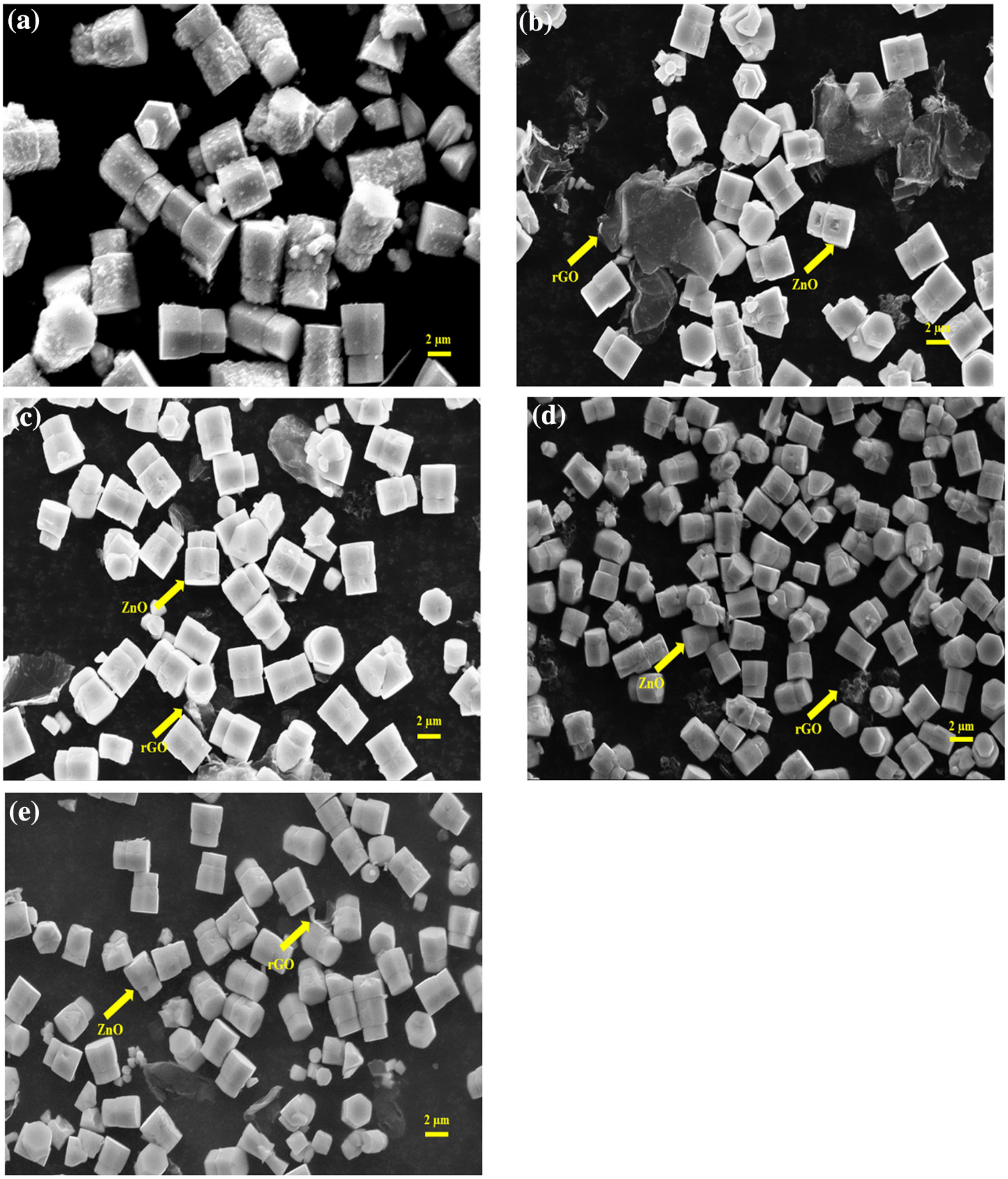

Fig. 3 SEM images of ZnO and ZnO-rGO nanocomposites: **a** ZnO, **b** ZG-1.25, **c** ZG-2.5, **d** ZG-5, and **e** ZG-10

the ZnO hexapods during the process of synthesis [46]. In addition to this, a small peak at 920 cm^{-1} and a pointed peak at 457 cm^{-1} corresponds to Zn–O stretching and deformation vibrations, respectively [46, 47]. FTIR spectrum of GO (Fig. S3a in the Supplementary Information) consists of broad peak 3290 cm^{-1} corresponding to O–H groups and narrow peaks at 2868 cm^{-1} corresponding to C–H stretching. In addition to this, the peak at 1705 cm^{-1} and 1577 cm^{-1} corresponds to C=O and C=C stretching. A small peak at 1395 cm^{-1} corresponds to O–H deformation. Finally, two peaks at 1230 and 1056 cm^{-1} confirm the epoxy C–O–C and alkoxy C–O stretching vibrations, respectively [48]. When GO is reduced to rGO using hydrazine hydrate, the oxygen-containing functional groups are significantly reduced and weakened which is clear in the FTIR spectrum of rGO (Fig. S3b in the Supplementary

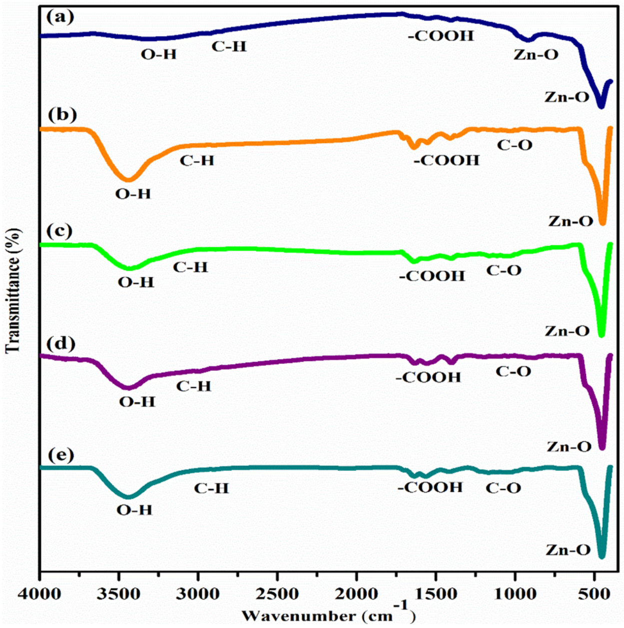

Fig. 4 FTIR spectra of ZnO and ZnO-rGO nanocomposites: a ZnO, b ZG-1.25, c ZG-2.5, d ZG-5, and e ZG-10

Information). The peak at 3450 cm^{-1} is attributed to O–H group. The two new peaks at 1640 cm^{-1} and 1369 cm^{-1} arise due to the cyclic hexagonal symmetry and the vibrations of skeletal of rGO, respectively [47]. Two peaks at 1230 and 1056 cm^{-1} confirm the epoxy C–O–C and alkoxy C–O stretching vibrations, respectively which are also present in GO. The FTIR spectrum of ZnO-rGO nanocomposites (Fig. 4b – e) contains a broad absorption band at 3440 cm^{-1} denoting the O–H groups and a few tiny peaks around 2900 cm^{-1} confirming C-H bonds. Various peaks in the range of 1350 to 1600 cm^{-1} are due to the stretching modes of the COOH group. Furthermore, few weak peaks around 1100 cm^{-1} are attributed to C–O stretching vibrations of rGO sheets. A peak around 457 cm^{-1} is the characteristic peak of ZnO and corresponds to the Zn–O bond confirms the presence of ZnO in all the nanocomposites [9, 21]. Hence, this indicates the coexistence of ZnO and rGO phase in all the prepared ZnO-rGO nanocomposites which is in good accordance with the SEM observations as well.

3.4 Raman Spectroscopy analysis

The Raman spectra of ZnO, GO, rGO and ZG-1.25, ZG-2.5, ZG-5, and ZG-10 nanocomposites is shown in Fig. 5 and the detailed parameters are calculated from Raman data are summarized in Table 2. Raman spectroscopy measurements of ZnO (Fig. 5a) show peaks at 332, 387, 437, 559, and 1145 cm^{-1}. The peak with Raman shift of 332 cm^{-1} corresponds to acoustic and optical phonon overtone with A_1 symmetry while the peak located at 387 cm^{-1} corresponds to A_1(TO) mode [30]. The peak at 437 cm^{-1} corresponds to the ZnO non-polar optical phonons ($E_{2\mathrm{high}}$). It signifies the crystal quality and is the characteristic peak of hexagonal wurtzite phase of ZnO [49]. A peak at 559 cm^{-1} confirms the A_1(LO) mode which is attributed to the surface defect formation of ZnO [50]. A spectral peak at 1145 cm^{-1} is attributed to the multi-phonons process [51].

Two characteristic peaks of GO are observed at 1352 cm^{-1} and 1600 cm^{-1} which corresponds to the D and G bands of graphene, respectively (Fig. S4a in the Supplementary Information). The D band represents lattice disorders in the sp^2-hybridized C atoms and the G band is related to the highly oriented sp^2 hexagonal graphitic lattice [52]. Structural changes from GO to rGO upon chemical reduction are reflected in the spectrum clearly (Fig. S4b in the Supplementary Information). The D and G bands of rGO are located at 1347 cm^{-1} and 1575 cm^{-1}, respectively. The intensity ratio (I_D/I_G) increased from 0.99 to 1.07 when GO is chemically reduced to rGO indicating the partial modification of surface

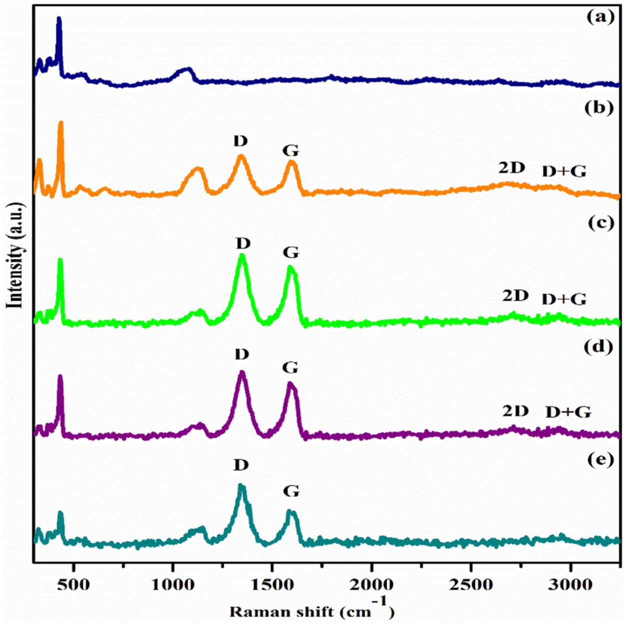

Fig. 5 Raman spectra of ZnO and ZnO-rGO nanocomposites: a ZnO, b ZG-1.25, c ZG-2.5, d ZG-5, and e ZG-10

Table 2 Parameters calculated from Raman data of (a) GO, (b) rGO, (c) ZG-1.25, (d) ZG-2.5, (e) ZG-5, and (f) ZG-10 nanocomposites

Sample	Position of D band/cm^{-1}	Position of G band/cm^{-1}	I_D/I_G	FWHM (cm^{-1})	
				D-band	G-band
GO	1352	1600	0.99	102	66
rGO	1347	1575	1.07	85	65
ZG-1.25	1343	1591	1.01	88	66
ZG-2.5	1347	1587	1.01	83	66
ZG-5	1351	1579	1.01	81	66
ZG-10	1339	1583	1.01	86	67

functional groups containing oxygen [52]. The results indicate that GO is successfully reduced to rGO after chemical reduction by hydrazine hydrate.

The Raman spectrum of all the prepared nanocomposites (Fig. 5b – e) contains the Raman bands of ZnO and rGO which confirms that the nanocomposites are successfully synthesized [53]. The I_D/I_G ratio of all the ZnO-rGO nanocomposites decreases to 1.01 compared to rGO which indicates that the sp^2 domain size of carbon atoms decreases with the incorporation of rGO in ZnO [10]. The D band shifts from 1343 to 1351 cm^{-1} and the G band decreases from 1591 to 1579 cm^{-1} as the weight percentage of rGO increases from 1.25 to 5% in ZnO. But, the same trend of shifting in the D and G band is not observed in ZG-10 nanocomposite.

A small shifting in the D and G band (Table 2) of the Raman spectrum of the nanocomposites is attributed to the electronic interactions of ZnO and rGO during the hydrothermal synthesis process [49]. In the nanocomposites, the 2D band is at ~ 2700 cm^{-1} and the D + G band is at ~ 2900 cm^{-1} which reconfirms the presence of rGO in the nanocomposites. The 2D and D + G bands of ZG-10 nanocomposite are not observed clearly.

To derive more quantitative information, the Raman spectra of GO (Fig. S4a in the Supplementary Information), rGO (Fig. S4b in the Supplementary Information), ZnO and ZnO-rGO nanocomposites is further deconvoluted (Fig. 6). The full-width half maximum (FWHM) is calculated using deconvoluted D and G bands (Table 2). It is found that when GO is reduced to rGO the FWHM values for both the bands decreases. The decrease in the width of the D-band of rGO is attributed to an increase in carbon-sp^2 content [54]. The lower the value of the width of G-band of rGO, higher its degree of crystallization [55]. Furthermore, with the addition of rGO (from 1.25 to 5%) in the ZnO-rGO nanocomposite, the width of the D-band first increases and then decreases as compared to rGO. Consequently, the carbon-sp^2 content of the ZG-5 nanocomposite is more than the ZG-1.25 nanocomposite. The width of the G-band remains almost the same in all the prepared nanocomposites. This indicates that the crystallization of rGO is maintained in all the nanocomposites. For ZG-10 nanocomposite, the width of D and G bands deviates from the trend as followed by all the other nanocomposites.

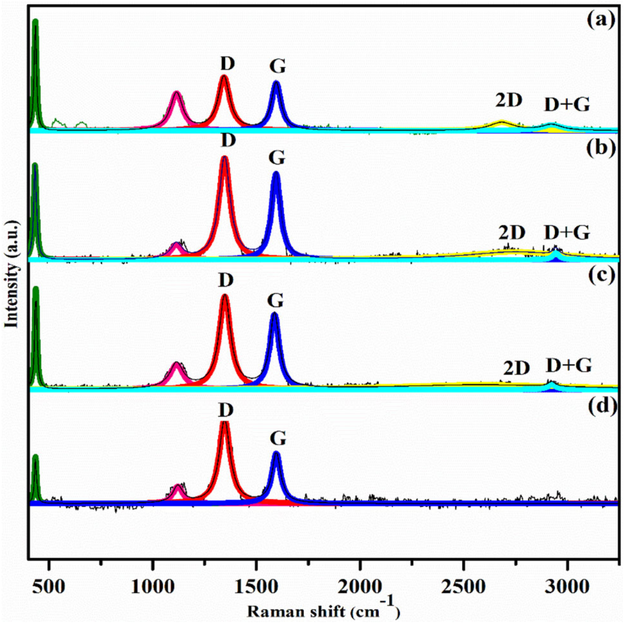

Fig. 6 The deconvoluted Raman data of ZnO and ZnO-rGO nanocomposites: a ZnO, b ZG-1.25, c ZG-2.5, d ZG-5, and e ZG-10

The reason for the deviation from the trend in Raman results of ZG-10 nanocomposite can be inferred as: The uncritical ratio of zinc ions to rGO does not lead to the synergetic effect between ZnO and rGO. Because of this, the ZG-10 nanocomposite cannot follow the trend as followed by the other nanocomposites. The co-observed Raman peaks of ZnO together with rGO confirm that the ZnO-rGO nanocomposites are synthesized successfully which is in good accordance with the SEM and FTIR Spectroscopy results as well.

3.5 Electrical analysis of films

The impact of incorporation rGO on electrical properties [56, 57] of ZnO is studied using room temperature I–V plots using Keithley 2450 SMU. Figure 7 shows the illustration of I–V measurement experimental setup. Figure 8 represents the current–voltage (I–V) characteristics for Al/ZnO/ITO and Al/ZnO-rGO/ITO films with variation in weight percentage of rGO in ZnO. Figure 9a–e shows the variation in dual-logarithmic I–V curves with a varying weight percentage of rGO from 1.25 to 10% in the prepared nanocomposite films.

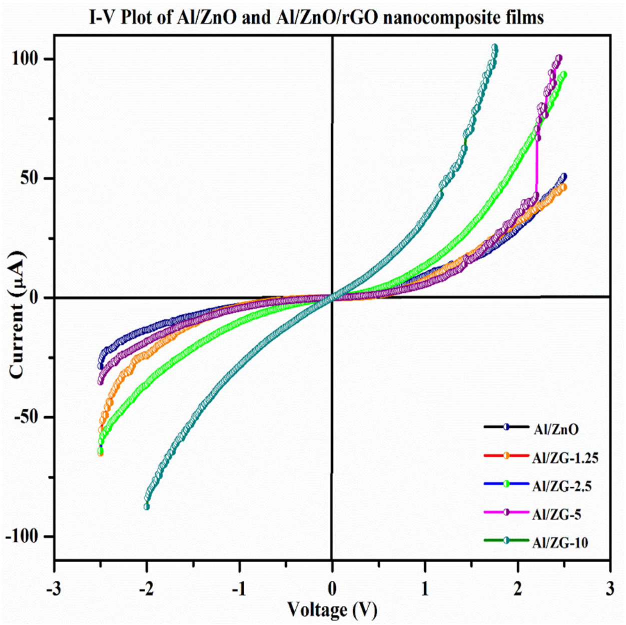

Fig. 8 Current–Voltage characteristics of ZnO and ZnO-rGO nanocomposite films

As can be seen from the I–V curves (Fig. 8), the forward current in the ZnO films is 51 µA at 2.5 V. When the weight percentage of rGO is increased from 1.25 to 10% in ZnO nanocomposite films (as confirmed from the EDX spectra), the forward current is found to be increasing from ≈ 51 to 105 µA (Table S1 in Supplementary Information). When rGO is incorporated from 1.25 to 5% in ZnO nanocomposite films, the leakage current under applied reverse bias voltage is found to be decreasing from 71 to 35 µA at 2.5 V. It is also found that the forward and reverse voltage in ZG-10 nanocomposite films could reach a maximum of 1.75 V after which the films breakdown. The enhancement in forward current and reduction in leakage current in the prepared nanocomposite films can be attributed to rGO nanosheets which provided a facile pathway for the direct transportation of charge carrier in the ZnO-rGO nanocomposite [58]. SEM and EDX observations, FTIR, and RAMAN Spectroscopy analysis support these results by showcasing the coexistence of ZnO and rGO in all the prepared ZnO-rGO nanocomposites. When an external bias is applied to the films, mobility as well as the drift velocity of the charge carriers increases which thereby increased the forward current. The increase in leakage current in the ZG-10 nanocomposite films can be ascribed to the formation of trap-level defects in ZnO due to the high concentration of rGO.

The rectification ratio (RR = I_F/I_R) is calculated for all the film samples [59]. In this case, the RR is calculated as: the forward current at 2.5 V divided by the reverse current at -2.5 V for all the films except for ZG-10 nanocomposite films. The RR for ZG-10 nanocomposite films is calculated as: the forward

Fig. 7 Illustration of I–V measurement experimental setup

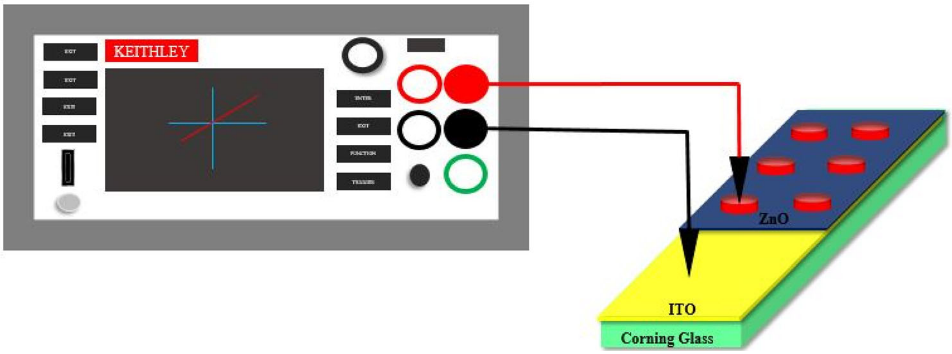

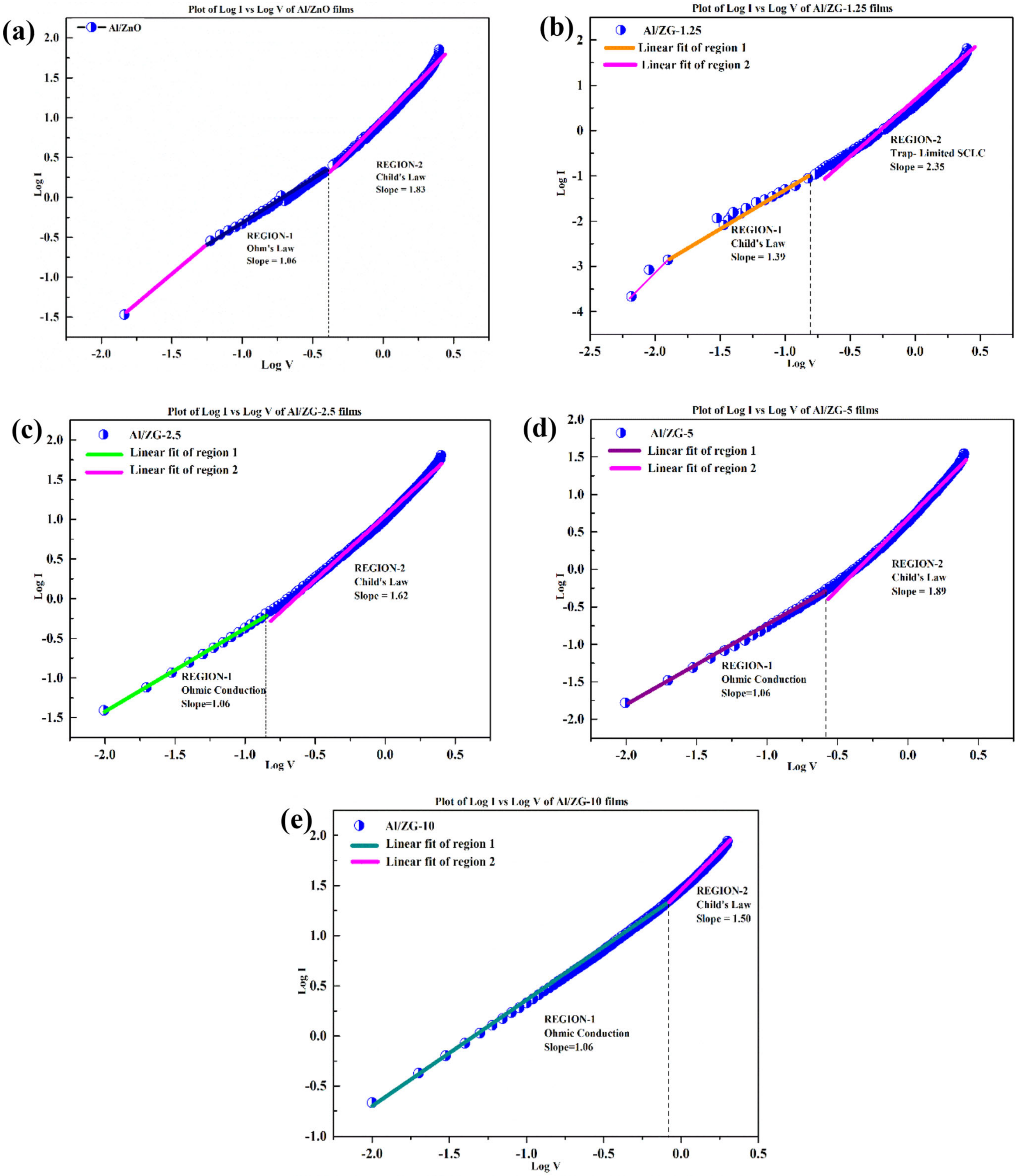

Fig. 9 Dual-logarithmic I–V curves obtained for **a** ZnO, **b** ZG-1.25, **c** ZG-2.5, **d** ZG-5, and **e** ZG-10 nanocomposite films with standard error ≤ ± 0.002

current at 1.75 V divided by the reverse current at − 1.75 V. The RR is found to be 0.7, 1.2, 1.5, 2.9, and 1.6 for Al/ZnO, Al/ZG-1.25, Al/ZG-2.5, Al/ZG-5, and Al/ZG-10 nanocomposite films, respectively.

The I–V curves of all the samples are almost symmetric in the forward and reverse direction, which results in low RR of Al/ZnO and Al/ZnO-rGO nanocomposite films. The reason can be attributed to the low work function contrast between the ZnO and Al electrodes, ZnO-rGO nanocomposite, and Al electrodes [60]. Table S1 in the Supplementary Information depicts the variation in electrical parameters of the fabricated ZnO and ZnO-rGO nanocomposite films with varying weight percentage of rGO from 1.25 to 10%.

To understand the effect of weight percentage variation of rGO in ZnO nanocomposite films on underlying current conduction mechanism, linear fittings of the obtained I–V curves are carried out. All the I–V curves are fitted by the space charge limited conduction (SCLC) mechanisms, which is similar to the results reported in the literature [18, 43, 61, 62]. The standard error for linear fitting of different regions in the current–voltage curves is found to be $\leq \pm 0.002$. The relationship between the current generated and applied voltages can be directly interpreted from the value of the obtained slopes from dual-logarithmic I–V curves. The obtained slopes imply that the charge transport mechanism in prepared ZnO-rGO nanocomposite films is governed by the three limiting laws of space charge limited conduction (SCLC) model, which are Ohm's law, Child's law, and trap-limited SCLC mechanism. The power-law relationship ($I \propto (V)^{\mathrm{m}}$, where m is the slope of the plots) is used to categorize the charge transport mechanism in all the films [43]. Such a mechanism is explained based on deep-level defects. Traps capture the electronic charges, which generally lie in the forbidden gap region or extended band tails. Energetically favored states or trap states strongly influence the conduction characteristics in semiconducting materials. The reason for the creation of traps could be (1) inadvertent impurities, (2) defects introduced during the film processing [63–66]. Moreover, the addition of rGO with different weight percentage in ZnO nanocomposite films could also be the cause of interfacial defect states in the prepared films which is supported by the XRD analysis as well. The XRD analysis clearly shows an increase in dislocation density, variation in lattice parameters, and decrease in crystallite size of ZnO with the increase in weight percentage of rGO in ZnO-rGO nanocomposites. Further, EDX spectra show the presence of sodium in the as-synthesized samples which may also be one of the reasons for the creation of traps inside ZnO and ZnO-rGO nanocomposite.

Figure 9a depicts the dual-logarithmic I–V curve of ZnO films. It is observed that for low applied voltages i.e., for $V \leq 0.9$ V (Region-1), the slope of the dual-logarithmic I–V plots comes nearly one. This implies linear dependence of current on the applied voltage. Hence, it is concluded that the conduction mechanism is governed by Ohm's law. Such behavior is because the density of thermally generated free carriers inside the ZnO films is more than those of the injected charge carriers [42]. The weak injection of charge carriers from the electrodes leads to the partial filling of the trap centers. Again to maintain the neutrality of the charges inside the films, redistribution of the charge carriers occurs. This redistribution occurs in such a manner that the injected carriers are still obstructed to travel across the films which results in a slope of 1.06. At higher applied voltage (V $\geq$ 0.9 V), the departure from ohmic behavior is observed thereby following the Child's Law. This is denoted by Region-2, where the electrons injected from the electrodes to the films are high. Due to which the accumulation of the charge carriers at the electrodes forms a space charge region which thereby affects the electrical distribution.

Figure 9b shows the log$I$—log$V$ curves of ZG-1.25 nanocomposite films. When rGO is introduced in the ZnO nanocomposite films, the charge carriers are increased. These charge carriers facilitate the injected charge carriers upto a certain limit to travel across the prepared films. But the effect due to traps overshadows the carriers of rGO and results in a slope of 1.39 at a low applied voltage (V $\leq$ 0.9 V) indicating Child's law SCLC mechanism. A transition from Child's Law to trap-limited SCLC mechanism is observed at a higher applied voltage (V $\geq$ 0.9 V). The strong injection of charge carriers at higher applied voltage occurs, due to which the carriers do not get enough transit time for reapportioning via thermally generated charge carriers or rGO charge carriers. This leads to the filling of trap centers. Hence, a slope greater than 2 is obtained which confirms the trap-limited SCLC conduction mechanism.

Figure 9c–e depicts the dual-logarithmic I–V curves of ZG-2.5, ZG-5, and ZG-10 nanocomposite films. It is observed that as the concentration of rGO is increased from 2.5 to 10% in the ZnO nanocomposite films, a clear transition of the voltage ranges for ohmic conduction keeps on increasing thereby decreasing the voltage range for Child's Law mechanism. Apart from the prepared ZG-1.25 nanocomposite films, in which the transported charge carriers are low in comparison to the other nanocomposite films with high rGO content, all the nanocomposite films followed the same trend. The reason for such a behavior is explained based on deep-level defects as: It can be observed that for low applied voltages i.e., (Region-1), the slope of the plots comes nearly one. The films are said to follow Ohm's law. The charge carriers due to rGO incorporation increases, which not only facilitates the injected charge carriers to travel across the films but also overshadows the effect of traps. As the voltage increases, the prepared films follow Child's Law. This implies that the strong injection of charge carriers occurs due to which accumulation of the charge carriers at the electrodes form a space charge region which thereby affects the electrical distribution. Hence, the dual-logarithmic I–V characteristics of the prepared ZnO and ZnO-rGO nanocomposite films are dominated by the SCLC conduction mechanism.

4 Conclusion

Motivated by the adjoining merits of ZnO and rGO, the present study addresses the fundamental charge transport properties of ZnO and ZnO-rGO nanocomposite films and their potency for the realization of film-based nanodevices. The nanocomposites are synthesized by a facile hydrothermal method and are analysed by various characterizations. Phase formation of ZnO and dispersion of rGO in ZnO are confirmed by XRD and SEM observations. The elemental composition of ZnO and ZnO-rGO nanocomposites is confirmed by EDX analysis. The coexistence of ZnO and rGO in the nanocomposites is confirmed by FTIR and Raman spectroscopy. Films of ZnO and the ZnO-rGO nanocomposites are fabricated on ITO coated corning-glass substrate using spin-coating technique. Charge transport properties of all the as-prepared films (Al/ZnO/ITO and Al/ZnO-rGO/ITO) have been studied via current–voltage (I–V) characteristics over the voltage range of − 2.5 to 2.5 V. The detailed I–V curves shows the enhancement in the performance characteristics of the nanocomposites films by varying the rGO concentration in ZnO-rGO nanocomposite. It is found that as the rGO concentration increases in ZnO nanocomposite films, the forward current in the films also increases. Furthermore, the dual-logarithmic I–V plots have been explained based on the space charge limited conduction (SCLC) model to identify the charge transport mechanism in the films. As the weight percentage of 1.25% of rGO is introduced in ZnO nanocomposite films, the dual-logarithmic I–V characteristics give a clear transition from Child's law to trap-limited SCLC mechanism (0.9 V being the cross-over voltage). On further incorporation of rGO (from 2.5 to 10%), the conduction is favored by Ohm's law at low applied voltages and Child's law at higher applied voltages. Experimental results show that the best percentage of rGO in ZnO-rGO nanocomposite films is 5% in respect of high forward current, low leakage current, and higher rectification ratio compared to other ZnO-rGO nanocomposites. Beyond 5% of rGO in ZnO-rGO nanocomposites, the critical ratio of zinc ions to rGO is not maintained, due to which the synergetic effect did not lead to expected results. Hence, manipulation of functional properties such as charge transport by the addition of highly conducting rGO may provide additional liberty during device fabrication suitable for applications such as UV-photodetection.

Acknowledgements

The authors gratefully acknowledge the Vice-Chancellor, Prof. Yogesh Singh, Delhi Technological University, Delhi, India for his meticulous support for arranging the research facilities. The authors are grateful to Dr. Kamal Arora, Ritika Khatri, Anurag Bhandari, and Saroj Kumar Jha for their continuous support in preparing the manuscript as well as in the analysis of characterization techniques. The authors sincerely thank the Advanced Instrumentation Research Facility (AIRF), JNU, Delhi, India for providing sophisticated characterization techniques.

Declarations

Conflict of interest The authors declare that there is no conflict of interest.

Supplementary Information: The online version contains supplementary material available at https://doi.org/10.1007/s10854-021-07445-6.

References

1. R. Ramírez-Amador, J. Alvarado, G. Flores-Carrasco, L. Morales-Delagarza, S. Alcántara-Iniesta, A. Luna-Flores, Y.P. Bernal, M.Á. Méndezrojas, J.J. Gervacio-Arciniega, H.P. Martínez Hernández, J.F. Curioca-Vega, The influence of deposition time on the structural, morphological, optical and electrical properties of ZnO-rGO nanocomposite thin films grown in a single step by USP. Curr. Comput.-Aided Drug Des. **10**(2), 73 (2020). https://doi.org/10.3390/cryst10020073
2. I. Sameera, R. Bhatia, V. Prasad, R.J.A.P.L. Menon, Temperature dependent current-voltage characteristics of zinc oxide nanowire/polypyrrole nanocomposite. Appl. Phys. Lett. **105**(23), 232112 (2014). https://doi.org/10.1063/1.4903923
3. Liyana, G.R., Sofyan, N., Dhaneswara, D., Subhan, A., Yuwono, A.H.: Optoelectronic properties of ZnO nanorods thin films derived from chemical bath deposition with different growth times. In: AIP Conference Proceedings, vol. 1, p. 030008. AIP Publishing LLC. (2020) https://doi.org/10.1063/5.0015869
4. D. Nath, S. Mandal, D. Deb, J. Rakshit, P. Dey, J.J.J.O.A.P. Roy, Light tuning DC and AC electrical properties of ZnO-rGO based hybrid nanocomposite film. J. Appl. Phys. **123**(9), 095115 (2018). https://doi.org/10.1063/1.5016098
5. J. Yin, F. Gao, C. Wei, Q.J.S.R. Lu, Water amount dependence on morphologies and properties of ZnO nanostructures in double-solvent system. Sci. Rep. **4**(1), 1–7 (2014). https://doi.org/10.1038/srep03736
6. M. Morsy, I. Yahia, H. Zahran, F. Meng, M.J.J.O.E.M. Ibrahim, Portable and battery operated ammonia gas sensor based on CNTs/rGO/ZnO nanocomposite. J. Electron. Mater. **48**(11), 7328–7335 (2019). https://doi.org/10.1007/s11664-019-07550-7
7. Y. Zhao, L. Liu, T. Cui, G. Tong, W.J.A.S.S. Wu, Enhanced photocatalytic properties of ZnO/reduced graphene oxide sheets (rGO) composites with controllable morphology and composition. Appl. Surf. Sci. **412**, 58–68 (2017). https://doi.org/10.1016/j.apsusc.2017.03.207
8. Y. Liu, Y. Hu, M. Zhou, H. Qian, X.J.A.C.B.E. Hu, Microwave-assisted non-aqueous route to deposit well-dispersed ZnO nanocrystals on reduced graphene oxide sheets with improved photoactivity for the decolorization of dyes under visible light. Appl. Catal. B **125**, 425–431 (2012). https://doi.org/10.1016/j.apcatb.2012.06.016
9. S.-C. Weng, S. Brahma, C.-C. Chang, J.L.J.I.J.E.S. Huang, Synthesis of self-assembled hollow-sphere ZnO/rGO nanocomposite as anode materials for lithium-ion batteries. Int. J. Electrochem. Sci **14**, 3727–3739 (2019). https://doi.org/10.20964/2019.04.63
10. Z.K. Bolaghi, S. Masoudpanah, M.J.M.R.B. Hasheminiasari, Photocatalytic activity of ZnO/RGO composite synthesized by one-pot solution combustion method. Mater. Res. Bull. **115**, 191–195 (2019). https://doi.org/10.1016/j.materresbull.2019.03.024
11. Z. Liu, L. Yu, F. Guo, S. Liu, L. Qi, M. Shan, X.J.A.S.S. Fan, Facial development of high performance room temperature NO2 gas sensors based on ZnO nanowalls decorated rGO nanosheets. Appl. Surf. Sci. **423**, 721–727 (2017). https://doi.org/10.1016/j.apsusc.2017.06.160
12. Z. Zhan, L. Zheng, Y. Pan, G. Sun, L.J.J.O.M.C. Li, Self-powered, visible-light photodetector based on thermally reduced graphene oxide–ZnO (rGO–ZnO) hybrid nanostructure. J. Mater. Chem. **22**(6), 2589–2595 (2012). https://doi.org/10.1039/C1JM13920G
13. H. Abdullah, N.A. Atiqah, A. Omar, I. Asshaari, S. Mahalingam, Z. Razali, S. Shaari, J. Mandeep, H.J.J.O.M.S.M.I.E. Misran, Structural, morphological, electrical and electron transport studies in ZnO–rGO (wt%= 0.01, 0.05 and 0.1) based dye-sensitized solar cell. J. Mater. Sci. **26**(4), 2263–2270 (2015). https://doi.org/10.1007/s10854-015-2679-y
14. K.P. Madhuri, K. Bramhaiah, N.S.J.M.R.E. John, Nanoscale photocurrent distribution in ultra-thin films of zinc oxide nanoparticles and their hybrid with reduced graphene oxide. Mater. Res. Exp. **3**(3), 035004 (2016). https://doi.org/10.1088/2053-1591/3/3/035004
15. S. Tiagulskyi, R. Yatskiv, H. Faitova, Š Kučerová, J. Vaniš, J.J.M.S.I.S.P. Grym, Electrical properties of nanoscale pn heterojunctions formed between a single ZnO nanorod and GaN substrate. Mater. Sci. Semicond **107**, 104808 (2020). https://doi.org/10.1016/j.mssp.2019.104808
16. Y. Al-Hadeethi, R.I. Badran, A. Umar, S.H. Al-Heniti, B.M. Raffah, S.J.M.E. Al-Zhrani, Electrical properties of Ga-doped ZnO nanowires/Si heterojunction diode. Mater. Exp. **10**(6), 794–801 (2020). https://doi.org/10.1166/mex.2020.1725
17. S. Nongthombam, S. Sinha, N.A. Devi, S. Rai, R. Bhujel, W.I. Singh, B.P. Swain, Charge Transfer Mechanism of Gallium Nitrite/Reduced Graphene Oxide (GaN/rGO) Nanocomposite. In: 2020 IEEE VLSI device circuit and system (VLSI DCS) 2020, pp. 171–175. IEEE. https://doi.org/10.1109/VLSIDCS47293.2020.9179877
18. M. Soylu, M.J.J.O.A. Coskun, Compounds: controlling the properties of ZnO thin films by varying precursor concentration. J. Alloys Compds. **741**, 957–968 (2018). https://doi.org/10.1016/j.jallcom.2018.01.079
19. S.K. Mandal, K. Dutta, S. Pal, S. Mandal, A. Naskar, P.K. Pal, T. Bhattacharya, A. Singha, R. Saikh, S.J.M.C. De, Physics: Engineering of ZnO/rGO nanocomposite photocatalyst towards rapid degradation of toxic dyes. Mater. Chem.

Phys. **223**, 456–465 (2019). https://doi.org/10.1016/j.matchemphys.2018.11.002

20. M. Darvishi, F. Jamali-Paghaleh, M. Jamali-Paghaleh, J.J.S. Seyed-Yazdi, Interfaces: Facile synthesis of ZnO/rGO hybrid by microwave irradiation method with improved photoactivity. Surf. Interfaces **9**, 167–172 (2017). https://doi.org/10.1016/j.surfin.2017.09.008
21. T.N. Reddy, J. Manna, R.K.J.A.A.M. Rana, interfaces: Polyamine-mediated interfacial assembly of rGO-ZnO nanostructures: a bio-inspired approach and enhanced photocatalytic properties. ACS Appl. Mater. Interfaces **7**(35), 19684–19690 (2015). https://doi.org/10.1021/acsami.5b04820
22. D.A. Reddy, R. Ma, T.K.J.C.I. Kim, Efficient photocatalytic degradation of methylene blue by heterostructured ZnO–RGO/RuO2 nanocomposite under the simulated sunlight irradiation. Ceram. Int. **41**(5), 6999–7009 (2015). https://doi.org/10.1016/j.ceramint.2015.01.155
23. M. Ghorbani, M.R. Golobostanfard, H.J.A.S.S. Abdizadeh, Flexible freestanding sandwich type ZnO/rGO/ZnO electrode for wearable supercapacitor. Appl. Surf. Sci. **419**, 277–285 (2017). https://doi.org/10.1016/j.apsusc.2017.05.060
24. P. Sengunthar, K. Bhavsar, C. Balasubramanian, U.J.A.P.A. Joshi, Physical properties and enhanced photocatalytic activity of ZnO-rGO nanocomposites. Appl. Phys. A **126**(7), 1–9 (2020). https://doi.org/10.1007/s00339-020-03753-6
25. D.C. Marcano, D.V. Kosynkin, J.M. Berlin, A. Sinitskii, Z. Sun, A. Slesarev, L.B. Alemany, W. Lu, J.M.J.A.N. Tour, Improved synthesis of graphene oxide. ACS Nano **4**(8), 4806–4814 (2010). https://doi.org/10.1021/nn1006368
26. O.J.C. Akhavan, The effect of heat treatment on formation of graphene thin films from graphene oxide nanosheets. Carbon **48**(2), 509–519 (2010). https://doi.org/10.1016/j.carbon.2009.09.069
27. R. Bomila, A. Venkatesan, S.J.O. Srinivasan, Structural, luminescence and photocatalytic properties of pure and octylamine capped ZnO nanoparticles. Optik **158**, 565–573 (2018). https://doi.org/10.1016/j.ijleo.2017.12.141
28. H.-H. Huang, K.K.H. De Silva, G. Kumara, M.J.S.R. Yoshimura, Structural evolution of hydrothermally derived reduced graphene oxide. Sci. Rep. **8**(1), 1–9 (2018). https://doi.org/10.1038/s41598-018-25194-1
29. J. Jayachandiran, J. Yesuraj, M. Arivanandhan, A. Raja, S.A. Suthanthiraraj, R. Jayavel, D.J.J.O.I. Nedumaran, O. Polymers, Materials: Synthesis and electrochemical studies of rGO/ZnO nanocomposite for supercapacitor application. J. Inorg. Organometall. Polym. Mater. **28**(5), 2046–2055 (2018). https://doi.org/10.1007/s10904-018-0873-0
30. G. Qu, G. Fan, M. Zhou, X. Rong, T. Li, R. Zhang, J. Sun, D.J.A.O. Chen, Graphene-modified ZnO nanostructures for low-temperature NO2 sensing. ACS Omeg **4**(2), 4221–4232 (2019). https://doi.org/10.1021/acsomega.8b03624
31. K. Ravi, B.S. Mohan, G.S. Sree, I.M. Raju, K. Basavaiah, B.V.J.I.J.C.S. Rao, ZnO/RGO nanocomposite via hydrothermal route for photocatalytic degradation of dyes in presence of visible light. Int J Chem Stud **6**(6), 20–26 (2018)
32. K. Arora, S. Srivastava, P.R. Solanki, N.K.J.I.S.J. Puri, Electrochemical hydrogen gas sensing employing palladium oxide/reduced graphene oxide (PdO-rGO) nanocomposites. IEEE Sens. J. **19**(18), 8262–8271 (2019). https://doi.org/10.1109/JSEN.2019.2918360
33. B.D. Cullity, *Elements of X-ray Diffraction* (Addison-Wesley Publishing, Boston, 1956)
34. A. Goktas, A. Tumbul, Z. Aba, M.J.T.S.F. Durgun, Mg doping levels and annealing temperature induced structural, optical and electrical properties of highly c-axis oriented ZnO: Mg thin films and Al/ZnO: Mg/p-Si/Al heterojunction diode. Thin Solid Films **680**, 20–30 (2019)
35. A. Tumbul, F. Aslan, S. Demirozu, A. Goktas, A. Kilic, M. Durgun, M.Z.J.M.R.E. Zarbali, Solution processed boron doped ZnO thin films: influence of different boron complexes. Mater. Res. Exp. **6**(3), 035903 (2018). https://doi.org/10.1088/2053-1591/aaf4d8
36. H. Mohseni, H. Shokrollahi, I. Sharifi, K.J.J.O.M. Gheisari, M. Materials, Magnetic and structural studies of the Mn-doped Mg–Zn ferrite nanoparticles synthesized by the glycine nitrate process. J. Magn. Magn. Mater. **324**(22), 3741–3747 (2012)
37. D. Bobade, S. Rathod, M.L.J.P.B.C.M. Mane, Sol–gel auto-combustion synthesis, structural and enhanced magnetic properties of Ni2+ substituted nanocrystalline Mg–Zn spinel ferrite. Physica B **407**(18), 3700–3704 (2012). https://doi.org/10.1016/j.physb.2012.05.017
38. P. Labhane, L. Patle, V. Huse, G. Sonawane, S.J.C.P.L. Sonawane, Synthesis of reduced graphene oxide sheets decorated by zinc oxide nanoparticles: crystallographic, optical, morphological and photocatalytic study. Chem. Phys. Lett. **661**, 13–19 (2016). https://doi.org/10.1016/j.cplett.2016.08.041
39. A. Goktas, F. Aslan, I.H.J.J.O.M.S.M.I.E. Mutlu, Annealing effect on the characteristics of La 0.67 Sr 0.33 MnO3 polycrystalline thin films produced by the sol–gel dip-coating process. J. Mater. Sci. **23**(2), 605–611 (2012)
40. A. Goktas, F. Aslan, B. Yeşilata, I.J.M.S.I.S.P. Boz, Physical properties of solution processable n-type Fe and Al co-doped ZnO nanostructured thin films: role of Al doping levels and annealing. Mater. Sci. Semicond. Process. **75**, 221–233 (2018). https://doi.org/10.1016/j.mssp.2017.11.033
41. Y.-L. Chen, Z.-A. Hu, Y.-Q. Chang, H.-W. Wang, Z.-Y. Zhang, Y.-Y. Yang, Wu, H.-Y.J.T.J.o.P.C.C., Zinc oxide/

reduced graphene oxide composites and electrochemical capacitance enhanced by homogeneous incorporation of reduced graphene oxide sheets in zinc oxide matrix. J. Phys. Chem. C **115**(5), 2563–2571 (2011). https://doi.org/10.1021/jp109597n

42. A. Göktaş, A. Tumbul, F.J.J.O.S.-G.S. Aslan, Technology: Grain size-induced structural, magnetic and magnetoresistance properties of Nd 0.67 Ca 0.33 MnO3 nanocrystalline thin films. J Sol-Gel Sci Technol **78**(2), 262–269 (2016)
43. S. Dewan, M. Tomar, R. Tandon, V.J.J.O.A.P. Gupta, Zn doping induced conductivity transformation in NiO films for realization of pn homo junction diode. J. Appl. Phys. **121**(21), 215307 (2017). https://doi.org/10.1063/1.4984580
44. X. Liu, L. Pan, Q. Zhao, T. Lv, G. Zhu, T. Chen, T. Lu, Z. Sun, C.J.C.E.J. Sun, UV-assisted photocatalytic synthesis of ZnO–reduced graphene oxide composites with enhanced photocatalytic activity in reduction of Cr (VI). Chem. Eng. J. **183**, 238–243 (2012). https://doi.org/10.1016/j.cej.2011.12.068
45. B. Li, H.J.J.O.M.C. Cao, ZnO@ graphene composite with enhanced performance for the removal of dye from water. J. Mater. Chem. **21**(10), 3346–3349 (2011). https://doi.org/10.1039/C0JM03253K
46. L. Shi, S.J.N.R.I. Gunasekaran, Preparation of pectin–ZnO nanocomposite. Nanoscale Res. Lett. **3**(12), 491–495 (2008). https://doi.org/10.1007/s11671-008-9185-6
47. N. Bano, I. Hussain, A. El-Naggar, A.J.A.P.A. Albassam, Reduced graphene oxide nanocomposites for optoelectronics applications. Appl. Phys. **125**(3), 1–7 (2019). https://doi.org/10.1007/s00339-019-2518-8
48. M.E. Uddin, R.K. Layek, N.H. Kim, D. Hui, J.H.J.C.P.B.E. Lee, Preparation and properties of reduced graphene oxide/polyacrylonitrile nanocomposites using polyvinyl phenol. Compos. B **80**, 238–245 (2015). https://doi.org/10.1016/j.compositesb.2015.06.009
49. S. Kumar, V. Pandit, K. Bhattacharyya, V.J.M.C. Krishnan, Physics: Sunlight driven photocatalytic reduction of 4-nitrophenol on Pt decorated ZnO-RGO nanoheterostructures. Mater. Chem. Phys. A **214**, 364–376 (2018). https://doi.org/10.1016/j.matchemphys.2018.04.113
50. C. Rodwihok, D. Wongratanaphisan, Y.L. Thi Ngo, M. Khandelwal, S.H. Hur, J.S.J.N. Chung, Effect of GO additive in ZnO/rGO nanocomposites with enhanced photosensitivity and photocatalytic activity. Nanomaterials **9**(10), 1441 (2019). https://doi.org/10.3390/nano9101441
51. R. Beura, P.J.J.O.P. Thangadurai, C.O. Solids, Structural, optical and photocatalytic properties of graphene-ZnO nanocomposites for varied compositions. J. Phys. Chem. Solids **102**, 168–177 (2017). https://doi.org/10.1016/j.jpcs.2016.11.024
52. H. Fan, X. Zhao, J. Yang, X. Shan, L. Yang, Y. Zhang, X. Li, M.J.C.C. Gao, ZnO–graphene composite for photocatalytic degradation of methylene blue dye. Catal. Commun. **29**, 29–34 (2012). https://doi.org/10.1016/j.catcom.2012.09.013
53. Y.T. Li, J.M. Xu, Z.J. Tang, T.T. Xu, X.J.J.J.O.A. Li, Compounds: Nearly white light photoluminescence from ZnO/rGO nanocomposite prepared by a one-step hydrothermal method. J. Alloys Compds. **715**, 122–128 (2017). https://doi.org/10.1016/j.jallcom.2017.04.286
54. X. Díez-Betriu, S. Álvarez-García, C. Botas, P. Álvarez, J. Sánchez-Marcos, C. Prieto, R. Menéndez, A.J.J.O.M.C.C. De Andrés, Raman spectroscopy for the study of reduction mechanisms and optimization of conductivity in graphene oxide thin films. J. Mater. Chem. C **1**(41), 6905–6912 (2013)
55. H. Liu, M. Xiang, X.J.J.O.M.S. Shao, Graphene/ZnO nanocomposite with seamless interface renders photoluminescence quenching and photocatalytic activity enhancement. J. Mater. Sci. **53**(19), 13924–13935 (2018). https://doi.org/10.1007/s10853-018-2605-9
56. S. Demirezen, A. Kaya, Ö. Vural, ŞJ.M.S.I.S.P. Altındal, The effect of Mo-doped PVC+ TCNQ interfacial layer on the electrical properties of Au/PVC+ TCNQ/p-Si structures at room temperature. Mater. Sci. Semicond. Process **33**, 140–148 (2015). https://doi.org/10.1016/j.mssp.2015.01.050
57. S.A. Yerişkin, M. Balbaşı, I.J.J.O.M.S.M.I.E. Orak, The effects of (graphene doped-PVA) interlayer on the determinative electrical parameters of the Au/n-Si (MS) structures at room temperature. J. Mater. Sci. Mater. Electron. **28**(18), 14040–14048 (2017). https://doi.org/10.1007/s10854-017-7255-1
58. S. Safa, R. Sarraf-Mamoori, R. Azimirad, The effects of reduced graphene oxide (rGO) on ZnO film UV-detector. In: Advanced Materials Research 2014, pp. 577–582. Trans Tech Publ. https://doi.org/10.4028/www.scientific.net/AMR.829.577
59. A. Eroğlu, S. Demirezen, Y. Azizian-Kalandaragh, S.S.J.J.O.M.S.M.I.E. Altındal, A comparative study on the electrical properties and conduction mechanisms of Au/n-Si Schottky diodes with/without an organic interlayer. J. Mater. Sci **31**(17), 14466–14477 (2020). https://doi.org/10.1007/s10854-020-04006-1
60. M. Mohiuddin, B. Kumar, S.J.B.C.I.E. Haque, Biopolymer composites in photovoltaics and photodetectors. Biopolym. Compos. Electron. **45**, 459–486 (2017). https://doi.org/10.1016/B978-0-12-809261-3.00017-6
61. B. Murali, S.J.D.T. Krupanidhi, Transport properties of CuIn 1–x Al x Se 2/AZnO heterostructure for low cost thin film photovoltaics. Dalton Trans. **43**(5), 1974–1983 (2014). https://doi.org/10.1039/C3DT52515E

62. X. Yan, H. Hao, Y. Chen, S. Shi, E. Zhang, J. Lou, Liu, B.J.N.R.l., Self-rectifying performance in the sandwiched structure of Ag/In-Ga-Zn-O/Pt bipolar resistive switching memory. Nanoscale Res. Lett. **9**(1), 1–6 (2014). https://doi.org/10.1186/1556-276X-9-548
63. E. Tanrıkulu, S. Demirezen, Ş Altındal, İJ.J.O.M.S.M.I.E. Uslu, Analysis of electrical characteristics and conduction mechanisms in the Al/(% 7 Zn-doped PVA)/p-Si (MPS) structure at room temperature. J Mater Sci **28**(12), 8844–8856 (2017). https://doi.org/10.1007/s10854-017-6613-3
64. S. Demirezen, S.A.J.P.B. Yerişkin, A detailed comparative study on electrical and photovoltaic characteristics of Al/p-Si photodiodes with coumarin-doped PVA interfacial layer: the effect of doping concentration. Polym. Bull. **77**(1), 49–71 (2020). https://doi.org/10.1007/s00289-019-02704-3
65. S. Demirezen, H. Çetinkaya, M. Kara, F. Yakuphanoğlu, ŞJ.S. Altındal, A.A. Physical, Synthesis, electrical and photo-sensing characteristics of the Al/(PCBM/NiO: ZnO)/p-Si nanocomposite structures. Sens. Actuators A **317**, 112449 (2021). https://doi.org/10.1016/j.sna.2020.112449
66. Chiu, F.-C., Pan, T.-M., Kundu, T.K., Shih, C.-H.: Thin film applications in advanced electron devices. In. Hindawi, (2014). https://doi.org/10.1155/2014/927358

Journal of Alloys and Compounds 955 (2023) 170178

Contents lists available at ScienceDirect

Journal of Alloys and Compounds

journal homepage: www.elsevier.com/locate/jalcom

Zinc oxide incorporated molybdenum diselenide nanosheets for chemiresistive detection of ethanol gas

Nikita Jain, Nitin K. Puri *,[1]

Nanomaterials Research Laboratory (NRL), Department of Applied Physics, Delhi Technological University, Delhi 110042, India

ARTICLE INFO

Article history:
Received 13 January 2023
Received in revised form 13 April 2023
Accepted 16 April 2023
Available online 17 April 2023

Keywords:
$MoSe_2$/ZnO nanocomposite
Electrophoretic deposition
Chemiresistive
Ethanol sensing
Heterojunction

ABSTRACT

Herein, a room-temperature chemiresistive ethanol gas sensor based on hydrothermally synthesized zinc oxide (ZnO) incorporated-molybdenum diselenide ($MoSe_2$) nanosheets was demonstrated. The sensing properties of the $MoSe_2$/ZnO nanocomposite sensor were investigated systematically by exposing the sensor to various ethanol gas concentrations (10–500 ppm) in dry N_2 and dry air. The synergistic effect due to the incorporation of ZnO nanorods in $MoSe_2$ nanosheets was found to enhance the sensor response to ethanol gas (when operated in dry N_2) with improved response and recovery time of 8.4 and 14.7 s respectively, high selectivity, stability, and reproducibility. The nanocomposite-based sensor showed high gas sensing response (R_g/R_a) of 37.8 to 500 ppm of ethanol gas. While the response of the nanocomposite-based sensor decreased to 15.3, to 500 ppm of ethanol gas in dry air which suggests that the sensor performs better when operated in dry N_2 than in dry air. On the basis of experimental results, a plausible mechanism has been proposed based on the formation of p-n heterojunction and potential barrier modulation at the interface of the $MoSe_2$/ZnO nanocomposite sensor. The results demonstrated that $MoSe_2$/ZnO-based nanocomposite may pave the way for the fabrication of ethanol gas sensors for real-time electronics applications.

1. Introduction

Rapid industrialization and socio-economic development have resulted in the release of volatile organic compounds (VOCs) in the environment [1,2]. Exposure to most VOCs, not only causes environmental pollution but is also detrimental to human health. One of the typical VOCs "ethanol gas", is extensively used as a valuable ingredient in alcoholic beverages, paints, medicines, cosmetics, etc [3,4]. Despite its numerous applications in a variety of fields, its long-term exposure causes various ailments such as eye and skin irritation, headaches, nausea, vomiting, kidney failure, and even damage the central nervous system [5,6]. Therefore, it is the need of the hour to timely monitor and detects ethanol gas, especially at room-temperature (RT) as a part of the safety system. Among various types of sensors developed by scientists for the effective detection of VOCs, chemiresistive sensors have generated huge interest due to their low-cost, simple monitoring techniques, easy design, and high chemical and thermal stability [7,8].

Recently molybdenum diselenide ($MoSe_2$), a two-dimensional (2D) transition metal dichalcogenides (TMDs) has attracted considerable attention for multifunctional applications due to its significant physical and chemical properties [9,10]. Its outstanding gas sensing properties have been explored owing to the large surface-to-volume ratio which provides elevated sites for the adsorption and desorption of target gasses [11]. In addition to this, it also exhibits higher adsorption energy with chemical molecules [12]. Some pioneering studies based on the gas sensing properties of $MoSe_2$ have been investigated (targeting several analytes like H_2S, NH_3, NO_2 C_2H_5OH, etc.) which led a path to explore this material in-depth [13–16]. Jha et al. studied the gas sensing properties of $MoSe_2$ for the detection of H_2S gas down to the ppb level. But pristine $MoSe_2$ showed a recovery time of 5 min at 90 °C [13]. Late et al. used a single-layer $MoSe_2$-based NH_3 gas sensor at RT. The sensor displayed a bit large response (2.5 min) and recovery (9 min) time [14]. In another report, Singh et al. made use of liquid-exfoliated $MoSe_2$ nanosheets for RT ammonia sensing. The corresponding response and recovery times were 15 s and 135 s respectively [15]. In another study, Zhang et al. reported the sensing potential of $MoSe_2$ toward ethanol gas at 90 °C. It was observed that the nanosheets took a long time to restore its original state at RT. Although the temperature was raised higher, still the recovery time was 5 min [16]. Therefore, these

---

* Corresponding author.
E-mail address: nitinkumarpuri@dtu.ac.in (N.K. Puri).
[1] ORCID: 0000-0003-2563-3747

https://doi.org/10.1016/j.jallcom.2023.170178
0925-8388/

studies demonstrate that pristine $MoSe_2$-based gas sensors exhibit sluggish response and recovery time which challenges the use of intrinsic $MoSe_2$-based gas sensors. In this regard, various strategies have been employed to improve the sensor performance of $MoSe_2$ gas sensors such as synthesizing composites, combining with noble metals (gold (Au), silver (Ag), platinum (Pt), etc.), surface functionalization, and many more. For instance, Jha et al. demonstrated the use of reduced graphene oxide/molybdenum diselenide nanocomposite for the detection of ammonia at RT. The sensor showed the limit of detection down to 300 ppb, with an operating voltage of 2 mV [17]. Li et al. prepared pristine $MoSe_2$ and Ag-modified $MoSe_2$-based ethanol gas sensors at RT. The sensor exhibited a low detection limit, good response properties, and excellent repeatability [10]. Abun et al. fabricated a hydrogen gas sensor based on p-n heterostructures comprising exfoliated $MoSe_2$ nanosheets doped on the surface of n-type ZnO nanorods. The hybrid p-n heterostructure showed better sensor response in comparison to pristine ZnO and $MoSe_2$ [18]. Hence it is clear from the above studies that modification of $MoSe_2$ with other elements provides alternate strategies for the development of practical gas sensors. This encourages us to explore $MoSe_2$/ZnO nanocomposite for ethanol sensing application which can effectively improve the response/recovery time of the existing 2D nanomaterials-based ethanol sensors.

To the best of our knowledge, there are no reports available focussing on hydrothermal synthesis of ZnO incorporated- $MoSe_2$ nanosheets-based nanocomposite towards their utilization for the chemiresistive detection of ethanol gas at RT. The sensor was recovered in two different environments i.e., in dry N_2 and dry air. Various characterization techniques are employed to confirm the successful synthesis of the as-synthesized nanocomposite. For fabricating the ethanol sensor, $MoSe_2$/ZnO nanocomposite powder so-obtained is deposited on indium tin oxide (ITO) coated corning glass substrate using a facile electrophoretic deposition (EPD) technique. The as-fabricated sensor is exposed to various ethanol gas concentrations (10–500 ppm) and its response is systematically investigated at RT. The synergistic effect due to the incorporation of ZnO in $MoSe_2$ is explained in detail and a sensing mechanism is proposed based on this.

2. Experimental

2.1. Chemical profile

The chemicals used in the synthesis were Sodium Molybdate Dihydrate ($Na_2MoO_4.2H_2O$), Selenium (Se) powder, Hydrazine Hydrate-86% ($N_2H_4.H_2O$), Zinc Acetate ($Zn(CH_3COO)_2{\cdot}2H_2O$), Sodium Hydroxide (NaOH) pellets, and Ethanol (C_2H_5OH). All the chemicals were purchased from Sigma Aldrich and were employed without further purification.

2.2. Synthesis procedure

A facile hydrothermal method was used to synthesize ZnO incorporated- $MoSe_2$ nanosheet-based nanocomposite. Fig. 1 displays the schematic of the fabrication process. Firstly, $MoSe_2$ nanosheets were synthesized. Typically, 2 mmol of sodium molybdate dihydrate was dissolved in deionized (DI) water and ethanol (volume 1:1) with stirring for 45 min to obtain a clear solution. Meanwhile, a solution containing selenium powder (4 mmol) was prepared separately in 10 mL hydrazine hydrate-86% with stirring. It was followed by the addition of selenium solution in sodium molybdate dehydrate solution dropwise under continuous stirring for 45 min. Then, the above mixture was transferred into a 50 mL hydrothermal autoclave and was kept at 220 °C for 24 h. After several washings with DI and ethanol, the black color powder was obtained which was then dried overnight at 100 °C.

Then, ZnO nanorods were prepared by dropping 5 mol of sodium hydroxide solution in 0.5 mol of zinc acetate dihydrate solution under continuous stirring for 45 min. Then, the above solution was kept in an oven at 120 °C in a 100 mL hydrothermal autoclave for 24 h. After washing it with DI water and ethanol, the white color powder so obtained was left for drying at 80 °C.

For preparing $MoSe_2$/ZnO nanocomposite, a quantitative amount of $MoSe_2$ and ZnO synthesized by the above procedure were dispersed in ethanol and sonicated for 2 h. The dispersed solution was transferred to a 100 mL hydrothermal autoclave and heated at 120 °C for 24 h. The final product was washed with DI and ethanol to yield gray color powder which was then dried overnight in a vacuum.

2.3. Sensor fabrication for ethanol gas sensing

For fabricating the ethanol sensor, $MoSe_2$/ZnO nanocomposite powder so-obtained was deposited on pre-hydrolyzed indium tin oxide (ITO) coated corning glass substrate using electrophoretic deposition (EPD) technique. $MoSe_2$/ZnO nanocomposite powder was dispersed in a suitable solvent with a concentration of 1 mg/mL. This dispersion was ultrasonicated for 2 h. The dispersed solution was then poured into a 2-electrode glass cell comprising copper as a connector to attach the working electrode (WE) and platinum as the counter electrode (CE). The ITO was attached to WE and an optimized constant potential was applied for 60 s. The film so formed of $MoSe_2$/ZnO nanocomposite was left for drying. Finally, silver (Ag) contacts were made on the prepared films with the help of the thermal evaporation technique. A similar process was devised to obtain pristine-$MoSe_2$ and pristine-ZnO films. These films were used for performing sensing measurements.

2.4. Gas sensing experimental set-up

The gas sensing behavior of the $MoSe_2$/ZnO nanocomposite-based chemiresistive gas sensor was investigated in a customized stainless steel (SS) chamber by the use of 1% ethanol balanced with nitrogen (N_2) gas. The chamber was attached to two gas mass flow controllers (MFC). The MFC was used to maintain the flow of the target gas analyte and dry N_2/ dry air (standard composition: N_2 = 79% and O_2 = 21% by volume) inside the chamber. A source measuring unit was employed to provide a constant current supply to the as-fabricated ethanol gas sensor. A rotary pump was connected to the SS chamber to create rough vacuum pressure. A digital hygrometer was employed to measure the relative humidity (RH) in the SS chamber. Ethanol gas sensing was performed by introducing the dry N_2/ dry air first to sustain standard ambient conditions for 50 s. Thereafter, ethanol (1%) / nitrogen (99%) mixture was introduced inside the SS chamber for 100 s at different concentrations like 10, 100, 200, 300, 400, and 500 ppm at RT. The formula given below (Eq. 1) was used to calculate the concentration of ethanol gas in the SS chamber:

$$C = \frac{22.4 \times \Psi \times \rho \times V_1}{M \times V_2} \times 1000 \tag{1}$$

In the above formula (Eq. 1), C is the concentration of ethanol gas (ppm), Ψ is the required gas volume fraction, ρ is the density of ethanol ($kg.m^{-3}$), V_1 is the volume of ethanol gas, M is the molecular weight of ethanol ($kg.mol^{-1}$), and V_2 is the volume of the SS chamber (m^3) [19,20]. The change in resistance of sensing films was recorded using a Lab-View data acquisition software connected to the source measuring unit. The gas sensing measurements of the sensing films were carried out at room-temperature (27 °C) and relative humidity (29 %). The selectivity performance of as-fabricated ethanol gas sensors was investigated with other VOC gases like acetone, benzene, and formaldehyde.

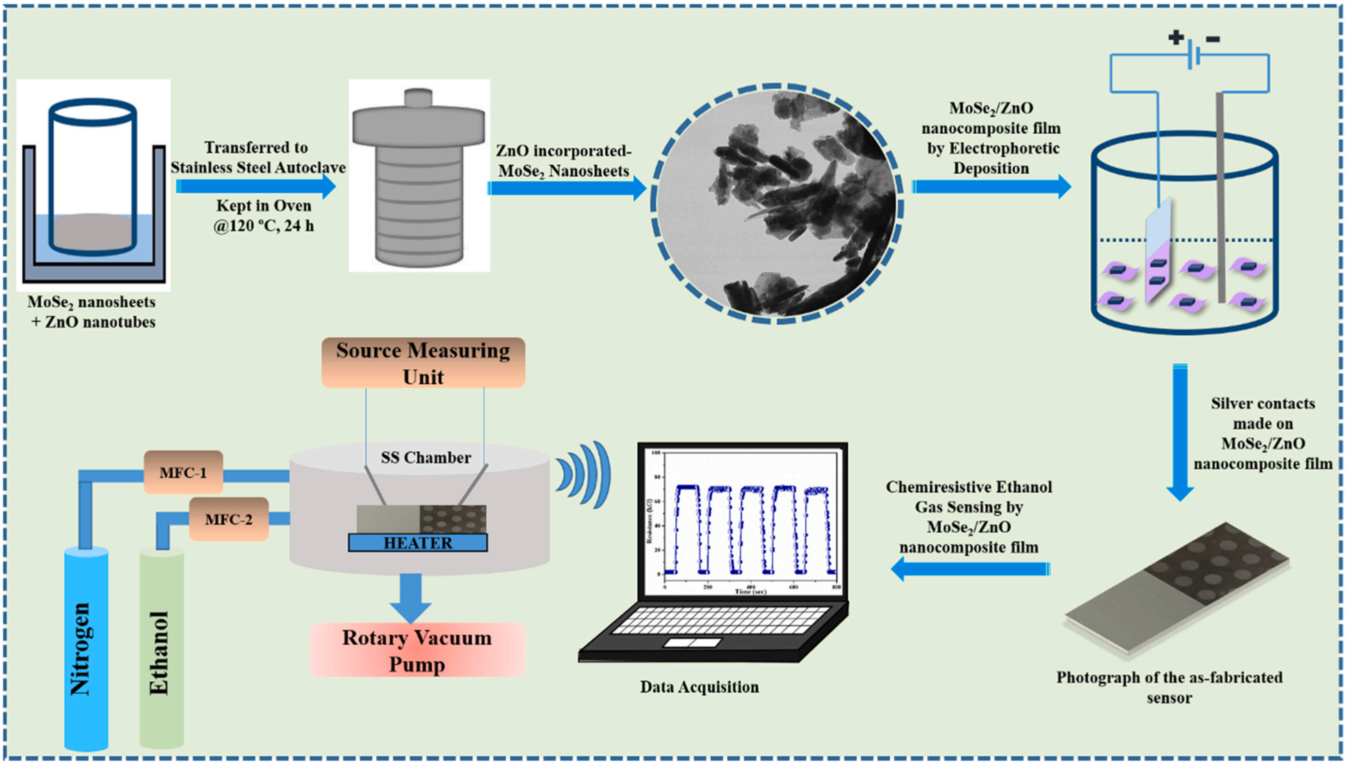

Fig. 1. Step-by-step preparation of $MoSe_2$/ZnO nanocomposite sensor for the detection of ethanol gas.

3. Results and discussions

3.1. Structural analysis using XRD

The crystallographic structure of the as-synthesized pristine-$MoSe_2$, pristine-ZnO, and $MoSe_2$/ZnO nanocomposite is investigated using XRD (Fig. 2). The diffraction peaks of as-synthesized pristine-$MoSe_2$ (Fig. 2a) are attributed to the (002), (100), (103) and (110) planes of the hexagonal phase of $MoSe_2$ (JCPDS 029–0914) [21]. XRD pattern of ZnO (Fig. 2b) shows all the diffraction peaks which are congruous with the standard data available for the wurtzite structure of ZnO (JCPDS 36–1451) [22]. The diffractogram of the $MoSe_2$/ZnO nanocomposite (Fig. 2c) consists of all the peaks corresponding to ZnO nanorods and some major planes of (002), (100), and (110) corresponding to $MoSe_2$ which indicates the successful interaction between $MoSe_2$ nanosheets and ZnO nanorods. The reason for the invisibility of two other planes of $MoSe_2$ i.e. (004) and (103) can be ascribed to the much higher intensity of ZnO diffraction peaks [23]. In addition to this, there is a decrease in the intensity of diffraction peaks of $MoSe_2$ and ZnO in $MoSe_2$/ZnO nanocomposite which further confirms the formation of nanocomposite [24].

It is also observed that there is a shift in the diffraction peaks of the nanocomposite with respect to the pristine materials in Figs. 2a and 2b. To confirm the shifting of diffraction peaks in the nanocomposite, zoomed highest intensity diffraction peaks of pristine-$MoSe_2$ (100) and ZnO (101) were considered (Fig. 2(d) and Fig. 2(e)) for comparison. As can be seen in Fig. 2(d), the (100) diffraction peak of $MoSe_2$/ZnO nanocomposite is slightly shifted to a higher diffraction angle (31.76°) compared to the (100) diffraction peak of pristine-$MoSe_2$ (31.67°). Similarly, in Fig. 2(e), the (101) diffraction peak of the nanocomposite is slightly shifted to a lower diffraction angle (36.24°) compared to the (101) diffraction peak of pristine-ZnO (36.27°). This shift can correspond to the lattice mismatch between the pristine materials or strain generated in the nanocomposite after interaction during the synthesis [25].

3.2. Microstructure analysis using HRTEM

The high-resolution transmission electron microscopy HR-TEM images of pristine-$MoSe_2$, pristine-ZnO, and $MoSe_2$/ZnO nanocomposite are shown in Fig. 3. Figs. 3a and 3b display a large area of $MoSe_2$ nanosheets stacked over one another, which are wrinkled and curled at the edges. The fine lattice fringes of $MoSe_2$ nanosheets can be seen in Fig. 3c with the interplanar spacing of 0.28 nm which is related to the (100) lattice plane of $MoSe_2$. Fig. 3d shows an HRTEM image of ZnO nanorods and Fig. 3e shows the measured interplanar spacing of 0.24 nm which corresponds to the (101) lattice plane of ZnO nanorods. Evidence for modification of the $MoSe_2$ nanosheets by ZnO nanorods is given in Figs. 3f and 3g, which shows the successful incorporation of ZnO nanorods in $MoSe_2$ nanosheets. A clear heterogeneous interface between $MoSe_2$ nanosheets and ZnO nanorods can be seen in $MoSe_2$/ZnO nanocomposite at a 200 nm and 100 nm scale bar. The corresponding selected area electron diffraction (SAED) pattern of the $MoSe_2$/ZnO nanocomposite is shown in Fig. 3h. Hence from the HRTEM analysis, the successful incorporation of ZnO nanorods in $MoSe_2$ nanosheets is evident, which is consistent with the XRD analysis as well.

3.3. Study of vibrational modes using Raman spectroscopy

The Raman spectrum of pristine-$MoSe_2$, pristine-ZnO, and $MoSe_2$/ZnO nanocomposite acquired using an excitation wavelength of 532 nm is shown in Fig. 4. Raman spectroscopy measurements of $MoSe_2$ shows a strong out-of-plane mode A_{1g} mode at 238 cm^{-1} which is the characteristic peak of $MoSe_2$ [26]. The other two in-plane modes E_{1g} and E^1_{2g} of $MoSe_2$ are observed at 167 cm^{-1} and 283 cm^{-1} which are in good agreement with the earlier reports [15]. Fig. 4 shows an intense Raman peak of ZnO at 437 cm^{-1} (E_2^{high}) which is the characteristic peak of the hexagonal wurtzite phase of ZnO [27].

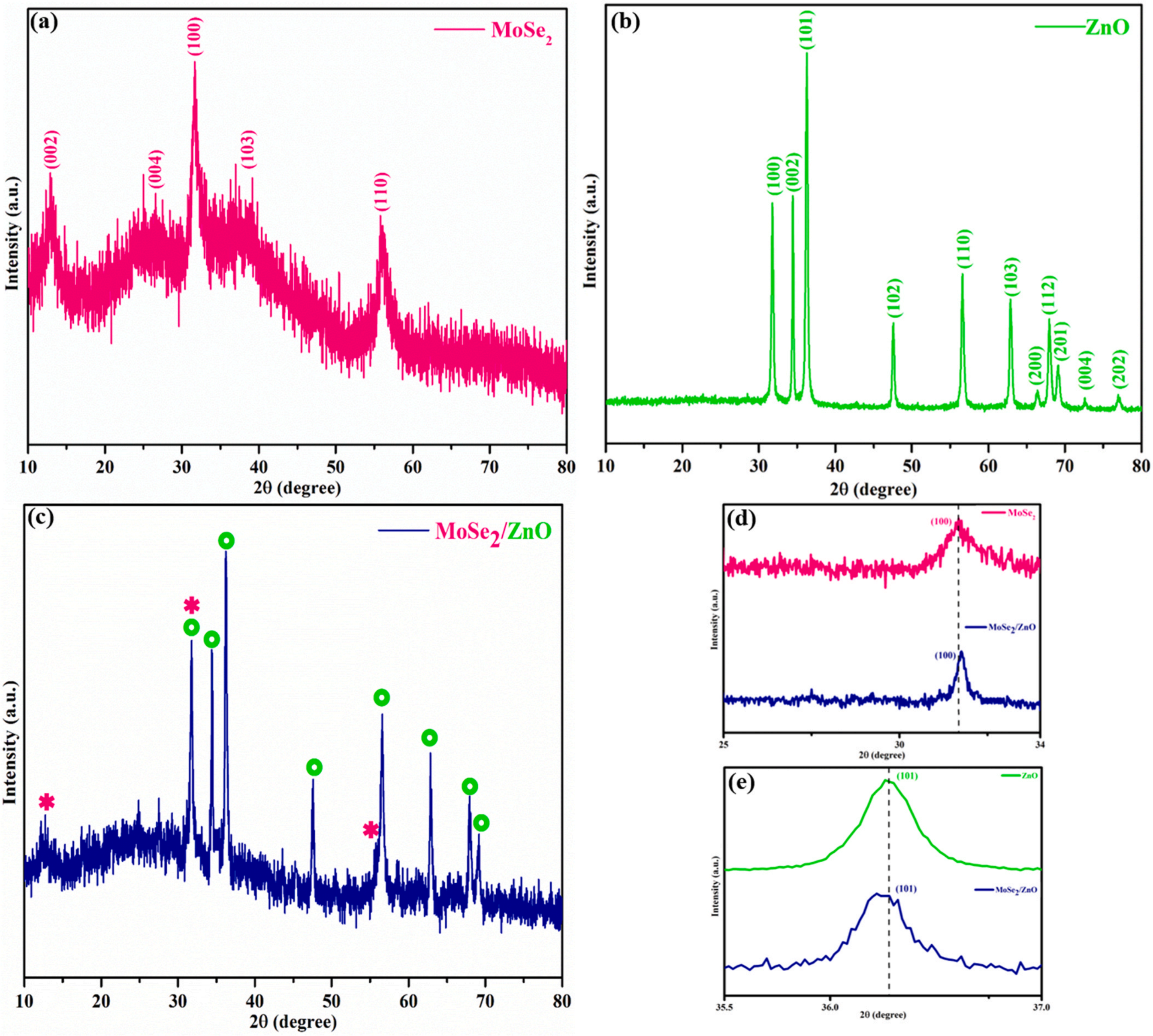

Fig. 2. XRD pattern of the as-synthesized (a) pristine-MoSe$_2$, (b) pristine-ZnO, (c) MoSe$_2$/ZnO nanocomposite, (d) zoomed (100) diffraction peak of pristine-MoSe$_2$ and MoSe$_2$/ZnO nanocomposite, and (e) zoomed (101) diffraction peak of pristine-ZnO and MoSe$_2$/ZnO nanocomposite.

The corresponding spectrum of MoSe$_2$/ZnO nanocomposite in Fig. 4 displays the presence of modes belonging to both MoSe$_2$ and ZnO. In addition to this, it is noted that the modes in MoSe$_2$/ZnO nanocomposite are shifted from their respective position in their individual spectrum in Figs. 4a and 4b. In the MoSe$_2$/ZnO nanocomposite, there is a red shift in the A_{1g} mode (233.7 cm^{-1}) corresponding to MoSe$_2$ as well as in the E_2^{high} (431.3 cm^{-1}) mode corresponding to ZnO. This is attributed to the defects produced due to electronic interactions between MoSe$_2$ and ZnO during the hydrothermal synthesis process [28]. Hence, the Raman spectrum of MoSe$_2$/ZnO nanocomposites confirms that the nanocomposite is successfully synthesized, as confirmed by XRD and HRTEM analysis.

3.4. Identification of functional groups using Fourier Transform Infrared Spectroscopy (FTIR)

FTIR Spectroscopy is performed to investigate and elucidate the presence of functional groups in the prepared samples of pristine-MoSe$_2$, pristine-ZnO, and MoSe$_2$/ZnO nanocomposite in the range of 400 – 4000 cm^{-1}. Peaks in the FTIR spectrum of MoSe$_2$ nanosheets are observed corresponding to O-H (3420 cm^{-1}), C-H (2910 cm^{-1}), COO^{-1} (1620 cm^{-1}), Mo-O (1000–750 cm^{-1}), and Se-O-Se (420 cm^{-1}) as shown in Fig. 5 [29,30]. The FTIR spectrum of ZnO nanorods (Fig. 5) consists of peaks corresponding to O-H (3438 cm^{-1}), COOH (1620 and 1480 cm^{-1}), Zn-OH (920 cm^{-1}), and Zn-O (577 and 427 cm^{-1}) [27]. The corresponding spectrum of MoSe$_2$/ZnO nanocomposite in Fig. 5 displays the peaks corresponding to both MoSe$_2$ and ZnO. Furthermore, the peaks in the as-synthesized nanocomposite are shifted as compared to pristine-MoSe$_2$ and ZnO indicating the electronic interaction between the pristine materials. Hence, from the FTIR spectrum of MoSe$_2$/ZnO nanocomposite, the co-existence of both MoSe$_2$ and ZnO is confirmed which is in good accordance with the XRD analysis, Raman spectroscopy, and HRTEM observations.

3.5. Gas sensing performance

The gas sensor response characteristics of pristine-MoSe$_2$, and MoSe$_2$/ZnO nanocomposite are investigated towards different

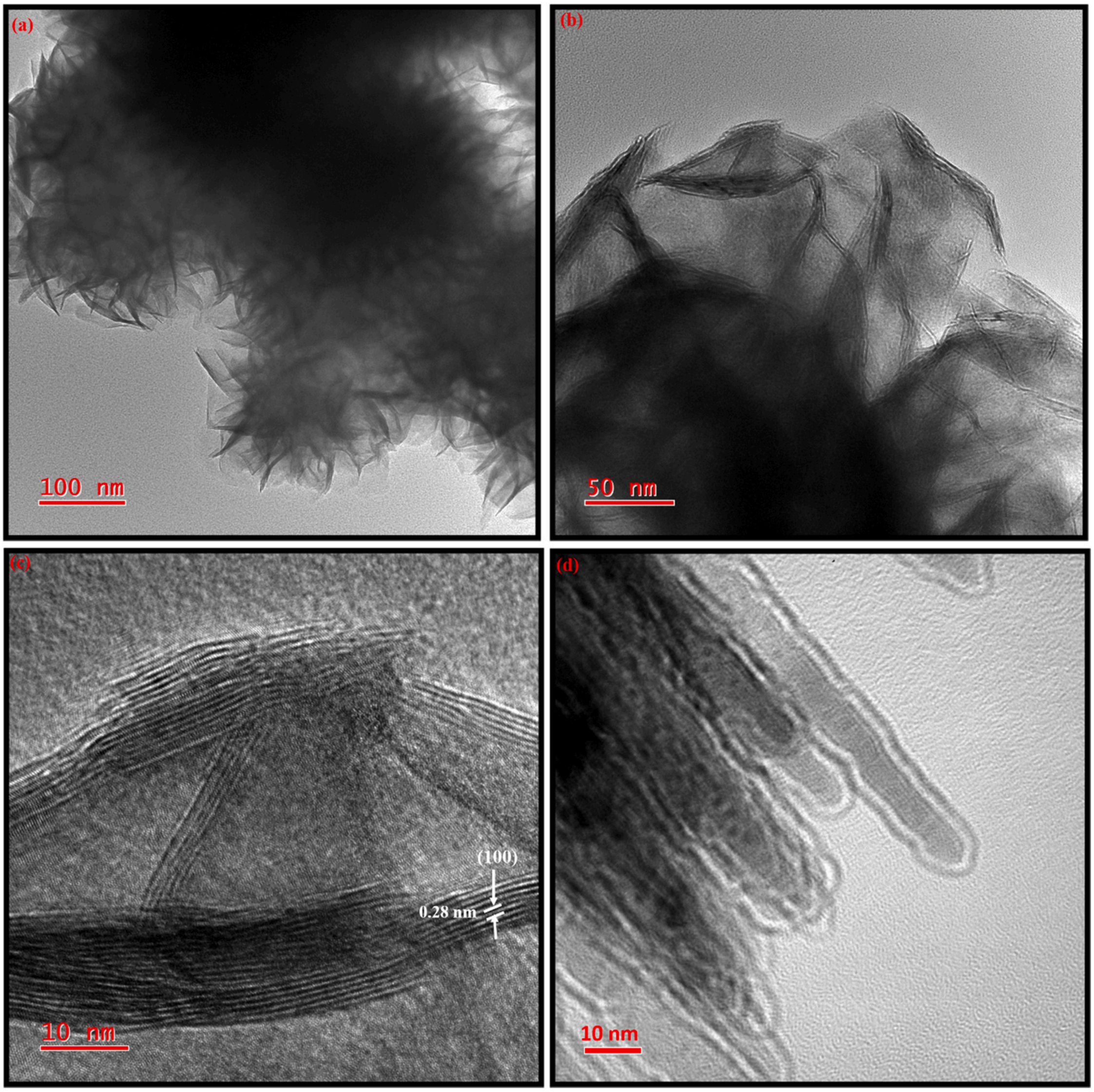

Fig. 3. HRTEM images of as-synthesized (a) and (b) pristine-$MoSe_2$ nanosheets (c) Lattice fringes of $MoSe_2$ nanosheets with measured interplanar spacing, (d) pristine-ZnO nanorods, (e) Measured Interplanar spacing of pristine-ZnO nanorods (f, g) $MoSe_2$/ZnO nanocomposite, and (h) corresponding SAED pattern of $MoSe_2$/ZnO nanocomposite.

ethanol concentrations ranging from 10-500 ppm at RT in dry N_2 as illustrated in Fig. 6a. Fig. S1 (Supporting Information) shows the response characteristics of pristine-ZnO towards different ethanol concentrations at RT in dry N_2. It can be observed in Fig. 6a that the sensing response (resistance versus time graph) of pristine-$MoSe_2$ is low and the resistance changes slightly under exposure to different concentrations of ethanol gas. However, the $MoSe_2$/ZnO nanocomposite sensor exhibited a much higher response towards the same concentration of ethanol gas. The response value (R_g/R_a) of the as-fabricated nanocomposite sensor is 37.8 to 500 ppm ethanol gas where R_g and R_a represent the value of the sensor's resistance in presence of ethanol gas mixture and dry N_2 respectively. But, the response from the same pristine-$MoSe_2$ and $MoSe_2$/ZnO nanocomposite sensor decreased significantly when recovered in dry air. Specifically, the response of 4.5 and 15.3 is obtained to 500 ppm ethanol gas for pristine-$MoSe_2$ and $MoSe_2$/ZnO nanocomposite sensor as shown in Fig. S2 (Supporting Information).

Therefore, the improved response of the nanocomposite sensor when operated in dry N_2 than dry air encouraged us to measure sensor performance in this environment. Fig. 6b defines three parameters that describe the properties of the sensor which are: the sensing response (R_g/R_a), the response time (t_{resp}), and the recovery time (t_{rec}). Firstly, we note that the resistance of the $MoSe_2$/ZnO nanocomposite sensor increased from base resistance R_a = 1.9 kΩ in dry N_2 to R_g = 71.9 kΩ when the sensor is exposed to 500 ppm of ethanol. The sensing response of the nanocomposite sensor is calculated using R_g and R_a values obtained and is found to be 37.8 at 500 ppm ethanol. This also suggests that the response of the nanocomposite sensor is p-type towards ethanol gas [10,16]. Furthermore, full recovery to the same base resistance is observed for both pristine and nanocomposite sensor. This reveals the reversible interaction between the as-fabricated nanocomposite sensor and ethanol gas due to the physisorption process. It is also evident from Fig. 6a and 6b. that the base resistance of the $MoSe_2$/ZnO nanocomposite sensor is higher as compared to the pristine-$MoSe_2$ sensor. The other two parameters are t_{resp} and t_{rec} which are calculated to be 11 s and 18 s for the pristine-$MoSe_2$ sensor respectively. An improvement in t_{resp} and t_{rec} is observed for $MoSe_2$/ZnO nanocomposite sensor and are found to be 8.4 s and 14.7 s respectively. A comparison of performance parameters such as sensing response, response, and recovery time of pristine- $MoSe_2$, pristine-ZnO, and ZnO/$MoSe_2$ nanocomposite sensor in dry N_2 is shown in Table S1 (Supporting Information). Therefore, the ZnO/$MoSe_2$ nanocomposite sensor exhibits a faster response than the pristine-$MoSe_2$.

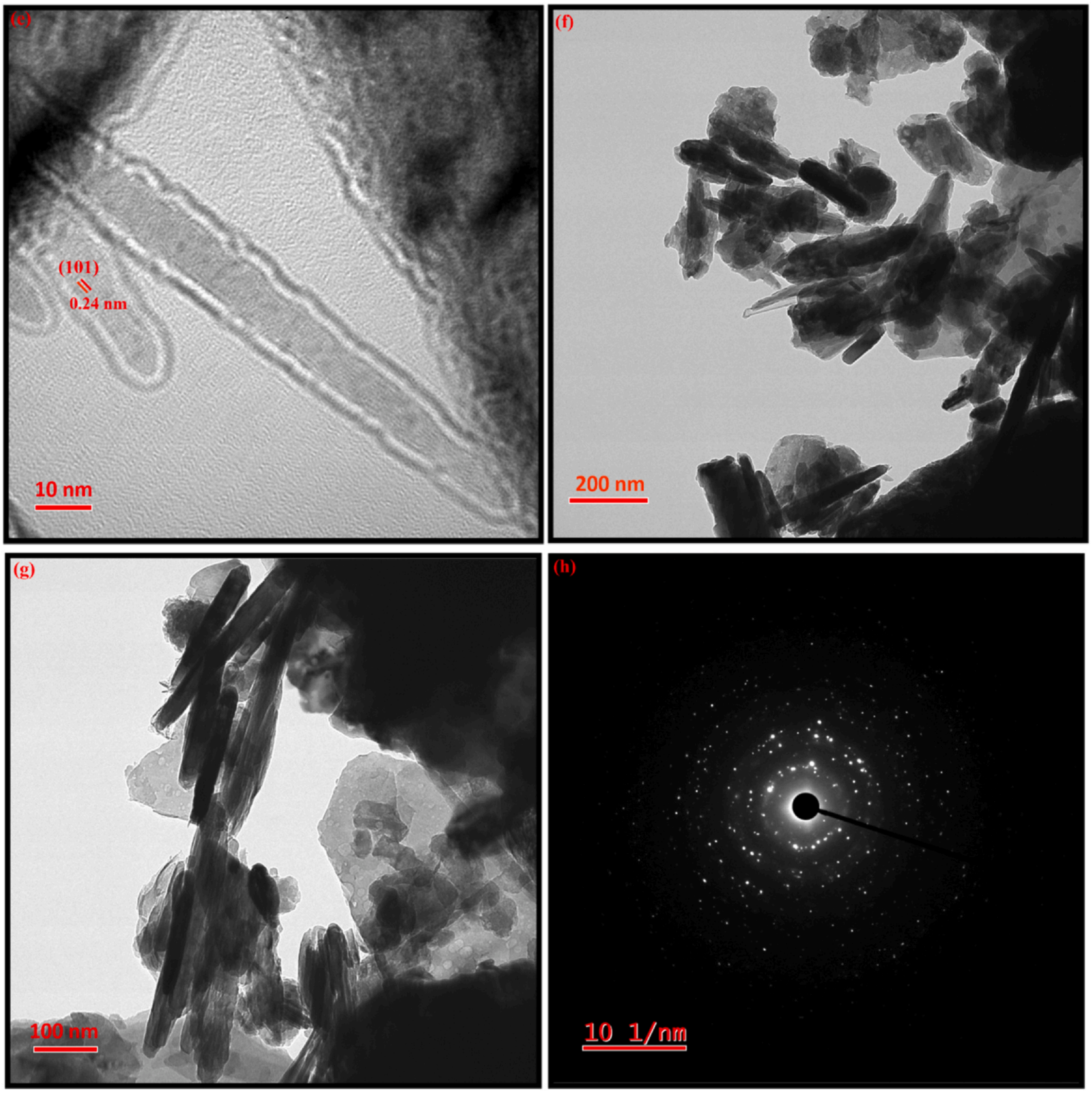

Fig. 3. (*continued*)

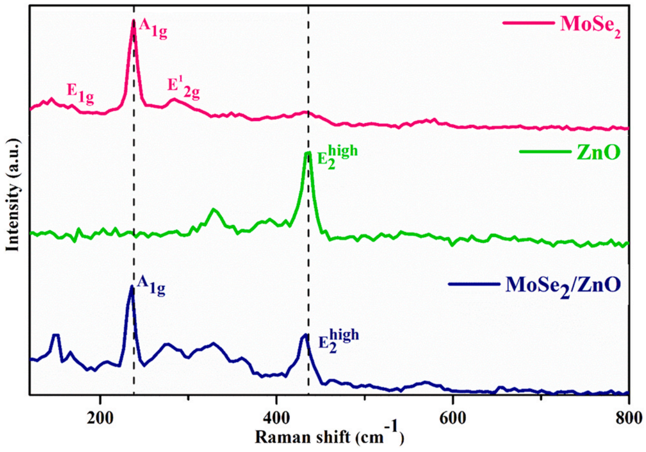

Fig. 4. Raman spectrum of the as-synthesized pristine-$MoSe_2$, pristine-ZnO, and $MoSe_2$/ZnO nanocomposite.

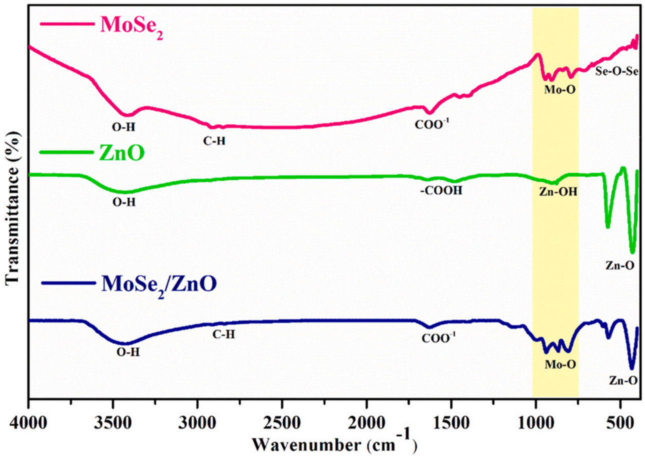

Fig. 5. FTIR spectrum of the as-synthesized pristine-$MoSe_2$, pristine-ZnO, and $MoSe_2$/ZnO nanocomposite.

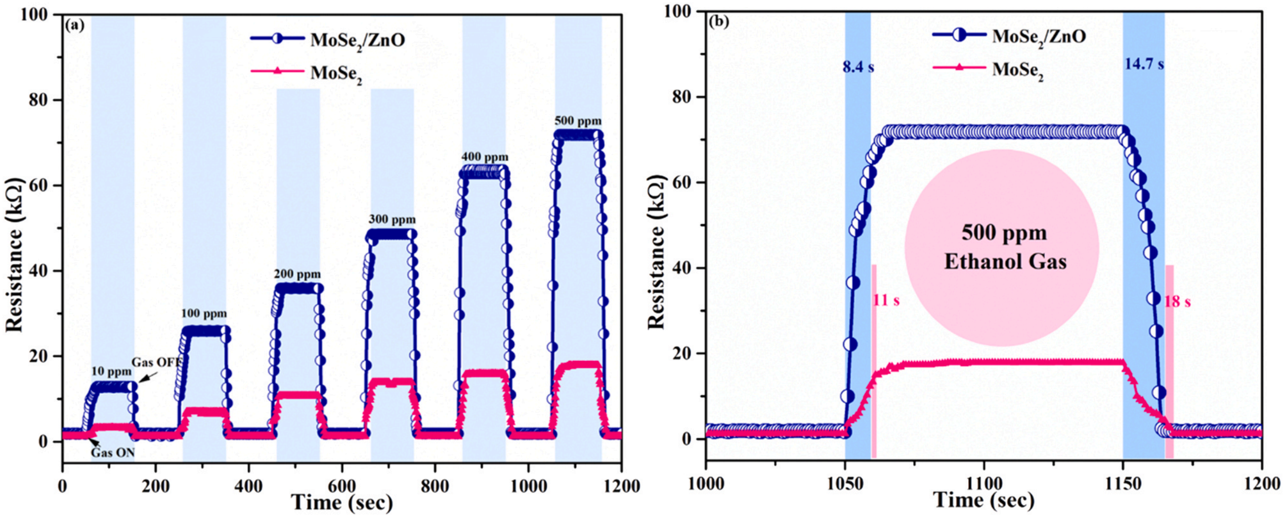

Fig. 6. (a) Resistance variation of pristine-$MoSe_2$ and $MoSe_2$/ZnO nanocomposite sensor wrt. to various ethanol concentrations at RT in dry N_2 and (b) The t_{resp} and t_{rec} characteristics of $MoSe_2$ and $MoSe_2$/ZnO nanocomposite sensor exposed to 500 ppm ethanol at RT in dry N_2.

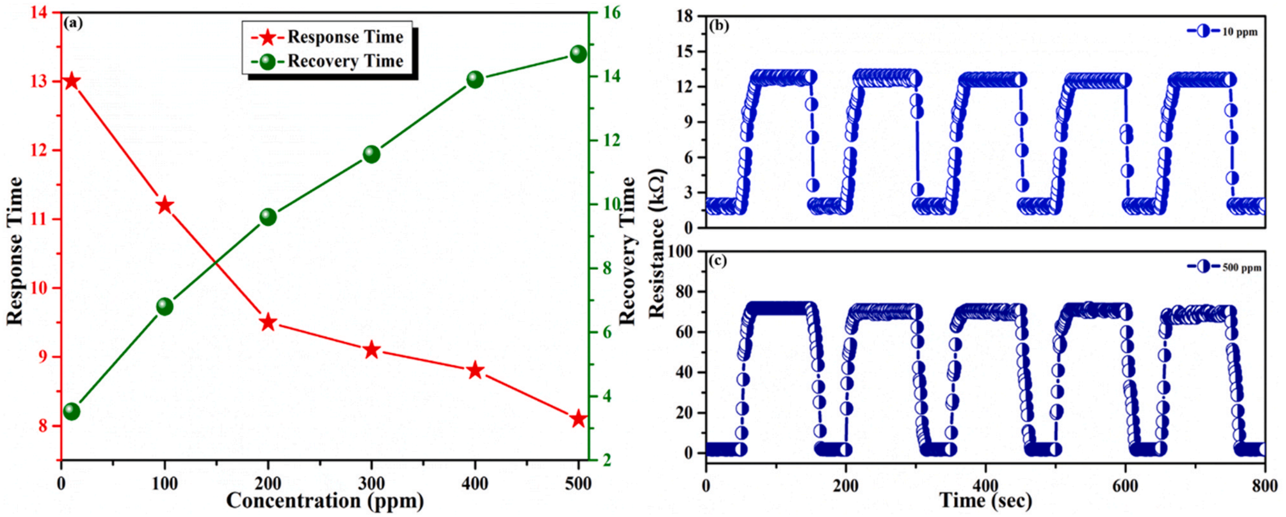

Fig. 7. (a) Response and recovery time versus concentration curves of ethanol for the $MoSe_2$/ZnO nanocomposite sensor at RT in dry N_2, (b) and (c) Five consecutive sensing cycles of the $MoSe_2$/ZnO nanocomposite sensor exposed to 10 and 500 ppm ethanol at RT in dry N_2.

Similarly, t_{resp} and t_{rec} of the $MoSe_2$/ZnO nanocomposite sensor are calculated for different ethanol gas concentrations and shown in Fig. 7a. It is observed that the t_{resp} decreases and the t_{rec} increases as the ethanol gas concentration increases from 10 to 500 ppm. The reason for a decrease in t_{resp} may be attributed to the availability of large sites on the sensor's surface for gas adsorption. On the other hand, the increase in t_{rec} may be due to the chemisorption of ethanol molecules and their reaction products which took time to desorb from the surface of the sensor [26].

Fig. 7b and 7c demonstrate the repeatability of the $MoSe_2$/ZnO nanocomposite sensor exposed to 10 ppm and 500 ppm ethanol gas at RT for five consecutive cycles respectively. The results suggest that the sensor exhibited almost the same response during each cycle.

For real-life applications, the gas sensor should have good stability. As shown in Fig. 8a the long-term stability of the $MoSe_2$/ZnO nanocomposite sensor is also conducted to evaluate its stability. The sensor is tested under 10 and 500 ppm of ethanol gas at RT at an interval of 7 days. The response values of the sensor showed no distinct changes in a month (30 days) which confirmed the excellent stability of the $MoSe_2$/ZnO nanocomposite sensor.

Selectivity is also a very important parameter for evaluating the sensor's performance. Fig. 8b shows the response of pristine-$MoSe_2$ and $MoSe_2$/ZnO nanocomposite sensors toward a few VOCs with a concentration of 500 ppm at RT, which involves ethanol, acetone, benzene, and formaldehyde. The corresponding bar chart depicts that $MoSe_2$/ZnO nanocomposite sensor is highly selective towards ethanol.

Table 1 compares the ethanol sensing properties of previous research work in terms of working temperature, response, and recovery time with our work. The comparative results demonstrate that $MoSe_2$/ZnO nanocomposite sensor have better response and recovery time, and operate at room-temperature. Therefore, $MoSe_2$/ZnO nanocomposite sensor has better sensing characteristics than others indicating that it can become a great potential candidate for ethanol gas sensing.

4. Ethanol sensing mechanism

The gas sensing mechanism is attributed to the change in resistance with respect to baseline due to the interaction of ethanol

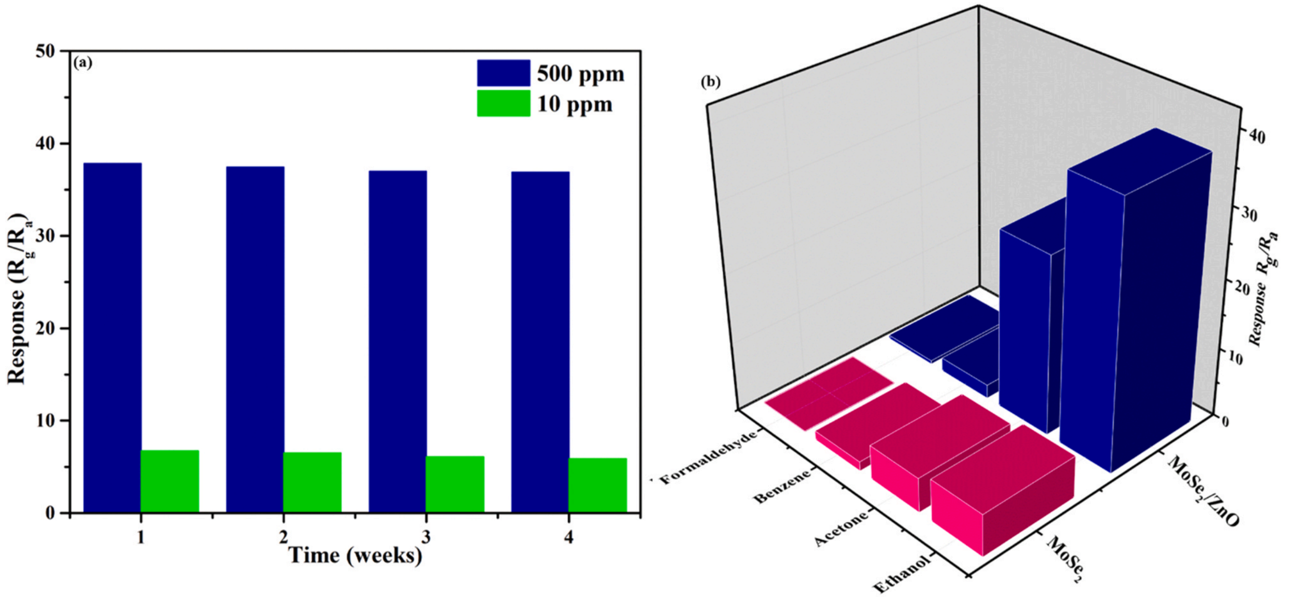

Fig. 8. (a) Long-term stability (30 days) under 500 ppm and 10 ppm ethanol at RT for the $MoSe_2/ZnO$ nanocomposite sensor in dry N_2, and (b) Corresponding response bar chart showing the selectivity of the $MoSe_2/ZnO$ nanocomposite sensor towards a few VOCs with a concentration of 500 ppm at RT in dry N_2.

Table 1
A comparison of performance parameters of this work with previous work for ethanol gas sensing.

Senor Materials	Concentration (ppm)	Sensor Response	Operating Temperature (°C)	Response/Recovery Time (sec)	Refs.
MoS_2/TiO_2	500	100%	300	70 ± 10 s / 90 ± 20 s	[3]
ZnO	500	32	160	14 / 13	[31]
Pd decorated ZnO	500	81%	260	6 / 95	[32]
WO_3/g-C_3N_4	500	62.5%	RT	30 / 25	[33]
$MoSe_2/ZnO$	500	37.8	RT	8.4 / 14.7	This work

molecules with the surface of the sensing material. From the response curves (Fig. 6a and 6 b), the pristine-$MoSe_2$ nanosheets exhibit a p-type character, pristine-ZnO exhibits an n-type character and $MoSe_2/ZnO$ nanocomposite sensor exhibits a p-type character. Based on these data, the sensing mechanism of pristine sensors as well as nanocomposite sensor is explained as follows:

The sensing behavior of $MoSe_2$ nanosheets showed a p-type characteristic response during ethanol gas exposure (Fig. 6a). It has been proved in the literature that, although semiconducting TMD nanosheets are intrinsically n-type, adsorption of oxygen molecules from the air atmosphere can introduce p-type doping [17,34]. During the synthesis, a number of defects are created in the $MoSe_2$ nanosheets. These defects act as an active point for the adsorption of oxygen molecules from the air atmosphere during the fabrication of process of the sensor [35]. The adsorbed oxygen molecules tend to trap electrons from the $MoSe_2$ nanosheets which creates a large number of oxygen ion species. These oxygen ion species induce the formation of a thick accumulation layer near the surface of $MoSe_2$ nanosheets. When the $MoSe_2$ nanosheets are exposed to ethanol gas, the electrons are donated by the ethanol to the $MoSe_2$ nanosheets as ethanol is a reducing agent. This results in decreasing the majority charge carrier concentration in $MoSe_2$ nanosheets and hence an increase in sensor resistance [13,36]. The gas sensing mechanism of pristine-ZnO is explained in Section-S.1. (Supporting Information).

A plausible mechanism for enhanced ethanol gas sensing of the $MoSe_2/ZnO$ nanocomposite sensor compared to the pristine-$MoSe_2$ and pristine-ZnO sensor can be explained by considering the p-n heterojunction generated at the interface of p-$MoSe_2$ and n-type ZnO [37]. Fig. 9a shows the schematic representation and energy band diagram of p-$MoSe_2$ nanosheets and n-type ZnO nanorods in air. The band gap of $MoSe_2$ and ZnO is 1.3 eV and 3.4 eV respectively [12,38,39]. The discrepancy of the bandgap in the nanocomposite is attributed to the formation of heterojunction between $MoSe_2$ and ZnO. The current-voltage characteristic curve of the $MoSe_2/ZnO$ nanocomposite sensor is also obtained at RT using Keithley 2450 SMU to confirm the existence of p-n heterojunction in the nanocomposite sensor (Supporting Information: Fig. S3). Under the scanning voltage of -2 V to +2 Vit can be seen that the reverse current of the nanocomposite sensor is smaller than the forward current which indicates the existence of p-n heterojunction at the interface of $MoSe_2$ nanosheets and ZnO nanorods [20,40]. The work function of n-type ZnO is 4.5 eV [39]. According to the literature, the work function of pure $MoSe_2$ is 4.65 eV, and the withdrawal of electrons from the nanosheets would increase the work function of $MoSe_2$ [41]. Therefore, the work function of ZnO is lower than that of $MoSe_2$. The distinction in the work function of $MoSe_2$ and n-type ZnO results in the diffusion of electrons from ZnO to $MoSe_2$ and the holes will diffuse from $MoSe_2$ to ZnO until an equilibrium of Fermi level is achieved. The energy band bends at the interface of $MoSe_2$ and ZnO as shown in Fig. 9b. An accumulation layer is formed at the interface of $MoSe_2$ to ZnO, where the electrons accumulate at the side of $MoSe_2$ and the holes accumulate at the side of ZnO. A potential barrier is formed due to carrier trapping at the interface of the $MoSe_2/ZnO$ nanocomposite which increased the resistance of the nanocomposite films in the air. As mentioned above, the R_a value of the $MoSe_2/ZnO$ nanocomposite sensor is higher as compared to the pristine-$MoSe_2$ sensor owing to the presence of an enhanced potential barrier (Fig. 6a). When the nanocomposite sensor is exposed to ethanol molecules (Fig. 9c), this results in thinning of the charge carrier accumulation layer near the surface of $MoSe_2$ nanosheets.

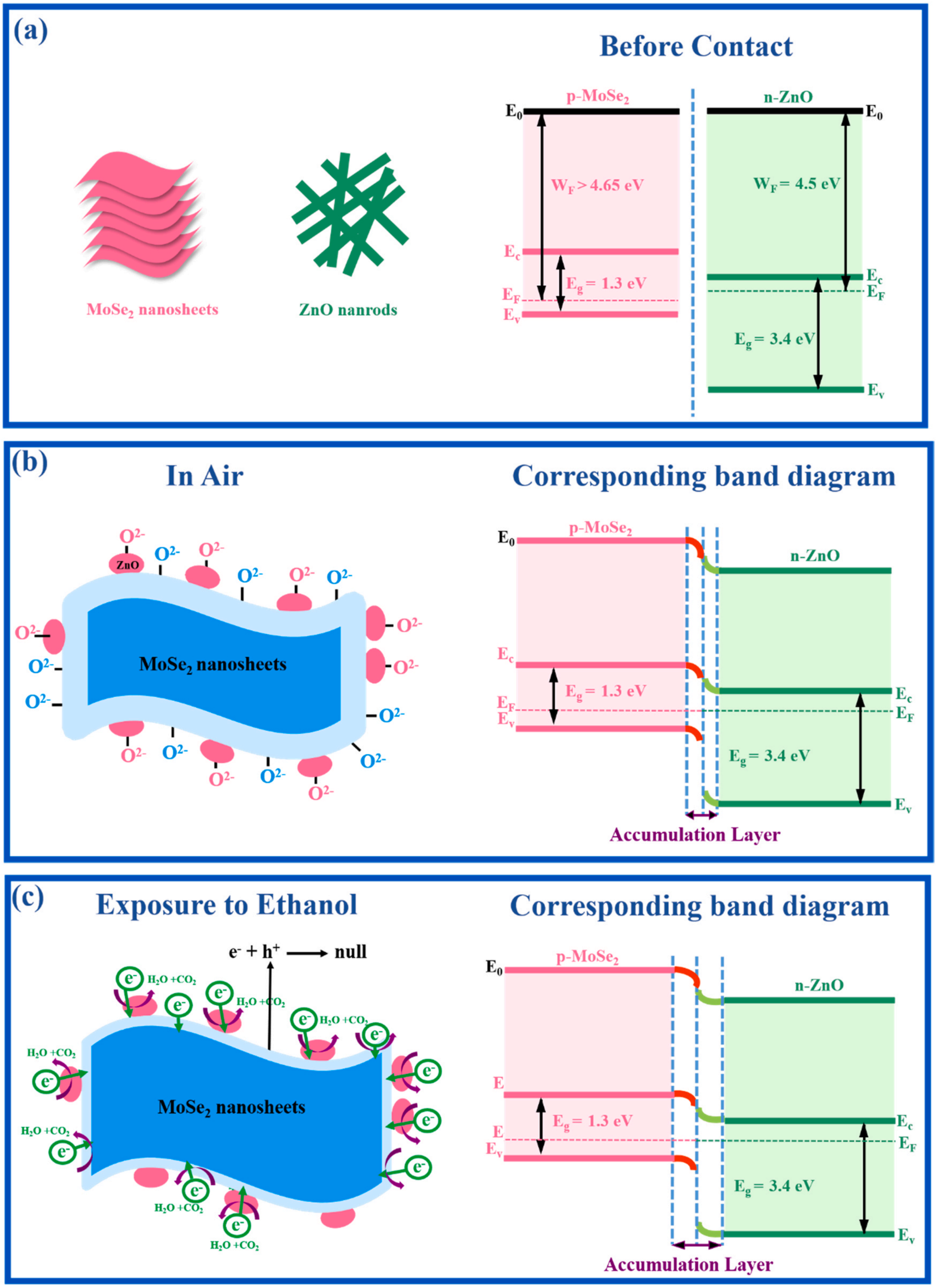

Fig. 9. Schematic representation and energy band diagram of ethanol gas sensing mechanism of $MoSe_2$/ZnO nanocomposite sensor in (a) before contact, (b) air condition, and (c) ethanol atmosphere.

The free electrons so released during this process neutralize the majority of charge carriers in the $MoSe_2$ nanosheets. Similarly, the released electrons on the surface of ZnO lead to more electron-hole recombination on the interface of $MoSe_2$ nanosheets and ZnO. Finally, the electron transfer from the ZnO to the $MoSe_2$ is impeded which overall results in an increased change in resistance and enhanced sensitivity [42]. The p-type behavior of the $MoSe_2$/ZnO nanocomposite sensor is similar to the pristine-$MoSe_2$ sensor, which suggests a synergistic effect between $MoSe_2$ nanosheets and ZnO nanorods in which p-type $MoSe_2$ nanosheets act as majority charge carriers [39,43].

The reason for a better response of pristine-$MoSe_2$ and $MoSe_2$/ZnO nanocomposite sensor to ethanol gas in dry N_2 than dry air can be explained as: It is evident from the literature that adsorption of oxygen on the surface of the $MoSe_2$ trap electrons from the $MoSe_2$ nanosheets by occupying the reactive sites on the surface of the sensing layer [35,44,45]. An increase in the baseline resistance of the sensor in the presence of dry air compared to dry N_2 (Supporting Information: Fig. S2) indicates that more reactive sites are occupied by oxygen thereby reducing the sensing response of the pristine-$MoSe_2$ sensor. As mentioned above, the p-type response of the nanocomposite sensor indicates that $MoSe_2$ nanosheets act as majority charge carriers. Hence, the response from the $MoSe_2$/ZnO nanocomposite sensor also decreased significantly when recovered in dry air.

From the above ethanol gas sensing results, we surmise that the superior gas sensing properties of $MoSe_2$/ZnO nanocomposite sensor in the presence of dry N_2 can contribute to the development of ethanol gas sensors with high sensitivity, good selectivity, stable repeatability, and fast adsorption/desorption at RT, which are suitable for practical applications.

5. Conclusions

A highly selective, stable, and reproducible chemiresistive ethanol gas sensor based on $MoSe_2$/ZnO nanocomposite was developed. Specifically, the response value of the as-fabricated nanocomposite sensor was 37.8 to 500 ppm ethanol gas when operated in dry N_2 and 15.3 to 500 ppm ethanol gas when operated in dry air. This suggests that the sensor performs better when operated in dry N_2 than in dry air. The sensor demonstrated a p-type characteristic response. Importantly, the sensor operates at room-temperature and can detect ethanol down to 10 ppm. The sensor also exhibited improved response (8.4 s) and recovery (14.7 s) time to 500 ppm ethanol gas compared to previously reported values. The enhancement in performance of the sensor was due to the formation of a p-n heterojunction at the interface of the $MoSe_2$ nanosheets and ZnO nanorods in $MoSe_2$/ZnO nanocomposite sensor. Furthermore, potential barrier modulation at the interface provided a positive effect on sensitivity performance. The results demonstrated that this work may open new avenues to engineer 2D nanomaterials/metal-oxide-based nanocomposites for the fabrication of ethanol gas sensors for real-time electronics applications.

CRediT authorship contribution statement

Nikita Jain: Conceptualization, Methodology, Investigation, Data curation, Writing – original draft. **Nitin K. Puri**: Conceptualization, Methodology, Writing – review & editing at different stages, Supervision.

Data availability

Data will be made available on request.

Declaration of Competing Interest

The authors declare that they have no known competing financial interests or personal relationships that could have appeared to influence the work reported in this paper.

Acknowledgments

The authors are grateful to the Hon'ble Vice-Chancellor, Delhi Technological University, Delhi, India for providing support and facilities for conducting quality research work. The authors are grateful to Dr. Saurabh Srivastava, Dr. Senthil Kumar Kandasamy, Dr. Kamal Arora, Dr. Archit Dhingra, Dr. Rishibrind K. Upadhyay, Ritika Khatri, Saroj Kumar Jha, Hemant K. Arora, Sunil Kumar, Anmol Aggarwal, and Ashi Mittal for their valuable review of the manuscript.

Appendix A. Supporting information

Supplementary data associated with this article can be found in the online version at doi:10.1016/j.jallcom.2023.170178.

References

[1] V. Shah, J. Bhaliya, G.M. Patel, P.J.T. i C. Joshi, Recent advancement in pd-decorated nanostructures for its catalytic and chemiresistive gas sensing applications: a review, Top. Catal. (2022) 1–41.
[2] A. Mirzaei, S. Leonardi, G.J.C. i Neri, Detection of hazardous volatile organic compounds (VOCs) by metal oxide nanostructures-based gas sensors: a review, Ceram. Int. 42 (14) (2016) 15119–15141.
[3] S. Singh, S.J.S. Sharma, A.B. Chemical, Temperature dependent selective detection of ethanol and methanol using MoS2/TiO2 composite, Sens. Actuators B Chem. 350 (2022) 130798.
[4] M.J. Ahemad, T.D. Le, D.-S. Kim, Y.-T.J.S. Yu, A.B. Chemical, Bimetallic AgAualloy@ ZnO core-shell nanoparticles for ultra-high detection of ethanol: potential impact of alloy composition on sensing performance, Sens. Actuators B Chem. 359 (2022) 131595.
[5] S.S. Scindia, R.B. Kamble, J.A.J.I.S.J. Kher, Organic surfactant assisted polypyrrole materials as effective chemiresistive gas sensors for VOCs and toxic gas detection, IEEE Sens. J. 20 (23) (2020) 14072–14080.
[6] D. Zhang, Y. Cao, J. Wu, X.J.A.S.S. Zhang, Tungsten trioxide nanoparticles decorated tungsten disulfide nanoheterojunction for highly sensitive ethanol gas sensing application, Appl. Surf. Sci. 503 (2020) 144063.
[7] T.T.N. Phan, et al., Hierarchically structured LaFeO3 with hollow core and porous shell as efficient sensing material for ethanol detection, Sens. Actuators B Chem. 354 (2022) 131195.
[8] N. Roy, et al., Paper based enzymatic chemiresistor for POC detection of ethanol in human breath, IEEE Sens. J. 20 (5) (2019) 2278–2286.
[9] G. Jeevanandham, K. Vediappan, Z.A. ALOthman, T. Altalhi, A.K.J.S. r Sundramoorthy, Fabrication of 2D-MoSe2 incorporated NiO nanorods modified electrode for selective detection of glucose in serum samples, Sci. Rep. 11 (1) (2021) 1–13.
[10] T. Li, S. Yu, Q. Li, M. Chi, P.J.N.J. o C. Li, Room temperature ethanol gas-sensing properties based on Ag-doped MoSe 2 nanoflowers: experimental and DFT investigation, New J. Chem. 45 (45) (2021) 21423–21428.
[11] S. Zhang, T.H. Nguyen, W. Zhang, Y. Park, W.J.A.P.L. Yang, Correlation between lateral size and gas sensing performance of MoSe2 nanosheets, Appl. Phys. Lett. 111 (16) (2017) 161603.
[12] Z. Yang, D. Zhang, D.J.S. Wang, Carbon monoxide gas sensing properties of metal-organic frameworks-derived tin dioxide nanoparticles/molybdenum diselenide nanoflowers, Sens. Actuators B Chem. 304 (2020) 127369.
[13] R.K. Jha, J.V. D'Costa, N. Sakhuja, N.J.S. Bhat, A.B. Chemical, MoSe2 nanoflakes based chemiresistive sensors for ppb-level hydrogen sulfide gas detection, Sens. Actuators B Chem. 297 (2019) 126687.
[14] D.J. Late, T. Doneux, and M.J. A p. l. Bougouma, Single-layer MoSe2 based NH3 gas sensor, Appl. Phys. Lett. 105 (23) (2014) 233103.
[15] S. Singh, J. Deb, U. Sarkar, S.J.A.A.N.M. Sharma, MoSe2 crystalline nanosheets for room-temperature ammonia sensing, ACS Appl. Nano Mater. 3 (9) (2020) 9375–9384.
[16] S. Zhang, W. Zhang, T.H. Nguyen, J. Jian, W.J.M.C. Yang, Synthesis of molybdenum diselenide nanosheets and its ethanol-sensing mechanism, Mater. Chem. Phys. 222 (2019) 139–146.
[17] R. Jha, A. Nanda, N.J.I.S.J. Bhat, Ammonia sensing performance of rGO-based chemiresistive gas sensor decorated with exfoliated MoSe 2 nanosheets, IEEE Sens. J. 21 (9) (2021) 10211–10218.
[18] A. Abun, B.-R. Huang, A. Saravanan, D. Kathiravan, P.-D.J.A.A.N.M. Hong, Exfoliated MoSe2 nanosheets doped on the surface of ZnO nanorods for hydrogen sensing applications, ACS Appl. Nano Mater. 3 (12) (2020) 12139–12147.
[19] Q. Chen, et al., Optimization ethanol detection performance manifested by gas sensor based on In2O3/ZnS rough microspheres, Sens. Actuators B Chem. 264 (2018) 263–278.
[20] J. Zhang, T. Li, J. Guo, Y. Hu, D.J.A.S.S. Zhang, Two-step hydrothermal fabrication of CeO2-loaded MoS2 nanoflowers for ethanol gas sensing application, Appl. Surf. Sci. 568 (2021) 150942.
[21] H.R. Inta, S. Ghosh, A. Mondal, G. Tudu, H.V. Koppisetti, V.J.A.A.E.M. Mahalingam, Ni0. 85Se/MoSe2 interfacial structure: an efficient electrocatalyst for alkaline hydrogen evolution reaction, ACS Appl. Energy Mater. 4 (3) (2021) 2828–2837.
[22] Y. Navale, S. Navale, M. Chougule, N. Ramgir, V.J.J. o M.S.M. i E. Patil, NO2 gas sensing properties of heterostructural CuO nanoparticles/ZnO nanorods, J. Mater. Sci. Mater. Electron. 32 (13) (2021) 18178–18191.
[23] Y. Huang, Y.-E. Miao, J. Fu, S. Mo, C. Wei, T.J.J. o M.C.A. Liu, Perpendicularly oriented few-layer MoSe 2 on SnO 2 nanotubes for efficient hydrogen evolution reaction, J. Mater. Chem. A 3 (31) (2015) 16263–16271.
[24] N. Elavarasan, et al., Integrating gC3N4 nanosheet with MoS2 and ZnO-Ag: remarkably enhanced photocatalytic performance under visible-light irradiation, Colloid Interface Sci. Commun. 44 (2021) 100474.
[25] N. Roy, R. Sinha, H.B. Nemade, T.K.J.J. o A. Mandal, Synthesis of MoS2-CuO nanocomposite for room temperature acetone sensing application, J. Alloy. Compd. 910 (2022) 164891.

[26] X.T. Tran, S. Poorahong, M.J.R. a Siaj, One-pot hydrothermal synthesis and selective etching method of a porous MoSe 2 sand rose-like structure for electrocatalytic hydrogen evolution reaction, RSC Adv. 7 (82) (2017) 52345–52351.

[27] N. Jain, S. Sharma, N.K.J.J. o M.S.M. i E. Puri, Investigation of charge transport mechanism in hydrothermally synthesized reduced graphene oxide (rGO) incorporated zinc oxide (ZnO) nanocomposite films, J. Mater. Sci. Mater. Electron. 33 (3) (2022) 1307–1323.

[28] U. Krishnan, et al., MoS2/ZnO nanocomposites for efficient photocatalytic degradation of industrial pollutants, Mater. Res. Bull. 111 (2019) 212–221.

[29] M.S. Vidhya, R. Yuvakkumar, P.S. Kumar, G. Ravi, D.J.T. i C. Velauthapillai, Hydrothermal synthesis of flower like MnSe2@ MoSe2 electrode for supercapacitor applications, Top. Catal. 65 (5) (2022) 615–622.

[30] A. Mishra, J. Narang, C.S. Pundir, R. Pilloton, M.J.A. o Khanuja, Morphology-preferable MoSe2 nanobrooms as a sensing platform for highly selective aptacapturing of salmonella bacteria, ACS Omega 3 (10) (2018) 13020–13027.

[31] G. Ren, et al., ZnO@ ZIF-8 core-shell microspheres for improved ethanol gas sensing, Sens. Actuators B Chem. 284 (2019) 421–427.

[32] P. Cao, et al., Ethanol sensing behavior of Pd-nanoparticles decorated ZnO-nanorod based chemiresistive gas sensors, Sens. Actuators B Chem. 298 (2019) 126850.

[33] S. Vijayakumar, S.J.O. Vadivel, L. Technology, Fiber optic ethanol gas sensor based WO3 and WO3/gC3N4 nanocomposites by a novel microwave technique, Opt. Laser Technol. 118 (2019) 44–51.

[34] H. Nan, et al., Strong photoluminescence enhancement of MoS2 through defect engineering and oxygen bonding, ACS Nano 8 (6) (2014) 5738–5745.

[35] H. Qiu, L. Pan, Z. Yao, J. Li, Y. Shi, and X.J.A.P.L. Wang, Electrical characterization of back-gated bi-layer MoS2 field-effect transistors and the effect of ambient on their performances, 100 (12) (2012) 123104.

[36] J. Jaiswal, A. Das, V. Chetry, S. Kumar, R.J.S. Chandra, NO2 sensors based on crystalline MoSe2 porous nanowall thin films with vertically aligned molecular layers prepared by sputtering, Sens. Actuators B Chem. 359 (2022) 131552.

[37] P. Zhao et al., One-dimensional MoS2-decorated TiO2 nanotube gas sensors for efficient alcohol sensing, 674 (2016) 252–258.

[38] S. Li, et al., Heterojunction engineering of MoSe2/MoS2 with electronic modulation towards synergetic hydrogen evolution reaction and supercapacitance performance, Chem. Eng. J. 359 (2019) 1419–1426.

[39] Y. Han, et al., Design of hetero-nanostructures on MoS2 nanosheets to boost NO2 room-temperature sensing, ACS Appl. Mater. Interfaces 10 (26) (2018) 22640–22649.

[40] Y. Zhou, G. Liu, X. Zhu, Y.J.S. Guo, Ultrasensitive NO2 gas sensing based on rGO/MoS2 nanocomposite film at low temperature, Sens. Actuators B Chem. 251 (2017) 280–290.

[41] P. Panigrahi, T. Hussain, A. Karton, R.J.A. s Ahuja, Elemental substitution of two-dimensional transition metal dichalcogenides (MoSe2 and MoTe2): implications for enhanced gas sensing, ACS Sens. 4 (10) (2019) 2646–2653.

[42] A.V. Raghu, K.K. Karuppanan, J. Nampoothiri, B.J.A.A.N.M. Pullithadathil, Wearable, flexible ethanol gas sensor based on TiO2 nanoparticles-grafted 2D-titanium carbide nanosheets, ACS Appl. Nano Mater. 2 (3) (2019) 1152–1163.

[43] M. Ikram, H. Lv, Z. Liu, K. Shi, Ys.J.J. o M.C.A. Gao, Hydrothermally derived p–n MoS 2–ZnO from p–p MoS 2-ZIF-8 for an efficient detection of NO 2 at room temperature, J. Mater. Chem. A 9 (26) (2021) 14722–14730.

[44] R. Kumar, et al., Growth of MoS2–MoO3 hybrid microflowers via controlled vapor transport process for efficient gas sensing at room temperature, Adv. Mater. Interfaces 5 (10) (2018) 1800071.

[45] W. Park, et al., Oxygen environmental and passivation effects on molybdenum disulfide field effect transistors, Nanotechnology 24 (9) (2013) 095202.

IOP Publishing
Nanotechnology
Nanotechnology **35** (2024) 405502 (13pp)
https://doi.org/10.1088/1361-6528/ad5cf9

A proposed device based on $MoSe_2$-ZnO heterojunctions on rGO for enhanced ethanol gas sensing performances at room temperature

Nikita Jain and Nitin K Puri[*]

Nanomaterials Research Laboratory (NRL), Department of Applied Physics, Delhi Technological University, Delhi 110042, India

E-mail: nitinkumarpuri@dtu.ac.in

Received 20 March 2024, revised 20 May 2024
Accepted for publication 28 June 2024
Published 17 July 2024

Abstract

In this research, we report an enhanced sensing response ethanol gas sensing device based on a ternary nanocomposite of molybdenum diselenide-zinc oxide heterojunctions decorated rGO ($MoSe_2$/ZnO/rGO) at room temperature. The sensing performance of the ternary nanocomposite sensing device has been analysed for various concentrations of ethanol gas (1–500 ppm). The gas-sensing results have revealed that for 500 ppm ethanol gas concentration, the sensing device has exhibited an enhanced response value (R_g/R_a) of 50.2. Significantly, the sensing device has displayed a quick response and recovery time of 6.2 and 12.9 s respectively. In addition to this, the sensing device has shown a great prospect for long-term detection of ethanol gas (45 days). The sensing device has demonstrated the ability to detect ethanol at remarkably low concentrations of 1 ppm. The enhanced sensing performance of the ternary nanocomposite sensing device has highlighted the effective synergistic effect between $MoSe_2$ nanosheets, ZnO nanorods, and rGO nanosheets. This has been attributed to the formation of two heterojunctions in the ternary nanocomposite sensor: a p-n heterojunction between $MoSe_2$ and ZnO and a p-p heterojunction between $MoSe_2$ and rGO. The analysis of the results has suggested that the proposed $MoSe_2$/ZnO/rGO nanocomposite sensing device could be considered a promising candidate for the real-time detection of ethanol gas.

Keywords: ternary nanocomposite, heterojunctions, room-temperature sensing, chemiresistive ethanol gas sensing

1. Introduction

Air pollution has become a major concern for society with the advancement in science and technology [1, 2]. The release of hazardous gases as well as volatile organic compounds (VOCs) in the environment is not only detrimental to the atmospheric environment but also deleterious to human health [3]. VOCs are organic substances that can quickly turn into vapor and float into the air, even at room temperature (RT) because they have a low boiling point [4]. As per the World Health Organisation, air pollution is the leading cause of early death and various diseases [4, 5]. As a result, it is critical to detect and control the release of these pollution-causing gases. As a typical representative of VOCs, ethanol is extensively used in various food industries, agricultural production, chemical and pharmaceutical communities, etc [6, 7]. But its long-term exposure causes health problems, such as difficulty in

---

[*] Author to whom any correspondence should be addressed.

breathing, kidney failure, headaches, drowsiness, eye and skin irritation, and even coma [1, 8, 9]. Thus, it becomes critically important to monitor and detect ethanol gas at the right time at RT [10–12].

Molybdenum diselenide ($MoSe_2$), a two-dimensional (2D) transition metal dichalcogenide (TMD) has gained focus in the fields of gas sensing, energy storage, solar cells, etc. owing to its intriguing physical and chemical properties [13–17]. It possesses high adsorption energy with chemical molecules, exceptional adsorption-desorption properties, and a large surface-to-volume ratio which makes it a suitable candidate to be explored in-depth for gas sensing applications [18, 19]. Over the past few years, significant efforts have been devoted to developing gas sensors based on $MoSe_2$ [3, 20, 21]. However, gas sensors relying on pristine $MoSe_2$ exhibit drawbacks such as poor response, slow response, and recovery time. This limits the utilization of pristine $MoSe_2$ for gas sensors [20–22]. To meet the requirements of practical gas sensors, recently $MoSe_2$-metal-oxide semiconductor (MOS) hybrids have aroused worldwide attention. For instance, Pan *et al* report an RT H_2S sensor based on metal-organic framework (MOF)- derived α-Fe_2O_3/$MoSe_2$ composite exhibiting prominent sensing performances compared to pristine- α-Fe_2O_3 and pristine- $MoSe_2$ sensors [23]. Yang *et al* designed a novel MOF-derived SnO_2/$MoSe_2$ nanocomposite sensor with improved CO sensing properties at RT compared to pristine $MoSe_2$ and SnO_2 sensors [19].

In order to further strengthen the sensing performance of 2D TMDs—MOS hybrids, researchers are focussing on compositing them with carbon materials forming a ternary nanocomposite [24, 25]. In comparison to the binary hybrids, ternary nanocomposites develop multiple heterojunctions which modulate the charge transfer behavior in the gas sensing process thereby enhancing the sensing performance of the ternary nanocomposite sensors [26, 27]. Carbon materials such as reduced-graphene oxide (rGO) have been employed in the field of gas sensing owing to the presence of abundant residual oxygen functional groups, superior specific surface area, high carrier mobility, and chemically active defect sites for the adsorption of gases [4, 24, 28–30]. Ding *et al* constructed an RT ppb-level CO gas sensor based on MoS_2/rGO/Cu_2O composite by hydrothermal and soft-template methods. The ternary composite sensor exhibits excellent sensing response, good selectivity, and long-term stability [24]. Yuan *et al* reports an NH_3 gas sensor based on MoO_3/MoS_2/rGO composite. The composite sensor operates at low temperatures with enhanced gas sensitivity compared to the pristine-MoO_3, pristine-MoS_2, and MoS_2/MoO_3 sensors [25]. Therefore, incorporating rGO in the binary hybrids serves to improve the uniform distribution of heterojunctions, thereby increasing the contact area between the sensing material and the gas. This improves the rate of gas adsorption [31, 32]. Furthermore, it creates a conductive network to transport carriers and improves the sensing material's ability to detect carriers generated in trace gas reactions [33, 34]. Thus, utilizing ternary nanocomposite promises enhanced sensing parameters for practical applications.

In our previous work [3], we explored $MoSe_2$/ZnO nanocomposite-based sensor for ethanol gas sensing at RT. The ethanol gas sensing results of the nanocomposite sensor exhibit higher response value, improved response time, and recovery time than the pristine- $MoSe_2$ sensor to 500 ppm ethanol gas. To further enhance the ethanol gas sensing properties of the sensing device at RT, we have explored a ternary nanocomposite of $MoSe_2$–ZnO heterojunctions decorated rGO ($MoSe_2$/ZnO/rGO) for the first time to the best of our knowledge. In the gas sensing performance, the as-fabricated sensing device has been exposed to various concentrations of ethanol gas ranging from 1 to 500 ppm at RT. A sensing mechanism has been proposed to explain the enhanced sensing parameters of the as-fabricated sensing device. This work may uncover insights into the potential of ternary nanocomposites for ethanol gas sensing, presenting new avenues for progress and applications in the field.

2. Experimental section

2.1. Chemicals used for the synthesis of the ternary $MoSe_2$/ZnO/rGO nanocomposite

The chemicals essential for the synthesis included sodium molybdate dihydrate ($Na_2MoO_4.2H_2O$), selenium (Se) powder, hydrazine hydrate-86% ($N_2H_4.H_2O$), zinc acetate ($Zn(CH_3COO)_2 \cdot 2H_2O$), sodium hydroxide pellets (NaOH), graphite powder, concentrated sulphuric acid (H_2SO_4), orthophosphoric acid (H_3PO_4), hydrogen peroxide (H_2O_2), potassium permanganate ($KMnO_4$), ethanol (C_2H_5OH), and isopropyl alcohol (IPA). These chemicals were purchased from Sigma Aldrich.

2.2. Synthesis of the ternary $MoSe_2$/ZnO/rGO nanocomposite

A hydrothermal approach was utilized to synthesize $MoSe_2$/ZnO/rGO nanocomposite. $MoSe_2$ nanosheets and ZnO nanorods were synthesized using a hydrothermal method while GO nanosheets were synthesized via a modified Hummer's method as reported earlier in our previous work [3, 28, 35, 36].

Briefly, for the synthesis of $MoSe_2$ nanosheets, 2 mmol of $Na_2MoO_4.2H_2O$ was dissolved in deionized (DI) water and ethanol (1:1 volume ratio) with stirring for 45 min to obtain a clear solution. Separately, Se powder solution (4 mmol) was prepared in $N_2H_4.H_2O$-86% with continuous stirring. This solution was then added to $Na_2MoO_4.2H_2O$ solution dropwise. Finally, this reaction mixture was shifted into a 100 ml Teflon beaker. The Teflon beaker containing the reaction mixture was placed in an autoclave which was kept inside the vacuum oven at 220 °C for 24 h. Subsequently, the obtained solution was thoroughly washed multiple times with ethanol and dried overnight at 100 °C.

For the synthesis of ZnO nanorods, a solution of $Zn(CH_3COO)_2 \cdot 2H_2O$ (0.5 M) and NaOH (5 M) was prepared separately under continuous stirring. After half an hour, the solution of NaOH was added to the solution of

$Zn(CH_3COO)_2 \cdot 2H_2O$ dropwise. This reaction mixture was shifted into a 100 ml Teflon beaker. The Teflon beaker was placed in an autoclave which was kept inside the oven at 180 °C. The resultant solution was centrifuged and dried to obtain a white-colored powder.

For the synthesis of GO nanosheets, H_2SO_4 and H_3PO_4 were added to 2 g of graphite powder in a ratio of 9:1. After some time, $KMnO_4$ was added to the above reaction mixture slowly which was followed by magnetic stirring at 50 °C overnight. Subsequent to this procedure, ice (300 ml) was introduced into the reaction mixture, followed by the addition of 2 ml of H_2O_2 to effectively quench the reaction. The resultant yellowish slurry was centrifuged until the pH reached 7 which was then dried to obtain GO.

Finally, $MoSe_2$, ZnO, and GO synthesized by the above procedure were taken in a quantitative amount and dispersed in a mixture of ethanol and DI water. This dispersion was subjected to ultrasonication for 4 h. This solution was put in a hydrothermal autoclave which was kept in a vacuum oven at 180 °C for 24 h. After cooling to RT, the black-color precipitate of the ternary $MoSe_2$/ZnO/rGO nanocomposite was centrifuged and dried subsequently in a vacuum oven.

2.3. Gas sensing device fabrication

A series of steps were followed to fabricate an ethanol sensing device using the ternary $MoSe_2$/ZnO/rGO nanocomposite. First, the glass slides coated with indium tin oxide (ITO) were hydrolyzed [37]. The hydrolyzed ITO slides were cleaned using IPA and DI water several times. After cleaning, the slides were dried at 60 °C in the oven for 30 min. Next, a film of $MoSe_2$/ZnO/rGO nanocomposite was prepared using the electrophoretic deposition (EPD) technique. The as-obtained powder was dispersed in acetonitrile ($0.75\ \mathrm{mg\ ml^{-1}}$). Afterwards, it was transferred into a 2-electrode EPD cell, consisting of the working electrode (WE) and the counter electrode (CE) as illustrated in figure 1. An optimized potential was applied to the ITO clipped to the WE for 120 s. The prepared film was left to dry overnight. Finally, the thermal evaporation technique (Smart Coat 3.0, Hind High Vacuum) was utilized to deposit silver (Ag) electrodes onto the prepared film. Figure 1 illustrates the stainless steel (SS) mask design employed in the silver electrode deposition on the sensing device. During the evaporation, the chamber was maintained at a pressure of 4×10^{-6} mbar. The resulting silver electrodes had a thickness of 100 nm. The as-fabricated sensing device was used for performing ethanol sensing measurements.

2.4. Gas sensing measurements

The gas sensing was carried out in a customized SS chamber. A constant current supply to the ternary $MoSe_2$/ZnO/rGO nanocomposite ethanol sensing device was provided by the source measuring unit (SMU). At the beginning of the ethanol detection process, rough vacuum pressure was created inside the SS chamber using a rotary pump. Then, dry air was introduced for 50 s to obtain the baseline resistance. After that 1% ethanol gas/ 99% dry nitrogen gas mixture was introduced inside the SS chamber. Inside the SS chamber, the concentration of ethanol gas was calculated in parts per million (ppm) according to the following equation:

$$C = \frac{22.4 \times \varphi \times \rho \times V_1}{M \times V_2} \times 1000 \quad (1)$$

In the above formula equation (1), the ethanol gas concentration is depicted by C (ppm), gas volume fraction is denoted as φ, density of ethanol is represented as $\rho\ \left(\mathrm{kg \cdot m^{-3}}\right)$, volume of ethanol gas is indicated as V_1 (L), molecular weight of ethanol is expressed as M ($\mathrm{kg \cdot mol^{-1}}$), and volume of the SS chamber is denoted as $V_2\ \left(\mathrm{m^3}\right)$ [38, 39]. A data acquisition software (Lab-View) attached to the SMU was used to record the change in resistance of the sensing film.

3. Results and discussions

3.1. Structural analysis of the ternary $MoSe_2$/ZnO/rGO nanocomposite using x-ray diffraction (XRD)

XRD is used to investigate the crystal structure of $MoSe_2$, ZnO, GO, and $MoSe_2$/ZnO/rGO nanocomposite as depicted in figure 2. All the diffraction peaks of as-synthesized $MoSe_2$ are attributed to the (002), (100), (103) and (110) planes of the hexagonal phase of $MoSe_2$ (JCPDS 029-0914) [40]. The XRD pattern of ZnO shows all the diffraction peaks which are congruous with the standard data available for the wurtzite structure of ZnO (JCPDS 36–1451) [41]. The XRD pattern of GO exhibits prominent and weak diffraction peak at 11.7° and 42.6° which corresponds to the (002) and (100) planes of GO respectively [42]. The XRD pattern of the ternary $MoSe_2$/ZnO/rGO nanocomposite consists of diffraction peaks of (002), (004), (100), and (110) planes belonging to $MoSe_2$ along with all the diffraction peaks of ZnO. The reason for the invisibility of the (103) plane of $MoSe_2$ can be attributed to the strong characteristic peak intensities of $MoSe_2$ and ZnO [3, 43].

Noticeably, it is also difficult to find the reflection peaks of rGO in the $MoSe_2$/ZnO/rGO nanocomposite. The much higher intensity of the characteristic peak of $MoSe_2$, as well as ZnO in the ternary $MoSe_2$/ZnO/rGO nanocomposite, can be the reason for the suppression of the rGO peak in the nanocomposite [36]. Also, we believe that the $MoSe_2$–ZnO might attach to the surfaces of rGO which prevents their restacking and aggregation, which might have weakened the diffraction peak of rGO [44–46]. Therefore, further characterizations have been done to provide evidence for the coexistence of rGO in the ternary $MoSe_2$/ZnO/rGO nanocomposite.

3.2. Study of vibrational modes of the ternary $MoSe_2$/ZnO/rGO nanocomposite using Raman spectroscopy

To confirm the presence of rGO in the as-synthesized ternary $MoSe_2$/ZnO/rGO nanocomposite, Raman spectroscopy is utilized. Figure 3 shows the Raman spectra of $MoSe_2$, ZnO, GO, and $MoSe_2$/ZnO/rGO nanocomposite. Figure 3(a) shows the Raman peaks at 238, 167, and 283 $\mathrm{cm^{-1}}$ which are ascribed to the A_{1g}, E_{1g} and E^1_{2g} modes of $MoSe_2$ respectively [20,

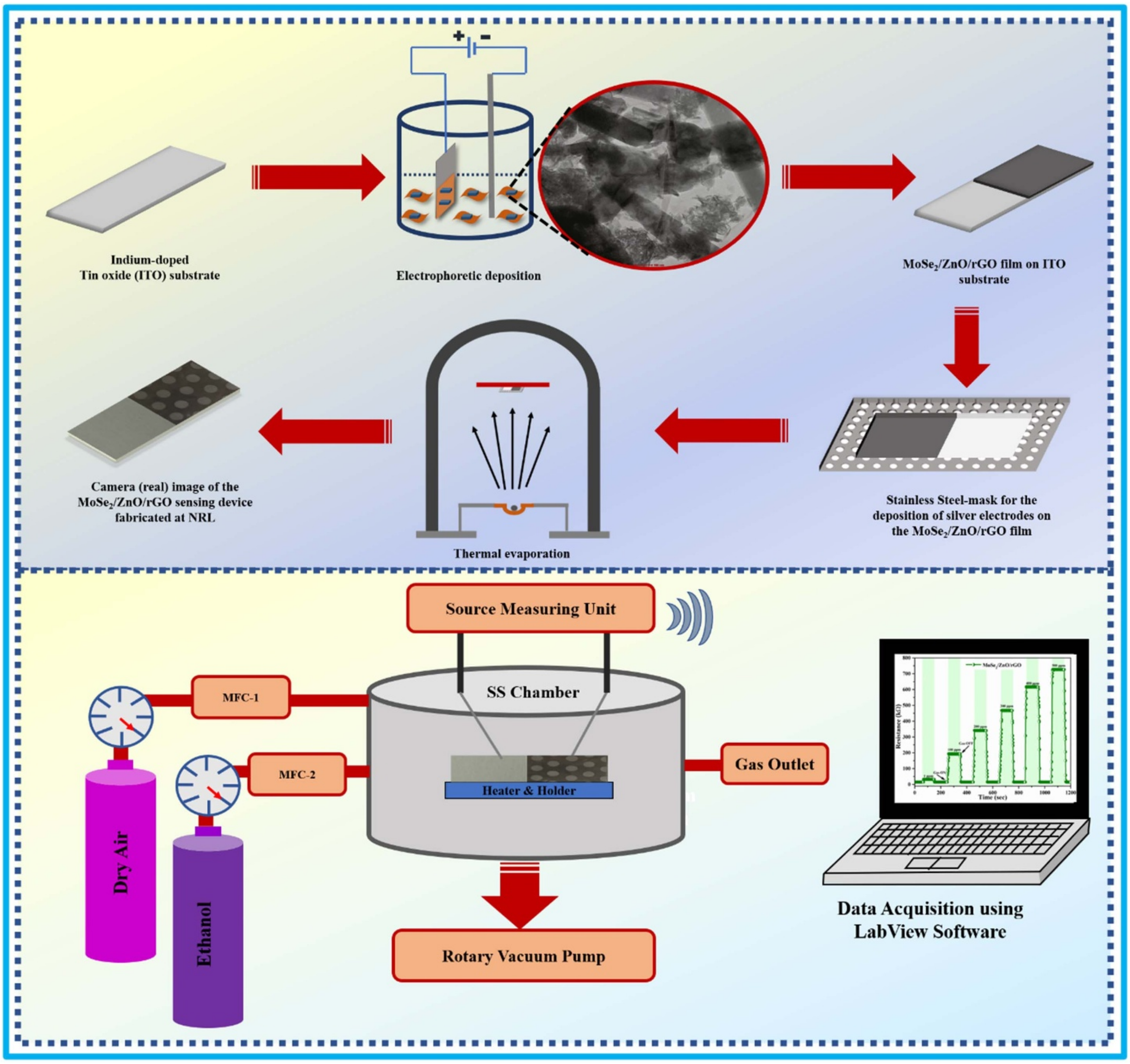

Figure 1. Diagrammatic representation of fabrication of the ternary MoSe$_2$/ZnO/rGO nanocomposite ethanol sensing device and gas sensing setup.

47]. Figure 3(b) shows a characteristic Raman peak of ZnO at 437 cm^{-1} (E_2^{high}) [35]. Figure 3(c) displays the two distinct peaks of GO at 1353 and 1590 cm^{-1} representing the D and G bands, respectively. The intensity ratio (I_D/I_G) corresponds to the ratio of the intensity of the D and G peaks respectively is determined to be 0.99.

The Raman spectrum of the ternary MoSe$_2$/ZnO/rGO nanocomposite is illustrated in figure 3(d). The peak at 233.7 cm^{-1} in MoSe$_2$/ZnO/rGO nanocomposite corresponds to the A_{1g} vibration mode of MoSe$_2$ and the characteristic peak identified at 431.3 cm^{-1} is specifically attributed to ZnO. Additionally, two prominant bands at 1345 and 1585 cm^{-1} in the Raman spectrum of MoSe$_2$/ZnO/rGO nanocomposite are attributed to the D and G bands of rGO respectively.

The I_D/I_G ratio of rGO in MoSe$_2$/ZnO/rGO nanocomposite is calculated to be 1.02 which is higher than that of GO. The increase in intensity ratio from 0.99 to 1.02 indicates that GO was successfully reduced to rGO during the hydrothermal synthesis of MoSe$_2$/ZnO/rGO nanocomposite [36, 48, 49]. Therefore, the concurrent presence of Raman peaks attributed to MoSe$_2$, ZnO, and rGO validates the successful synthesis of the ternary MoSe$_2$/ZnO/rGO nanocomposite.

3.3. Microstructure analysis of the ternary MoSe$_2$/ZnO/rGO nanocomposite using high-resolution transmission electron microscopy (HRTEM)

The microstructure of MoSe$_2$, ZnO, GO, and MoSe$_2$/ZnO/rGO nanocomposite is analysed by high-resolution transmission electron microscopy (HRTEM) as displayed in figure 4. The wrinkled nanosheets of MoSe$_2$ stacked over one another is shown in figure 4(a). In addition to the wrinkles, the nanosheets are curled at the edges. Figures 4(b) and (c) display the nanorods of ZnO and creased nanosheets of GO.

The HRTEM image of the ternary MoSe$_2$/ZnO/rGO nanocomposite (figures 4(d) and (e)) suggests that rGO nanosheets

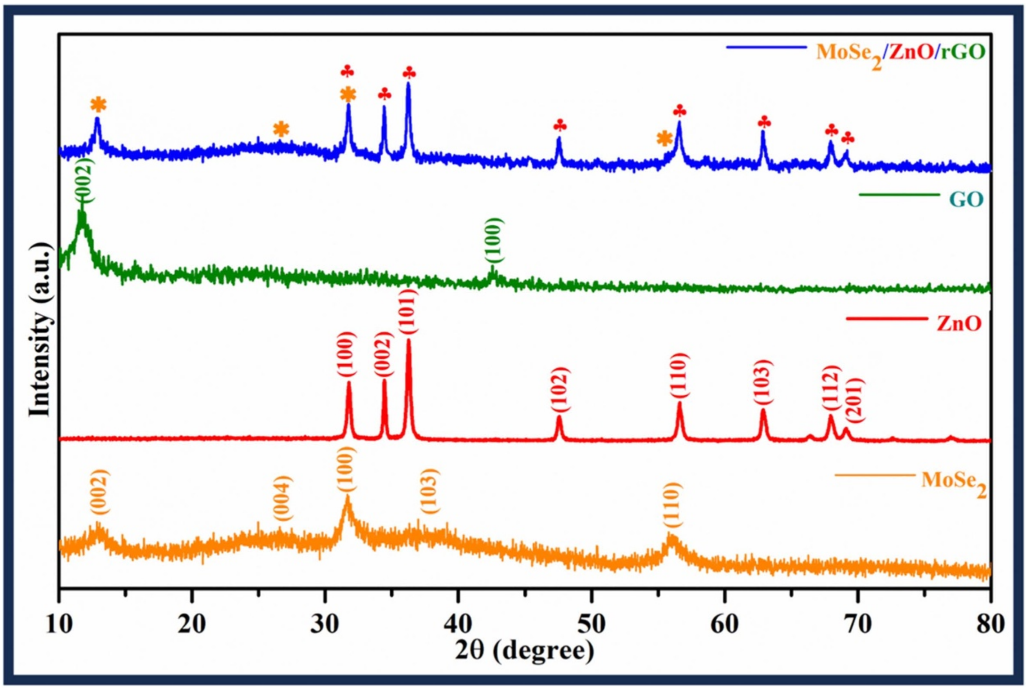

Figure 2. XRD spectra of $MoSe_2$, ZnO, GO, and $MoSe_2$/ZnO/rGO nanocomposite.

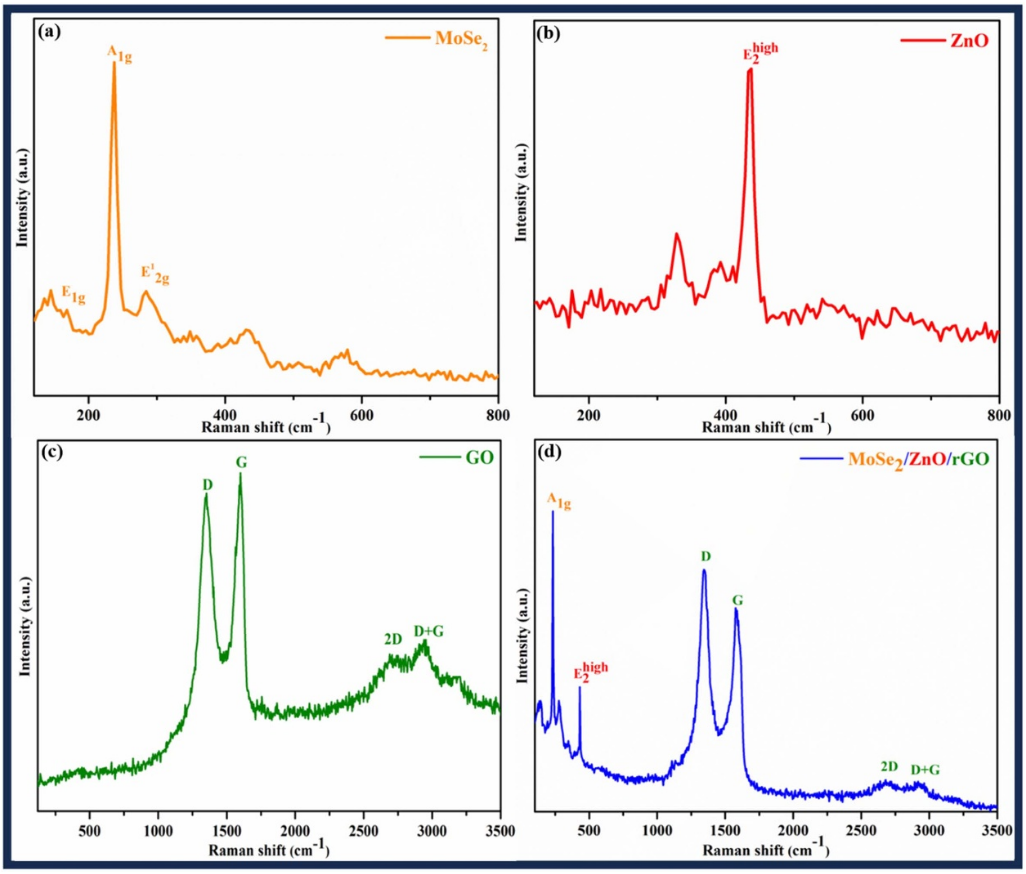

Figure 3. Raman spectra of (a) $MoSe_2$, (b) ZnO, (c) GO, and (d) $MoSe_2$/ZnO/rGO nanocomposite.

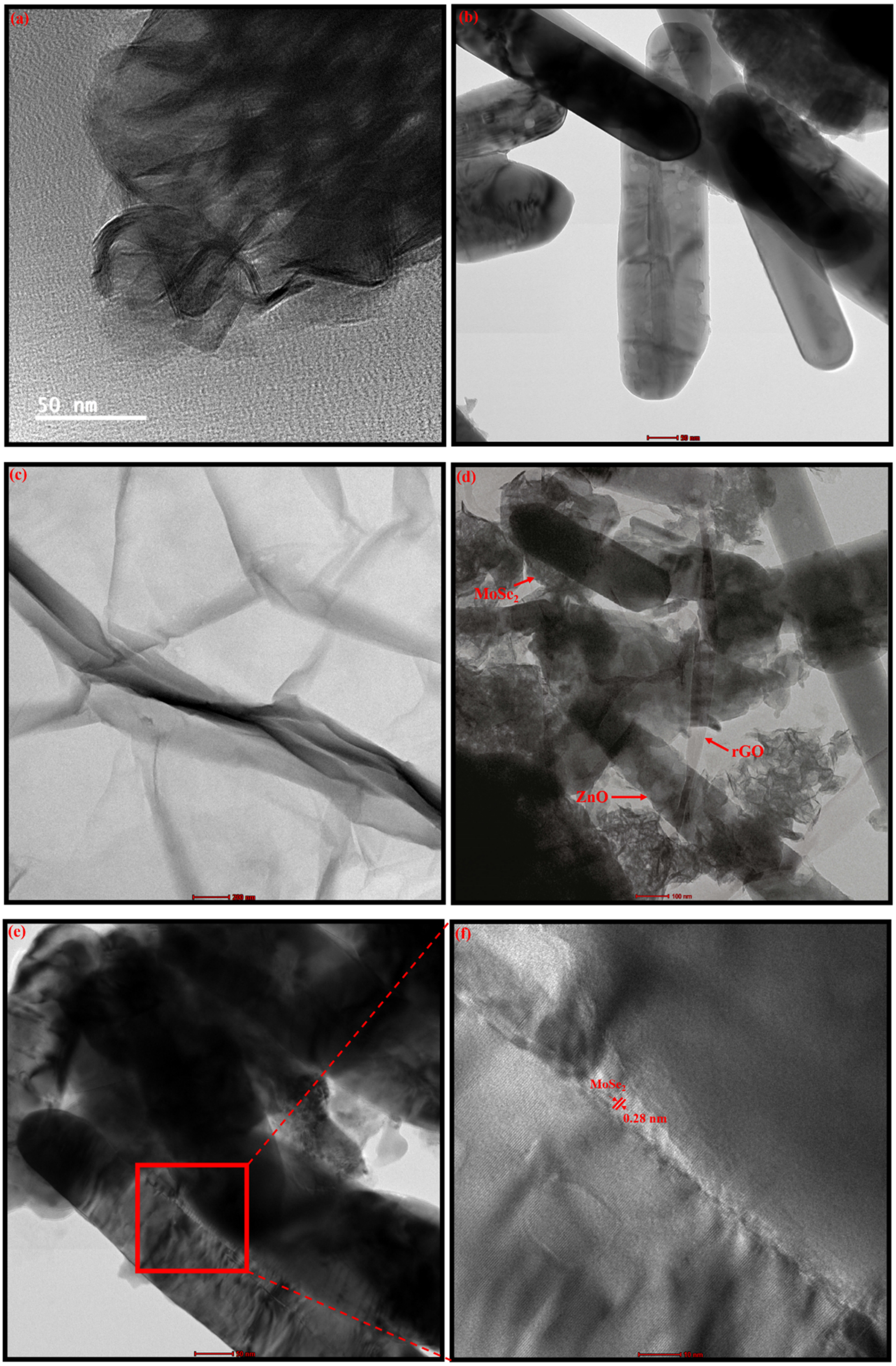

Figure 4. HRTEM images of (a) MoSe$_2$ nanosheets (b) ZnO nanorods, (c) GO nanosheets, (d) and (e) MoSe$_2$/ZnO/rGO nanocomposite, and (f) Heterogeneous interface between MoSe$_2$ nanosheets and ZnO nanorods.

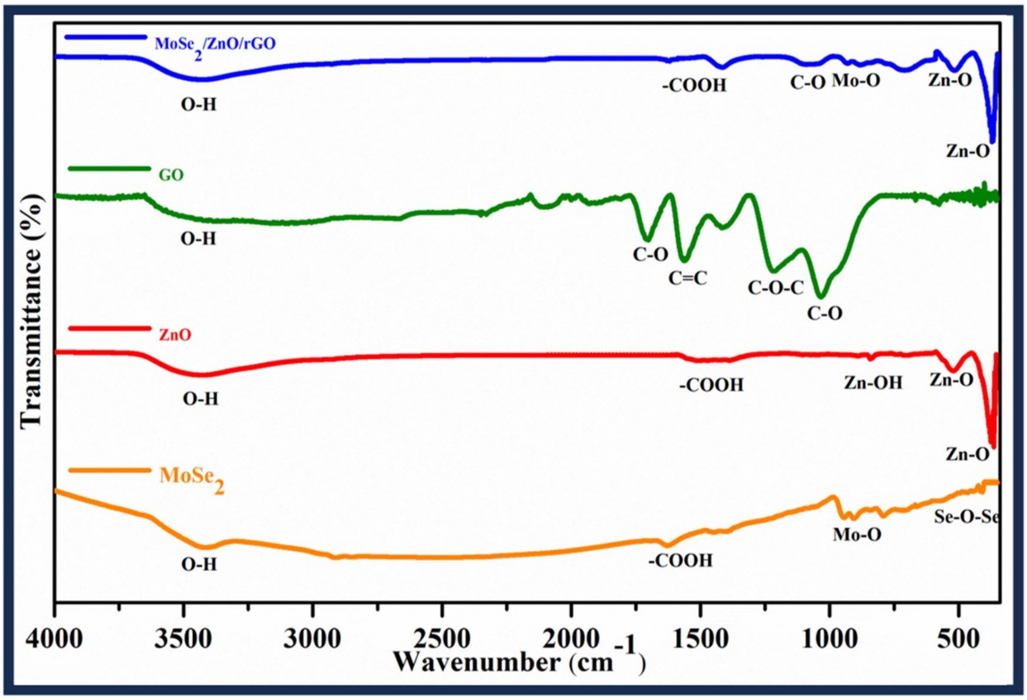

Figure 5. FTIR spectra of MoSe$_2$, ZnO, GO, and MoSe$_2$/ZnO/rGO nanocomposite.

have been successfully decorated with MoSe$_2$ nanosheets wrapping the ZnO nanorods. These rGO nanosheets provide a large specific surface area and active sites for the deposition of MoSe$_2$ nanosheets and ZnO nanorods. Also, figure 4(f) shows the fine lattice fringes of MoSe$_2$ nanosheets wrapping the ZnO nanorods. This indicates the formation of a heterogeneous interface between MoSe$_2$ nanosheets and ZnO nanorods. The interplanar spacing of MoSe$_2$ nanosheets is calculated to be 0.28 nm corresponding to the (100) lattice plane of MoSe$_2$ as labeled in figure 4(f). Hence HRTEM results confirm the successful decoration of ZnO nanorods wrapped by MoSe$_2$ nanosheets onto rGO nanosheets in the ternary MoSe$_2$/ZnO/rGO nanocomposite.

3.4. Functional groups identification of the ternary MoSe$_2$/ZnO/rGO nanocomposite using fourier transform infrared spectroscopy (FTIR)

The FTIR spectra of MoSe$_2$, ZnO, GO, and MoSe$_2$/ZnO/rGO nanocomposite are depicted in figure 5. The spectrum of MoSe$_2$ spectrum exhibits a peak at 3424 cm^{-1} indicative of O–H stretching vibrations. Additionally, within the range of 1000–750 cm^{-1} peaks are observed corresponding to Mo–O bonds, while the peak at 464 cm^{-1} corresponds to Se–O–Se bonds [50, 51]. Peaks in the FTIR spectrum of ZnO are observed corresponding to O–H (3427 cm^{-1}), COOH (1510–1380 cm^{-1}), Zn–OH (836 cm^{-1}), and Zn–O (510 and 370 cm^{-1}) [35]. The FTIR spectrum of GO reveals several distinctive peaks: a broad peak at 3280 cm^{-1} is attributed to O–H groups, and peaks at 1700 and 1562 cm^{-1} indicate C=O and C=C stretching, respectively. Additionally, a minor peak at 1400 cm^{-1} corresponds to O–H deformation, while two peaks at 1215 and 1030 cm^{-1} correspond to epoxy C–O–C and alkoxy C–O stretching vibrations, respectively [35, 52]. The spectrum of ternary MoSe$_2$/ZnO/rGO nanocomposite displays the peak corresponding to Mo–O bonds, and Zn–O bonds. In addition to these peaks, some peaks corresponding to oxygen-containing functional groups with decreased intensity compared to GO are also seen. This implies a successful thermal reduction of GO into rGO during the hydrothermal synthesis of the ternary MoSe$_2$/ZnO/rGO nanocomposite [36, 53]. Hence, the presence of functional groups associated with MoSe$_2$, ZnO, and rGO in the MoSe$_2$/ZnO/rGO nanocomposite confirms its successful formation.

3.5. Ethanol gas sensing performance of the ternary MoSe$_2$/ZnO/rGO nanocomposite sensing device at RT

3.5.1. Response of the sensing device toward various concentrations of ethanol gas. The gas sensing performance characteristics of the ternary MoSe$_2$/ZnO/rGO nanocomposite sensing device are analysed towards various ethanol gas concentrations ranging from 1 to 500 ppm at RT as illustrated in figure 6(a). It is observed in figure 6(a) that as the ethanol concentration increases, there is an increase in resistance change of the device. As a result, the response value (R_g/R_a) of the ternary nanocomposite sensing device to ethanol gas concentrations of 1, 100, 200, 300, 400, and 500 ppm at RT is calculated as 2.2, 14.0, 23.5, 32.4, 42.6, and 50.2 respectively. R_a and R_g are the resistance of the device in the air and ethanol gas respectively.

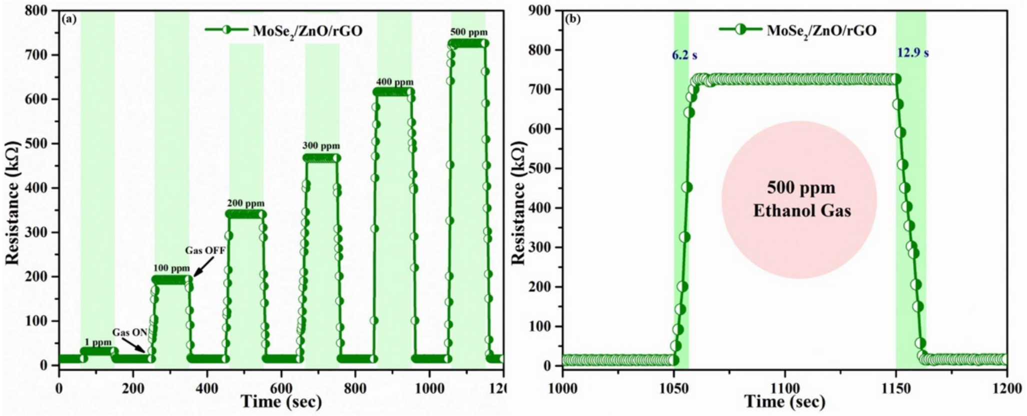

Figure 6. (a) Ethanol concentration-dependent resistance change curves and (b) Response time and recovery time of the ternary MoSe$_2$/ZnO/rGO nanocomposite sensing device at RT.

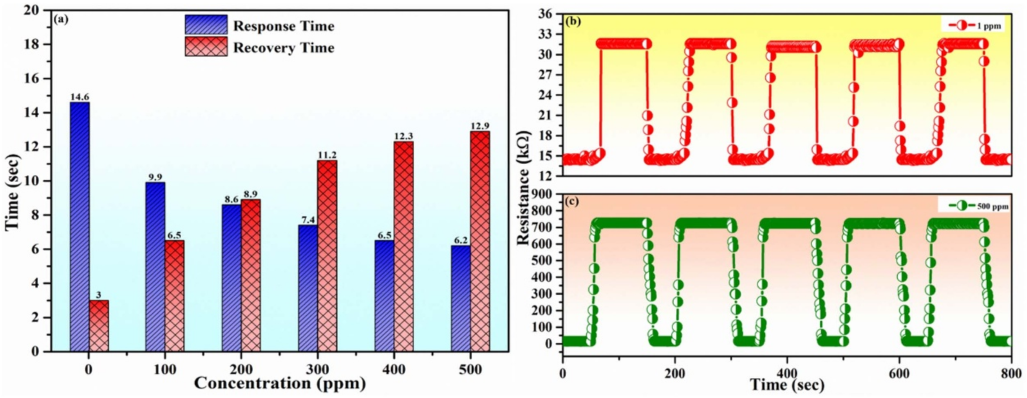

Figure 7. (a) $t_{\mathbf{resp}}$ and $t_{\mathbf{rec}}$ versus concentration curves, (b) and (c) Repeatability toward 1 and 500 ppm ethanol gas of the ternary MoSe$_2$/ZnO/rGO nanocomposite sensing device.

3.5.2. Response and recovery time of the sensing device.

Figure 6(b) describes the response time (t_{resp}), and the recovery time (t_{rec}) of the ternary MoSe$_2$/ZnO/rGO nanocomposite sensing device. The device exhibited a t_{resp} of 6.2 and t_{rec} of 12.9 s to 500 ppm ethanol gas. Moreover, the ternary nanocomposite sensing device exhibits a typical *p*-type gas sensing behavior, that is, an increased resistance induced by reducing gas. In addition to this, full recovery to the initial state is observed for the ternary MoSe$_2$/ZnO/rGO nanocomposite sensing device which reveals that the interaction is due to the physisorption process.

The response time and recovery time of the ternary MoSe$_2$/ZnO/rGO nanocomposite sensing device are systematically evaluated for various concentrations of ethanol gas ranging from 1 to 500 ppm as depicted in figure 7(a). It is noticed that the as-fabricated ternary nanocomposite sensing device shows low t_{resp} and large t_{rec} when the device is exposed to a higher concentration of ethanol gas (500 ppm). The fall in t_{resp} could be explained by the abundant sites on the sensor's surface for gas adsorption. Conversely, the rise in t_{rec} may be attributed to a large number of ethanol gas molecules involved in the interaction with the sensor which required time to desorb from the sensor's surface [27].

3.5.3. Repeatability of the sensing device.

A practical gas sensor should possess good repeatability under exposure to the same concentration of target gas. The repeatability of the ternary nanocomposite sensing device is tested for five successive cycles to 1 and 500 ppm ethanol gas in the order of dry air-ethanol-dry air as shown in figures 7(b) and (c). It is observed that the resistance change of the as-fabricated ternary nanocomposite sensing device is approximately the same, exhibiting good repeatability to ethanol gas over cyclic measurements.

3.5.4. Selectivity of the sensing device.

Another vital aspect of a practical gas sensor is selectivity. The selectivity study of the ternary MoSe$_2$/ZnO/rGO nanocomposite sensing device is conducted with a primary focus on developing a VOC gas sensor. The radar plot in figure 8(a) shows the response of the sensing device toward a few VOCs (including ethanol, acetone, benzene, and formaldehyde) each at a concentration of 500 ppm at RT. It can be seen that the ternary MoSe$_2$/ZnO/rGO nanocomposite sensing device displays a response of 50.2 to ethanol gas. This suggests that the ternary nanocomposite sensing device displays a higher response

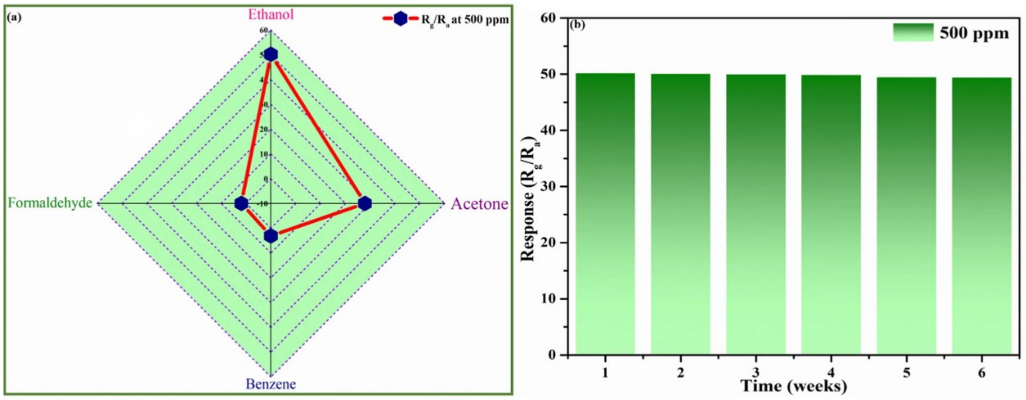

Figure 8. (a) Selectivity test to 500 ppm of different VOCs, and (b) Long-term stability of response (45 days) towards 500 ppm of ethanol for the ternary $MoSe_2$/ZnO/rGO nanocomposite sensing device at RT.

Table 1. A comparison of ethanol gas sensing performances of the ternary $MoSe_2$/ZnO/rGO nanocomposite sensor with other reported literature[e].

Sensor materials	Operating temperature (°C)	Concentration (ppm)	Sensor response (S)	Response time (s)	Recovery time (s)	Stability (days)
$MoSe_2$/ZnO [Previous work] [3]	27 (RT)	500	37.8[a]	8.4	14.7	30
MoO_2/MoO_3/MXene [12]	RT	100	10.8[c]	—	—	15
CuO-ZnO/g–C_3N_4 [54]	260	500	16[c]	87	169	30
Pd decorated ZnO [55]	260	500	81[d]	6	95	22
MoS_2/TiO_2 [56]	300	500	100[b]	70 ± 10 s	90 ± 20 s	56
ZnO [57]	275	500	33[c]	25	12	60
ZnO/rGO/g–C_3N_4 [58]	300	100	178[c]	76	6	14
In_2O_3/ZnO/$Ti_3C_2T_X$ [59]	RT	100	6.5[c]	—	—	30
$MoSe_2$/ZnO/rGO [This work]	**27 (RT)**	**500**	**50.2**[a]	**6.2**	**12.9**	**45**

[a] Indicates that $S = (R_g/R_a)$.
[b] Indicates that $S = (R_g - R_a/R_a) \times 100$.
[c] Indicates that $S = R_a/R_g$.
[d] Indicates that $S = (R_a - R_g/R_a) \times 100$.
[e] Indicates that the literature provided has been structured to follow the chronological order of their publishing.

to ethanol gas compared to other gases, which is ∼1.8 times of acetone gas, ∼16.2 times of benzene gas, and ∼26.4 times of formaldehyde gas. In future reports, we intend to broaden the scope of our selectivity studies to include a diverse array of reducing gases.

3.5.5. Stability of the sensing device. To evaluate the extended stability of the ternary $MoSe_2$/ZnO/rGO nanocomposite sensing device, its response to 500 ppm ethanol gas at RT is observed over a period of 45 days, with measurements taken at regular intervals of 7 days. As represented in figure 8(b), no obvious variation in the responses of the as-fabricated sensing device is observed within 45 days, inferring that the sensor has a great prospect for long-term detection of ethanol gas at RT.

The detailed comparison of ethanol gas sensing performances of the ternary nanocomposites and other reported literature with the present work is shown in table 1. Compared to previously reported ethanol gas sensors, the ethanol sensor based on the ternary $MoSe_2$/ZnO/rGO nanocomposite exhibits higher response value (R_g/R_a), fast response and recovery time, outstanding long-term stability, and importantly operates at RT.

3.5.6. Ethanol gas sensing mechanism. The gas-sensing mechanism of the sensor is based on the change in resistance due to the adsorption and desorption of ethanol molecules on the surface of the sensing material [60]. In general, $MoSe_2$ and rGO nanosheets show a *p*-type behavior, and ZnO nanorods show an *n*-type behavior towards ethanol gas [3, 61]. From the response curves (figures 5(a) and (b)), the $MoSe_2$/ZnO/rGO nanocomposite sensing device shows a *p*-type behavior which suggests that $MoSe_2$ and rGO nanosheets act as majority charge carriers during the ethanol sensing mechanism.

The ternary $MoSe_2$/ZnO/rGO nanocomposite sensor enhancement mechanism to ethanol gas primarily involves four main aspects: Firstly, the gas sensing performance of the ternary $MoSe_2$/ZnO/rGO nanocomposite sensing device is closely related to the formation of heterojunctions. Figure 9(a) shows the schematic representation and energy band diagram of p-$MoSe_2$ nanosheets, *n*-type ZnO nanorods, and p-rGO nanosheets. The discrepancy of the work functions and band gap of $MoSe_2$, ZnO, and rGO in the nanocomposite is attributed to the formation of p-n heterojunction between $MoSe_2$ and ZnO and p-p heterojunction between $MoSe_2$ and rGO. The differences in fermi levels result in rapid movement of

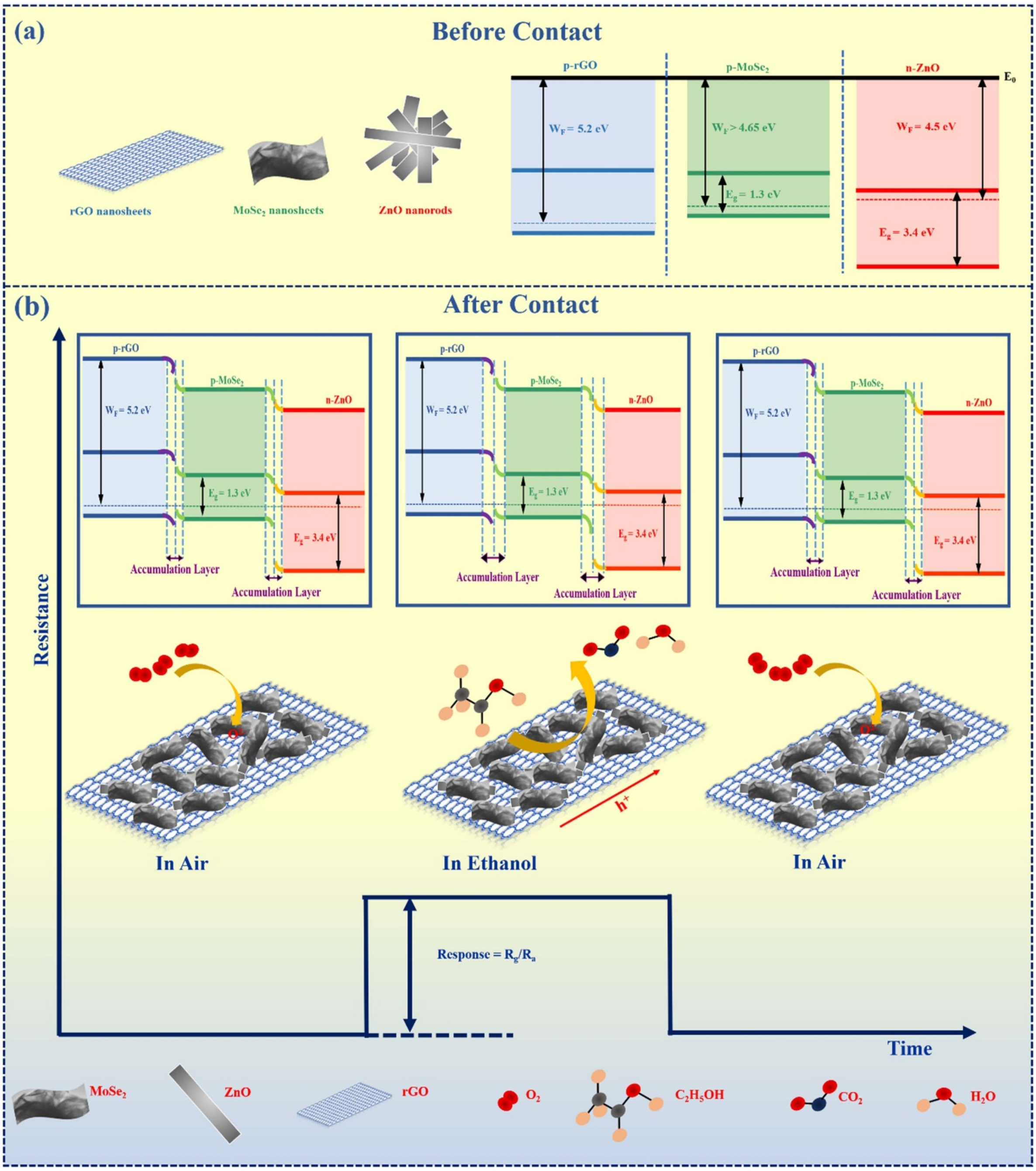

Figure 9. Schematic representation of ethanol gas sensing mechanism of the ternary $MoSe_2$/ZnO/rGO nanocomposite sensing device.

charge carriers (electrons/holes) until an equilibrium of fermi level is achieved. The energy band bends at the interface of $MoSe_2$/ZnO and $MoSe_2$/rGO and an accumulation layer is formed as shown in figure 9(b). A potential barrier is formed due to carrier trapping at the interface of the $MoSe_2$/ZnO and $MoSe_2$/rGO in the ternary $MoSe_2$/ZnO/rGO nanocomposite sensing device. Under normal air atmosphere, the adsorption of oxygen molecules on the surface of the ternary $MoSe_2$/ZnO/rGO nanocomposite sensor plays a crucial role as depicted in figure 9(b). When the sensing device is exposed to air, the oxygen molecules adsorbed on the surface of the sensor are transformed into oxygen species (O_2^-) by trapping free electrons from the conduction band of the $MoSe_2$/ZnO/rGO nanocomposite sensor [24]. Generally, at RT the oxygen molecules can react as follows to produce O_2^- [12, 62]:

$$O_2\,(\text{gas}) \rightarrow O_2\,(\text{ads}) \tag{2}$$

$$2O_2\,(\text{ads}) + 2e^- \leftrightarrow 2O_2\,(\text{ads})\,. \tag{3}$$

Upon exposure of the sensing device to ethanol gas, the ethanol gas molecules react with the oxygen species adsorbed on the surface of the ternary $MoSe_2$/ZnO/rGO nanocomposite sensor. This causes the ternary nanocomposite to recapture the electrons carried away by the adsorbed oxygen in the air. This results in the broadening of the charge carrier accumulation layer formed at the two interfaces. The simultaneous existence of two distinct accumulation layers and potential barriers is particularly noteworthy. This coexistence significantly enhances the number of heterojunctions present in the nanocomposite device, resulting in a marked enhancement of ethanol gas sensitivity [63]. The entire process leads to an overall increase in the resistance of the ternary nanocomposite sensor. The reaction is shown in equation (4).

$$2C_2H_5OH + 6O_2^- \text{(ads)} \rightarrow 4CO_2 + 6H_2O + 6e^-. \quad (4)$$

Secondly, a large number of active sites are provided by rGO for the deposition of $MoSe_2$ nanosheets and ZnO nanorods [46, 64]. This is also evident in HRTEM images (figures 4(d)–(f)) that $MoSe_2$ nanosheets and ZnO nanorods are deposited onto the rGO matrix. The specific ternary structure provides increased active sites, enhancing the adsorption and desorption of ethanol molecules thereby improving the sensing response appreciably. Third, rGO also acts as a conductive network facilitating rapid electron transfer between $MoSe_2$ nanosheets and ZnO nanorods [42]. This leads to quick response and recovery time as shown in figure 5(b). Fourth, the bandgap of rGO is small, and slight changes in the carrier concentration on the surface of rGO have an obvious influence on the electrical conductivity of the $MoSe_2$/ZnO/rGO nanocomposite sensor [46]. Therefore, there is a great contribution of rGO in enhancing the ethanol gas sensing performance of the ternary $MoSe_2$/ZnO/rGO nanocomposite sensor.

Thus, we conclude that the as-fabricated ternary nanocomposite sensing device is capable of detecting ethanol gas at low concentration (1 ppm) with high sensitivity, good selectivity, long-term stability, fast adsorption and desorption, and stable repeatability.

4. Conclusions

In conclusion, a highly stable, exceptionally selective, and reliably repeatable ethanol gas sensing device has been successfully developed using the ternary $MoSe_2$/ZnO/rGO nanocomposite, promising long-term stability. Importantly, the ternary nanocomposite sensing device exhibits a fantabulous sensing response of 50.2 to 500 ppm ethanol gas. The ternary nanocomposite sensing device can detect ethanol down to 1 ppm at RT. The developed ternary nanocomposite sensing device exhibits a considerably fast response time (6.2 s) and recovery time (12.9 s) to 500 ppm ethanol gas. Besides, the sensing device also establishes prolific long-term stability of 45 days. The superior performance of the developed ternary nanocomposite sensing device is owed to the formation of two heterojunctions: a p-n heterojunction between $MoSe_2$ and ZnO and a p-p heterojunction between $MoSe_2$ and rGO. Furthermore, the abundance of active sites is provided by rGO for the attachment of the $MoSe_2$ nanosheets and ZnO nanorods. Consequently, this increases the sites for the adsorption and desorption of ethanol molecules. This improves the gas-sensing response of the sensing device toward ethanol significantly. In addition to this, the conductive network of rGO nanosheets facilitates fast electron transfer between $MoSe_2$ nanosheets and ZnO nanorods, endowing the ternary nanocomposite sensing device with quick response and recovery time. The result provides a facile and effective approach for developing a ternary nanocomposite for the fabrication of ethanol gas sensing devices with enhanced properties.

Data availability statement

The data that support the findings of this study are available upon reasonable request from the authors.

Acknowledgments

The authors are grateful to the Hon'ble Vice-Chancellor, Prof. Prateek Sharma, Delhi Technological University, Delhi, India for providing support and facilities for conducting quality research work. The authors would like to thank Dr. Pawan Kr Tyagi, Dr. Rishibrind Kr Upadhyay, Dr. Senthil Kumar Kandasamy, Dr. Savita Sharma, Dr. Kamal Arora, Dr. Ritika Khatri, Saroj Kumar Jha, Hemant K Arora, Sunil Kumar, and Anmol Aggarwal for their valuable review of the manuscript.

Conflict of interest

The authors declare that there is no conflict of interest.

ORCID iDs

Nikita Jain https://orcid.org/0009-0002-8718-6153
Nitin K Puri https://orcid.org/0000-0003-2563-3747

References

[1] Hu J, Guan W, Xiong X, Chen Y and Long H 2022 Modulation of rGO-Co_3O_4 heterojunction with multi-walled carbon nanotubes for efficient ethanol detection *Sens. Actuators* B **368** 132202

[2] Wang X, Gao Y, Zhang Q, He X and Wang X 2023 Synthesis of MoO_3 (1D)@ SnO_2 (2D) core-shell heterostructures for enhanced ethanol gas sensing performance *Sens. Actuators* B **382** 133484

[3] Jain N and Puri N K 2023 Zinc oxide incorporated molybdenum diselenide nanosheets for chemiresistive detection of ethanol gas *J. Alloys Compd.* **955** 170178

[4] Tiwary P, Chatterjee S, Singha S, Mahapatra R and Chakraborty A K 2021 Room temperature ethanol sensing by chemically reduced graphene oxide film *Flat Chem* **30** 100317

[5] Yan W, Liu Y, Shao G, Zhu K, Cui S, Wang W and Shen X 2021 Chemical surface adsorption and trace detection of alcohol gas in graphene oxide-based acid-etched SnO_2 aerogels *ACS Appl. Mater. Interfaces* **13** 20467–78

[6] Ahemad M J, Le T D, Kim D-S and Yu Y-T 2022 Bimetallic AgAualloy@ ZnO core-shell nanoparticles for ultra-high detection of ethanol: potential impact of alloy composition on sensing performance *Sens. Actuators* B **359** 131595

[7] Fan H, Zheng X, Shen Q, Wang W and Dong W 2022 Hydrothermal synthesis and their ethanol gas sensing performance of 3-dimensional hierarchical nano Pt/SnO_2 *J. Alloys Compd.* **909** 164693

[8] Rao S K, Kamath S M, Abhinav E M, Gopalakrishnan C, Gopalakrishnan C, Gopalakrishnan C and Gopalakrishnan C 2022 Unraveling the potential of Gd doping on mullite $Bi_2Fe_4O_9$ for fiber optic ethanol gas detection at room temperature *Mater. Chem. Phys.* **278** 125646

[9] Roy N, Mitra S, Das N M, Mandal N, Bandyopadhyay D, Nemade H B and Mandal T K 2019 Paper based enzymatic chemiresistor for POC detection of ethanol in human breath *IEEE Sens. J.* **20** 2278–86

[10] Wang X, Wang S, Tian J, Cui H and Wang X 2022 Synthesis of 1D SnO_2 nanorods/2D NiO porous nanosheets pn heterostructures for enhanced ethanol gas sensing performance *Vacuum* **205** 111399

[11] Cao P *et al* 2020 Preparation and characterization of a novel ethanol gas sensor based on $FeYO_3$ microspheres by using orange peels as bio-templates *Vacuum* **177** 109359

[12] Zhang S, Song P, Zheng Y, Ding Y and Wang Q 2022 MoO_2/MoO_3/MXene ternary nanocomposites for high-performance ethanol detection at room temperature *J. Alloys Compd.* **925** 166663

[13] Jeevanandham G, Vediappan K, ALOthman Z A, Altalhi T and Sundramoorthy A K 2021 Fabrication of 2D-$MoSe_2$ incorporated NiO Nanorods modified electrode for selective detection of glucose in serum samples *Sci. Rep.* **11** 13266

[14] Li T, Yu S, Li Q, Chi M and Li P 2021 Room temperature ethanol gas-sensing properties based on Ag-doped $MoSe_2$ nanoflowers: experimental and DFT investigation *New J. Chem.* **45** 21423–8

[15] Anichini C, Czepa W, Pakulski D, Aliprandi A, Ciesielski A and Samorì P 2018 Chemical sensing with 2D materials *Chem. Soc. Rev.* **47** 4860–908

[16] Al-Tahan M A, Dong Y, Shrshr A E, Kang X, Guan H, Han Y, Cheng Z, Chen W and Zhang J 2022 Modulating of $MoSe_2$ functional plane via doping-defect engineering strategy for the development of conductive and electrocatalytic mediators in Li-S batteries *J. Energy Chem.* **75** 512–23

[17] Yao Z, Yu C, Dai H, Zhou J, Liu X and Sun G 2022 Hybrid fibers assembled from $MoSe_2$/graphene heterostructures endow improved supercapacitive performance *Carbon* **187** 165–72

[18] Zhang S, Nguyen T H, Zhang W, Park Y and Yang W 2017 Correlation between lateral size and gas sensing performance of $MoSe_2$ nanosheets *Appl. Phys. Lett.* **111** 161603

[19] Yang Z, Zhang D and Wang D 2020 Carbon monoxide gas sensing properties of metal-organic frameworks-derived tin dioxide nanoparticles/molybdenum diselenide nanoflowers *Sens. Actuators* B **304** 127369

[20] Singh S, Deb J, Sarkar U and Sharma S 2020 $MoSe_2$ crystalline nanosheets for room-temperature ammonia sensing *ACS Appl. Nano Mater.* **3** 9375–84

[21] Zhang S, Zhang W, Nguyen T H, Jian J and Yang W 2019 Synthesis of molybdenum diselenide nanosheets and its ethanol-sensing mechanism *Mater. Chem. Phys.* **222** 139–46

[22] Jha R K, D'Costa J V, Sakhuja N and Bhat N 2019 $MoSe_2$ nanoflakes based chemiresistive sensors for ppb-level hydrogen sulfide gas detection *Sens. Actuators* B **297** 126687

[23] Pan W, Zhang Y, Yu S, Liu X and Zhang D 2021 Hydrogen sulfide gas sensing properties of metal organic framework-derived α-Fe_2O_3 hollow nanospheres decorated with $MoSe_2$ nanoflowers *Sens. Actuators* B **344** 130221

[24] Ding Y, Guo X, Kuang D, Hu X, Zhou Y, He Y and Zang Z 2021 Hollow Cu_2O nanospheres loaded with MoS_2/reduced graphene oxide nanosheets for ppb-level NO_2 detection at room temperature *J. Hazard. Mater.* **416** 126218

[25] Yuan Z, Liu Y, Zhang J, Meng F and Zhang H 2021 Rose-like MoO_3/MoS_2/rGO low-temperature ammonia sensors based on multigas detection methods *IEEE Trans. Instrum. Meas.* **70** 1–9

[26] Liu J, Lu X, Han G, Si C, Zhao Y, Hou Z, Zhang Y and Ning J 2023 Mo_2C/MoO_3@rGO ternary nanocomposites as high-performance gas sensor for trace NH3 detection at room temperature *ACS Appl. Electron. Mater.* **5** 5061–73

[27] Li G, Shen Y, Zhao S, Li A, Zhao T, Tang C, Yan C, Gao S, Yuan Z and Meng F 2023 Detection of ppm-level H2 via rGO-SnO_2-ZnO nanocomposites: considering compositional matching in designing heterostructured gas-sensing materials *Sens. Actuators* B **396** 134560

[28] Arora K, Srivastava S, Solanki P R and Puri N K 2019 Electrochemical hydrogen gas sensing employing palladium oxide/reduced graphene oxide (PdO-rGO) nanocomposites *IEEE Sens. J.* **19** 8262–71

[29] Choudhari A, Bhanvase B A, Saharan V K, Salame P H and Hunge Y 2020 Sonochemical preparation and characterization of rGO/SnO_2 nanocomposite: electrochemical and gas sensing performance *Ceram. Int.* **46** 11290–6

[30] Meng F, Yang Z, Yuan Z, Zhang H and Zhu H 2023 Hydrothermal synthesis of CuO/rGO nanosheets for enhanced gas sensing properties of ethanol *Ceram. Int.* **49** 5595–603

[31] Duy L T *et al* 2015 High performance three-dimensional chemical sensor platform using reduced graphene oxide formed on high aspect-ratio micro-pillars *Adv. Funct. Mater.* **25** 883–90

[32] Gao R *et al* 2021 The controllable assembly of the heterojunction interface of the ZnO@ rGO for enhancing the sensing performance of NO_2 at room temperature and sensing mechanism *Sens. Actuators* B **342** 130073

[33] Yang Y, Li S, Yang W, Yuan W, Xu J and Jiang Y 2014 In situ polymerization deposition of porous conducting polymer on reduced graphene oxide for gas sensor *ACS Appl. Mater. Interfaces* **6** 13807–14

[34] Hummers W S Jr and Offeman R E 1958 Preparation of graphitic oxide *J. Am. Chem. Soc.* **80** 1339

[35] Jain N, Sharma S and Puri N K 2022 Investigation of charge transport mechanism in hydrothermally synthesized reduced graphene oxide (rGO) incorporated zinc oxide (ZnO) nanocomposite films *J. Mater. Sci., Mater. Electron.* **33** 1307–23

[36] Khatri R and Puri N K 2022 Electrochemical biosensor utilizing dual-mode output for detection of lung cancer biomarker based on reduced graphene oxide-modified reduced-molybdenum disulfide multi-layered nanosheets *J. Mater. Res.* **37** 1451–63

[37] Khatri R and Puri N K 2022 Electrochemical studies of biofunctionalized MoS_2 matrix for highly stable immobilization of antibodies and detection of lung cancer protein biomarker *New J. Chem.* **46** 7477–89

[38] Chen Q, Ma S Y, Xu X L, Jiao H Y, Zhang G H, Liu L W, Wang P Y, Gengzang D J and Yao H H 2018 Optimization ethanol detection performance manifested by gas sensor based on In_2O_3/ZnS rough microspheres *Sens. Actuators* B **264** 263–78

[39] Zhang J, Li T, Guo J, Hu Y and Zhang D 2021 Two-step hydrothermal fabrication of CeO_2-loaded MoS_2 nanoflowers for ethanol gas sensing application *Appl. Surf. Sci.* **568** 150942

[40] Inta H R, Ghosh S, Mondal A, Tudu G, Koppisetti H V and Mahalingam V 2021 $Ni_{0.85}Se$/$MoSe_2$ interfacial structure: an efficient electrocatalyst for alkaline hydrogen evolution reaction *ACS Appl. Energy Mater.* **4** 2828–37

[41] Navale Y, Navale S, Chougule M, Ramgir N and Patil V 2021 NO_2 gas sensing properties of heterostructural CuO nanoparticles/ZnO nanorods *J. Mater. Sci., Mater. Electron.* **32** 18178–91

[42] Zhang J, Wu J, Wang X, Zeng D and Xie C 2017 Enhancing room-temperature NO_2 sensing properties via forming heterojunction for NiO-rGO composited with SnO_2 nanoplates *Sens. Actuators* B **243** 1010–9

[43] Huang Y, Miao Y-E, Fu J, Mo S, Wei C and Liu T 2015 Perpendicularly oriented few-layer $MoSe_2$ on SnO_2 nanotubes for efficient hydrogen evolution reaction *J. Mater. Chem.* A **3** 16263–71

[44] Xu C, Wang X, Zhu J, Yang X and Lu L 2008 Deposition of Co_3O_4 nanoparticles onto exfoliated graphite oxide sheets *J. Mater. Chem.* **18** 5625–9

[45] Chen S, Zhu J, Wu X, Han Q and Wang X 2010 Graphene oxide− MnO_2 nanocomposites for supercapacitors *ACS Nano* **4** 2822–30

[46] Wang C, Zhu J, Liang S, Bi H, Han Q, Liu X and Wang X 2014 Reduced graphene oxide decorated with CuO–ZnO hetero-junctions: towards high selective gas-sensing property to acetone *J. Mater. Chem.* A **2** 18635–43

[47] Tran X T, Poorahong S and Siaj M 2017 One-pot hydrothermal synthesis and selective etching method of a porous $MoSe_2$ sand rose-like structure for electrocatalytic hydrogen evolution reaction *RSC Adv.* **7** 52345–51

[48] Rana S, Singh V and Singh B 2022 Tailoring the output performance of PVDF-based piezo–tribo hybridized nanogenerators via B, N-codoped reduced graphene oxide *ACS Appl. Electron. Mater.* **4** 5893–904

[49] Komal K, Gupta G, Singh M and Singh B 2022 Improved resistive switching of RGO and SnO_2 based resistive memory device for non-volatile memory application *J. Alloys Compd.* **923** 166196

[50] Vidhya M S, Yuvakkumar R, Kumar P S, Ravi G and Velauthapillai D 2021 Hydrothermal synthesis of flower like $MnSe_2$@ $MoSe_2$ electrode for supercapacitor applications *Top. Catal.* **65** 1–8

[51] Mishra A, Narang J, Pundir C S, Pilloton R and Khanuja M 2018 Morphology-preferable $MoSe_2$ nanobrooms as a sensing platform for highly selective apta-capturing of salmonella bacteria *ACS Omega* **3** 13020–7

[52] Uddin M E, Layek R K, Kim N H, Hui D and Lee J H 2015 Preparation and properties of reduced graphene oxide/polyacrylonitrile nanocomposites using polyvinyl phenol *Composites* B **80** 238–45

[53] Kumar S, Sharma V, Bhattacharyya K and Krishnan V 2016 Synergetic effect of MoS_2–RGO doping to enhance the photocatalytic performance of ZnO nanoparticles *New J. Chem.* **40** 5185–97

[54] Qin C, Wang Y, Gong Y, Zhang Z and Cao J 2019 CuO-ZnO hetero-junctions decorated graphitic carbon nitride hybrid nanocomposite: hydrothermal synthesis and ethanol gas sensing application *J. Alloys Compd.* **770** 972–80

[55] Cao P, Yang Z, Navale S T, Han S, Liu X, Liu W, Lu Y, Stadler F J and Zhu D 2019 Ethanol sensing behavior of Pd-nanoparticles decorated ZnO-nanorod based chemiresistive gas sensors *Sens. Actuators* B **298** 126850

[56] Singh S and Sharma S 2022 Temperature dependent selective detection of ethanol and methanol using MoS_2/TiO_2 composite *Sens. Actuators* B **350** 130798

[57] Zhang Y, Dong Z and Jia H 2023 Preparation of ZnO nanorod-based gas sensor and its ethanol gas sensing performance *Bull. Mater. Sci.* **46** 180

[58] Meng F *et al* 2019 ZnO-reduced graphene oxide composites sensitized with graphitic carbon nitride nanosheets for ethanol sensing *ACS Appl. Nano Mater.* **2** 2734–42

[59] Zhang S, Ding Y, Wang Q and Song P 2023 MOFs-derived In_2O_3/ZnO/Ti_3C_2TX MXene ternary nanocomposites for ethanol gas sensing at room temperature *Sens. Actuators* B **393** 134122

[60] Kalidoss R, Umapathy S and Sivalingam Y 2018 An investigation of GO-SnO_2-TiO_2 ternary nanocomposite for the detection of acetone in diabetes mellitus patient's breath *Appl. Surf. Sci.* **449** 677–84

[61] Kumar R and Ghosh R 2020 Selective determination of ammonia, ethanol and acetone by reduced graphene oxide based gas sensors at room temperature *Sens. Bio* **28** 100336

[62] Luo Y, Zhang D and Fan X 2020 Hydrothermal fabrication of Ag-decorated $MoSe_2$/reduced graphene oxide ternary hybrid for H_2S gas sensing *IEEE Sens. J.* **20** 13262–8

[63] Zhang H, Li Y, Yuan Z, Lei Y, Li X and Meng F 2023 Enhanced ammonia sensing performance based on $FeCo_2O_4/WO_3$/rGO ternary nanocomposites *IEEE Sens. J.* **23** 25698–707

[64] Sen S and Kundu S 2021 Reduced graphene oxide (rGO) decorated ZnO-SnO_2: a ternary nanocomposite towards improved low concentration VOC sensing performance *J. Alloys Compd.* **881** 160406

BIO-DATA

Nikita Jain is a research scholar at Delhi Technological University (DTU), Delhi, currently pursuing her research in the Department of Applied Physics since January 2019. She holds a Master of Technology (M.Tech.) degree in NanoScience & Technology (NST) from the Department of Physics, Delhi Technological University (DTU), Delhi, in 2014 and a Bachelor of Technology (B.Tech.) in Electronics & Communication Engineering (ECE) from Bhagwan Mahaveer Institute of Engineering & Technology (BMIET), Maharshi Dayanand University (MDU), Haryana in 2012.

She was a merit holder in her B.Tech. and qualified GATE-2012. She has been recognized for her academic excellence, receiving the Commendable Research Award from DTU in both 2023 and 2024. She also won the Best Poster Presentation Award at the International Conference on Nanomaterials and Optoelectronic Devices (ICNOC) 2022, held at Jamia Millia Islamia, New Delhi, from November 28th to 30th, 2022. Her current research focuses on developing ethanol gas sensors operating at room temperature, self-powered ethanol gas sensors, and exploring water splitting through hydroelectric cells (HEC).